THE PRINTING OF LASER GENERATED

HEAT IMAGES IN COBALT OXIDE

ON GLASS SUBSTRATES

by

William Maxwell Steen

A thesis presented for the
Degree of Doctor of Philosophy
of the University of London

ABSTRACT

The mass transfer effects between a jet of thermally sensitive chemicals and a spot heated by a laser, onto which the chemicals are blown, is studied. The system used is that of cobalt acetyl acetonate in a nitrogen carrier gas depositing cobalt oxide on a glass substrate.

The process is modelled mathematically.

The development of apparatus, and experimental techniques are described.

The process parameters are identified and their effects analysed and it is shown that shaped deposits can be made.

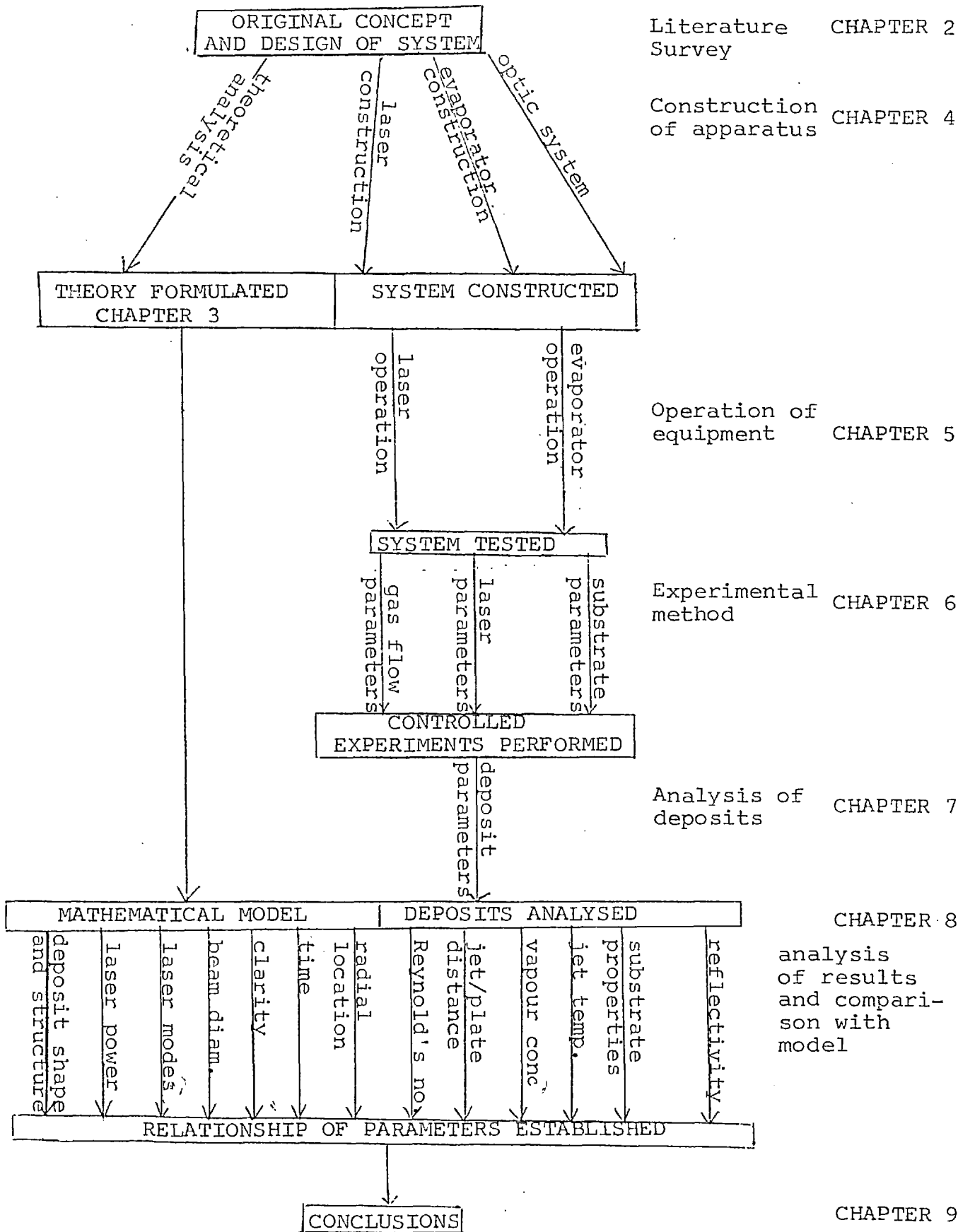A flow chart of the layout of this thesis is shown over the page.

ORIGINAL CONCEPT AND DESIGN OF SYSTEM

Literature Survey   CHAPTER 2

theoretical analysis   laser construction   evaporator construction   optic system

Construction of apparatus   CHAPTER 4

THEORY FORMULATED CHAPTER 3   SYSTEM CONSTRUCTED

laser operation   evaporator operation

Operation of equipment   CHAPTER 5

SYSTEM TESTED

gas flow parameters   laser parameters   substrate parameters

Experimental method   CHAPTER 6

CONTROLLED EXPERIMENTS PERFORMED

parameters   deposit

Analysis of deposits   CHAPTER 7

MATHEMATICAL MODEL   DEPOSITS ANALYSED

CHAPTER 8

analysis of results and comparison with model

deposit shape and structure   laser power   laser modes   beam diam.   clarity   time   radial location   Reynold's no.   jet/plate distance   vapour conc.   jet temp.   substrate properties   reflectivity

RELATIONSHIP OF PARAMETERS ESTABLISHED

CONCLUSIONS

CHAPTER 9

TABLE OF CONTENTS

CHAPTER 1

DEFINITION OF THE PROCESS TO BE INVESTIGATED AND

ITS POSSIBLE APPLICATION

1.1 The Process

A heat image of a suitably shaped aperture is formed on
a substrate by passing a laser beam of sufficient power through
the aperture and scaling with a lens. The hot image is then
printed by blowing a vapour of thermally sensitive chemicals
onto it. Decomposition of the vapour occurs only on the
heated regions of the substrate since the vapour is trans-
parent to the 10.6μ radiation beam and decomposition
temperature is only attained by the vapour at or very near
the substrate hot spot.

The laser is chosen as the source of power for two reasons:-
(i) It is capable of producing the power required.
(ii) It produces a nearly parallel beam of pure monochromatic
radiation capable of clear imaging. In particular, spot sizes
approaching the diffraction limit can be attained allowing
intricate shapes of the order of 2 x beam wavelength to be
imaged.

1.2 Possible applications

The object of this process is to be able to print intricately
shaped films of metal or metal oxide in a single step with a
non-contacting mask at near atmospheric pressure.

Such a printing method would be a new and potentially
useful tool, particularly in the manufactureof micro-electronic
circuits and components. In particular the possibility would
exist, if this system could be proven, of having a single
machine, which is readily automated, and could deposit, trim,
cut, drill, fill and weld. The commercial advantage this offers,
can be appreciated by comparison with the costly and time

consuming processes used at present - see appendix 1.

The size of the deposit depends at one extreme on the power available and at the other on the diffraction limit of the wavelength used. Apart from printing trade marks and decorative patterns, patterned surface hardening and surface alloying, all the major size groupings shown in table 1.1 of micro-electronic parts, could be printed.

Component	Approx Area	Track Width	Track Thickness
Printed circuit board	Xcm x Xcm	.02-1.0cm	$1\mu-200\mu$
Thin film circuits	2cm x 2cm	$20\mu-2mm$	$5A-200\mu$
Integrated circuits, monolithic, L.S.I.	2mm x 2mm	1μ	$1\mu-5\mu$

Table 1.1

The smaller components would require a shorter wavelength than the 10.6μ used here. For example that from a YAG laser (1.06μ) or an Argon laser ($4880°A$).

The possible composition of the deposits formed from the thermal decomposition of a vapour could be of any metal or metallic oxide - see Appendix 7. Alloys or doped layers could be deposited by mixing vapours as is common practice today. Epitaxial growth is also possible by thermal decomposition from the vapour, as for Si from SiH_4.

The method of shaping the power beam could be a shaped aperture, as is studied here; or advantage could be taken of the coherent, pure monochromatic characteristics of laser light. Thus the beam could be split and recombined to form Young's fringes - a possible method of making diffraction gratings,

basic circuit patterns etc. - or it could be reflected or
transmitted by a hologram to produce a beam of any power
structure required, as in the recent work at Loughborough
under Professor Butters on computer generated holograms,
called KINOFORMS. (46, 5).

The present study shows that good structured deposits
are possible, though difficult to achieve. It reveals the
main operating parameters and shows some of the main problems,
notably differential heating of different areas, 'skirt'
formation, and thermal damage of the substrate.

The causes of these problems are elucidated and solutions
suggested.

CHAPTER 2

PREVIOUS WORK

No work on the recording of an image by means of a laser beam as reported here is known to the author.

2.1 Previous imaging with a laser

A small amount of work of a similar nature has been reported recently. Most of this reported work uses the movement of a point focussed laser beam over a substrate to form the pattern. Thus Lydhin and Wilden[1] of the Philips Company in Aachen have recently developed a machine in which tracks are laid by chemical vapour deposition at the point focus of a laser beam. By this method they are reported to have deposited silicon, carbon, and silicon carbide on aluminium.

Von Gutfield and Chaudhari[2] and others[3] have studied writing and erasing on chalcogenide films with a Q switched laser producing a 5ns pulse at 0.3 nJ/μ^2 . This low power they showed by an analytical solution of the inhomogeneous thermal diffusion equations . . was sufficient to cause melting of this semi-transparent material to a depth of 100 °A; causing an optical switching effect due to a change from the mostly crystalline to the amorphous state. It is hoped that this may lead to an application using fast optical memories[4].

Other imaging techniques using a laser are more speculative and at present not fully written up. Professor Butters[5] group at Loughborough University are developing 'KINOFORMS'[46] as previously noted. Although considerable loss is expected from such a system it could be capable of producing any shaped wavefronts and in particular could give correct power densities over varying area shapes as is shown by this work to be necessary. Moran[127] has used a holographic lens for machining and there is a suggestion in the 'New Scientist'[128] to print a page of a book at a time by using a CO_2 laser, hologram of the page and heat sensitive powder. In fact type setting by scanning point focussed lasers is now practiced (Laser Focus, Jan 1976 p22).

Also using the coherent optical properties.
of a laser beam Dr. Little[6] of the Royal Holloway College is
reported to have devised a novel technique for depositing gold
in parallel lines by condensation on a zone heated by Young's
interference fringes formed by recombining a split 10.6μ wave-
length laser beam.

There is a proposal in Scott and Hodgett's paper[7] to use
a "printing mask" to shape a pulsed laser beam in order to etch
shapes in a thin film with a single pulse. They foresaw the
power control difficulties, problems with the thermal load on
the substrate and the difficulties with edge effects as found
here, but including "splashing" at high powers.

However no report has been found of a quantitative study
of the laser imaging process discussed here. Consequently the
background to this study is more removed and falls into four
categories:

a) previous thermal imaging work
b) previous work of a laser as a heat source
c) previous use of vapour deposition to form shaped
    deposits
d) other previous methods of forming shaped deposits.

2.2. Previous thermal imaging work

The imaging of high power radiation to a "point" focus
has been practiced using the sun as a heat source since the
lens was first invented or even prior to that by water droplets
in primeaval forests.

Scientific investigation of thermal imaging was being
conducted before the laser was invented (1960 for the ruby
laser, 1964 for the CO_2/N_2 laser) in arc image furnaces[8,9] and
in solar furnaces[9]. The size of the optics and the wide
frequency band employed in these techniques gave "ideal" image
diameters as reported by Cotton (p177 ref.9) of 0.63-20cms.
Thus although the power density of these furnaces ($40kw/m^2$-34.5
MW/m^2) is comparable to laser power densities[10] the focus and

optical properties are far cruder. The laser beam can be brought
to a point focus whose diameter is of the order of the wavelength
used. Consequently the application of these furnaces in mainly
for the heating of comparatively large areas and they have not
been used to produce a specific shaped image.

Deposition of material in localised patterns by means of
shaped heating elements is suggested by Powell et al[11] (p268).
A patent to this effect has been taken out by Toulmin[12] in which
he proposes to have shaped heating elements on the back of a thin,
low conductivity substrate.

The imaging of an electron beam is reported in R. Bakish's
book[13] in which a localised deposit, shaped by a mask, is formed
on the area heated by an electron beam. Due to the low penetration
required very good focus is possible, yielding spot sizes down to
0.1μ diameter. Two deposition routes were noted

a) at lower temperatures: by bombardment of the adsorbed
monolayer by electrons.

b) at high temperatures: by thermal degradation.

Very low deposition rates were recorded (0.5 x 10^{-5}μ/s @ 1000°C
for Ti) due to the vacuum requirements of the electron beam.
These rates make this technique disappointing.

Imaging with the shorter wavelength infra red and visible
radiation is a well established subject as in infra red and
normal photography but the power densities considered are many
orders too low to be of relevance to the present subject and
can not be considered as thermal imaging but rather photochemical
imaging.

2.3   Previous use of a laser as a heat source.

The imaging of high power laser beams has been mainly
confined to focussing by mirror or lens for the purpose of:-

(i)   drilling

(ii)   cutting and machining

(iii) welding

(iv)   micrometallisation

(v)   sputtering and spot image formation as previously
       described.

(vi)   surface alloying and surface hardening.

These activities are well described and reviewed in Ready's book[1]
and summarised in the papers by Scott and Hodgett[7] and Cohen and
Epperson[15]. Certain features of these processes are particularly
relevant to the present study and are noted below.

2.3.1 (i) Drilling

The review by Cohen and Epperson[15] highlights some of the
important physical aspects of working with power laser beams with
particular relevance to drilling. They are:

(i)   The problem of finding the beam spot size

(ii)   The significance of surface reflectivity and condition
       in deciding initiation power densities.

(iii) The importance of the temporal shape of a laser
       pulse due to the rapidly changing surface reflections.

(iv)   The problems in modelling the heat transfer due to
       the convective movement of a molten puddle, and the
       addition of latent heat effects due to both melting
       and vaporisation. Such models are typified by those
       of Landau[20] and Ready[21].

(v)   The obscure part played by the vaporisation plume.
       Ready[16] reports that it behaves as a black body while
       Sepole[17] has measured the absorption of plumes from
       low power interactions and found the plumes to be almost
       totally transparent.

(vi)   The effect of atmosphere on hole shape and peripheral
       debris. Gonsalves and Duley[18] also noted that higher
       powers were needed when drilling under vacuum than
       under atmospheric air. They considered this to be due
       to the reduced emissivity under vacuum.

(vii) Scott and Hodgett[7] note that the lens position affects
       the hole shape, being conical for short lens gaps and
       bottle shaped for longer ones.

Returning to point (i); Gonsalves and Duley[18,19] also noted the difficulties of measuring the beam spot size. On this parameter depends the calculation of power densities and thus any theoretical modelling relies critically on knowing its value. This is discussed in section 6.3.2.2.1 where their assumption that the hole diameter and beam diameters were the same is criticised. In modelling their work they built an approximate model based on a cylindrical source which would fit their results well if the beam diameter was half the size of the hole drilled. Considering the gaussian power distribution in the beam and the definition of the spot diameter as the diameter at which the power intensity has fallen to a value of $(1/e^2)$ the central value they would probably have witnessed this suggested diameter to be correct if they had calculated the beam diameter in a manner similar to that described here (sec. 6.3.2.2.)

Gonsalves and Duley[18] noted in drilling quartz that the critical value for a vaporisation front to be created was 390 W/cm. For the soda glass used here this would be expected at 220 W/cm (see section 8.2.9). The maximum power intensity used here was 60 ^{W}/cm and hence drilling or vaporisation is not expected to be a feature of this work.

2.3.2 Cutting and Machining

Cutting or machining with a laser, as for drilling, necessitates the formation of a vaporisation front, requiring power densities O [$5kW/mm^2$][132] which has no part in the present study.

So although much experimental work has been done on cutting (ref: 7, 23, 24, 25, 74, 31, 135, 132, 67)- notably after the work of Sullivan and Houldcroft[22] who showed that great gains could be made by using a concentric gas jet , particularly oxygen - most of this is irrelevant to the present study.

However two aspects are relevant:
  a) Patterning: The processes of cutting, machining or scribing a pattern in a thin film, mask material or

silicon wafer are now accepted commerical processes[15,27,28].
Considerable care is needed to avoid damaging the substrate
beneath a thin film when trimming resistors or capacitors
and short pulses from a Q switched laser are advocated.
These short sharp bursts are capable of vaporisation without
much thermal penetration. .In particular when trimming films
greater than $1500^{\circ}A$ thick a lip of resolidifed material may
form on the edge of the trimmed line. It is thought this is
due to lateral conduction in the film and could be cured by
even shorter pulses.

The He/Ne laser is now used to cut out photolithographic
masks for micro-electronic circuit manufacture by trimming
thin films on borosilicate glass as described by Rowe. and
Moule[29]. The advantages of using a laser are expected to
be their adaptability to computer control, the elimination
of detailed artwork and their ability to produce one off.
samples quickly. They chose not to use a $CO_2/N_2/He$ laser
because of the poor resolution possible with 10.6μ radiation
and the power absorption by the substrate at these longer
wavelengths.

b)   Modelling: A growing number of mathematical models of the
cutting process have and are being developed.

That of Gonsalves and Duley[30] is a relatively simple one of
a moving point source. It correlates quite well with their
fairly scattered results on cutting rate as a function of cut
width, power, material thickness and spot diameter. They
introduce the concept of the fraction of the beam striking
the target if a cut has removed some of the target.

That of Swifthook and Gick[53] is a more complex line source.
Gonsalves and Duley have another model, previously mentioned of
a cylindrical source.[57] While Scott and Dutta[74] are reported to have
developed a complex finite difference model, which includes mass
transfer effects in the slag layer.

2.3.3 Welding

Very attractive welds of quality equal to an electron beam
weld but with even less heat affected zone have been produced by
a laser[132,133,134]. Lack of sufficient depth of penetration is
one of the main difficulties. This relies on the little under-
stood process of keyholing, which appears to depend in a non
linear way on the incident power[32,132]. The welding of quartz
is discussed by Pfitzer and Turner[33]. Welding work up to 1972
is reviewed by Banas[34] and pulsed laser welding by Cohen and
Epperson[15]. Useful welding is possible with continuous powers
above 1kW[32]. The present study uses powers of up to 30W and
is thus not concerned with many of the problems identified by
welding studies.

2.3.4 Micrometallisation

A. Young is at present working with the author on the
localised condensation of the laser induced plasma plume. This
technique produces fairly thick ($1-2\mu$) traces having moderately
neat edges in a few milliseconds. It is a form of micrometallisatio
since the deposit is made of condensed vapour and ejected droplets.
The process is simple to engineer. The 1.06μ radiation from a
YAG laser is focussed through a glass slide or any transparent
sheet onto a target material lying directly beneath the trans-
parent sheet. If the power is adequate a plume of target material
bursts away from the hot spot ($\sim 5000-10,000^{\circ}C$[35]) and condenses
on the transparent sheet some 0.1mm away. Traces of conducting
copper and zinc have been prepared this way by Clarke[36], and it
seems possible to prepare fairly coarse conducting patterns.

2.3.5 Sputtering

Thin films have been laid down using a laser as the heat
source in a vacuum sputtering system. The advantage being that
the heat source is absolutely clean. Thus platinum has been
deposited by heating a small bead of Pt in a vacuum chamber by

Hess and Milkosky[37] who report an easily controlled process producing defect free uniform deposits. Smith and Turner used a ruby laser to evaporate various powders[38]. Groh[39] used a CO_2 CW laser on pressed tablets producing relatively high deposition rates. Even very high boiling point material has been deposited this way. Zavitsanos et al[40] deposited carbon from a graphite source using a ruby laser. But this method does not allow the formation of a shaped deposit, except by conventional contact masking.

2.3.6 Surface hardening and surface alloying

Industrial lasers are being used for localised surface hardening of transformation hardening metals, and also for localised surface alloying[131].

Much lower power densities are required for this than for welding and cutting. Seaman[131] suggests power densities of $230W/mm^2$ are necessary. Although this is several orders larger than the power densities discussed here, it is of interest in that the mathematical model derived here should fit this system, and the formation of hardened or alloyed patterns is a possible application of this process.

2.4 Previous use of vapour deposition to form shaped deposits

The subject of chemical vapour deposition has been thoroughly reviewed in the book by Powell, Oxley and Blocher (1966)[11]. The general trend in vapour deposition work has been to concentrate on "throwing power" or "covering power" producing uniform deposits over large areas. Thus in the electronics industry, a shaped deposit is made from a uniform deposit by differential etching using some masking technique - see appendix 1, rather than differential deposition.

The direct production of a shaped deposit from the vapour was studied by Davies[41] who examined the deposit shape formed in a varying mass transfer field under an impinging jet. This work which was done under the author's supervision, forms the background

to the mass transfer side of this present study.

A patterning process which could perhaps qualify as being a vapour deposition process not dependent on a thermal image is that reported by Jackson and Eldridge[42] who deposited Nichrome films in lines by spark deposition. Their process had a minimum line width of 50μm.

However, nearly all shaped deposits from the vapour are at present made by some contact masking technique not by localised deposition.

2.5 Previous methods of forming shaped deposits

To delineate the shape of a deposit requires some differential field property for example a differential thermal field is the subject of the present study. It has been seen that this is not the common route for making shaped deposits.

Differential field properties which could be used for patterning can be listed:-

(i)   Pressure fields – This includes standard printing, scribing, writing, engraving, gold leaf work and silk screening processes. They can all, particularly the silk screening process, be used in conjunction with electroplating by forming the pattern in a conducting ink on a nonconducting substrate. On heating, the the ink becomes a sintered metal layer which can be electroplated. – see appendix 1.

(ii)   Chemical potential fields – achieved by masking or deactivating certain areas which will then be differentially etched.

        This is a normal shaping technique in the electronics industry.

The process is to form a uniform film on a substrate, coat it with a u/v sensitive varnish, expose this to a pattern in u/v light, the exposed areas harden and the unexposed can be dissolved, leaving a contact mask on the original film. This can now be etched only where there is a hole in the mask. Wax can also be used as the mask and patterned mechanically or by heat.

Alternatively plating only through the mask holes is possible.

The resolution of this method is dependent on the resolution of the mask pattern, using u/v light it is $O[.1\mu]$.

(iii) Electric fields:
Using shaped electrodes localised deposition or erosion is possible. The resolution is only $O[50\mu]$ [43,44] due to the movement of the electrodes caused by the flow of electrolyte and the surface movement due to the formation of the shape.

(iv) Thermal fields - as already discussed, and studied here.

(v) Mass transfer or concentration fields:
Impinging jets are the usual method of forming these fields. These are quantitatively discussed by Davies[41] and commercially used in tinting some types of float glass. Metallisation and spray coating techniques also fall into this category; as does Young's method of micrometallisation (page 20). None have a high level of resolution. Young's method is the most accurate with a resolution of $O[0.2mm.]$

(vi) Electromagnetic radiation field - normal photography, infra red photography, x-ray photography etc. This plays a particular part in making masks using light or u/v sensitive varnishes as in (ii). The resolution is $O[.1\mu]$.

(vii)   Magnetic fields – as in tape recorders etc.
        Visible 3D shapes are not normally, if ever, made this
        way.

(viii) Gravity or centrifugal fields – possibly the shaping
        processes for continents but not small patterns.

(ix)   Surface adhesion – glitter patterns etc. formed on
        differentially glued surfaces.

CHAPTER 3

THEORETICAL ANALYSIS

3.1 Introduction

Laser interactions with solid matter fall into four distinct subject areas.

    (i)   Heat transfer studies

   (ii)   Hydrodynamic studies

 (iii)   Thermal and shock stress studies

 (iv)   Atomic physics studies

The heat transfer studies are usually based on a classical thermal conduction model starting with an analytically soluble geometry. More advanced models allowing for melting[14], vaporisation[14,57], keyholing[136] and plasma[47,48] formation have been developed. These phenomena, more complex than straight heating, can be expected for power densities in excess of $10^6 W/cm^2$ which is a clear two to three orders of magnitude greater than that discussed here.

Hydrodynamic effects become significant when vaporisation occurs at the surface, particularly when sonic shock waves occur due to the emission of hot vapour as in the deflagration model of Pert[47] and Bobin[48]. These phenomena can be expected with energy intensities $10^8 W/cm^2$.

Thermal stress is important in this study and is discussed in section 8.2.1.2.1.. Shock stress due to sudden heating generating a shock wave capable of reflection within the substrate resulting in chipping of the surface requires power intensities $\sim 2000 W/cm^2$ as a 10ns pulse and is not expected in this present study.

Atomic physics studies are concerned with the interaction of photon avalanches with matter (the inverse Bremsstrahlung effect

—ejection of electrons by collision with photons), Or the
possibility of increasing material density by shock and thermal
effects to stimulate atomic fusion, this requires power intensities
$>10^{13}$W/cm^2 [14] and is well beyond the power range discussed
here.

In this chapter a mathematical model of the laser heating
and vapour deposition process is drawn up. Since none of the
work reported here uses power intensities $>10^4$W/cm^2 most of the
phenomena just reviewed do not occur. It is thus hypothesised
that a thermal conduction model with surface heat loss would
describe the present deposition process.

3.2 Physical Definition of the process to be modelled

For the purpose of this calculation the process is assumed
to be as follows:-

An axi-symmetric laser beam, having a defined power distribution
strikes the surface of an infinitely extensive opaque substrate
of semi-infinite thickness, for a defined length of time.
Some of the incident radiation is reflected, the rest is absorbed
in a thin surface layer. Some of the absorbed energy is lost by
radiation and convection from the surface while the rest flows
into the bulk of the substrate by conduction.

A jet of hot vapour blows on the laser heated spot enhancing
the convective heat transfer and causing the formation of a deposit
due to the thermal decomposition of the vapour. The surface
reflectivity of this deposit may vary with thickness and mode of
deposition.

3.3 Previous Solutions

The problem as just stated has two stages firstly to
calculate the temperature profiles at any given moment, and
secondly using these temperatures to calculate the rate of
deposition from an impinging jet of thermally sensitive vapour.

No attempt at a solution for the temperature and deposit thickness formed in a process such as this is known to the author.

However, the solution to the transient heat conduction equations

$$\left(\frac{\delta T}{\delta t}\right)_{x,y} = \alpha \nabla^2 (T)$$ (3.0)

commonly ascribed to Fourier

as his second law has been the subject of numerous papers since they were first conceived in the 18th century. The whole of this work up to 1947 has been elegantly and methodically condensed by Carslaw and Jaegar[50] who list most cases in which an analytical solution exists.

The search for an analytical solution to the disc source, and moving disc source problems has fascinated workers with lasers[51,52,53,54,136] and those in the field of welding.[112] They have produced solutions for formal models which do not always suit the practical problem.

The solutions follow a similar pattern in each case. It is in summary:-

a) The temperature history within an unbounded medium due to and instantaneous point source of heat is (ref. 50 p256)

$$T_{r,\phi,z} = \frac{Q}{8(\pi\alpha t)^{3/2}\rho c} \exp(\frac{-r^2 + \bar{r}^2 - 2r\bar{r}\cos(\phi - \bar{\phi})}{4\alpha t})$$

$$x \exp\left(-\frac{(z - \bar{z})^2}{4\alpha t}\right)$$ (3.1)

where:-

$T_{r,\phi,z}$ = temperature at location (r, ϕ, z) $^\circ$K

α = thermal diffusivity m^2/s

t = time   s

Q = incident energy J

$\bar{r}, \bar{\phi}, \bar{z}$ = coordinates of the point source in radius, radial direction, and depth.

ρc = heat capacity J/m^3 $^\circ$K

b) The temperature history of an instantaneous point
   source in a bounded medium of thickness, D, is
   found by the method of images (ref. 50 section 10.10).
   In this method it is observed that a symmetric array
   of sources creates an adiabatic line between them, and
   other arrangements, constant temperature lines. The
   effect of each source or sink is described by equation
   3.1 and since the equation being integrated ($(\frac{\delta T}{\delta r})_{r,\phi,z} = \alpha \nabla^2 T$)
   is a linear equation the effect of all the sources
   together is the sum of all their 3.1 type equations.

Thus:-

$$T_{r,\phi,t \atop bounded} = \frac{Q}{8(\pi\alpha t)^{3/2}\rho C} \exp\left(\frac{-r^2 + \bar{r}^2 - 2r\bar{r}\cos(\phi - \bar{\phi})}{4\alpha t}\right)$$

$$x \sum_{n=-\infty}^{n=+\infty} \sigma_n \exp\left(-\frac{(z - 2\pi D \pm \bar{z})^2}{4\alpha t}\right) \qquad (3.2)$$

where the notation is as given for equation 3.1 and

σ_n = 1 when both sides are insulated

σ_n = $(-1)^n$ when only the side z = 0 is insulated the
      other being held at T = 0 $^{\circ}$K

D   = thickness of the bounded medium of infinite extent.

c) The temperature history within a bounded medium due to an
   instantaneous disc source of given incident power distribution
   is found by integrating the effects of a number of point
   sources of varying power over an area.

Thus, following Brugger[52], for an instantaneous surface disc
source of radius R and of Gaussian profile on a slab of
thickness D:-

$$T_{i \atop gauss} = \frac{\hat{Q}}{\rho C(\pi\alpha t)^{\frac{1}{2}}} \frac{R^2}{R^2 + 4\alpha t} \exp\left(-\frac{r^2}{R^2 + 4\alpha t}\right)$$

$$x \sum_{n=-\infty}^{n=+\infty} \sigma_n \exp\left(\frac{(z - 2nD)^2}{4\alpha t}\right) \qquad (3.3)$$

and for an instantaneous uniform disc source:-

$$T^*_{i \, \text{uniform}} = \frac{\hat{Q}R}{\mathcal{C}C(\pi\alpha t)^{\frac{1}{2}}} \sum_{n = -\infty}^{n = +\infty} \sigma_n \exp\left(-\frac{(z-2nD)^2}{4\alpha t}\right)$$

$$\times \int_0^\infty e^{-kt\lambda^2} J_0(r \lambda) \, J_1(R\lambda) \, d\lambda$$

$\hat{Q}$ = incident central energy density J/m^2

J_0, J_1 are Bessel functions.

For a semi infinite slab, $D = \infty$ (i.e. $n = 0$ case only), the uniform disc source solution has been solved numerically and graphed by Deming et al[51].

d)   The temperature history within a bounded medium due to a continuous disc source of given power distribution is found by integrating the instantaneous disc source with respect to time.

Thus for a uniform continuous disc source on the surface of an infinitely extensive medium of thickness D[(52)]:

$$T_{c \, \text{uniform}} = \frac{Q'R}{C2\alpha} \sum_{n = -\infty}^{n = +\infty} \int_0^\infty J_0(r \lambda) \, J_1(R\lambda) \, S_n(z,\lambda) \, d\lambda \quad (3.5)$$

with:

$$S_n(z\lambda) = \frac{1}{\lambda}\left[\exp(-\lambda|z - 2nD|) \, \text{erfc}\left(\frac{|z \, T \, 2nD|}{(4\alpha t)^{\frac{1}{2}}} - \lambda(\alpha t)^{\frac{1}{2}}\right)\right.$$

$$\left. - \exp(\lambda|z - 2nD|) \, \text{erfc}\left(\frac{|z - 2nD|}{(4\alpha t)^{\frac{1}{2}}} + \lambda(\alpha t)^{\frac{1}{2}}\right)\right]$$

where Q' = central power density W/cm^2

Once more for $D \longrightarrow \infty$, i.e. $n = 0$ terms only, the numerically derived solutions have been graphed by Deming et al [51]. They are shown in figure 3.1. These solutions do not agree with the results of Guenot and Racinet[54] nor with those found here.

This is probably due to truncation errors in solving the
Bessel functions.

The solution for the case of a continuous disc source of
Gaussian power profile is only available for the centre point
$r = z = 0$ on a semi-infinite slab, $D \longrightarrow \infty$[14], (the units do
not balance in Bruggers alternative)

Thus
$$T_{c(0,0,t)gauss.} = \frac{Q'r_b}{k\pi} \tan^{-1} (\frac{4\alpha t}{r^2_b})^{\frac{1}{2}} \qquad (3.7)$$

where $Q' = (P_t/\pi r_b^2)$ Wm^{-2}

$\quad$ k $\quad$ = thermal conductivity $\quad Wm^{-1}$ $^{\circ}K^{-1}$

$\quad$ P_t = total incident power $\quad$ W

and in particular the central equilibrium temperature is:-

$$T_{c(0,0,)gauss.} = \frac{Qo\ r_b\sqrt{\pi}}{2k} \ ^{\circ}K \qquad (ref: 14\ p83) \qquad (3.8)$$

These analytical solutions have been applied to laser work with
fair success, yielding good semi-quantitative evaluation for
drilling and cutting etc. Gonsalves and Dules[55] used a moving
point source solution as an approximation to the solution for
a small moving disc source. This model, straight from Carslaw
and Jaegar, gives reasonable agreement with the fairly scattered
results. Asmus and Baker[126] developed a cylindrical source model
for explaining phenomena in drilling this was developed by
Gonsalves and Dules[18] who acknowledge that although the correct
trends are revealed the experimental fit was poor. Similarly
Swifthook and Gick[53] developing Rosenthal's work[112] attempted
to describe the hypothesised and hoped for key holing with a line
source. This model does give fair agreement with weld pool
dimensions but does not give any indication on depth of penetration.

However, in the words of Brugger[52], "in other cases the
resulting series expansions offer no advantage over numerical
techniques". It might be added that even armed with this class
of analytical solution, to obtain a number from it would require
$\quad$ a numerical

technique as Deming et al[51] found and even then the incompatibility
of their graphs (fig.3.1) for $R^* = 0.0$ and $R^* = 0.01$, bears witness
to the possibility of truncation errors when obtaining an answer
this way.

These cases, however, are not the solution to the problem
as stated, because:-

a) They lack any convection and radiation heat loss from the
    surface. They could not satisfy this condition without losing
    the linearity upon which all integration from an instantaneous
    point source depended.

b) They are not able to allow for variation in surface reflectivity
    during deposition, which might be important.

c) They are not adaptable to a pulsating power input which could
    be a development of this process.

The way ahead is seen to be an analogue computer technique[56]
or a finite difference method with the answers checked against an
analytical solution for a special case.

Few models of this form have been developed partly due to the
very large computer time and storage required for a solution. Scott[57] &
Dutta[74] have developed a refined model including melting and
vaporisation. Ready[14] deduces the relevant differential equations
for various situations, including melting, but does not attempt a
solution. Landau[137] developes some useful dimensionless forms of
the differential equations for problems involving moving melting
boundaries.

3.4 Choice of numerical technique

The solution of linear second order partial differential
equations which are elliptic in the space coordinate system and
parabolic in the time coordinate system as presented here can be
achieved by both explicit and implicit methods. (ref: Dorn and
McCracken[58]).
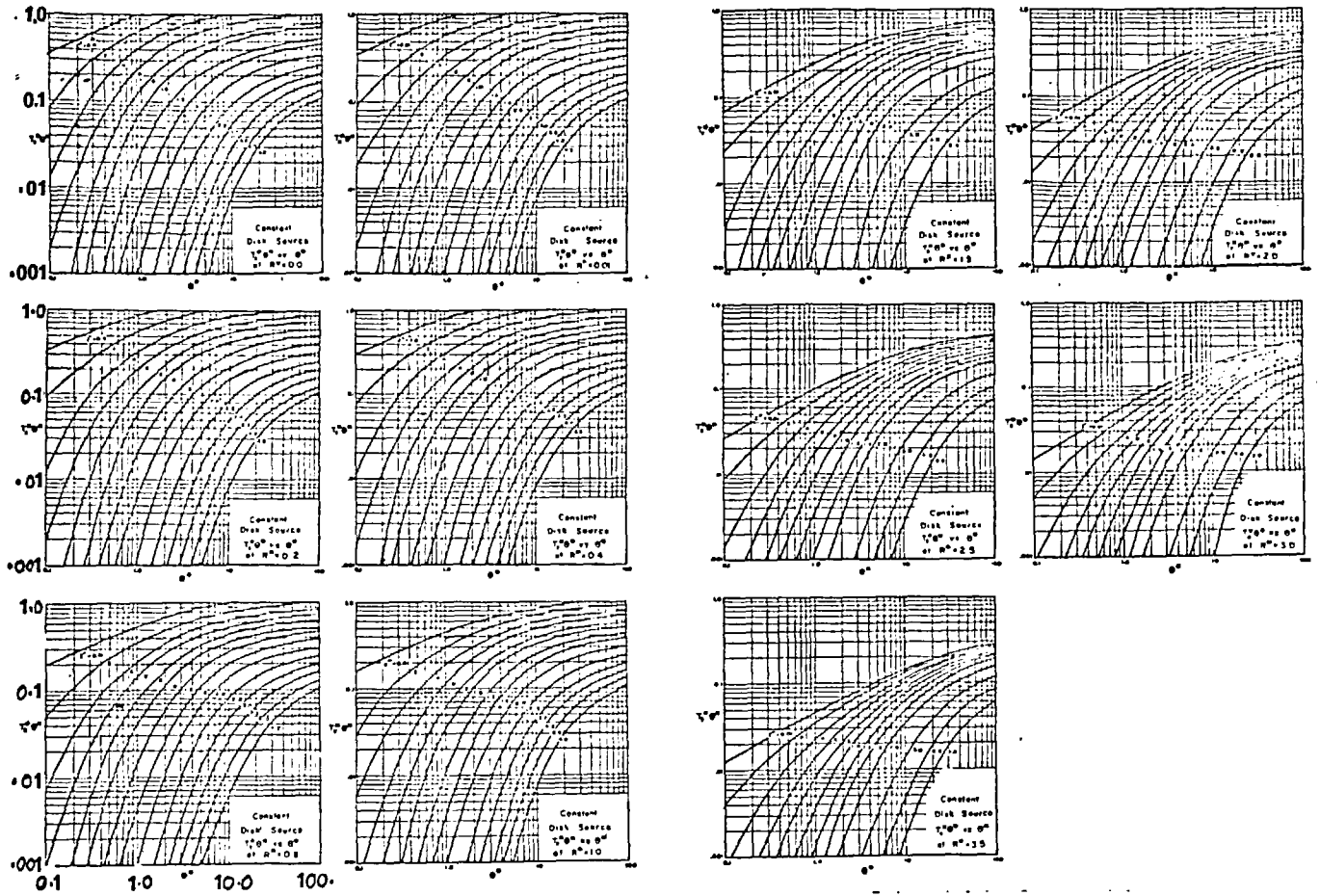
Fig 3.1

Thermal History Curves according to Deming et al (51) for a constant disc source with no surface heat loss

$$T_2 {}^* \Theta^* = \frac{T \pi k d_b}{P(1-r_f)} = \text{dimensionless temperature } T^*$$

$$\Theta^* = \frac{4 \alpha t}{r_b^2} = \text{dimensionless time} \qquad \Theta^*$$

$$z^* = y/r_b = \text{dimensionless depth}$$

$$R^* = r/r_b = \text{dimensionless radius} \qquad R^*$$

Within each class different solving techniques are as numerous as patent medicines, though more effective. The points of merit between them are:-

  a) accuracy
  b) stability
  c) speed of computation.

The explicit methods calculate the temperature after one time interval from a knowledge of the temperatures and rates of change of temperature at the start of the interval. No iteration is required. But a flux signal cannot be moved by this calculation more than one, or possibly two graticules per calculation step. If the signal in reality should have moved further but is mathematically barred from doing so instability ensues. Thus the explicit methods are stable only with very small steps. The finite difference equation for an explicit method is shown for the simpler unidirectional case:

when:
$$\frac{\delta T}{\delta t} = \alpha \frac{\delta^2 T}{\delta x^2} \qquad (3.9)$$

by the forward difference equation:

$$T_{p_{t+1}} = T_p + \frac{\alpha \Delta t}{\Delta x^2} \left[T_w + T_e - 2T_p \right] \qquad (3.10)$$

in which the truncation error E_{o_t} found from the Taylor's expansion for each term is bounded by :

$$\left| E_{pt} \right| \leq \frac{\lambda (6\lambda - 1)}{12} \phi \Delta x^4 \qquad (3.11)$$

where
$$\lambda = \frac{\alpha \Delta t}{\Delta x^2} \qquad (3.12)$$

and
$$\phi \geq \left| (\frac{\delta^4 T}{\delta x^4}) \right| \qquad (3.13)$$

This forward difference equation is similar to the Euler solution for ordinary differential equations which is one of a family of solutions known as the Runge Kutta methods.

A special case of this forward difference equation is that of E. Schmidt[59] for unidirectional heat flow. It illustrates the point on stability.

By rearranging 3.10

$$T_{p,t+1} = \frac{T_{p+1} + T_{p-1}}{M} + (\frac{2}{M} - 1) T_p \qquad (3.14)$$

and if

$$M = 2 = \frac{\Delta x^2}{\alpha \Delta r}$$

$$T_{p,t+1} = \frac{T_{p+1} + T_{p-1}}{2}$$

which thereby makes his graphical plot method possible. Notice that the point B can not gain any signal of the coming heat in the first time interval.

temp / distance
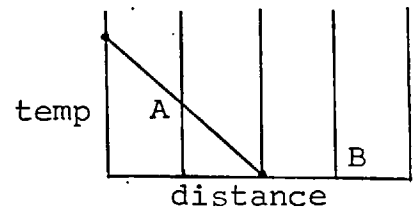
Taking the differential form of 3.14

$$\left| dT'_p \right| \leq \frac{1}{M} \left| dT_{p+1} \right| + \frac{1}{M} \left| dT_{p-1} \right| + (\frac{2}{M} - 1) \left| dT_p \right|$$

For errors not to grow $\left| dT'_p \right| \leq \left| dT_p \right|$

and assuming $\left| dT_{p+1} \right| \approx \left| dT_{p-1} \right| \approx \left| dT_p \right|$

Then $\left| dT'_p \right| \leq \left[\frac{2}{M} + (\frac{2}{M} - 1) \right] \left| dT_p \right|$

Thus for stability $M \geqslant 2$ and Schmidt's method is seen to lie on this limit. The accuracy of Schmidt's method is poor due to the large values of Δx and Δt used (see 3.11). Greater accuracy is obtained by taking finer steps as in the method of Dusinberre[60] in which M >> 2 or by a reconsideration of the forward difference equation used as in the Runge - Kutta - Simpson method[61,63,62].

Implicit methods fall into two main groups; relaxation type solutions, typified by Liebmann's[64] method of backward difference equations, and centre difference solutions typified by the Crank-Nicholson[65] method. The backward difference equations are:-

$$\left(\frac{\delta T}{\delta t}\right)_p = \left(\frac{T_{p,t} - T_{p,t-1}}{\Delta}\right) \tag{3.15}$$

and

$$\left(\frac{\delta^2 T}{\delta x^2}\right) = \frac{T_{p-1,\,t} + T_{p+1,\,t} - 2T_{p,t}}{\Delta x^2} \tag{3.16}$$

substituting for the simplified equation of heat flow (equation 3.9) gives

$$T_{p-1,\,t} + T_{p+1,\,t} - \left(2 + \frac{\Delta x^2}{\alpha \Delta t}\right) T_{p,t} + \frac{\Delta x^2}{\alpha \Delta t} T_{p\,t-1} = 0 = R(p,t) \tag{3.17}$$

In this it is seen that the temperatures around the point p at time t are calculated from the temperature at p for time t-1 only. The solution is possible by a relaxation technique.

This technique has been shown by Liebmann to be stable for all values of $\frac{\Delta x^2}{\alpha \Delta t}$ though the truncation error E_{pt} is bounded by

$$\left| E_{p,t} \right| \leq \frac{\lambda(6\lambda + 1)}{12} \, \emptyset \, \Delta x^4 \tag{3.18}$$

where

$$\lambda = \frac{\alpha \Delta t}{\Delta x^2} \tag{3.12}$$

and

$$\emptyset > \left| \left(\frac{\delta^4 T}{\delta x^4}\right) \right| \tag{3.13}$$

as for forward difference equation.

The small allowable step size for the explicit methods makes Liebmann's approach attractive. Since for the explicit methods $\lambda_{max} \leq \frac{1}{2}$ and requires about half as much work/step[58] as

Liebmann's method, so if $\lambda > 1$ using the Liebmann method will result in less computational work. The truncation error would, however, be greater. Liebmann found thatthis error is likely to be largest initially and so he suggested using very short initial time intervals.

The truncation error could be further reduced by considering a method similar to Richardson's[66] "deferred approach to the limit"; where if T_C is the true temperature, T_1 is its calculated estimate using a time interval of δt_1 and T_2 is another calculated estimate using a time interval δt_2 then:

$$T_C = T_2 + K_2 \, \delta t_2^2 \qquad\qquad (3.19)$$

$$\text{and} \quad T_C = T_1 + K_1 \, \delta t_1^2 \qquad\qquad (3.20)$$

assuming $K_2 = K_1 = K$ we get

$$K = (T_1 - T_2)/(\delta t_2^2 - \delta t_1^2) \qquad\qquad (3.21)$$

$$\therefore \, T_C = T_1 + (T_1 - T_2)\delta t_1^2/(\delta t_2^2 - \delta t_1^2) \qquad (3.22)$$

For a full comparison of explicit and implicit methods it is not enough to compare the truncation errors just quoted since there is also a rounding off error which is a function of the number of steps taken and thus would weigh in favour of implicit methods with large time steps.

The centre difference equations emphasise the fact that the partial differential equations, such as equation 3.9 are correct at a certain place and instant of time. All finite difference approximations are consequently made to centre on the same place and instant of time.

Considering the equation 3.9 for comparison and arranging the finite difference approximations to centre on the point p and time interval $(t + \Delta t/2)$ it becomes :
(

$$\left[\frac{T_{p_{t+\Delta t}} - T_{p_t}}{\Delta t}\right] = \frac{\alpha}{2}\left[\frac{T_{p+1_t} + T_{p-1_t} - 2T_{p_t}}{\Delta x^2}\right.$$

$$\left. + \frac{T_{p+1_{t+\Delta t}} + T_{p-1_{t+\Delta t}} - 2T_{p_{t+\Delta t}}}{\Delta x^2}\right] \qquad (3.23)$$

in which it is seen that

$$\left(\frac{\delta^2 T}{\delta x^2}\right)_{p_{t+\Delta t/2}} = \left[\frac{\left(\frac{\delta^2 T}{\delta x^2}\right)_{p_t} + \left(\frac{\delta^2 T}{\delta x^2}\right)_{p_{t+\Delta t}}}{2}\right] \qquad (3.24)$$

The truncation error E_{pt} for this method is bounded by

$$\left|E_{p,t}\right| \leq \frac{\lambda}{12} \emptyset \Delta x^4 \qquad (3.25)$$

which is smaller than Liebmann's method by a factor of $(6\lambda + 1)$. Further, by doubling λ the truncation error is only doubled not qua drupled as in Liebmann's method.

Crank and Nicholson have shown that these equations, not including the non linear radiation term as here, are stable for all values of λ though for large values a slowly damped oscillation may occur which would absorb considerable computing time in the iteration step to calculate $T_{t+\Delta t}$.

The accuracy and stability of this route is attractive and if modified to have small time steps initially, with large ones later, quite large time spans could be covered within the standard computing categories allowed.

This computing route was chosen and is discussed in greater detail in the following sections.

3.5 Derivation of the mathematical model

3.5.1 Assumptions

The model has to fit the situation described in section 3.2

The assumptions recalled are:-
a) The system is axi-symmetric
b) The substrate is infinitely extensive and of either finite or infinite depth.
c) The jet size is large compared to the heat spot
d) Thermal properties of the substrate are independent of temperature over the temperature range considered.

Assumptions b, c, and d are not necessary to the calculation but are felt to describe the system being investigated with sufficient accuracy.

3.5.2 Mathematical statement of the problem

The heating of a semi-infinite body by a disc surface source with convective and radiant cooling is governed by the following set of equations :-

within the body of the substrate:

$$\left(\frac{\delta T}{\delta t}\right)_{r,y,t} = \alpha\left(\frac{\delta^2 T}{\delta r^2}\right)_{r,y,t} + \frac{\alpha}{r}\left(\frac{\delta T}{\delta r}\right)_{r,y,t} + \alpha\left(\frac{\delta^2 T}{\delta y^2}\right)_{r,y,t} \quad (3.26)$$

at surface boundary:

$$-k\left(\frac{\delta T}{\delta y}\right)_{r,o,t} = \frac{P(1 - r_f) - h_{tot}\Delta T}{A} \quad y = 0 \quad t > 0 \quad (3.27)$$

at eastern boundary:

$$\lim_{r \to \infty} T_{r,y,t} = T_\infty \quad \text{and} \quad \lim_{r \to \infty}\left(\frac{\delta T}{\delta r}\right) = 0 \quad (3.28)$$

at southern boundary:

$$\lim_{y \to \infty} T_{r,y,t} = T_{\infty} \text{ and } \lim_{y \to \infty} \left(\frac{\delta T}{\delta r}\right) = 0 \qquad (3.29)$$

at start (temporal boundary):

$$T_{r,y,o} = T_{initial} \quad \text{for } t = 0 \qquad (3.30)$$

at axial boundary:

$$\left(\frac{\delta T}{\delta t}\right)_{o,y,t} = \alpha \left(\frac{\delta^2 T}{\delta y^2}\right)_{o,y,t} + \frac{4\alpha}{\delta r}\left(\frac{\delta T}{\delta r}\right)_{\frac{\delta r}{2},y,t} \qquad (3.31)$$

$$\text{or } \left(\frac{\delta T}{\delta r}\right)_{o,y,t} \longrightarrow 0 \quad \text{as } r \to 0$$

3.5.3   The Various Calculation Regimes

A 40 x 40 space lattice was identified on a vertical section through the substrate as shown in the diagram (fig. 3.2).

This matrix of points was arranged to expand exponentially from the (1,1) corner, which is the surface point at the centre of the incident laser beam. It was divided into regions governed by different sets of equations i.e. the body and boundary regions. These regions are identified in the diagram (fig. 3.2) together with some of the FORTRAN coding used to identify individual lattice points.

The derivation of the governing equations and their finite difference forms are now discussed by regions.
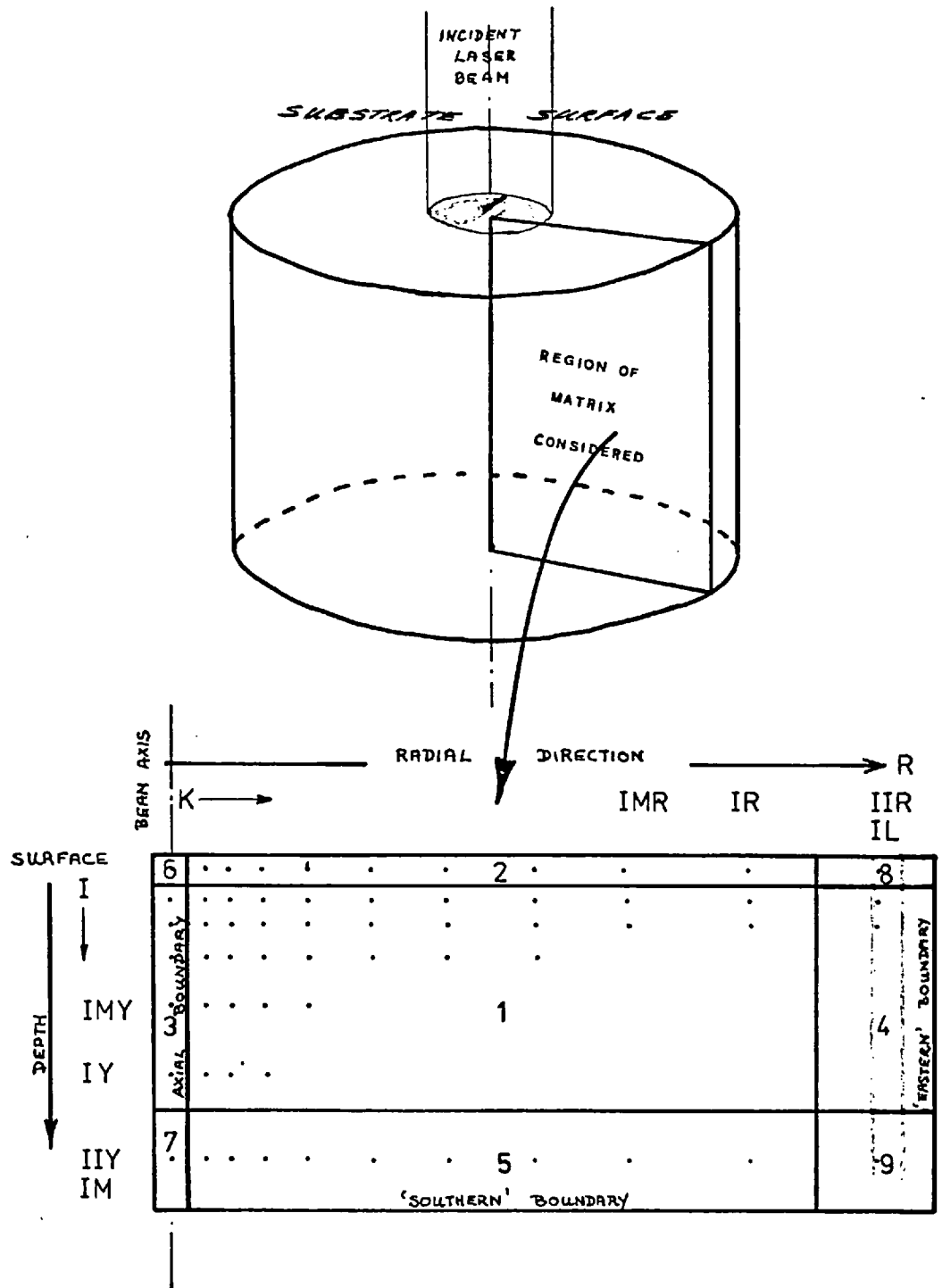
Fig 3.2   DIVISION OF THE SPACE LATTICE INTO DIFFERENT
CALCULATION   REGIMES

3.5.4 Derivation of the finite difference equation for each region

3.5.4.1 Within the body of the substrate - Region 1

Within the body of the substrate heat is flowing by conduction only. This is true since:

(a) There is no convection unless the substrate melts which is not the case here.

(b) Incident radiation of 10.6μ wavelength is totally absorbed by glass (see section reflectivity). The depth of penetration of the radiation would be expected to be of the order of a few microns only. The depth of penetration defined from Beer Lambert's law is the depth at which the incident radiation intensity has fallen to (1/e) the incident value.

The absorptivity of glass, k', to 10.6μ radiation is approximately 10^5 m^{-1} from Harry (ref 103).
Thus the depth of penetration would be expected to be: $I = I_o e^{-k'x}$.
where it is seen the depth of penetration, $d_p = \dfrac{1}{k'} \approx 10^{-5}$ m
for 10.6μ radiation. This distance is small compared to the space lattice considered ($\Delta y \approx 0.1$ mm)
Thus the incident radiation is effectively absorbed in the surface layer only.

(c) Any radiation produced within the glass is absorbed by the glass and does not constitute a bulk heat transfer mechanism of any significance. This is particularly true for the temperatures considered here ($< 800^{\circ}$C)

In drawing up a finite difference equation describing the flow of heat within a lattice of points there are two basic approaches:

a) Solve the differential equation for the flow of heat across each point.

In this case solve Fourier's 2nd law expressed in cylindrical coordinates:

$$\left(\frac{\delta T}{\delta t}\right)_{r,y,t} = \alpha\left(\frac{\delta^2 T}{\delta r^2}\right)_{r,y,t} + \frac{\alpha}{r}\left(\frac{\delta T}{\delta r}\right)_{r,y,t} + \alpha\left(\frac{\delta^2 T}{\delta y^2}\right)_{r,y,t} \qquad (3.26)$$

b) Solve the heat conservation equation about a finite annular block.

Method (a) was initially chosen and worked successfully using a constant spaced lattice for short heating times. However, it was proved (sec 3.5.4.4) that the 'southern' and 'eastern' boundaries could not be safely used at temperatures above $300^\circ C$ above ambient unless an overall heat balance was built into the calculation.

To avoid this added complexity an exponentially expanding lattice was created. The differentials of equation 3.26 were then carefully centred by using appropriately weighted gradients. Physically this meant that:

$$\left(\frac{\delta T}{\delta r}\right)_{r,y,t} = \left[\frac{(R_E - R_O)\,\dfrac{T_O - T_W}{R_O - R_W} + \dfrac{T_E - T_O}{R_E - R_O}\,R_O - R_W}{R_E - R_W}\right]$$

In which it is seen that the contribution to the slope at a point from, say the west, is different from the contribution of that point to the slope calculated at the western point. Such a situation was considered intrinsically unstable; so although considerable useful work had been obtained from this model a new one was made based on the block conservation interpretation of method (b) above.

Conservation of heat over a finite annular element
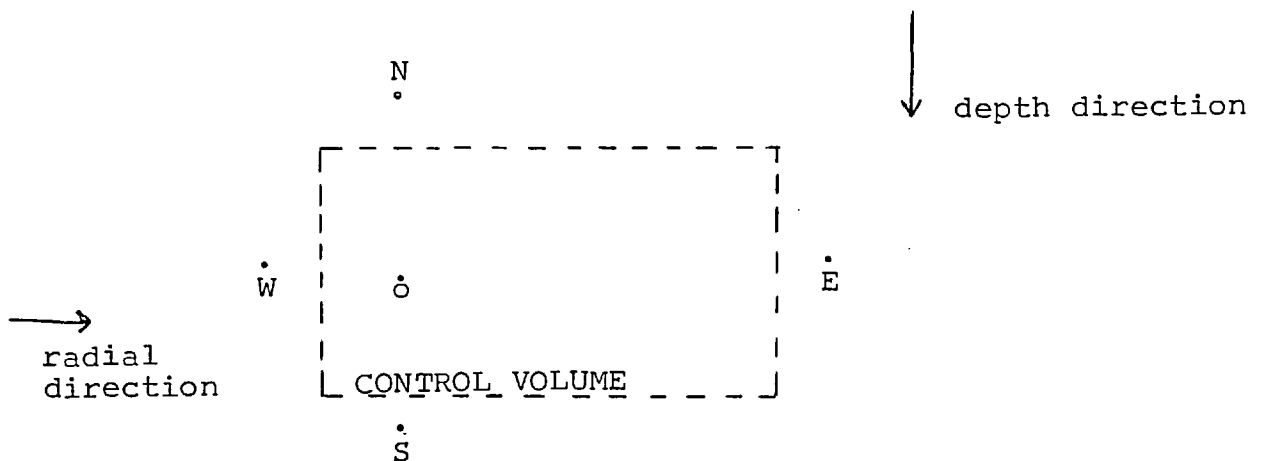
Fig 3.3   Showing location of lattice points to control volume

Flow of heat into block radially (r-direction):-

$$-k\left(\frac{\delta T}{\delta r}\right)_{wo,t+\frac{\Delta t}{2}} \delta y_W \ 2\pi \left(\frac{r_w + r_o}{2}\right) + k\left(\frac{\delta T}{\delta r}\right)_{Eo,t+\frac{\Delta t}{2}} \delta y_E \ 2\pi\left(\frac{r_E + r_o}{2}\right)$$

Flow of heat into block depth - y direction:-

$$-k\left(\frac{\delta T}{\delta y}\right)_{No,\ t+\frac{\Delta t}{2}} \delta r_N \ 2\pi r_M + k\left(\frac{\delta T}{\delta y}\right)_{os,\ t+\frac{\Delta t}{2}} \delta r_S \ 2\pi r_M$$

Heat accummulated within element:-

$$\rho C_p \ \delta r_N \ 2\pi r_M \ \delta y_W \left(\frac{\delta T}{\delta t}\right)_{o,t+\frac{\Delta t}{2}}$$

where $r_M = \left(\frac{r_E + r_w}{2}\right)$; $\delta r_N = \delta r_S$ and $\delta y_W = \delta y_E$ by construction

and $\delta r_N = \left(\frac{r_E - r_w}{2}\right)$ and $\delta y_W = \left(\frac{Y_s - Y_N}{2}\right)$

Expressed in finite difference form the heat balance becomes:-

$$\frac{T_o' - T_o}{\Delta t}\left(\frac{r_E - r_w}{2}\right)\left(\frac{Y_s - Y_N}{2}\right) = \alpha \left[\frac{r_E - r_w}{2}\left\{\left(\frac{T_s - T_o}{Y_s - Y_o}\right) - \left(\frac{T_o - T_N}{Y_o - Y_N}\right)\right\}\right]$$

$$+ \alpha \left[\frac{Y_s - Y_N}{2}\left\{\frac{r_E'}{r_M}\left(\frac{T_E - T_o}{r_E - r_o}\right) - \frac{r_w'}{r_M}\left(\frac{T_o - T_w}{r_o - r_w}\right)\right\}\right]$$

and defining $r'_E = \frac{r_e + r_o}{2}$ and $r'_w = \frac{r_w + r_o}{2}$

$$\therefore \ T_o' = T_o + \frac{2\alpha \ \Delta t}{Y_s - Y_N}\left[\left(\frac{T_s - T_o}{Y_s - Y_o}\right) - \left(\frac{T_o - T_N}{Y_o - Y_N}\right)\right]$$

$$+ \frac{2\alpha \ \Delta t}{r_E - r_w}\left[\frac{r_E'}{r_M}\left(\frac{T_E - T_o}{r_E - r_o}\right) - \frac{r_w'}{r_M}\left(\frac{T_o - T_w}{r_o - r_w}\right)\right] \qquad (3.32)$$

Equation 3.32 needs refining such that all the gradients are located in time at the same interval. The interval chosen depends on the interpretation of $\left(\dfrac{\delta T}{\delta t}\right)$ if $\dfrac{T_{o_{t+1}} - T_{o_{t-1}}}{2 \ \Delta t}$ had been chosen

it would have been centred at $t = t$ conveniently but would have been taking time steps of $2\Delta t$. This approach has been used by Richardson[66] in which he ran two parallel calculations one on even time intervals, the other on odd ones. This led to instabilities but allowed him to apply his "deferred approach to the limit" method (see p36).

Here the simpler interpretation $\left(\dfrac{\delta T}{\delta t}\right) = \left(\dfrac{T_o' - T_o}{\delta t}\right)$ is taken

and hence all gradients need to be expressed for the time interval $(t + \Delta t/2)$ as in the Crank-Nicholson method. It should be noted that only if the rate of rise of temperature is effectively linear over the time interval δt would the reference time t^* be $(t + \Delta t/2)$. If it were non linear then t^* would be:-

$$t^* = \left.\int_t^{t+\Delta t} t \ \frac{dT}{dt}dt \middle/ \int_t^{t+\Delta t} \frac{dT}{dt}dt\right.$$

However, whatever the value of t^* it is important that all gradients etc. are located on it; and thus even if a non linear rate of rise of temperature over δt is experienced provided all gradients vary with time in the same manner time average values of the form

$\dfrac{T_o' + T_o}{2}$ would all be located at the same value of t^*.

Thus the final form of equation 3.32 which was used within the body of the substrate is:-

$$T'_o = T_o + \frac{2\alpha \, \Delta t}{Y_s - Y_N}\left[\frac{\left(\dfrac{T_s - T_o}{Y_s - Y_o} + \dfrac{T'_s - T'_o}{Y_s - Y_o}\right)}{2} - \frac{\left(\dfrac{T_o - T_N}{Y_o - Y_N} + \dfrac{T'_o - T'_N}{Y_o - Y_N}\right)}{2}\right]$$

(3.33)

$$+ \frac{2\alpha \, \Delta t}{r_E - r_W}\left[\frac{r'_E}{r_M}\frac{\left\{\dfrac{T_E - T_o}{r_E - r_o} + \dfrac{T'_E - T'_o}{r_E - r_o}\right\}}{2} - \frac{r'_W}{r_M}\frac{\left\{\dfrac{T_o - T_W}{r_o - r_W} + \dfrac{T'_o - T'_W}{r_o - r_W}\right\}}{2}\right]$$

3.5.4.2 Surface Boundary - Region 2

3.5.4.2.1 Consider the surface grid points including a ficticous "northern" temperature above the surface
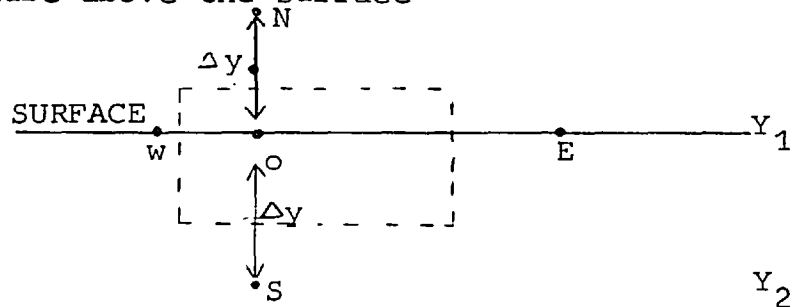
The relationship of the temperatures at these neighbouring locations to the central temperature after time δt is still given by the equation 3.33 provided T_N can be properly specified.

Now the surface heat flux is (assuming zero depth of penetration)

$$\frac{P_{net}}{A} = -k\left(\frac{\delta T}{\delta y}\right)_{r,surf,t} \qquad \text{for } t \geqslant 0, \ y = 0 \qquad (3.27)$$

$$\frac{P_{net}}{A} = -k\,\frac{T_s - T_N}{2\Delta y} \qquad \text{using finite difference form}$$

$$\therefore \ T_N = T_s + \frac{2\,P_{net}\,\Delta Y_1}{Ak}$$

where $\Delta y_1 = (Y_2 - Y_1)$

and similarly
$$T'_N = T'_S + \frac{2P_{net}\,\Delta Y_1}{Ak}$$

Thus the finite difference equation governing surface points only is:

$$
T'_O = T_O + \frac{\alpha\,\Delta t}{Y_S - Y_O}\left[\frac{\left(\dfrac{T_S - T_O}{Y_S - Y_O} + \dfrac{T'_S - T'_O}{Y_S - Y_O}\right)}{2}\right.
$$

$$
\left. - \frac{\left(\dfrac{T_O - T_S - \dfrac{2P_{net}(Y_S - Y_O)}{Ak}}{Y_O - Y_N} + \dfrac{T'_O - T'_O - \dfrac{2P_{net}(Y_S - Y_O)}{Ak}}{Y_O - Y_N}\right)}{2}\right]
$$

$$
+ \frac{2\,\alpha\,\Delta t}{r_E - r_w}\left[\frac{r'_E}{r_M}\frac{\left\{\dfrac{T_E - T_O}{r_E - r_O} + \dfrac{T'_E - T'_O}{r_E - r_O}\right\}}{2}\right.
$$

$$
\left. - \frac{r'_w}{r_M}\frac{\left\{\dfrac{T_O - T_w}{r_O - r_w} + \dfrac{T'_O - T'_w}{r_O - r_w}\right\}}{2}\right] \tag{3.34}
$$

It remains to define the meaning of $\left(\dfrac{P_{net}}{A}\right)$ the net power density absorbed by the surface layer. This term is made up of the fraction of incident radiation absorbed/unit area - $P(r)(1 - r_f)$ less the heat losses from the surface by convection $(h_c(T_{surf} - T_a))$ and reradiation $h_r(T_{surf} - T_a)$.

Thus
$$\frac{P_{net}}{A} = \left[P(r)(1 - r_f) - (h_c + h_r)(T_{surf} - T_a)\right] \tag{3.35}$$

where h_c = convective heat transfer coefficient $W/m^2\ {}^{\circ}K$

h_r = radiative heat transfer coefficient $W/m^2\ {}^{\circ}K$

T_{surf} surface temperature = $f(r)\ {}^{\circ}K$

T_a = ambient temperature $\quad {}^{\circ}K$

r_f = surface reflectivity to 10.6μ radiation

$P(r)$ = incident laser power density W/m^2 at radial location, r.

The calculation of $P(r)$, h_c and h_r is now discussed.

3.5.4.2.2. Laser power density distribution $P(r)$

Two distributions were investigated, a uniform disc source in order to check the model against the analytical solutions of Brugger[52], Ready[14], Deming et al[51], and Guenot and Racinet[54] and a Gaussian source in order to best approximate the actual distribution used in the experiments. The difference is shown in figure 3.4.

(i) Uniform Disc source

This is defined as a uniform power density over the incident area.

The power density was calculated as:

$P_L(r)$ power intensity W/m^2

radius r

beam radius r_b

fig 3.4

$$P(r) = \frac{P_{TOTAL}}{\pi r_b^2} \quad \text{for } 0 < r \leq r_b \qquad (3.36)$$

$$P(r) = 0 \qquad \text{for } r_b < r \qquad (3.37)$$
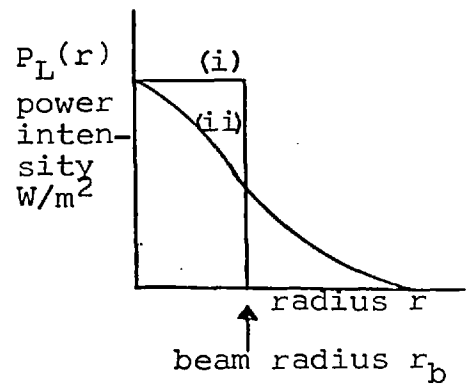
This distribution is equivalent to the ' disc' distribution of Brugger's and possibly the calculation of Deming et al though they did not specify which distribution they used but did however report using equations from Carslaw and Jaegar which assume this distribution.

(ii) Gaussian source

If the laser had produced a classic mode structure described by Kogelnik and Li[67] then the intensity distribution would be defined by a Laguerre - Gaussian profile for circular symmetry or a Hermite-Gaussian profile for rectangular symmetry (some cylindrical cavities are reported to have rectangular symmetrical modes - Ready[14] p 13) (see section on mode of oscillation 5.1. 3.) . For a laser operating in the fundamental $Te.m_{oo}$ mode the power density profile in either case is given as a Gaussian distribution of the form:

$$P(r) = P_o \exp(- r^2/r_b^2) \qquad (3.38)$$

from which:

$$P_{TOTAL} = \int_{o}^{\infty} P_o \exp(- r^2/r^2_b) \, 2\pi r dr$$

$$= P_o \, \pi r^2_b$$

where r_b = beam radius defined as the radial distance at which the power density has fallen to $1/e$ the central value.

Thus $$P(r) = \frac{P_{TOTAL}}{\pi r^2_b} \, e^{-(r/r_b)^2} \qquad (3.39)$$

3.5.4.2.3 Convective heat transfer coefficient

From Gardon and Cobonpue[68] at the stagnation point of a vertically impinging jet:

$$Nu_o = 13 \, Re^{0.5} \, \frac{D_j}{B} \qquad (3.40)$$

allowing for the standard correlations due to Polhausen[69] this becomes:

$$Nu_o = 13 \, Re^{0.5} \, \frac{D_j}{B} Pr^{0.33} = \frac{h_c D_j}{k_{gas}}$$

and hence $$h_c = 13 \, Re^{0.5} \, Pr^{0.33} \, \frac{k_{gas}}{B} \qquad (3.41)$$

where k_{gas} = thermal conductivity in W/m^oK of the boundary layer gas (i.e. nitrogen in this case) at the boundary layer film temperature

B = jet/plate distance $\quad$ m

D_j = diameter of jet nozzle $\quad$ m

This correlation has been extensively discussed by Davies[41] and applies to vertically impinging jets. The jets used in these experiments where mostly angled at 45° to avoid blocking the laser beam. Thus, this correlation is unlikely to be perfectly correct. However, it is fairly clear from the large number of correlations in this area that a dependence on $Re^{0.5} \, Pr^{0.33}$ is highly likely in the impingement zone and thus the correlation quoted would vary

correctly with Reynold's number but may require a more refined constant multiplier. Values of the thermal conductivity of nitrogen and the Prandtl number ($C_p \mu/k$) were taken for an average film temperature. It was not considered necessary to recalculate these values as the surface temperature changed in view of the relatively small convective loss term being calculated.

Further, the variation of the convective heat transfer coefficient with radial position relative to the jet axis on the edge of the impingement zone and in the wall jet region was ignored since:

(i) These calculations were assuming deposition in the stagnation region.

(ii) The stagnation zone extends over $R/D_j \leqslant 1.0$, (ref 41 p.79) ie $\pm$ 0.5cms from centre of impact which is a factor of 5 larger than the larger heated spots and so small radial displacements between jet and laser beam would not be expected to move the deposit out of the stagnation zone.

(iii) Experimentally measurable deposits could not be formed outside the impingement zone due to the fairly rapid condensation of the chelate on mixing with the cooler laboratory air.

3.5.4.2.4 Radiative heat transfer coefficient

The radiation loss from a hot spot of area A and temperature T_{surf} to hemispherical surroundings at a uniform temperature of T_a is given by the Stefan-Boltzmann equation:-

$$q_{loss} = A \sigma (1 - r_f)(T_{surf}^4 - T_a^4) \qquad (3.42)$$

upon expanding, this becomes:-

$$q_{loss} = A \sigma (1 - r_f)(T_{surf}^2 + T_a^2)(T_{surf} + T_a)(T_{surf} - T_a)$$

By definition the radiative heat transfer coefficient, h_r, is given by

$$q_{loss} = h_r A(T_{surf} - T_a) \qquad (3.43)$$

and thus

$$h_r = \sigma (1 - r_f)(T_{surf}^2 + T_a^2)(T_{surf} + T_a) \qquad (3.44)$$

Where T_a is the ambient radiative temperature here taken - as a first approximation - as the boundary layer bulk temperature. In actual fact it would be some integral over the hemispherical solid angle of the temperature of all surfaces with a view of the spot. The difference is considered negligeable.

3.5.4.3 Axial boundary - region 3

In the axial zone the control volume over which the heat balance is performed becomes a solid cylinder of radius $\Delta r/2$ as opposed to a hollow cylinder for all other regions.

The radial heat flow is:-

$$q_r = -k\left(\frac{\delta T}{\delta r}\right)_{\delta r/2,y,t} 2\pi \frac{\delta r}{2} \delta y$$

The depth heat flow is:-

$$q_y = +k\left(\frac{\delta T}{\delta y}\right)_{N_o} \frac{\pi \delta r^2}{4} - k\left(\frac{\delta T}{\delta y}\right)_{os} \frac{\pi \delta r^2}{4}$$

heat accummulated in the element:-

$$= \rho C_p \frac{\pi \delta r^2}{4} \delta y \left(\frac{\delta T}{\delta t}\right)_{1,y,t}$$

drawing up the conservation relationship and dividing by $\rho C_p \frac{\pi \delta r^2}{4} \delta y$:

$$\left(\frac{\delta T}{\delta t}\right)_{1,y,t} = \alpha\left[-\frac{4}{\delta r}\left(\frac{\delta T}{\delta r}\right)_{\frac{\delta r}{2},Y,t} + \left(\frac{\delta T}{\delta y}\right)_{N_o}\frac{1}{\delta y} - \left(\frac{\delta T}{\delta y}\right)_{os}\frac{1}{\delta y}\right] \quad (3.45)$$

expressing this in a finite difference form:

$$T_o' = T_o + \alpha \Delta t\left[\left(\frac{T_o - T_E}{r_{E1}}\right)_{av}\frac{4}{r_{E1}} + \left(\frac{T_o - T_N}{Y_o - Y_N}\right)_{av}\frac{2}{(Y_s - Y_N)}\right.$$

$$\left. -\left(\frac{T_s - T_o}{Y_s - Y_o}\right)_{av}\left(\frac{2}{Y_s - Y_N}\right)\right] \quad (3.46)$$

where subscript 'av' represents the time average value, as before

3.5.4.4. Eastern boundary - region 4

To the east the substrate is assumed infinite. Thus the temperatures calculated for the boundary region 4 must imply the subsequent thermal gradient to infinity.

The boundary conditions to be satisfied are:-

$$\lim_{r \to \infty} T_{r, y, t} = T_\infty \quad \text{and} \quad \lim_{r \to \infty} \frac{\delta T}{\delta r} = 0 \qquad (3.28)$$

It is not possible in this numerical technique to allow $r = \infty$ and so some approximation to the expected gradient at finite values of r is required.

To allow $\frac{\delta T}{\delta r} = 0$ at $r = r_{last}$ would alter the physical picture to that of a thermally insulated cylinder of radius r_{last}, and is therefore unacceptable.

To use a Liebmann[64] style backward difference at this boundary would avoid the need to know a temperature just outside the calculation region but it was found to lead to feed back instabilities and negative boundary temperatures which this technique then amplifies; arranging for all negative temperatures to equal zero only had partial success. The backward difference equation used was:-

$$(3.47)$$

$$\frac{T_O - T_{O_{t-\Delta t}}}{\Delta t} = \alpha \left[\frac{T_S + T_N - 2T_O}{\Delta y^2} + \frac{1}{r} \frac{T_W - T_E}{2\Delta r} + \frac{T_E + T_W - 2T_O}{\Delta r^2} \right]_{t - \frac{\Delta t}{2}}$$

using a constant spaced grid.

Thus knowing all Ts, except T_{E_t}, at times t & $t - \Delta t$ allows the calculation of T_{E_t} and similarly $T_{E_{t+\Delta t}}$.

What is required at this boundary, and the semi infinite southern boundary, is a relationship of the form:

$$T_{IL} = A \, T_{IR}$$

where IL and IR are shown in figure 3.2

Once the temperature just beyond the location IR is known T'_{IR} can be calculated.

At the eastern boundary where $r \gg \Delta r$ it is reasonable to expect the temperature profile for a limited distance, $2 \Delta r$, to be approximated by the profile for a linear transient flow of heat viz

$$T_{IR} = A + B \, \mathrm{erf}\left(\frac{X_{IR}}{\sqrt{4\alpha\Theta}}\right) \qquad (3.48)$$

where X_{IR} is an arbitrary distance of the order of the distance of location IR from the edge of the disc source.

$$\left(\frac{\delta T}{\delta X}\right)_{IR} = \frac{B}{\sqrt{4\alpha\Theta}} \, \frac{2}{\sqrt{\pi}} \, e^{-\left(\frac{X_{IR}}{\sqrt{4\alpha\Theta}}\right)^2} \qquad (3.49)$$

and similarly:

$$\left(\frac{\delta T}{\delta X}\right)_{IMR} = \frac{B}{\sqrt{4\alpha\Theta}} \, \frac{2}{\sqrt{\pi}} \, e^{-\left(\frac{X_{IMR}}{\sqrt{4\alpha\Theta}}\right)^2} \qquad (3.50)$$

where $IMR = IR - 1$.

Thus:

$$\emptyset = \frac{\left(\frac{\delta T}{\delta X}\right)_{IR}}{\left(\frac{\delta T}{\delta X}\right)_{IMR}} = \frac{e^{-\left(\frac{X_{IR}}{\sqrt{4\alpha\Theta}}\right)^2}}{e^{-\left(\frac{X_{IMR}}{\sqrt{4\alpha\Theta}}\right)^2}} \qquad (3.51)$$

$$\emptyset = e^{-\left\{\dfrac{(x_{IR}^2 - x_{IMR}^2)}{4\alpha\Theta}\right\}} \qquad (3.52)$$

Now
$$\left(\dfrac{\delta T}{\delta x}\right)_{IR} = \dfrac{T_{IL} - T_{IMR}}{X_{IL} - X_{IMR}}$$

and
$$\left(\dfrac{\delta T}{\delta X}\right)_{IMR} = \dfrac{T_{IR} - T_{IR-2}}{X_{IR} - X_{IR-2}}$$

$$\therefore \quad \emptyset = \dfrac{T_{IL} - T_{IMR}}{T_{IR} - T_{IR-2}} \dfrac{(X_{IR} - X_{IR-2})}{(X_{IMR} - X_{IL})}$$

$$= k \left[\dfrac{T_{IL} - T_{IMR}}{T_{IR} - T_{IR-2}}\right] = e^{-K/\Theta} \qquad (3.53)$$

where $K = \left[(x_{IR}^2 - x_{IMR}^2)/4\alpha\right]$

Assuming a relationship of the form $T_{IL} = T_{IR} \, e^{-\Psi}$ exists
Then it would be approximately true to say that;

$$\dfrac{T_{IMR}}{kT_{IR-2} \, e^{-K/\Theta}} \simeq \dfrac{T_{IL}}{kT_{IR} \, e^{-K/\Theta}} \simeq 1 \quad \text{for any given instant}$$

and thus the relationship just derived of $\quad T_{IL} = T_{IMR} + k(T_{IR}$
$- T_{IR-2}) \, e^{-K/\Theta} \qquad$ should be separable into two equations, one
of which is:

$$T_{IL} = k \, T_{IR} \, e^{-K/\Theta}$$

where $k \simeq 1$ and $K = f(r_{IR})$

i.e. $T_{IL} = T_{IR} \, e^{-\left[(r_{IR}^2 - r_{IMR}^2/4\alpha\Theta\right]} \qquad (3.54)$

Such a relationship between the temperatures near the eastern boundary was tested. The fit was found to be reasonable for situations where the flow of heat was approximately unidirectional radially - as in the small constant grid case -.Where the flow of heat was transverse to the assummed radial direction anomalous results were obtained - as with the large exponentialgrid where remote radial points were heated mainly by convection from above. In this latter case the peripheral temperatures were so low that the anomalous results were still not in gross error. An example of the fit is given in Table 3.5.1.

Table 3.5.1.

	Model value T_{IR-4}	Estimated T_{IR-3}	Model value T_{IR-3}	Estimated T_{IR-2}	Model value T_{IR-2}
Exp: grid	6.337	0.0	6.337	0.0	6.337
Const. grid	262.01	256.47	252.4	246.7	245.6

This relationship is not precise but appears to adequately describe this boundary until substantial gradients are being specified. In fact it appeared successful until the eastern boundary temperatures exceeded 300°C, when small errors in gradient upset the overall heat balance of the total region. This was sufficient to cause large accummulative errors (see figure 3.7).

The best safeguard against this both here and on the southern boundary was to use the exponential grid to remove these boundaries from having more than a few degrees temperature rise during the calculation period.

3.5.4.5. Southern Boundary - region 5

Two conditions are to be examined here;
a) semi-infinite condition and b) finite thickness

Case (a) Semi-infinite boundary condition

This is handled as for the Eastern boundary
with

$$T_{IM} = T_{IY} \; e^{-\; [(Y(M)^2 \; - \; Y(IMY2)/4\alpha\theta)]} \tag{3.55}$$

This was found to fit the previous three sets of temperatures tolerably well similar to the analysis of table 3.5.1

Case (b) Finite thickness

a) no heat transfer from the undersurface

$$T_{IM} = T_{IY} \tag{3.56}$$

b) with heat transfer by natural convection

$$- \; k \; (\frac{T_{IM} \; - \; T_{IMY}}{2 \, \Delta Y}) \; = \; h_{nat} \; (T_M \; - \; T_a)$$

$$\therefore \; T_{IM} = T_{IMY} \; - \; 2h_{nat}(T_M \; - \; T_a) \; \frac{\Delta Y}{k} \tag{3.57}$$

where $h_{nat} = f(Gr, \; Pr)$.
This case was not developed further.

3.5.4.6 The axial surface point - region 6

This point has both a surface and axial location and is hence described by the axial finite difference equation with the ficticious northern temperature T_N, and T_N' described by $T_N = T_S + \dfrac{2P_{net} \Delta y}{Ak}$ and $T_N' = T_S' + \dfrac{2P_{net} \Delta y}{Ak}$

as for surface points.

3.5.4.7 Axial southern boundary point - region 7

This point is only required for the calculation of the adjacent northern axial point. It is not used in calculating

its eastern neighbour.

Thus for the southern boundary points

$$T_{IM_{axial}} = T_{IY_{axial}} \ e^{-(Y(IY)^2 - Y(IMY)^2)/4\alpha\Theta} \tag{3.55}$$

for the semi infinite conditions and

$$T_{IM} = T_{IY}$$

for the finite condition without under surface cooling.

3.5.4.8 Surface point on Eastern periphery - region 8

This point is calculated as for all the eastern boundary from:-

$$T_{IL} = T_{IR} \ e^{-(R(IR)^2 - R(IMR)^2)/4\alpha\Theta} \tag{3.54}$$

3.5.4.9 Point within substrate at region 9'

This point is never used in the calculations

3.6 Calculation of the temperature profiles

The equations for the conservation of heat at each grid point just discussed, were solved simultaneously to calculate the temperatures at the next time interval.

The calculation is started by zeroing all the temperatures for the first and second time steps. These values are used to recalculate the values of the temperature at the second time step. A comparison of the newly calculated second time step temperature T_2 with the one used to calculate it, reveals the largest difference in the whole field - "BIG". If BIG is larger than some convergency limit, "TEST", then the calculation is repeated after resetting the values of T_2. A system of weighting whose value, W, depended on the iteration count, was used to damp oscillations which appeared if large gradients were encountered. Thus the reset value was:

$$TEMP(K,I,M) = (\frac{TEMP(K,I,M)*W + TEMP(K,I,IJ)}{W + 1}) \tag{3.58}$$

where TEMP(K,I,M) is the temperature at location K,I, and is
the most recent calculation of the 2nd time step temperature
which was calculated from the previous 2nd time step temperature
TEMP(K,I,IJ).

The value of TEST was chosen as (0.5 + TEMP(1,1,1)/1000)
to allow it to grow with the temperature scale of the system
being examined.

3.7 Calculation of deposit thickness and extent

3.7.1 Introduction

There are two mechanisms which control the rate of deposition;
a) the speed with which the chemicals can get to the surface
   (mass transfer control) and
b) the speed with which the chemicals on reaching the surface
   can react (chemical control). Which ever of these two
   mechanisms is the slower will decide the actual rate.

The previous stage of the calculation yielded , in particular,
the surface temperature profile. The rate of deposition of CoO
from the chelate vapour will depend upon this temperature whether
it is controlled by chemical rates or mass transfer rates.
So the quantities deposited during each time interval were
calculated from these temperatures and accummulated as the total
thickness.

3.7.2.1 Mass transfer controlled deposition rate

The work of Davies[41] was designed to establish the mass transfer
rates for a system similar to that used here.

From figure 9.1 of Davies the best fit for the rate of
deposition of CoO from a low concentration of Cobalt acetyl acetonate
vapour in a Nitrogen jet vertically impinging on a substrate without
recirculation in a chamber is:-

$$Sh_o \frac{B^2}{D_j^2} = 0.625 \, Re^{0.8} \, Sc^{1/3} \quad \text{for} \quad 1000 < Re < 5000 \tag{3.59}$$

where

$$Sh_o = \frac{k_m D_j}{D_{AB}} = \frac{\Delta s}{\Delta t} \frac{\rho_{AS}}{\rho_{Ae}} \frac{D_j}{D_{AB}} \tag{3.60}$$

$$Sc = \frac{\mu}{D_{AB}\rho}$$

$$k_m = \frac{\Delta s}{\Delta t} \frac{\rho_{AS}}{\rho_{Ae}}$$

ρ_{AS} = density of Co in solid CoO

ρ_{Ae} = density of Co in gas at jet exit

This equation allows for entrainment in the free jet prior to the stagnation point by one of the (B/D_j) factors. The other (B/D_j) factor allows for the effect of jet/plate distance on the boundary layer thickness.

For higher Re in the range 4000 $\rightleftharpoons$ Re $\rightleftharpoons$ 16000 Davies found:

$$Sh_o \frac{B^2}{D_j^2} = 5.7 \ Re^{0.52} \ Sc^{1/3} \qquad (3.61)$$

as the best fit to his data or:

$$Sh_o \frac{B^2}{D_j^2} = 10.0 \ Re^{0.5} \ Sc^{1/3} \qquad (3.62)$$

for the functional relationship theoretically predicted for the stagnation zone.

Since in this present work a jet exit Re in the range $300 \leqslant Re \leqslant 5000$ was used, equation 3.59, which allows for the slower flow conditions in the jet, was considered the most applicable.

Thus rearranging the relationship 3.59 and substituting 3.60 the differential thickness Δ s grown in time Δ t becomes:-

$$\Delta s = 0.625 \ Re^{0.8} \ Sc^{1/3} \frac{D_j \rho_{Ae} D_{AB} \Delta t}{B^2 \rho_{AS}} \qquad (3.63)$$

To calculate this requires the calculation of:

(i)   The jet exit Reynolds number, Re, with gas physical
        properties calculated at the film temperature.

(ii) The Schmidt number, Sc, at the film temperature

(iii) The diffusion coefficient, D_{AB}, of cobalt acetyl acetonate in N_2 at the film temperature

(iv) Density of cobalt in the cobalt oxide deposit, ρ_{AS}.

The reason for choosing to evaluate the gas physical properties at the film temperature is that the dimensionless correlation is trying to describe the concentration boundary layer and in particular the concentration gradient at the surface. Thus the boundary layer properties, which would be approximated by the properties at the film temperature, are nearest to the facts of the case.

3.7.2.2. Evaluation of the jet exit Reynolds number

By definition:-

$$Re = \frac{\rho u D_j}{\mu} = \frac{4G}{\mu D_j \pi} \tag{3.64}$$

where:
G = mass flow rate kg/s
D_j = jet diameter m
ρ = gas density kg/m^3
μ = gas viscosity kg/ms
u = gas exit velocity m/s

From Arnold's correlation (Perry[70] p 3.230)

$$\frac{\mu_2^o}{\mu_1^o} = \left(\frac{T_2}{T_1}\right)^{3/2}\left(\frac{T_1 + 1.47\,T_b}{T_2 + 1.47\,T_b}\right) \simeq \left(\frac{T_2}{T_1}\right)^{\frac{1}{2}}$$

where:
T_b = boiling point of gas, in this case N_2 (77.2°K)°K
T_1 = temperature for viscosity μ_1 °K
T_2 = temperature for viscosity μ_2 °K
o = at low pressures.

Since neither G nor D_j varies with temperature:

$$Re_1 = Re_2 \times \left(\frac{T_2}{T_1}\right)^{\frac{1}{2}} \tag{3.65}$$

where $Re_{0^oC} = \dfrac{4G}{\mu_{0^oC} \, D_j \pi}$

and μ_{0^oC} of nitrogen from Starling and Woodall (71) (p 103) is 1.67×10^{-5} kg/ms.

3.7.2.3. Evaluation of the Schmidt number, Sc

By definition: $\qquad Sc = \dfrac{\mu}{\rho \, D_{AB}}$

The gas density, ρ :

the gas density may be obtained from the gas law relationship:

$$\frac{1}{\rho_1} = \frac{zRT_1}{P \, m}$$

where z = compressibility factor obtainable from Nelson–Obert charts (70, p218) in this case $\simeq 1.0$.

$\quad$ m = molecular weight of gas, in this case 28

$\therefore \quad \rho_1 = \dfrac{Pm}{RT} = \dfrac{101.3 \times 28}{8.314 \times 273} = 1.249$ kg/m^3 at 0^oC

This value is to be compared with the value of 1.25 kg/m^3 at 0^oC given in the handbook of Chemistry and Physics 45th edition.

In general $\quad \rho_1 = 1.249 \times \dfrac{273}{T_f}$

The gaseous diffusion coefficient, D_{AB}:

$$D_{AB} = 0.32 \times 10^{-4} \text{ m}^2/\text{s} \quad \text{at} \quad 0^oC \text{ (see sec 3.7.2.4)}$$

for cobalt acetyl acetonate diffusing through N_2.

From these values:–

$$Sc_{0^oC} = \frac{\mu}{\rho \, D_{AB}} = \frac{1.67 \times 10^{-5}}{1.25 \times 0.32 \times 10^{-4}} = 0.417 \qquad (3.66)$$

To find the variation of Sc with temperature it is observed that:-

$$\frac{\mu_1}{\mu_2} = (\frac{T_1}{T_2})^{\frac{1}{2}}$$ Arnolds correlation (see 3.7.2.2)

$$\frac{\rho_1}{\rho_2} = (\frac{T_2}{T_1})$$ ideal gas law (see 3.7.2.3)

$$\frac{D_{AB1}}{D_{AB_2}} = (\frac{T_1}{T_2})^{3/2}$$ Chapman - Einskog equation (see 3.7.2.4)

$$\therefore \quad SC_2 = SC_1 (\frac{T_2}{T_1})^{\frac{1}{2}} . (\frac{T_2}{T_1}) . (\frac{T_1}{T_2})^{3/2}$$

$$\therefore \quad SC_2 \simeq SC_1$$

In fact the Schmidt number is approximately independent of the temperature.

3.7.2.4 Evaluation of the gaseous diffusion ceofficient : D_{AB}

From the Chapman - Einskog formula
(ref. Bird, Stewart and Lightfoot (72) 1960, Perry 14.20 (70)).

$$D_{AB} = 0.0018583 \sqrt{\frac{T^3 [1/M_A + 1/M_B]}{P\sigma_{AB}^2 \ \Omega_{AB}}}$$ (3.67)

where σ_{AB} = Leonard Jones parameter $\simeq \frac{1}{2}(\sigma_A + \sigma_B) \simeq 5.2$ A$^\circ$
(ref. Davies (41))

σ_A = atomic volume of species A — CoAcAt $\simeq 6.94$ A$^\circ$
(ref. Davies (41))

σ_B = atomic volume of species B — $N_2 \approx 3.56$ $^\circ$A (ref Davies (41)

Ω_{AB} = Leonard Jones function dependent on the dimensionless temperature and intermolecular potential field.

P = total pressure, atmospheres

D_{AB} = diffusivity of A through B cm^2/s

T = absolute temperature of the system ^{O}K

M_A = molecular weight of species A, CoAcAt

M_B = molecular weight of species B, N_2

Ω_{AB} is found from tables against the parameter $\frac{kT}{\varepsilon_{AB}}$ where $\varepsilon_{AB} = \sqrt{\varepsilon_A \varepsilon_B}$.

From melting point data Davies showed that for CoAcAt $\frac{\varepsilon_A}{k}$ = 1.92 Tm

= 384.0

and for N_2 $\frac{\varepsilon_B}{k}$ = 91.53 from established data

$$\therefore \qquad \frac{\varepsilon_{AB}}{k} = \sqrt{91.53 \times 382.0} = 187.4$$

and $$\frac{kT}{\varepsilon_{AB}} = 0.005 \ T$$

From which Ω_{AB} = 0.999 @ 500°K

= 0.84 @ 1000°K

For this work we will take Ω_{AB} = 0.98

σ_{AB} = 5.2 , M_A = 247.0, M_B = 28.0, P = 1 atmos.

$$\therefore \ D_{AB} = 0.0018583 \sqrt{\frac{T^3 \left[\frac{1}{247} + \frac{1}{28} \right]}{1.0(5.2)^2 \ (0.98)}}$$

$$= 71.247 \times 10^{-6} \ T^{3/2} \quad cm^2/s \qquad\qquad (3.68)$$

In particular D_{AB} = 0.798 cm^2/s @ 500°K in agreement with Davies results

and D_{AB} = 0.32 x 10^{-4} m^2/s @ 0°C.

The variation of D_{AB} with temperature is apparent as:

$$\frac{D_{AB1}}{D_{AB2}} = \left(\frac{T_1}{T_2}\right)^{\frac{3}{2}} \tag{3.69}$$

3.7.2.5 Evaluation of the density of Cobalt in CoO solid, ρ_{AS}

The density of CoO from Chemistry Handbook = 6450 kg/m^3

$\therefore$ density of Co in CoO = 6450 x $\frac{58.9}{74.9}$ = 5072 kg/m^3

It is assummed that the deposit is not significantly porous.

3.7.2.6 Evaluation of the incremental growth ΔS due to mass transfer

Substituting the temperature corrections for the Re equn 3.65 ρ_{Ae} and D_{AB} (3.69) into equation 3.63 gives:

$$\Delta S = 0.625 \ Re_1^{0.8} \ Sc^{\frac{1}{3}} \ \frac{D_i}{B^2} \ \frac{\rho_{Ae}}{\rho_{AS}} \ D_{AB1} \ \Delta t \ (\frac{T_2}{T_1})^{0.4} \cdot (\frac{T_1}{T_2}) \cdot (\frac{T_2}{T_1})^{1.5}$$

and substituting for the value of ρ_{AS}:

$$\Delta S = .000123 \ Re_1^{0.8} \ Sc^{\frac{1}{3}} \ \frac{D_i}{B^2} \ \rho_{Ae} \ D_{AB1} \ \Delta t \ (\frac{T_2}{T_1})^{0.9} \tag{3.70}$$

where T_2 = film temperature $^\circ$K, calculated as: $\frac{1}{2}$(bulk gas temperature .above boundary layer and average surface temperature during time interval)

T_1 = reference state, 273°K

3.7.3 Chemically controlled deposition rate

Davies (41) has shown experimentally that the chemically controlled heterogeneous thermal decomposition of cobalt acetyl acetonate proceeds at a rate described by the Arrhenius type first order equation:-

$$\log_{10}(\text{rate} \times 10^7) = 10.200 - 5.2214 \times \frac{1000}{T} \qquad (3.71)$$

at Re = 4637 and B = $9.07D_j$
the rate being measured in mm/s and T, the film temperature, in $^\circ K$. From this data on a first order reaction

$$\frac{\Delta s}{\Delta t} = 1.585 \times 10^{-\frac{5221}{T}} \frac{c_{AO}}{c_{AO_{Davies}}} \qquad \text{m/s} \qquad (3.72)$$

The concentration used by Davies was $c_{AO_{Davies}} = 0.68 \times 10^{-5}$ kg/m^3. The film concentration, c_{AO}, is related to the jet exit concentration, c_{Ae}, by:- $\quad c_{AO} = c_{Ae} \dfrac{D_j}{B}$

due to mixing in the free jet before impingement

$$\therefore \quad \frac{\Delta s}{\Delta t} = \frac{1.585 \times 10^{-\frac{5221}{T}}}{0.68 \times 10^{-5}} \; c_{Ae} \frac{D_j}{B}$$

which reduces to:-

$$\frac{\Delta s}{\Delta t} = 2.33 \times 10^5 \; e^{\frac{-12008}{T_f}} \; c_{Ae} \frac{D_j}{B} \qquad \text{m/s}$$

and $\therefore \quad \Delta s = 2.33 \times 10^5 \, \Delta t \; e^{\frac{-12008}{T_f}} \; c_{Ae} \frac{D_j}{B} \qquad \text{m} \qquad (3.73)$

3.7.4 Computation of thickness and extent of deposit

After the temperature profiles have been calculated for one incremental time step both the quantity deposited under mass

transfer control (3.70) and the quantity deposited under
chemical control (3.73) were calculated. The smaller was
the rate determining step and was taken as the incremental
thickness. A marker flag was stored with this value to show
which route had been chosen.

3.8 Special surface condition of variable reflectivity

It will be shown in chapter 7 that certain deposits formed
with black centres. SEM studies showed the blackness to be due
to the rough surface of the deposit in these areas. Such roughness
will reduce the reflectivity not only to visible radiation, as
shown by the blackness, but also to 10.6μ radiation.

In order to try and explain any effects due to this the surface
reflectivity was made to change in the mathematical model from
0.18 to 0.0 when the surface temperature exceeded $600^\circ C$, a
temperature at which these black centres are expected.

This is fairly simply arranged as in line 0280 after
introducing a dimensioned variable for the reflectivity at every
surface grid point (see appendix 5).

A very small, to negligible, reflectivity change from 0.18
to approximately 0.2 may occur as discussed in section 6.3.4.4
when very thin deposits are formed. To see if such a change could
explain the ease with which very thin deposits formed this change
was allowed in one computer run when the deposit thickness was less
than 0.1μ but greater than 0.001μ.

3.9 Convergency and operating efficiency of the programme

3.9.1 Selection of grid size

By varying the number of grid intervals within the beam
radius the accuracy of the programme could be tested. Obviously
the temperature profile should not depend upon this arbitrary
division. However, the fewer intervals chosen the faster will
be the computation due to the fewer points to be considered.
Figure 3.5 shows that the grid divisions cease to be a variable
for more than 5 intervals within the beam radius, and little
increased accuracy is gained by having more.

Fig 3.5   Matrix studies

Comparison of accuracy for various grid sizes

A — 10 sections in the beam radius

B — 5   "   "   "   "   "

C — 2·5 "   "   "   "   "

Calculation based on: $P/D_b = 16·6$ W cm^{-1}

$D_b = 0·00048$ m

$P = 8$ W

$Re = 2086$

$time = 2·3$ s

Surface Temperature °C

500

1000

Dimensionless radius R*
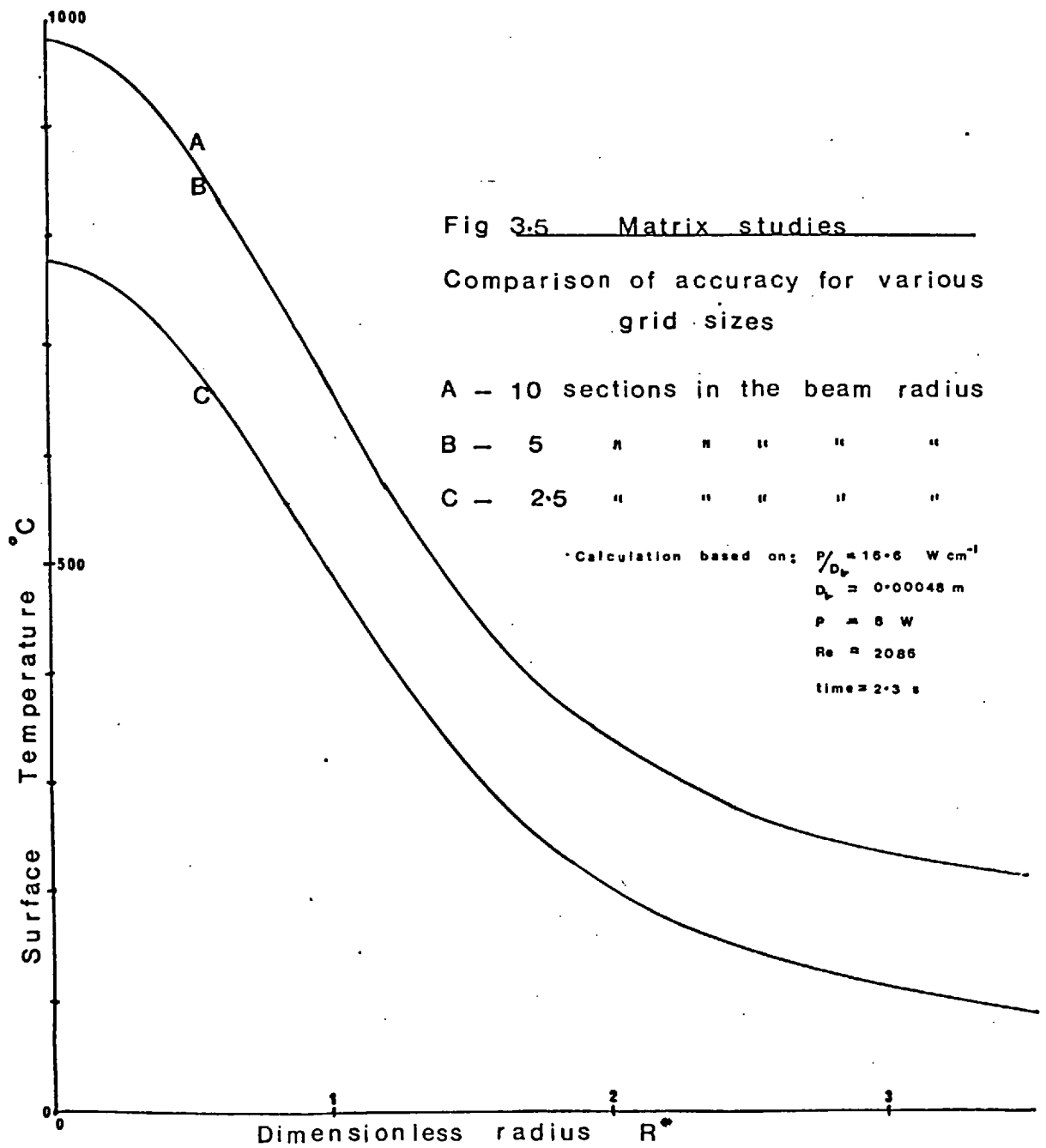
3.9.2 Selection of the best overall matrix

The time required for the solution of the equations about one grid point was found to be a fairly constant figure of 2.3 ms/ iteration using the Imperial College CDC 6400 computer. Thus the smaller the overall matrix the less computing time would be required. A further gain by using a smaller matrix was that it required less iterations to find a solution, though this is related to the value set for the convergency criterion. The penalty of a small matrix is poor accuracy.

Table 3.9.1 shows the analysis leading up to the chosen matrix of 24 x 10 exponentially expanding grid points.

3.9.3 Selection of the convergency limit, TEST

A too stringent value of the convergency limit, TEST, would achieve a degree of accuracy not needed and incur a considerable penalty in computing time.

Accordingly the value of TEST was varied to establish the value which gave reasonable agreement with the answers from stricter values of TEST but which had a lower iteration count. Table 3.9.2 shows the variation of iteration count and accuracy as a function of TEST. The runs were done on a 24 x 10 exponential matrix with the first 6 time intervals at $t = \Delta r_{1-2}^2/8\alpha$ followed by subsequent steps of $t = \Delta r_{1-2}^2/\alpha$. The final value selected was TEST = 0.5 + TEMP(1,1,1)/1000, allowing the limit to vary slightly with the scale of temperatures encountered.

3.9.4 Selection of the best value of Δt

A large value of Δt is required in order to solve the problem quickly but the value must not be so great that the model does not converge on a solution or that it converges on an inaccurate one.

The Crank-Nicholson method using only linear equations has been shown to be stable for all values of Δt. However, using the non linear boundary condition of radiation heat loss this model developed unstable oscillations for values of $\Delta t > 2 \Delta r_{1-2}^2/\alpha$. The oscillations could be damped out up to $(2\Delta r_{1-2}^2/\alpha)$ using the weighting system refered to on p 56 without a serious computing time penalty.

Table 3.9.1

Grid dimensions	central processor time/solution seconds	No iterations/ solution	approx: time/grid pt/iteration	(comparison with 40 x 40 solution) accuracy
10x10 constant	2.3	10	2.3.	poor
20x20 constant	12.4	12	2.6	good
40x40 constant	66.5	14	2.9	assumed correct
24x10 exp	6.2	10	2.58	v. good

Table 3.9.2

Value of 'TEST'	ITERATION COUNT			Notes on accuracy compared to 0.5 value
	1st-6 intervals	7-10	11-15	
0.5	6	8	8	--
1.0	5	8	8	+ 0.054%
10.0	3	8	8	+ 1.33%
100.0	1	1	8	+ 4.2% ── 2%

The accuracy, $E_{p,t}$, of this method is bounded by

$$|E_{p,t}| \leqslant \frac{\lambda}{12} \emptyset \Delta t^4 \qquad \text{see section 3.4}$$

and is consequently highly dependent on the value of Δt.

The variation of iteration count with the value of Δt is shown in table 3.9.3

Table 3.9.3

Value of Δt	$\dfrac{\text{iteration count}}{\text{step}}$
$\dfrac{\Delta r_{1\text{-}2}^2}{\alpha} \times \dfrac{1}{8}$	6
$\times 1$	8
$\times 2$	13
$\times 4$	Did not converge

The critical value of $\dfrac{2\Delta r_{1\text{-}2}^2}{\alpha}$ had to be achieved slowly. Thus the values of Δt chosen were: $\dfrac{\Delta r_{1\text{-}2}^2}{\alpha} \times \dfrac{1}{8}$ for the first 6 steps at 6/7 iteration/step then $\dfrac{\Delta r_{1\text{-}2}^2}{\alpha}$ for the next 194 steps at 8 iteration/step then $\dfrac{2\Delta r_{1\text{-}2}^2}{\alpha}$ for the subsequent steps at 13/14 iteration/step.

3.9.5 Computation over extended lengths of problem times

The first 250 iterations took around 1600 s of central processor time, the maximum run length allowed on the present J13 operation at Imperial College. However for a spot size of 1.1mm diameter on glass this is only equivalent to 6.8 s of problem time or $\Theta^* = 25.5$ (note the first 250 iterations includes the variable Δt period).

Extended runs for all operating conditions were thus out of the question however, an extended run on the no heat loss case was made in order to give the lead for the extrapolation of all other runs.

This run was achieved by running the programme for 250 iterations and then storing the values of the time, thickness, and temperatures in binary on a direct access file by the write statement line no 0484 (appendix 5). This file was saved and then reloaded as data with the programme permanent indirect access file which was modified to read the data file and start execution where the previous file had finished. After a further 250 iteration the process was repeated. Operating this knock on process from the terminals using a procedure file ____ and the QUEUE command would have been very simple if the QUEUE command had been a strict queuing process. Unfortunately this was not the case necessitating queuing the first stage, waiting an hour or so and then queuing the next and so on.

3.9.6 Accuracy

In all numerical solutions there is a chance that the model is successfully converging but doing so on the wrong solution and thus it requires checking against a solution found by a different technique.

The analytical solution of Guenot and Racinet (54) for a uniform disc source with no surface heat loss was used to check the programme.

The fit between the two calculation methods is very good as shown in figure (3.6).

Also shown in figure 3.6 is the different thermal contours resulting from a Guassian power profile, where, as expected, the surface temperature is more diffuse.

Considerable effort was expended in trying to relate Deming et al's well tabulated results with the model. It is unfortunate that they did not specify their power distribution though the equations they used from Carslaw and Jaegar suggested they meant to use a uniform disc source. Their results are shown im figure (3. 6) which clearly shows this was not the case. Further there is an incompatibility between their own graphs for $R^* = 0$ and $R^* = 0.01$ (see figure 3.1). The values for $R^* = 0.01$ are shown.

ISOTHERMS AT $\Theta^* = 1 \cdot 0$
FOR VARIOUS NO SURFACE HEAT LOSS
SOLUTIONS
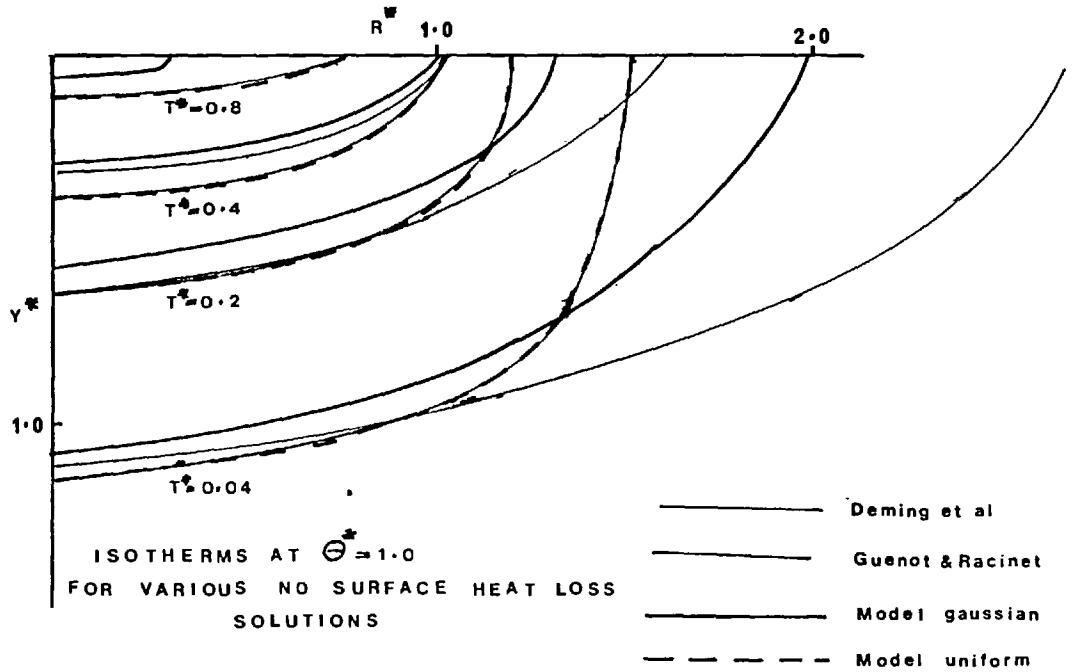
Fig 3.6

Fig 3.7

Theoretical thermal history curves for a gaussian beam and no surface heat loss

EXPONENTIAL MATRIX 24 x 10

CONSTANT MATRIX 20 x 6

DEMING ET AL analytic solution

Dimensionless temperature T^*

Dimensionless time Θ^*

$R^* = 0.01$

$R^* = 1.0$

$R^* = 2.0$

$R^* = 3.5$

$R^* = 0.0$

analytic point

extrapolated →

$R^* = 1.0$

$R^* = 2.06$

$R^* = 3.4$

$R^* = 4.3$

$R^* = 5.4$

72
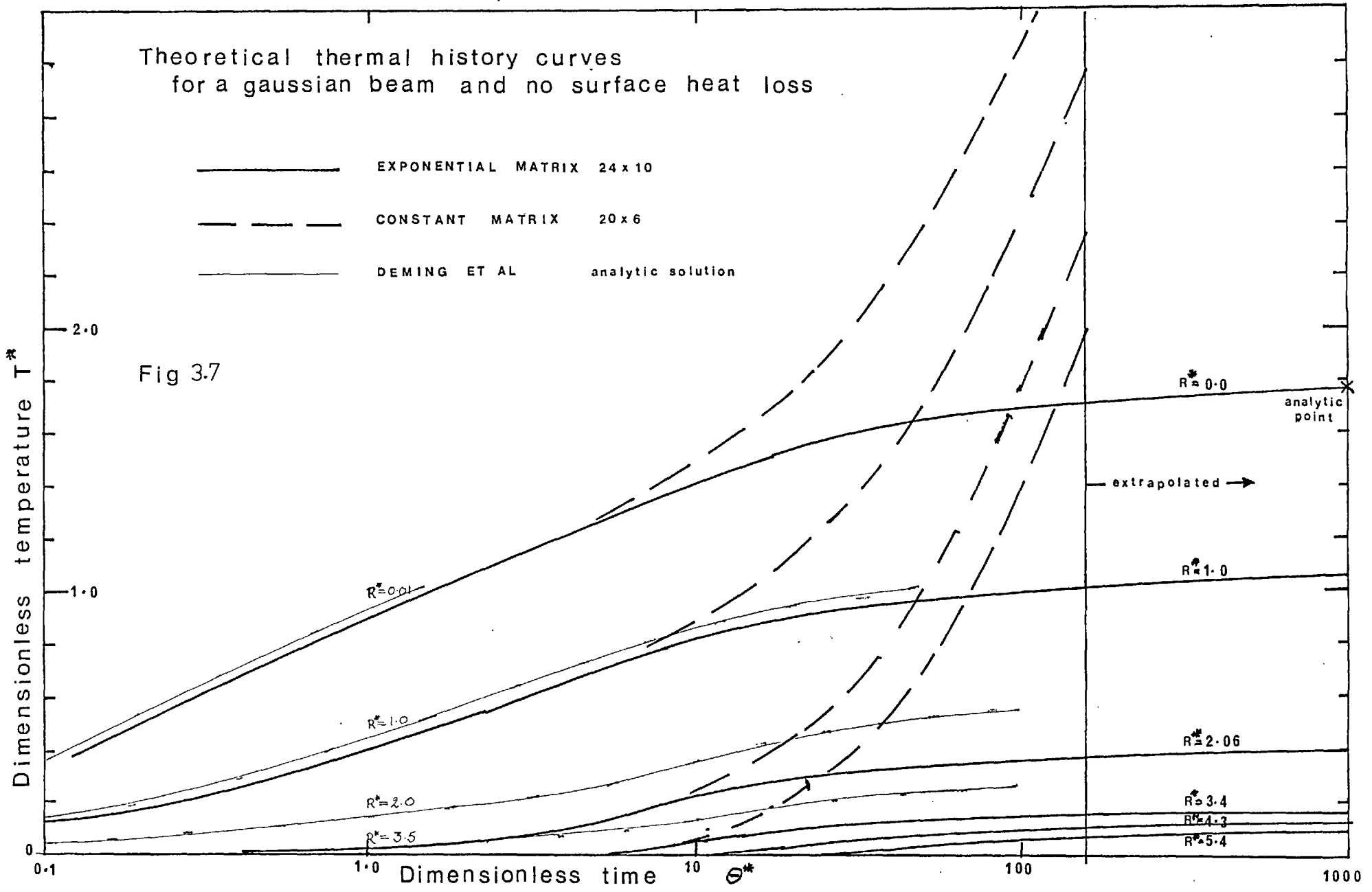
The fit over an extended problem time was examined using the knock on process described in section (3.9.5).

The results are shown compared to Deming et al in figure (3.7) bearing in mind the previous criticism of their work a trend fit only was expected and was found.

The knock on process calculated the curves up to $\Theta^* = 159.0$ The extreme value of T_∞^* for $R^* = 0.0$ is seen by an expected trend to lie between 1.7 and 1.8. A value of 1.77 was chosen that being the analytically predicted value for the central temperature of a spot heated by a Gaussian beam (ref. 14 p 83).

$$T_{\substack{cont \\ gaus}} (0,0 \infty) = \frac{P_t}{2Kr_b \pi}$$

$$\therefore T_\infty^* = \left[\frac{Tk \ D_b \pi}{P_t} \right] = 1.77 \qquad\qquad 3.74$$

Figure 3.7 also shows the instablility which occurred using the constant matrix model when the southern and eastern boundaries were in excess of 300°C. The instability is due to a lack of overall heat balance on that model.

3.10 Presentation of the computational results

Dimensional Analysis

The problem has two stages; firstly the calculation of the temperature profile and secondly the extent of deposition based on these temperatures.

The temperature profile is calculated from the solution of the equations 3.26 - 3.31 which reveal the relevant parameters as:

$P(1 - r_f)$ — the net power absorbed at the surface W

with r_f being the surface reflectivity

r — radial position m

y	—	depth	m
$T(r,y,t)$	—	temperature	$^{\circ}K$
t	—	time	s
α	—	thermal diffusivity	m^2/s
k	—	thermal conductivity	$W/m^{\circ}K$
h	—	convective and radiative heat transfer coefficient $=(h_c + h_r)$	$W/m^{2\,\circ}K$
r_b	—	beam radius	m

From these 9 variables, 4 of which (P, r_b, t, T) do not form a dimensionless group, Buckingham's π theorem predicts 5 dimensionless groups. They are:-

$$\pi_1 - \frac{2Tk\pi r_b}{P(1-r_f)} = T^* \qquad \text{dimensionless temperature}$$

$$\pi_2 - \frac{r}{r_b} = R^* \qquad \text{dimensionless radius}$$

$$\pi_3 - \frac{4\alpha t}{r_b^2} = \Theta^* \qquad \text{dimensionless time}$$

$$\pi_4 - \frac{y}{r_b} = Y^* \qquad \text{dimensionless depth}$$

$$\pi_5 - \frac{h(T - Ta)\pi r_b^2}{P(1 - r_f)} = \eta \qquad \text{dimensionless heat loss}$$

T^* is arranged to agree with the work of others, in particular Guenot and Racinet (54), and Deming et al (51). It is basically the ratio of (conduction loss/power input)

Θ^* is the classical dimensionless time.

η is defined as (surface heat loss/power input)

$$= \frac{(h_c + h_r)(T_{r,\Theta} - T_a)\pi r_b^2}{P(1 - r_f)} \qquad \text{and is a function of } (r,t)$$

it reduces to:-

$$\eta_\infty^o = \frac{(hc + hr)(To_\infty^* - T^*a)}{P(1 - r_f)} \frac{P(1 - r_f)}{2\pi k r_b} \pi r_b^2$$

$$= \frac{(hc + hr_\infty)(To_\infty^* - T^*a)r_b}{2k} \qquad (3.75)$$

likewise $\quad \eta_{25.5}^o = \dfrac{(hc + hr_{25.5})(To_{25.5}^* - Ta^*)r_b}{2k} \quad$ etc.

The dimensionless groups T^*, R^*, Θ^*, Y^* were calculated as part of the programme output and including $\eta(r,\Theta)$ were used in most plots of the thermal events.

It should be noted, in particular, that for the case of no surface heat loss from a semi-infinitesubstrate a plot of T^* vs R^* vs Θ^* represents a unique solution for all powers, materials and spot sizes. This is shown as the 'no loss' line on the thermal plots.

The extent of deposition resulting from a given thermal profile depended upon the deposition route be it chemical control or boundary layer control. An examination of the governing equations (3.70, 3.73) shows the relevant parameters other than temperature to be Re, B/D_j, Sc.

3.11 Operation of the mathematical model

From the results of a series of runs of the mathematical model a set of generalised thermal curves were drawn (figs. 3. 8 - 3. 19) From these curves a system for predicting the thermal profile history under different operating conditions was devised. This method was checked against further computer runs and found to be sufficiently accurate for this analysis. The ability to predict, without further recourse to the computer, was not only a saving in calculating time generally but a vast saving of computer time.

Fig 3.8 T^* vs Θ^* for spots initially at the same temperature but having different equilibrium heat loss, η_∞
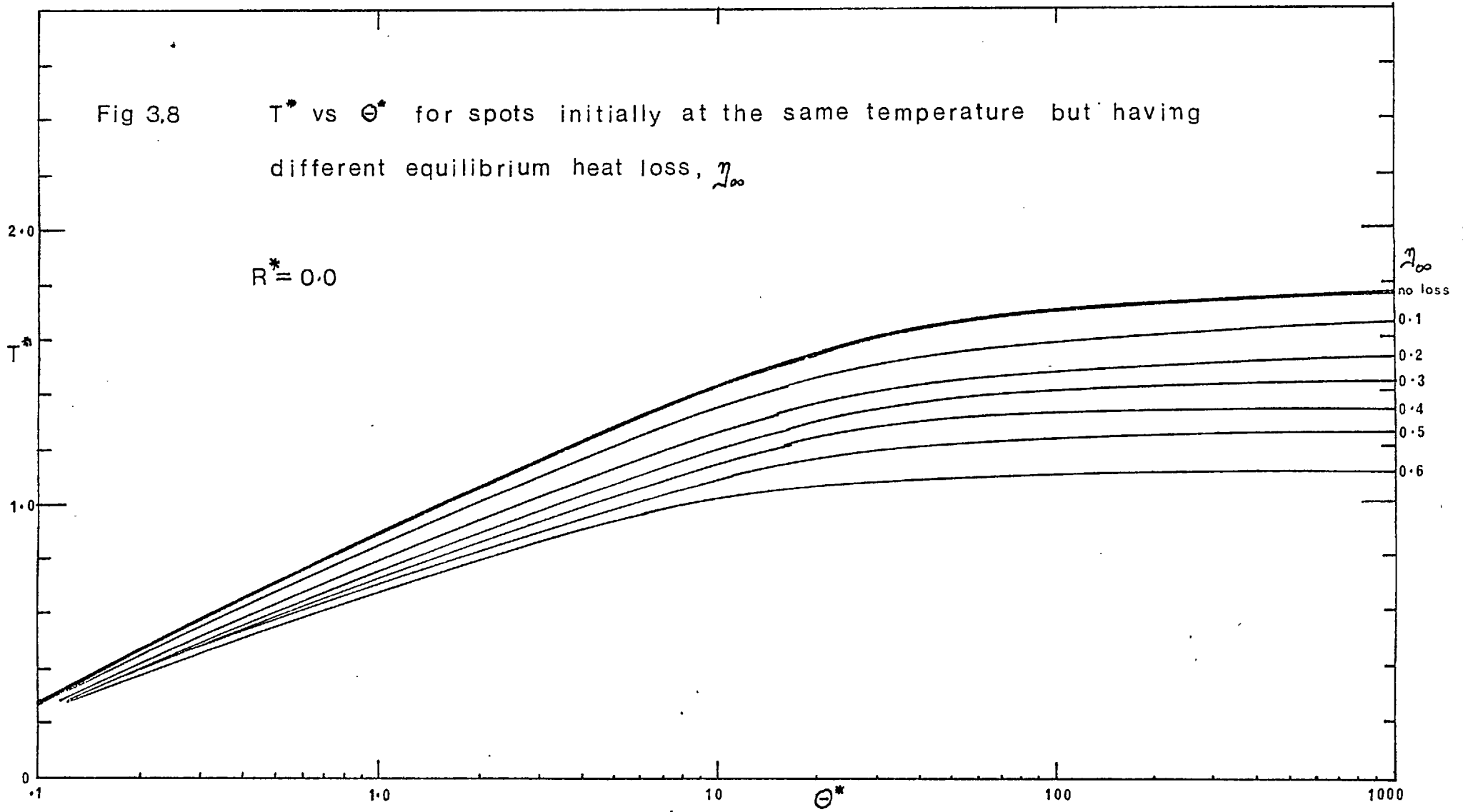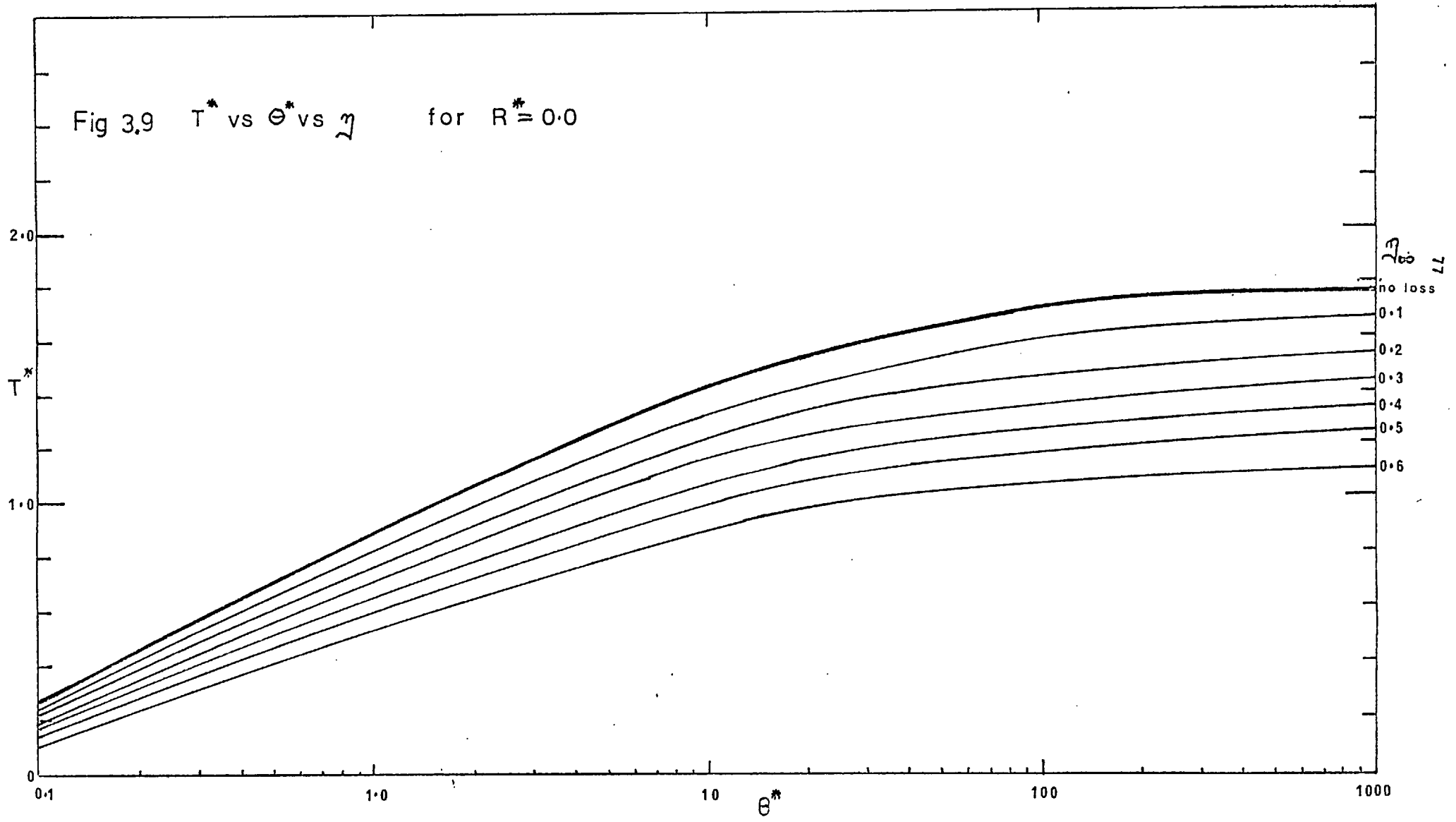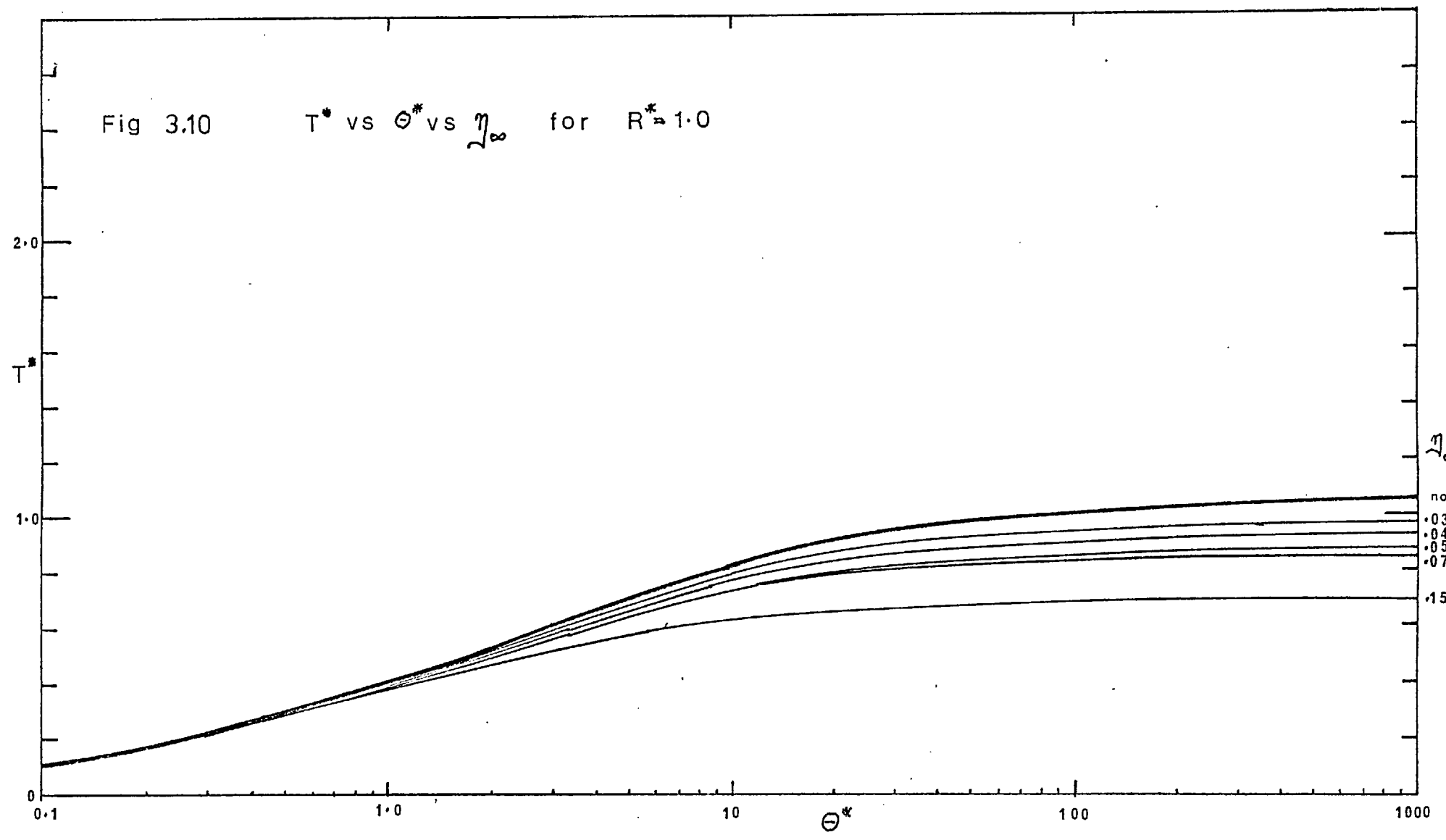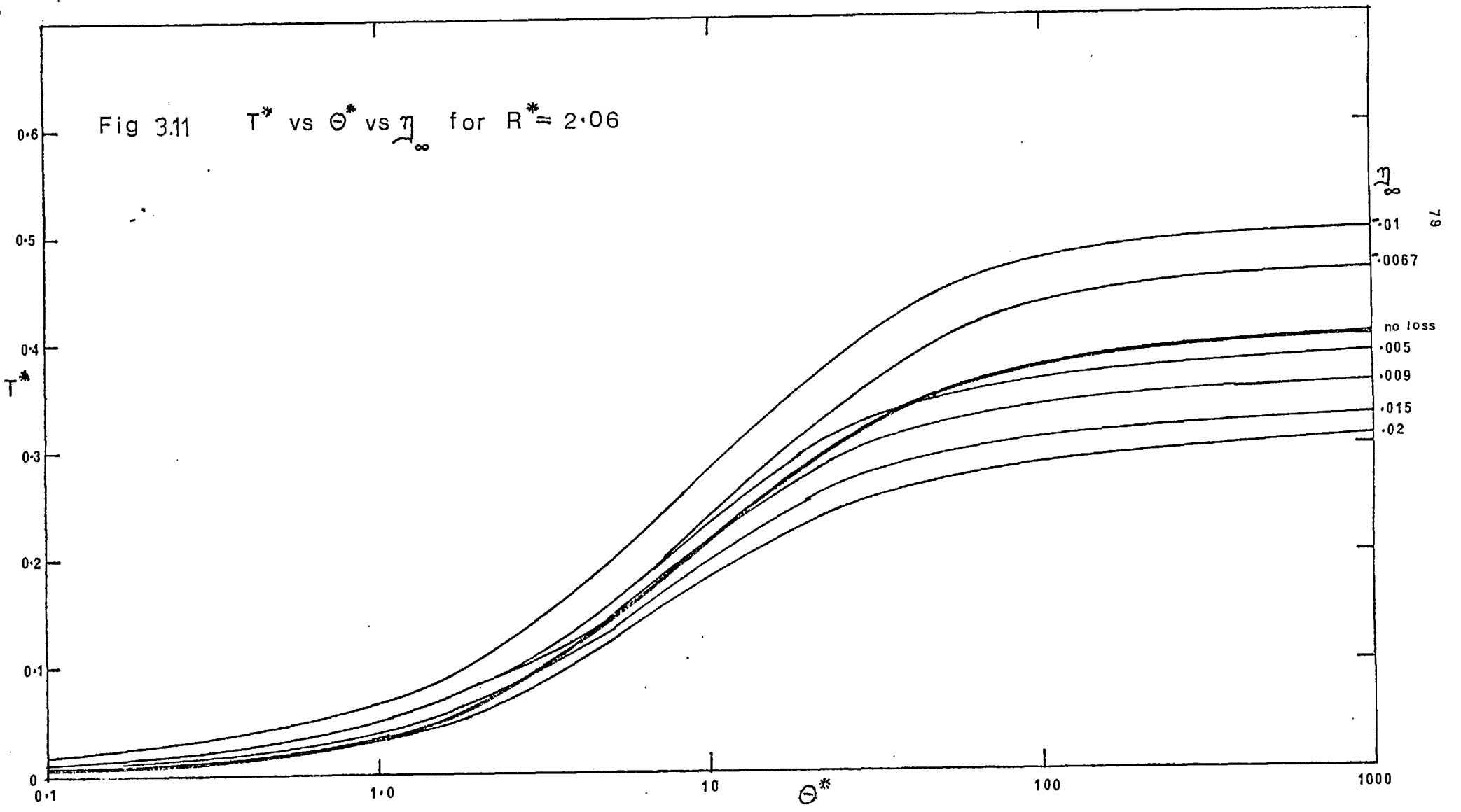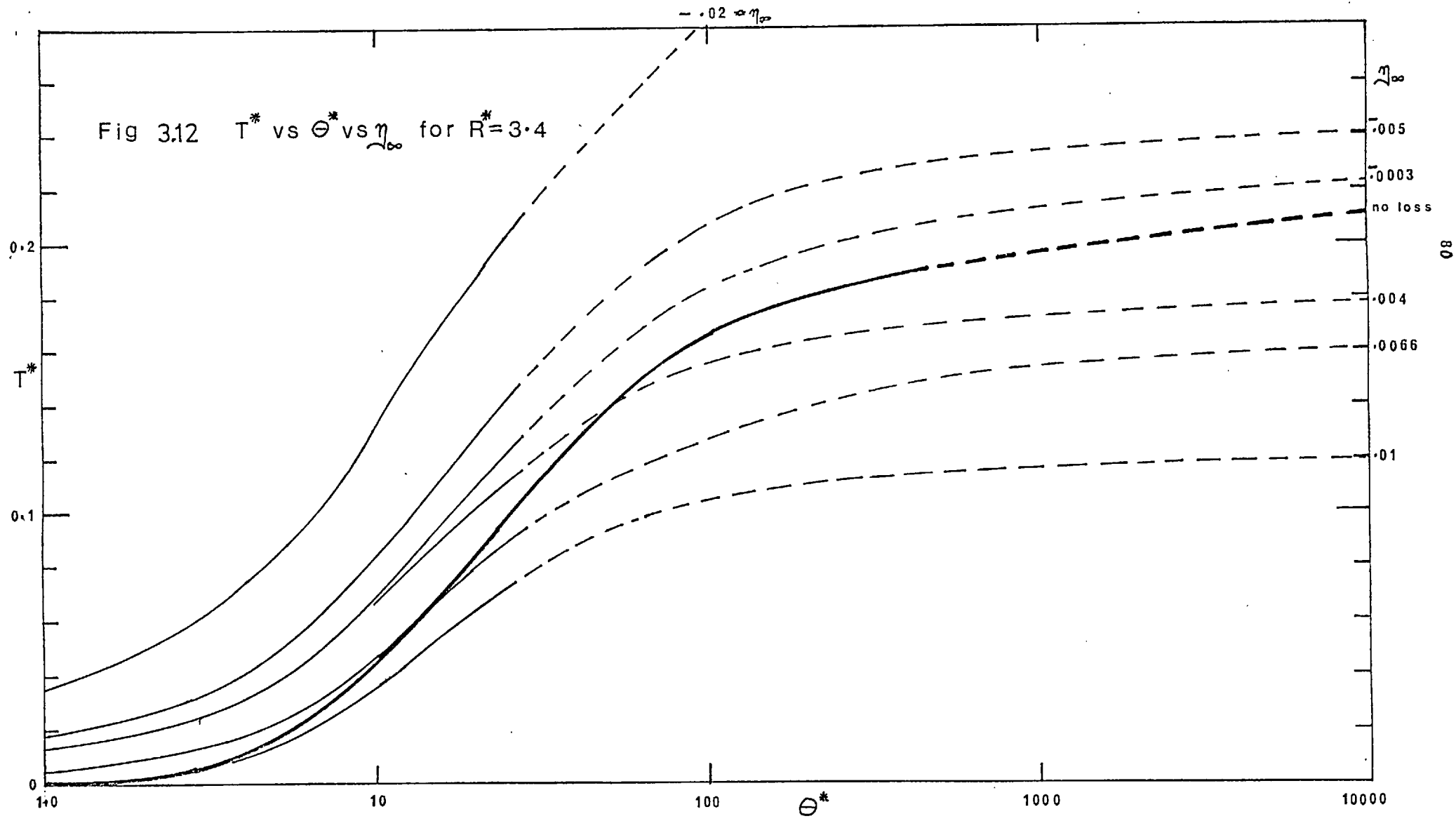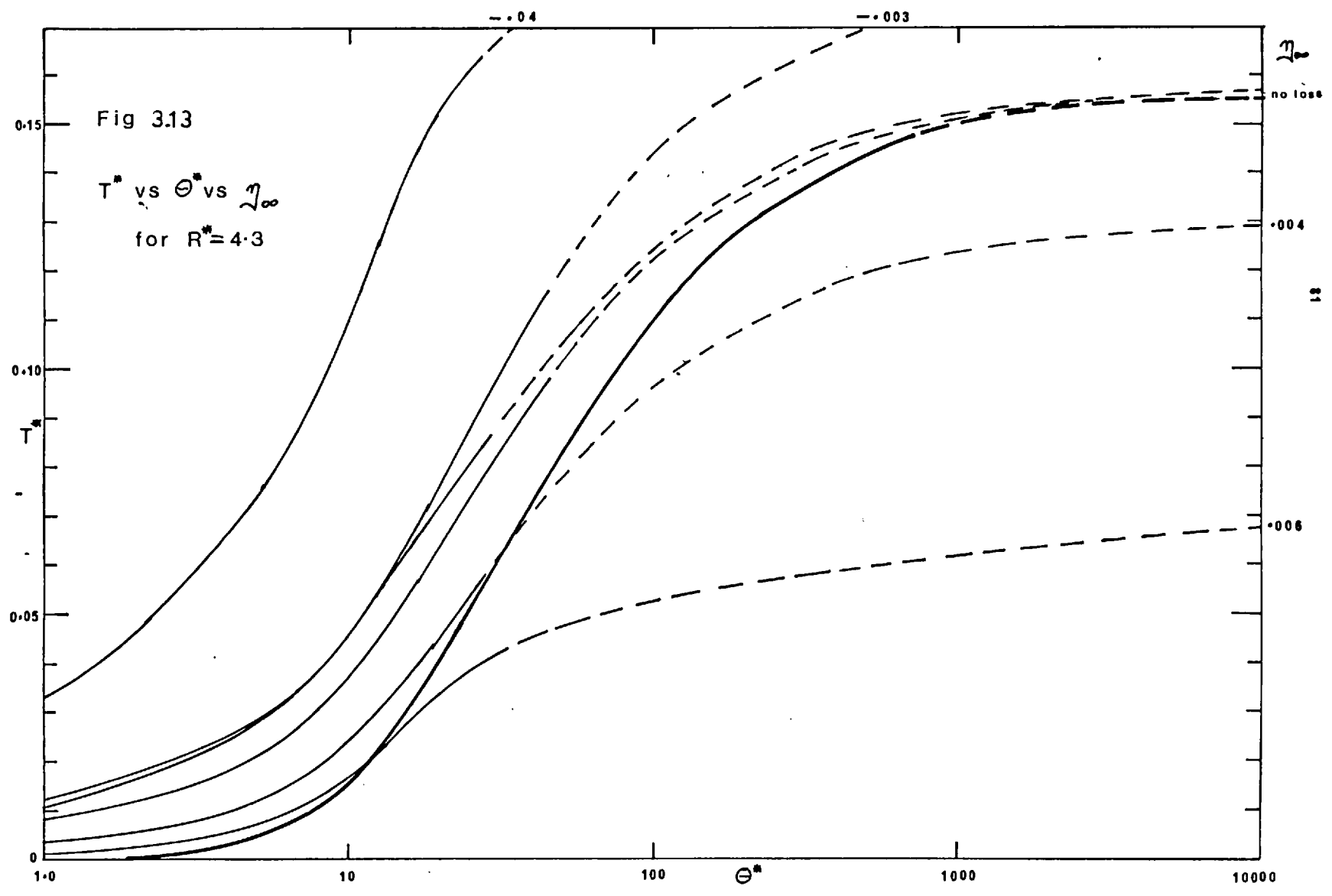
$R^* = 0.0$

Fig 3.9 T^* vs Θ^* vs η for $R^* = 0.0$

Fig 3.10 T^* vs Θ^* vs η_∞ for $R^* \simeq 1.0$

η_∞

no loss

.039
.048
.058
.073

.157

T^*

2.0

1.0

0

0.1   1.0 Θ^* 10   100   1000

78

Fig 3.11 T^* vs Θ^* vs η_∞ for $R^* = 2 \cdot 06$

Fig 3.12 T^* vs Θ^* vs η_∞ for $R^*=3\cdot4$

Fig 3.13

T^* vs Θ^* vs η_∞

for $R^* = 4 \cdot 3$

Fig 3.14   T* vs Θ* vs η_∞ for   R* = 5·4

Fig 3.15   Variation of T^* with dimensionless heat loss η
for various R^*

Fig 3.16 T^* vs η (larger scale)
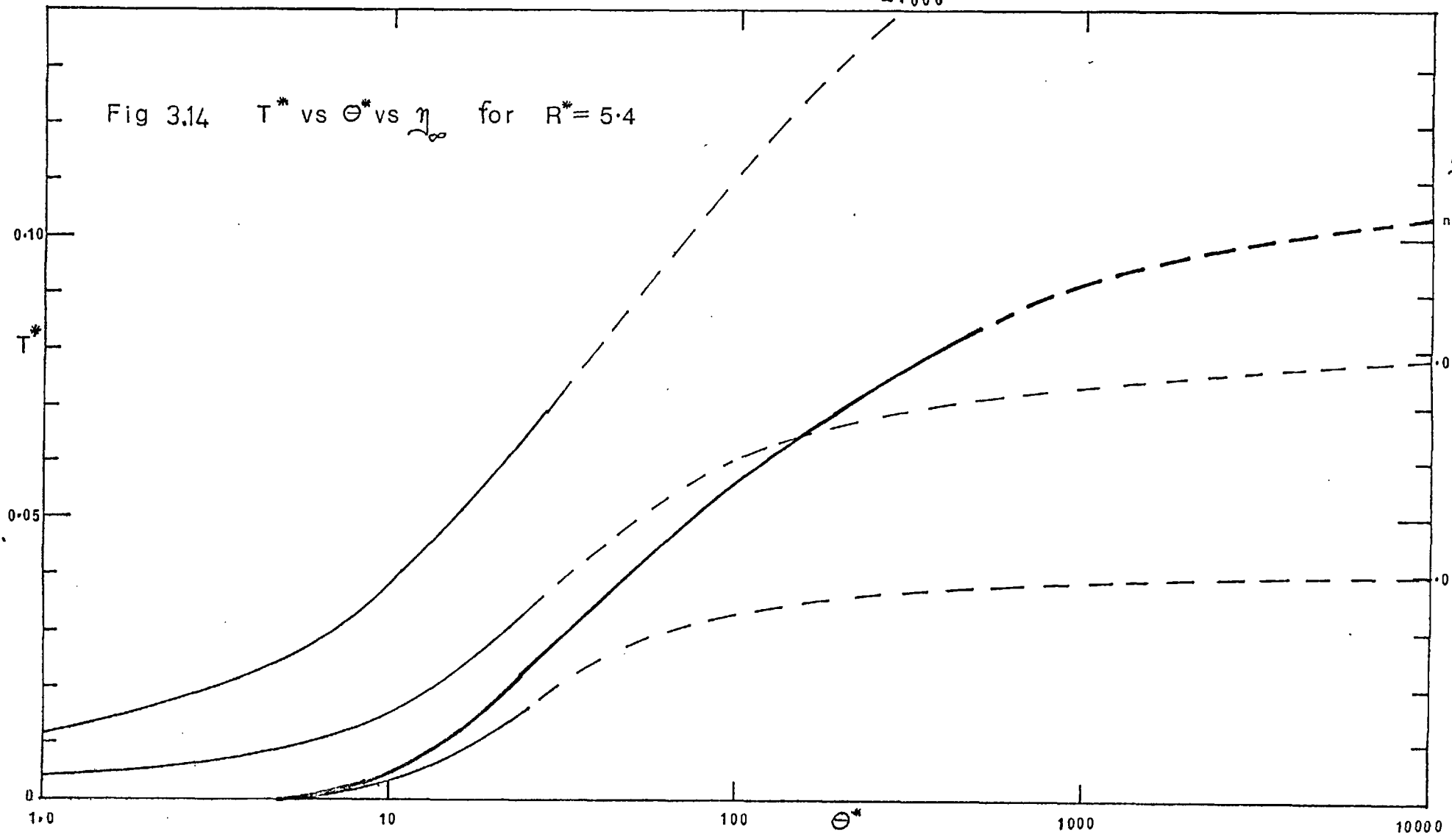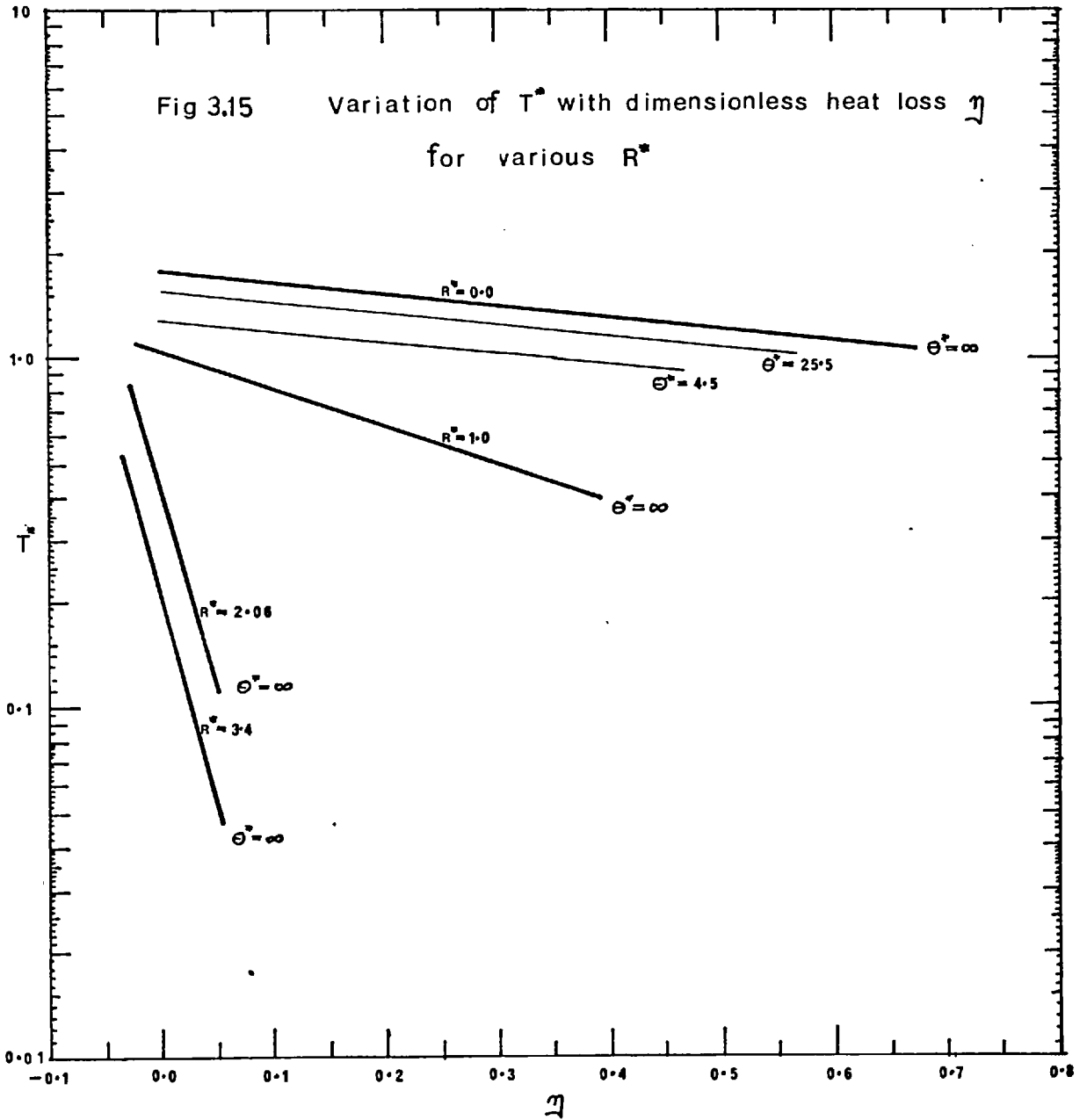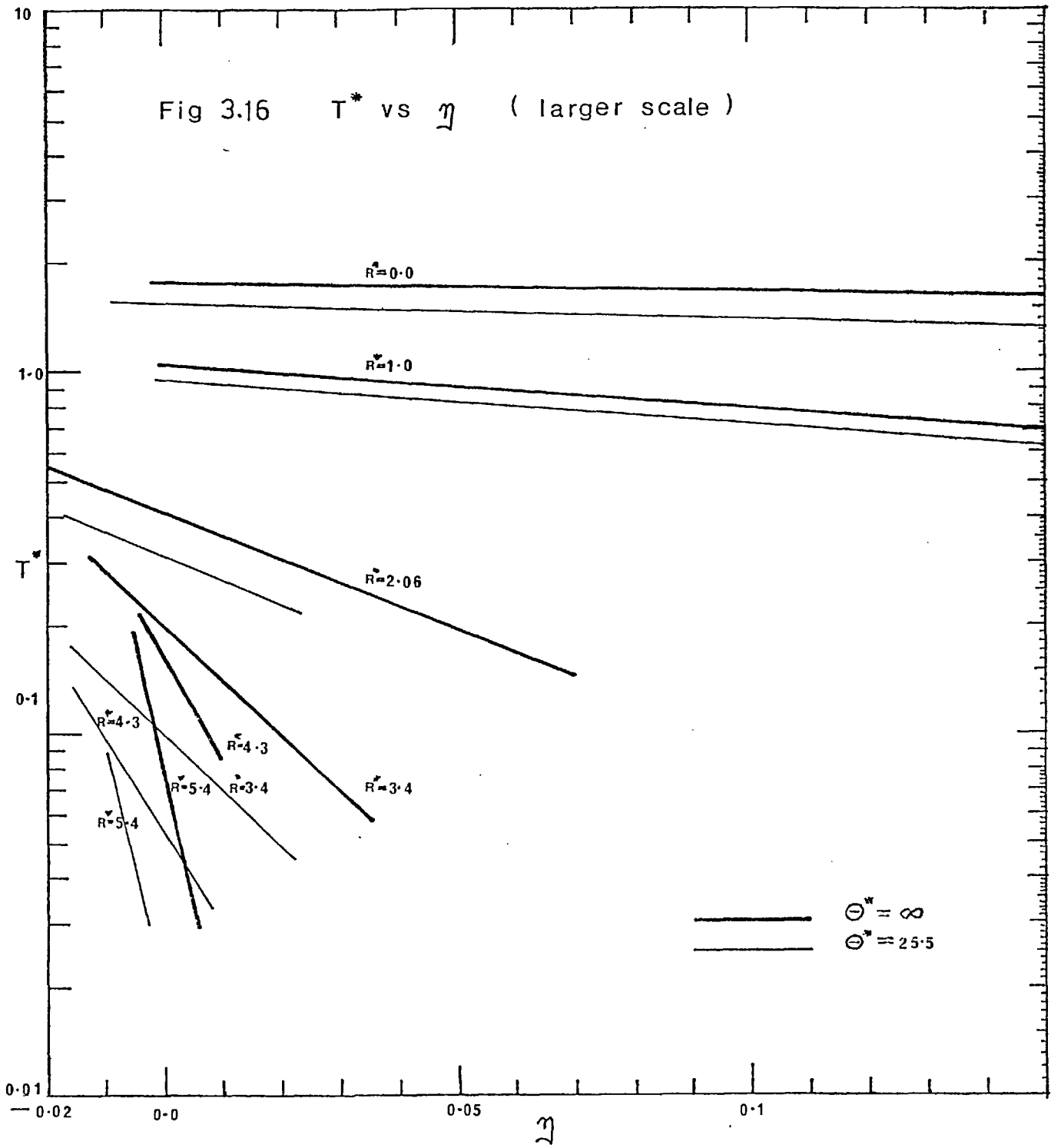
Fig 3.17   Dimensionless   thermal   profiles T^* vs R^* vs η
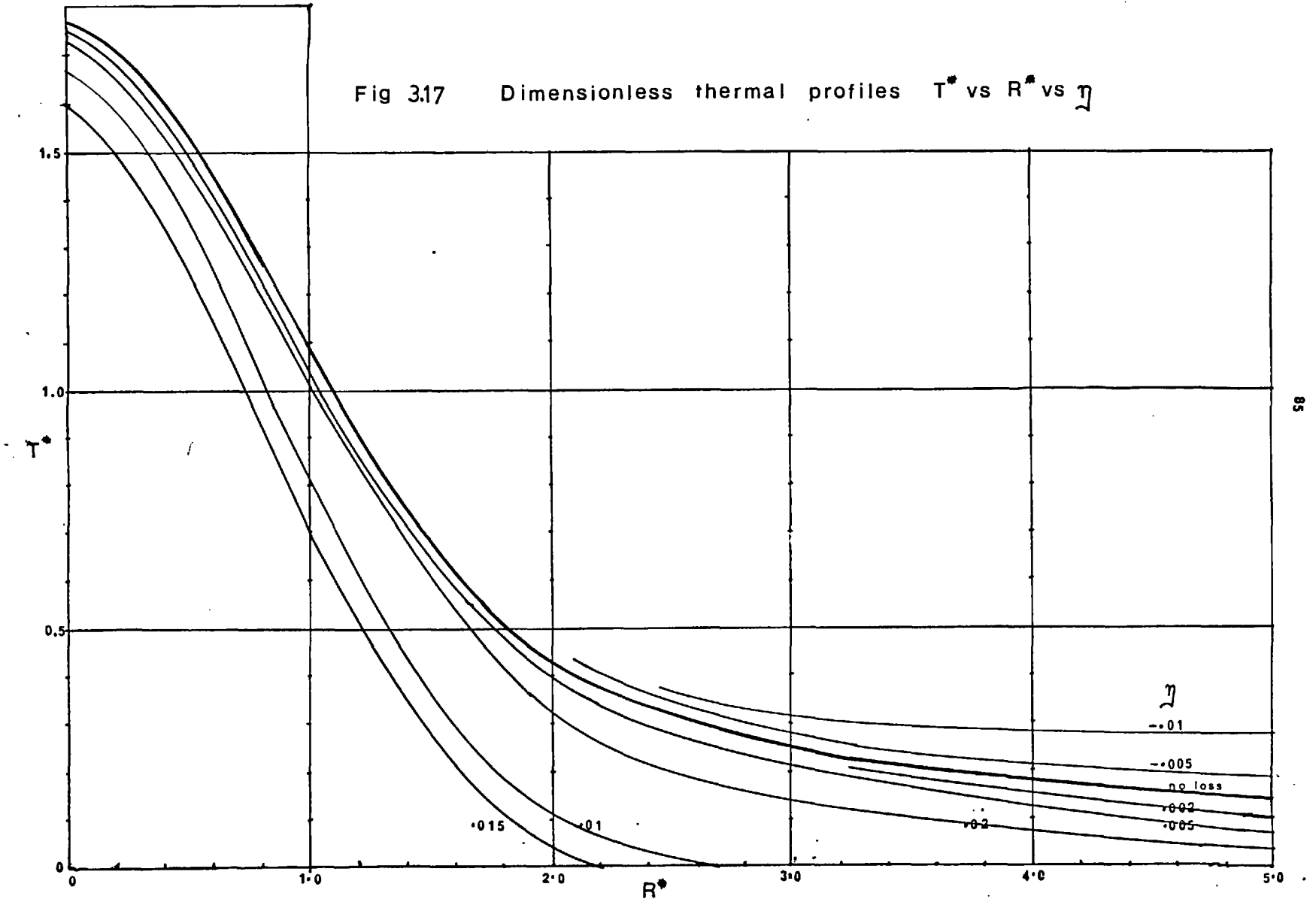
Fig 3.18   Variation of the convective heat transfer coefficient with Re

and the radiative heat transfer coefficient with surface temperature
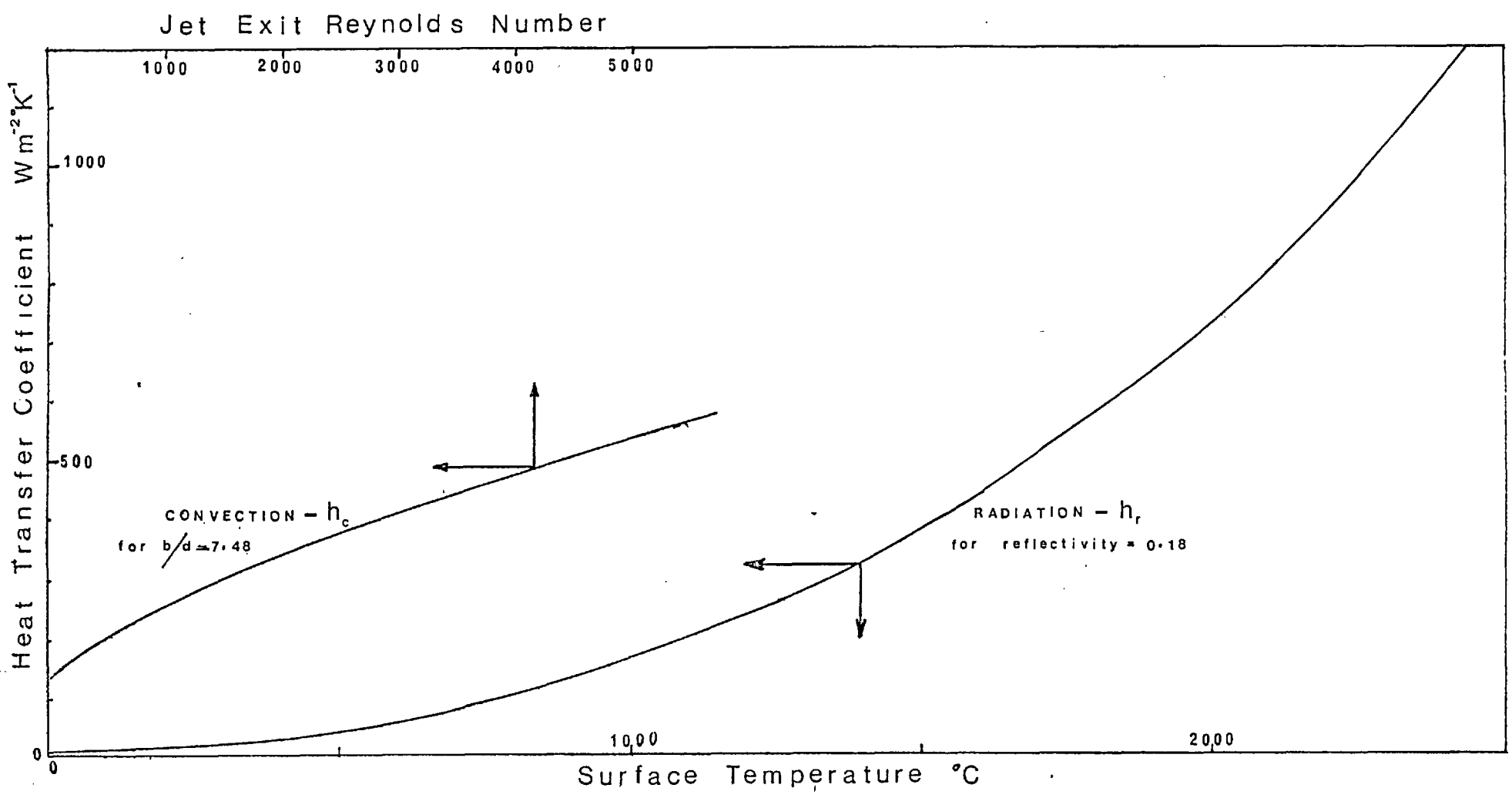
Fig 3.19 Temperature dependence of the growth rate

For: jet concentration = ·306 ppm

B/D_j = 7·48
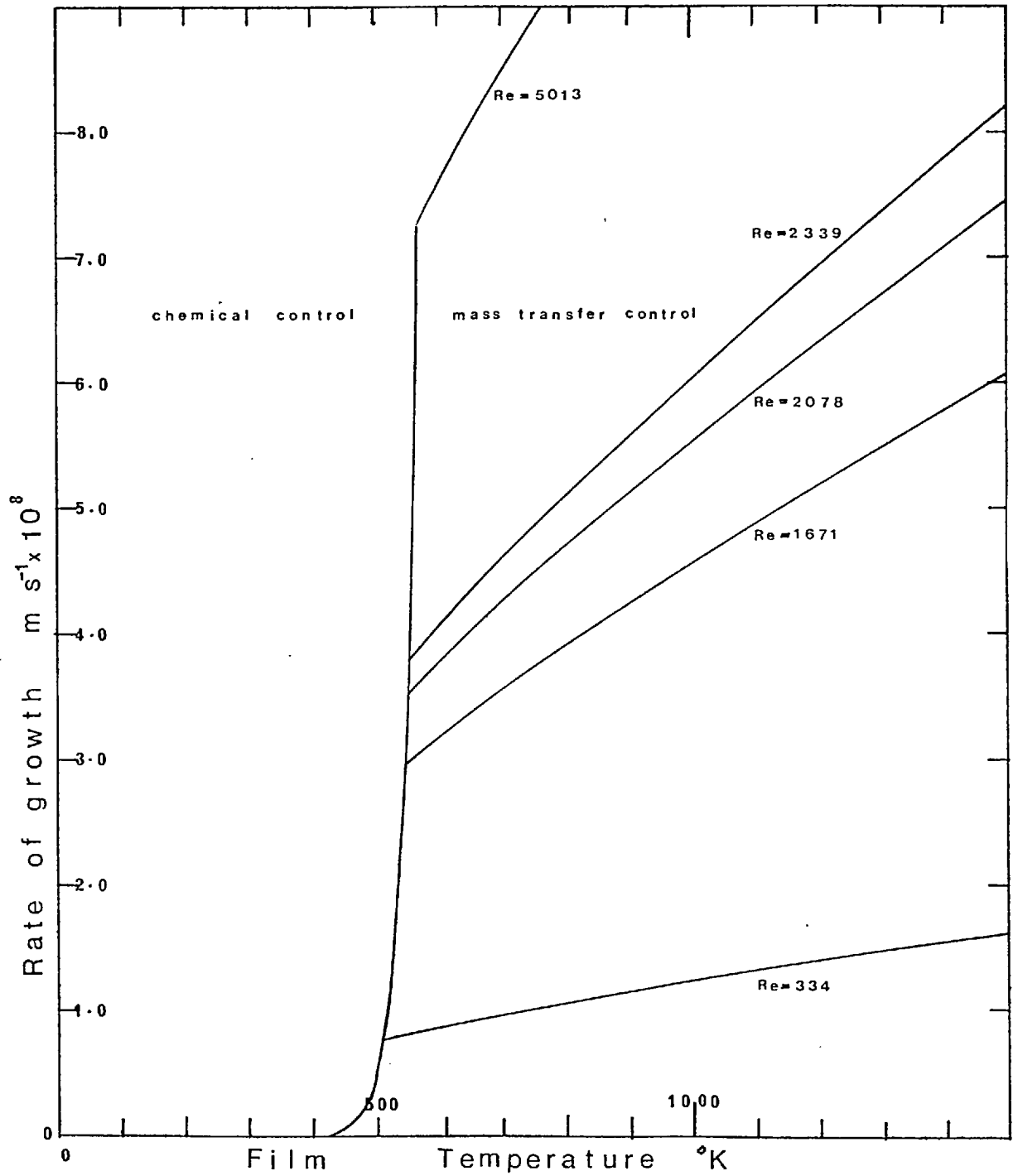
Table 3.11.1

Conditions under which mathematical model was operated

	1	2	3	4	5	6	7	8	9	10	11	12	13	14	15	16	17	18	19	20	21	22	23	24	25
Power W	2.0	.25	.5	1.0	1.5	2.0	5.0	2.0	1.0	→									1.4	—	—	2.0	2.0	10.0	2.0
Radius mm	.24	→						.48	.24	→									.55	→					
P/D w/cm	41.6	5.2	10.4	20.8	31.2	41.6	104	20.8	→										12.8	→		18.2	18.2	91.0	18.2
T °C	—	100	→						0.0	50	140	100	→						140	→		100	→		140
Re	—	2079	→						1671	334	2339	5013	2079	→											
ρ kg/m³	2490	→															2660	8930	2490	←					
C_p J/kg°K	1176	→														668	838	396	1176	→					
k w/m °K	.84	→															1.44	38.5	.84	→					
B/D	7.5	→																	2.5	5.0	7.5	→			
r_f	.18	→																	>600				.18	>600	>600

no loss run (col 1)

alt: glass (col 17) quartz (col 18) copper (col 19)

The conditions under which the model was run are shown in table (3.11.1).

Run 1 was run for 4 successive "knock on" runs up to $\Theta^* = 159$, all other runs were taken to $\Theta^* = 25.5$.

3.12 Calculation of the generalised thermal history curves

As already seen, the case of no surface heat loss from a semi-inifite substrate would be represented as a single set of curves of T^* vs R^* vs Θ^*, a similar generalisation allowing for surface heat loss was sort.

Firstly, the case of no surface heat loss was established by calculating up to $\Theta^* = 159$. The extrapolation of the curves to higher values of Θ^* was considered fairly accurate for $R^* = 0$ since an analytic solution as well as the linear trend were available (see p 73). The extrapolation for $R^* = 1.0$ was also considered fairly safe, but the extrapolation became progressively riskier with increasing R^* since thermal equilibrium was established later at these more remote locations. However, using these extrapolations, the no surface heat loss curves were fixed.

Secondly, heat loss was allowed for by calculating the parameter

$$\eta = \frac{(h_c + h_r(r,\overset{*}{\Theta}))(T_o^* - T_a^*)}{2k} \, \Theta$$

for each computer run for various values of R^* and Θ^*. The computer model yielded values of h_r and h_c. While T_o^* was taken as the "no surface heat loss" value for the location and time under consideration. This means that 'η' was not the fraction of heat lost but could be easily calculated subsequently. These extensive calculations are shown in figures (3.8 - 3.14). From these curves it is possible to draw graphs of log T^* vs Θ^* vs R^* (figure 3.17) and finally a plot of T^* vs R^* vs η for $\Theta^* \rightarrow \infty$ (figs 3.15, 3.16). This graph shows most clearly the order of error introduced if the surface heat loss is neglected, as is common practice.

For example in welding or cutting the following values might hold:

spot diameter	0.00012 m
power	100 W
k	20 W/m $^{\circ}$K
h_r	80,000 W/m^2 $^{\circ}$K
Ta*	0.0075
Nu_o	0.030
yielding η_o	0.2.

Such a value of η_o causes a reduction of T* by 0.27 which, for

$$\frac{\pi k^D b}{P(1-r_f)} \simeq 0.000075 \ ^{\circ}C^{-1}$$

represents a drop of 3600°C. In these lower power experiments, the heat loss will be seen as crucial.

From graphs ('3.15-19) together with hand calculated values of η_{R_θ} predictions under other operating conditions can be made. Some examples of such calculations are shown in table 3.11.2.

3.13. Use of generalised thermal curves

For different conditions from those used on a computer run the heat loss Nusselt No $\sum \frac{h \ r_b}{2k}$ was calculated from a knowledge of h_c as a function of Re and h_r as a function of T (graph 3.18) The value of T chosen for calculating h_r was taken initially as that for the no heat loss case and was finally established approximately by iteration.

(To* - Ta*) was found, as before, from the no heat loss value of To* and the ambient dimensionless temperature Ta*. This yielded a value of $\eta_{R_{\theta*}}^{*}$ which using graph (3.15-.16) gave a value for T* as a function of R* and hence the profile at θ*. From this profile the central temperature could be calculated which gave from graph (3.19) the rate of deposition from which,after allowing for the thermal rise time (graph 3.8,9), the deposit thickness could be estimated.

Also from the graph T* vs R* (fig 3.17) ' the various values of outer, inner, burnt and blue radii could be estimated after assuming these events to be associated with some special temperature.Table (3.11.2) shows the format of these calculations.

The results of these calculations and those direct from computer runs are shown in the ·theoretical curves in the results and discussion sections.

PREDICTION		1	2	3
BEAM DIAMETER m	D_b	.00096	.00096	.00192
TOTAL INCIDENT POWER W	P	1.0	3.84	2.0
W/cm	(P/D_b)	10.4	40.0	10.4
SURFACE REFLECTIVITY	r_f	.18	.18	.18
THERMAL CONDUCTIVITY W/m$^\circ$K	k	.84	.84	.84
$\dfrac{\pi k D_b}{P(1 - r_f)} \times 10^3$		3.08	.769	3.08
CENTRAL SPOT TEMP. ESTIMATE $^\circ$C	T_s no loss	574	2223	574
RADIANT HEAT TRANSFER COEF. W/m^2 $^\circ$K (graph 3.18)	h_r	50	500	50
JET EXIT Reynolds number	Re	2079	2079	2079
CONVECTIVE HEAT TRANSFER COEF. W/m^2 $^\circ$K (graph 3.18)	h_c	346	346	346
LOCAL NUSSELT NUMBERS Nu $\Sigma = \dfrac{(h)D_b}{4k}$	R* 0.0	.113	.24	.226
	R* 1.00	.099	.20	.198
	R* 2.06	.099	.11	.198
	R* 3.4	.099	.099	.198
AMBIENT TEMPERATURE $^\circ$C	T_a	100	100	100
DIMENSIONLESS T_a	T_a^*	.308	.0796	.308
LOCAL HEAT LOSS PARAMETER $(\eta = Nu(T_0^* - T_a^*))$ $(\eta = Nu(1.77 - T_a^*))$	R* 0.0	.165	.405	.330
	R* 1.0	.074	.196	.149
	R* 2.06	.009	.035	.019
	R* 3.4	.009	.013	.019
	R* 4.3	.015	.0075	.030
	R* 5.4	.022	.00003	.045
CENTRAL TEMP (graph 3.8	$T_{\theta o}^*$	1.58	1.36	1.42
CENTRAL SURFACE TEMPERATURE $^\circ$C	To	512	1708	461
SURFACE (R* = 0.0) FILM TEMPERATURE $^\circ$K	T_{film}	579	1177	553
RATE OF DEPOSITION m/s x 10^8 (graph 3.19)		3.65	6.2	3.8
TIME TO θ^* = 20 s		4.0	4.0	16.1
DEPOSIT THICKNESS AFTER 120s μ		4.23	7.2	3.9
	$T^*_{150}{}^\circ C$	.462	.119	.462
OUTER DIAMETER / BEAM DIAMETER	D^*_{outer}	1.65	3.64	1.54
	$T^*_{374}{}^\circ C$	1.65	.297	1.15
INNER DIAMETER / BEAM DIAMETER	D^*_{inner}	.68	1.9	.50

Table 3.11.2

Example of Predictive Calculations

CHAPTER 4

DESIGN AND CONSTRUCTION OF THE APPARATUS

4.1 Introduction

The essential features of the laser deposition system as just described are:

1) A broad, uniform intensity, power beam of sufficient power.
2) An optical system to manipulate the power beam
3) A steady vapour supply of adequate concentration
4) Instrumentation to monitor the most important variables
5) A suitable substrate.

These parts were built to several designs, culminating in the final arrangement on which all reported runs were made. The reasoning behind the chosen designs is now discussed.

4.2 The Power Beam

4.2.1 Choice of a laser

A laser is an optically reasonant cavity in which is a medium capable of producing the stimulated emission phenomena after being 'pumped' to an excited state by some energy injection system. A very brief summary of different lasers is given in Appendix 2

At the start of this work in 1968 the CO_2/N_2/He laser was the only one available with a multiwatt continuous output potential. More recently YAG and Nd glass lasers have become available with a similar capability. The lasing action of the CO_2/N_2/He laser is described in Appendix 3.

The design and construction of such a laser calls for a choice of: (i)   cavity
(ii)   lasing medium
(iii)   pumping system
(iv)   cooling system.

These are now discussed in turn.
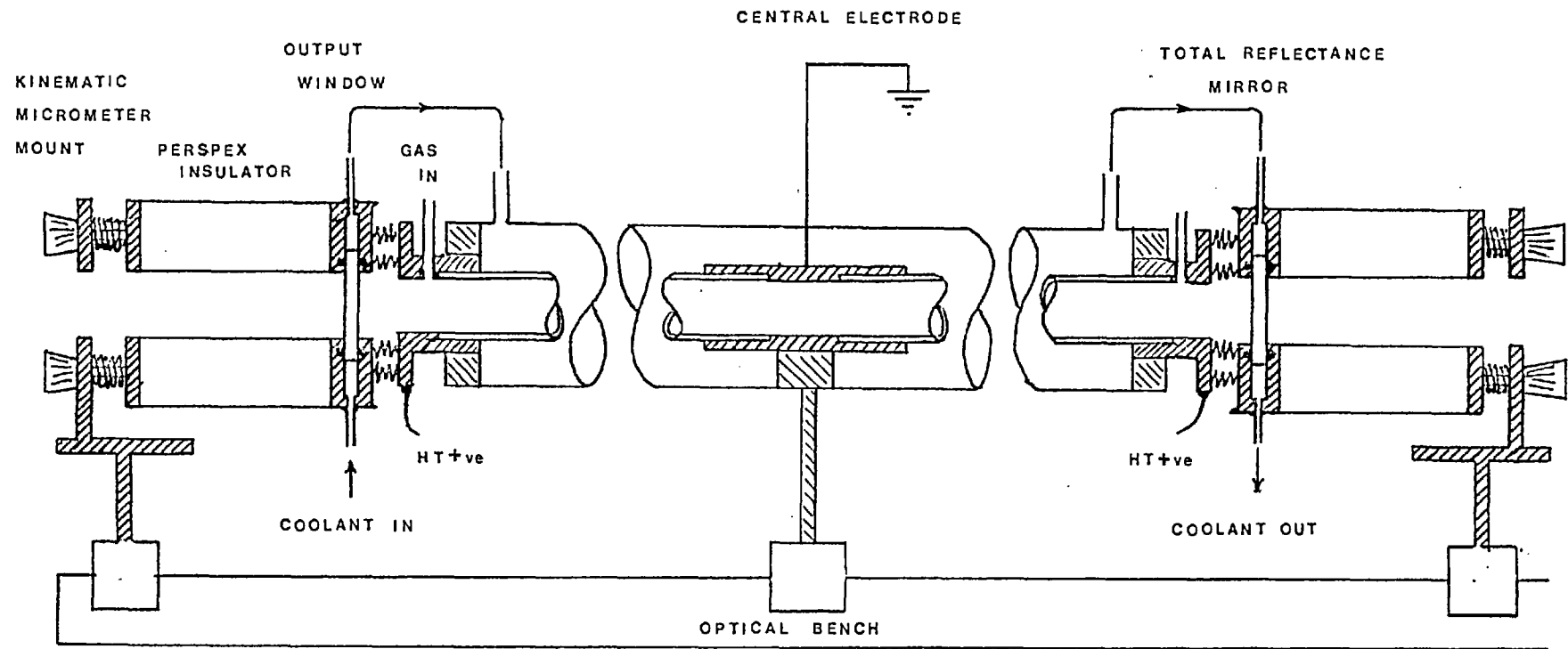
Fig 4.1   THE CARBON DIOXIDE LASER

4.2.2 Design of Cavity

The various parts of the cavity are shown in figure 4.1.

4.2.2.1 Plasma tube design

TUBE DIAMETER: The output power from a gas laser is a function of the quantity of active lasing medium. This means, for high powers, large volumes of lasing medium at high pressures are required. Thus the power output α (tube diameter)^2 for a constant gain coefficient. However, for the $CO_2/N_2/He$ system external cooling is required to remove the $CO_2(01'0)$ to the ground state (see Appendix 3) and only narrow bore tubes are capable of adequate cooling for an axial subsonic flow system . Because of this cooling requirement the gain coefficient α (1/tube diameter). This results in an optimum diameter of plasma tube for a given flowrate. For the flowrates considered here (50 tube volume/min) this optimum is around 1-3cms. For tubes below 1cm diameter wall losses may prevent lasing, for tubes above 3cm diameter, there is no power advantage to be gained due to inadequate cooling. This can be overcome by using high velocities or side blown lasers[10]. There are other advantages to broad tubes in that the mirrors are more easily aligned and a multimode beam or broad Gaussian beam would be generated which it was felt would be nearest to the ideal of a broad uniform intensity beam. Thus the internal diameter was chosen as 2.54cms.

TUBE LENGTH: For tubes of this diameter, operating at about 15 torr, the power output is optimally 70W/m for the first 10 metres, after which length the gas becomes poisoned with CO and CO_2 (01'0) contamination. A tube length of 1m was chosen initially. This tube functioned satisfactorily but it was felt more power would be useful and so when that tube, purchased initially from Scientifica and Cooke Limited, failed due to corrosion of the central anode, a longer tube, 1.5m long was used. On this tube all the work reported here was performed.

4.2.2.2 The cavity mirrors

The resonant stability of an optical cavity resonator depends upon whether a beam, after multiple reflections within the cavity, will be reflected out of the cavity or towards the centre. It can be shown from simple ray diagrams that the conditions for this are:

$$0 < (1 - \frac{d}{R_1})(1 - \frac{d}{R_2}) < 1$$

where R_1 and R_2 are the radii of curvature of mirrors 1 and 2 respectively. d is the distance between the mirrors.

This is illustrated in figure 4.2 . It has also been most ably proven by Kogelnik and Li[91] using ray transfer matrices and elegantly displayed in graphical form figure 4.3 .

The term 'stability' as used here is perhaps misleading since some recent high powered lasers (Avco Everett, 20kW and Welding Institute 4kW lasers) operate with an 'unstable' cavity the reason being that the output power is deliberately taken from around the periphery of the totally reflecting mirrors instead of through a partially transmitting mirror as in the equipment used in these experiments. The mode structure for these unstable cavities has been discussed by Sigmund[75], the modes from cavities as used here have been described by Kogelnik and Li[91].

Initially a double concave system with integral 2m radius mirrors at both ends was chosen, since it was part of the tube supplied by Scientifica and Cooke Limited. It will be noticed (figure 4.3) that this falls in a region of good stability, $g_1 = g_2 = \frac{1}{2}$. The mirrors were both gold plated stainless steel. The output mirror had a 2mm diameter hole through the centre which was sealed with a thin sheet of polycrystalline NaCl.

The performance of this system was very poor. Eventually it was unable to produce sufficient power due to fouling of the sodium chloride window. This window, at the bottom of a narrow

$$g_1 = \left(1 - \frac{d}{R_1}\right) < 0$$

$$g_2 = \left(1 - \frac{d}{R_2}\right) > 0$$

$$g_1 > 1$$

$$g_2 = 1$$

$$g_1 = 1$$

$$g_2 = 1$$
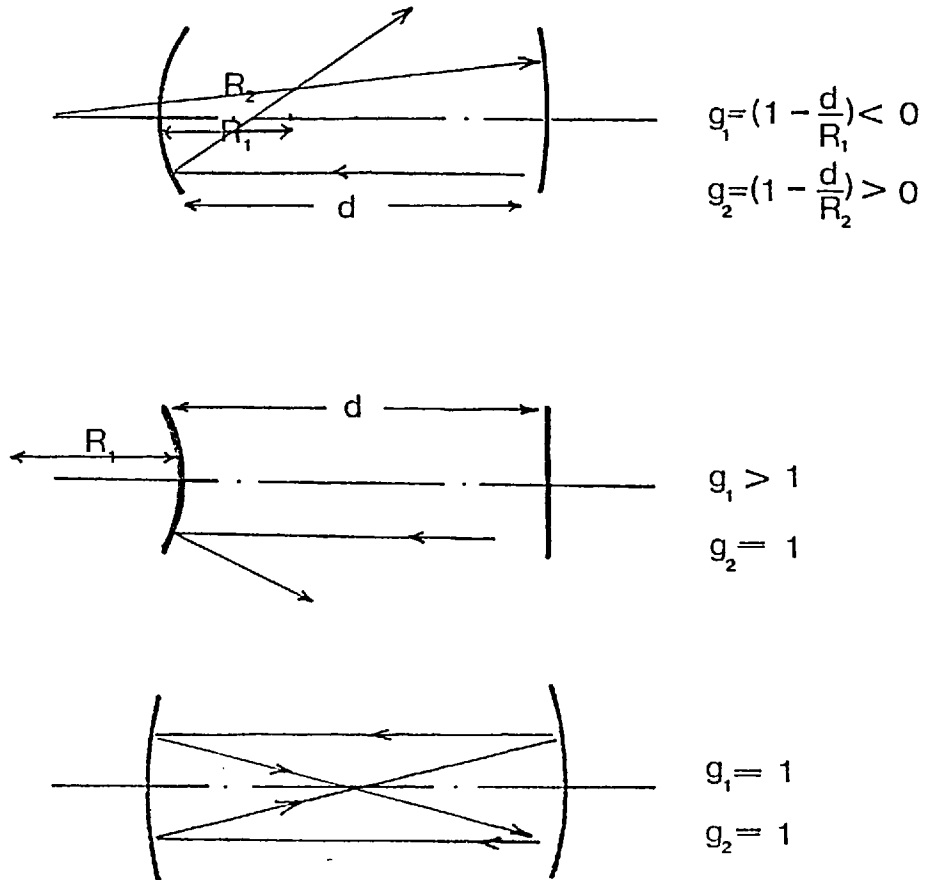
Fig 4.2   Illustration of   stability criterion
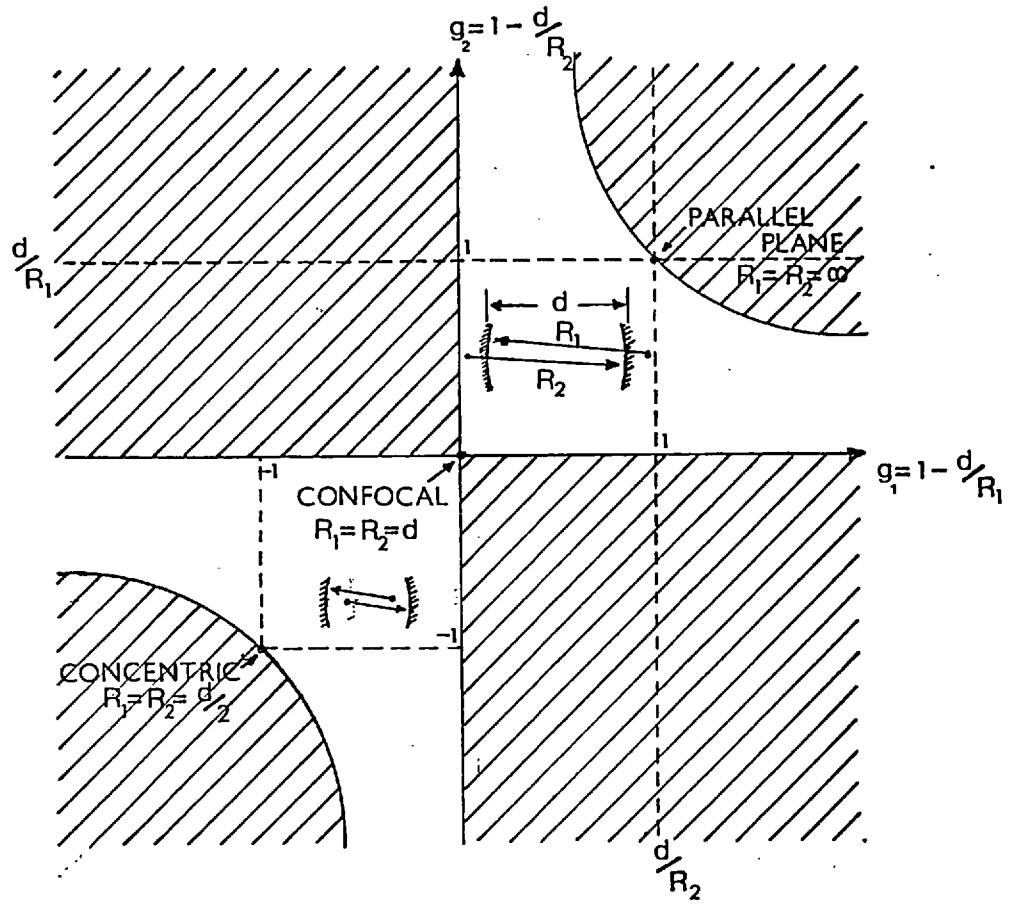
Fig 4.3   Stability diagram. Unstable systems shaded. (91)

hole, was difficult to clean, particularly since sodium chloride
is so soft. A further disadvantage of this mirror system was
the highly divergent beam it produced (see figure 6.17)
requiring all optical work to be done very close to the output
mirror.

A more satisfactory resonant system was designed and built.
It consisted of a plane germanium output mirror and a concave
gold plated total reflectance mirror. The plane germanium output
mirror, supplied by ITT, was surface coated with either 65%,
70% or 80% reflectance patented coating on the cavity side and
an antireflectance coating on the output side. These coatings
were in turn coated with Ge to allow for cleaning. The total
reflectance mirror had a gold coating on a copper base with a
radius of curvature of 5m, 8m, 10m or 20m. The soft gold film
was coated with an ITT patented protective layer, containing
Rhodium, to allow for gentle cleaning. These plano. – concave
systems are seen in figure 4.3 to be in the "stable" region.
This new arrangement gave approximately 5 times the power obtained
from the Scientifica and Cooke system.

The transmissivity of the output mirror has been shown
by Allen[76] to affect the output power. Too large a transmissivity
causes excessive cavity loss and stops the lasing action, too
little unnecessarily reduces the power output. Allen derived
a theoretical relationship:-

$$ I = \frac{\varepsilon_o C^2}{2\beta d} \; \delta(2\bar{\delta} - \delta) $$

where I = output power   W

ε_o = electrostatic constant = 8.85 x 10^{-12} farads/m

C = velocity of light = 3 x 10^8 m/s

δ = transmissivity of the output window

$\bar{\delta}$ = optimum value of δ

d = resonator length m

β = quantity dependent on the gas mixture and excitation.

Anderson[77] working with an SERL laser of fresnel No $\simeq$ 8 found
fair experimental agreement (figure 4.4). From experiments at
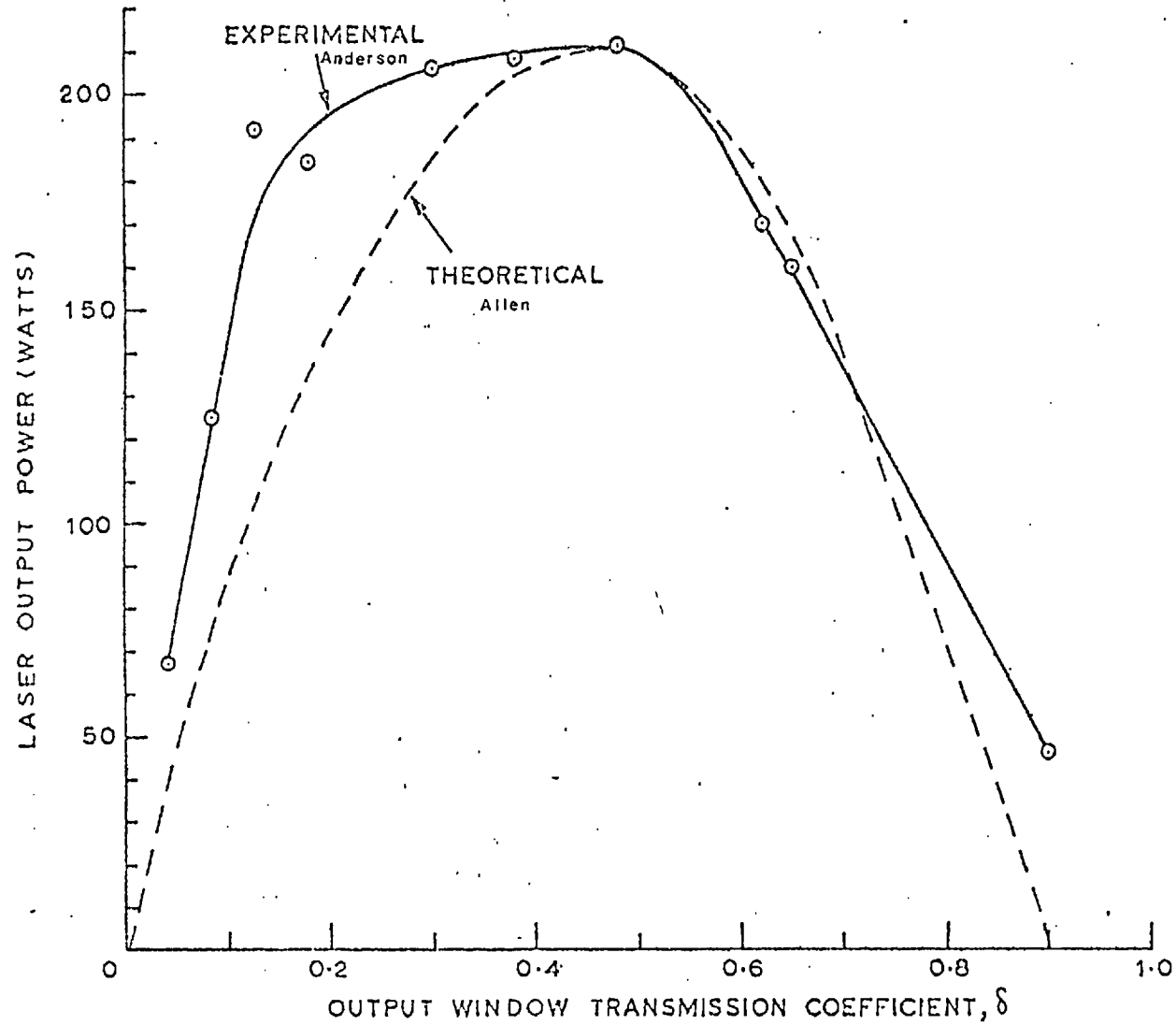
FIG. 4.4. Variation of laser output power with transmission of output window. Discharge current = 60 mA. Partial pressures He 15 torr, N_2 3 torr, CO_2 1 torr. Mirror radius = 40 m. Gas flow 400 volume changes per minute.(77)

SERL, Baldock,the optimum transmissivity has been found to be
70% reflectance for 1m tubes
50%   "   " 2m   "
20%   "   " 10m   "

For the chosen cavity 80%, 70%, and 65% reflectance mirrors were
tried. The 80% mirror was preferred.

4.2.2.3 Mirror mounts

The mirrors were mounted in kinematic mounts as shown in
figure 4.1 and photographs .Plate 1.

The integral mounting of the mirrors followed the Scientifica
and Cooke design, the micrometer holders were from an SERL
design. Integral mirrors had the advantage of a better quality
cavity than would be the case with external mirrors and KCl
Brewster windows sealing the plasma tube. However, they suffered
more from fouling by sputtering and from movement due to thermal
warping during operation (see section 5.1.8).

The Germanium output mirror was watercooled to avoid thermal
runaway effects (see section 4.3.1).

4.2.2.4 The cathode

The cathode in the cavity is subject to a fairly abusive
environment. Difficulties with cathodes have been encountered due to
excessive sputtering, evaporation, reactivity with the lasing gas
plasma and cleaning up of the gas fill.

Sputtering, in particular, is a great nuisance due to
fouling of integral mirrors. This is reduced in the present design
by making the mirrors positive with respect to the central earth
electrode and by building the cathode of aluminium which has an
exceptionally low sputtering rate when used as a cold cathode in
a noble gas discharge (magnesium and tantalum are similarly
successful).This is considered due to the tenacious oxide coating
which is highly resistant to ion bombardment yet allows electrons
to tunnel through it.
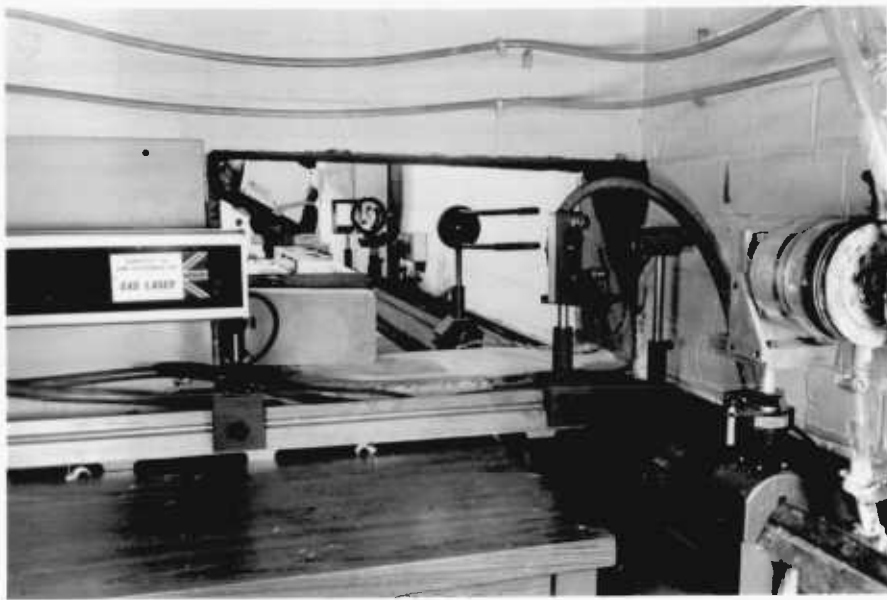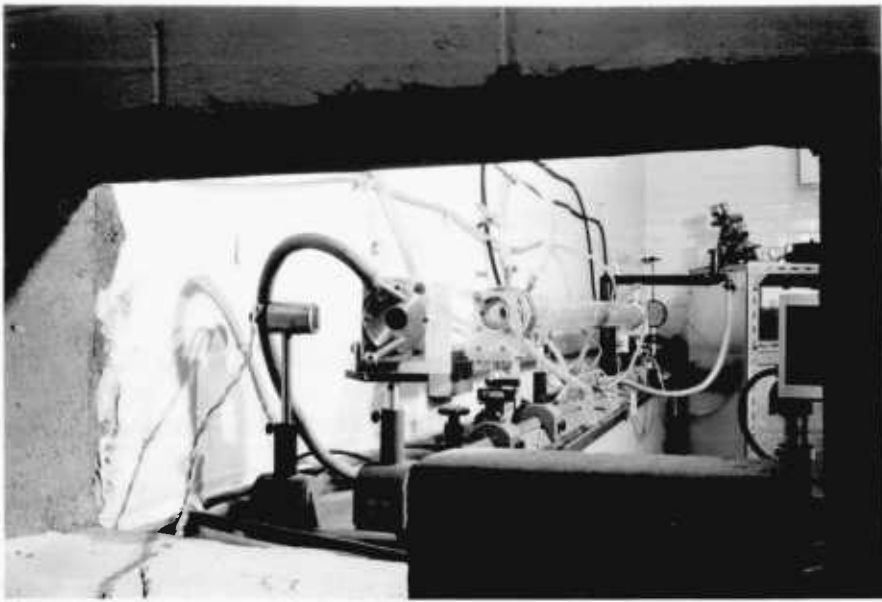
Plate 1 - Apparatus - General view of arrangement
for deposition

Care was taken in the cavity construction to avoid areas of
Araldite adhesive, used to join the glass tube to the metal
electrodes, which could be exposed to bombardment and consequent
heating. Such effects appeared to cause excessive sputtering.
The original design (tube glued by Scientifica and Cooke Limited)
had such areas which could occasionally be seen to glow white
hot, possibly due to the mirror alignment exposing them to the
lasing radiation.

4.2.2.5 The lasing medium

The lasing medium for this type of laser had to be $CO_2/N_2/$
He for the reasons described in Appendix 3. The only remaining
problem was their proportions. Wright[78] showed that for a laser
of around 1m in length with gas flowing at 4.65m/s in the plasma
tube the optimum gas composition is in the region 7 torr He,
3 torr N_2, 1.2 torr CO_2. He further showed that the ratio of
$CO_2:N_2$ is crucial whereas the quantity of the He had only to be
above a certain level (6 torr in his experiments). Within this
region the performance was not very sensitive to gas composition.

The choice was either to build a gas mixing system or
purchase premixed gas. In view of Wright's work it was decided
to use premixed gas and so reduce the complexity of the total
laser unit. Gas mixtures of 82%He, 12.3%N_2, 5.7%CO_2 and 78%He,
13%N_2, 9%CO_2 were used.

The gas supply system is shown in figure 4.5 . The 1/4"
diameter gas delivery lines with the 1/8" diameter inlet pipes
on the tube together with the size of the vacuum pump (Speedivac
ES150) only allowed relatively slow flow rates (up to approximately
50 tube volume/min). The flow rate was controlled by an Edwards
fine control needle valve (Model LB2B). Such a sensitive needle
valve was essential since the output power was a major variable
of the pressure. The pressure was accordingly used to control
the laser power.

LASER   TUBE

20-0 TORR
PRESSURE GUAGE

ROTAMETER

NEEDLE
VALVE

PREMIXED
$CO_2/N_2/He$
GAS CYLINDER

NON RETURN
VALVE

VACUUM PUMP
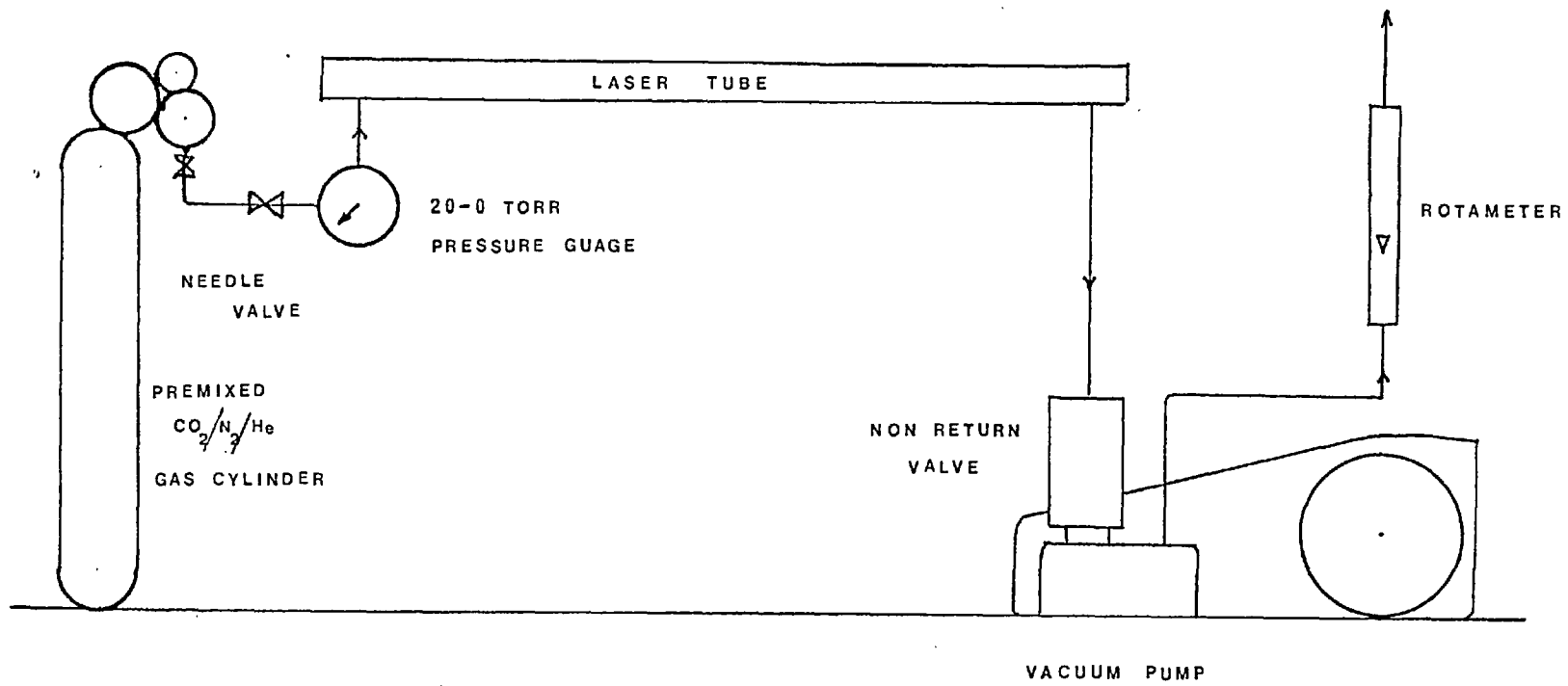
Fig 4.5   GAS   SUPPLY   SYSTEM

4.2.3 <u>Laser power supply</u>

There are various ways of pumping a $CO_2/N_2/He$ laser; RF, AC or DC electric discharges will all inject sufficient energy to allow lasing.

Since RF discharges are far less dangerous than AC or 3000 volt DC discharges an RF pumping system was originally tried using a 1kW 1464 Redifon RF generator. Suitable, watercooled, copper coils were wrapped around the plasma tube. A plasma was produced but it formed in standing waves down the tube. Since no output could be obtained it was surmised that the oscillating lasing beam suffered too much loss in passing through non glowing regions.

AC discharges only offered pulsed output and so a DC discharge was tried.

A full wave rectifier unit to supply 100mA at 11000 volts was built to a circuit designed by SERL and shown in figure 4.6 and photograph of apparatus Plate 2   . This worked satisfactorily.

4.2.4 <u>Cooling system</u>

A non electrically conducting fluid was required to cool the laser tube to below 40°C, above which temperature considerable power loss could be expected if not actual thermal damage to the glass/metal connections.

Oils or deionised water were possible. Deionised water is a better coolant and clean. So a deionised water cooling system was built as shown in figure 4.7 .

4.3 <u>The design and construction of the optical system</u>

The 1.5 cm diameter beam of 10.6μ radiation of up to 30 watts coming from the output window of the laser first passed through a 3.8 cm diameter germanium beam splitter, antireflectance coated on both sides, which was set at 45° to the beam and was watercooled. Some 5% of the beam power was reflected into a

A 13 amp plug

B Circuit breaker

C 2 pole switch. Arrow Electric

D Neon indicator

E 13 amp fuse

F Single pole switch

G cooling fan

H 3 pole relay 250 volt 20 amp

J microswitch push on spring back

K single pole switch

L neon indicator

M 20 amp variac

N 20 amp fuse

O 20,000 volt transformer – Simpsons

P Rectifying panels

Q 20 kΩ load resistance

R 0-100mA ammeter

S 30MΩ 20W. resistor

T .1μF capacitor

W 20 MΩ 1mA resistor

X 0-1mA ammeter

Y H.T. terminal connectors

Z Neon Indicators for meter failure
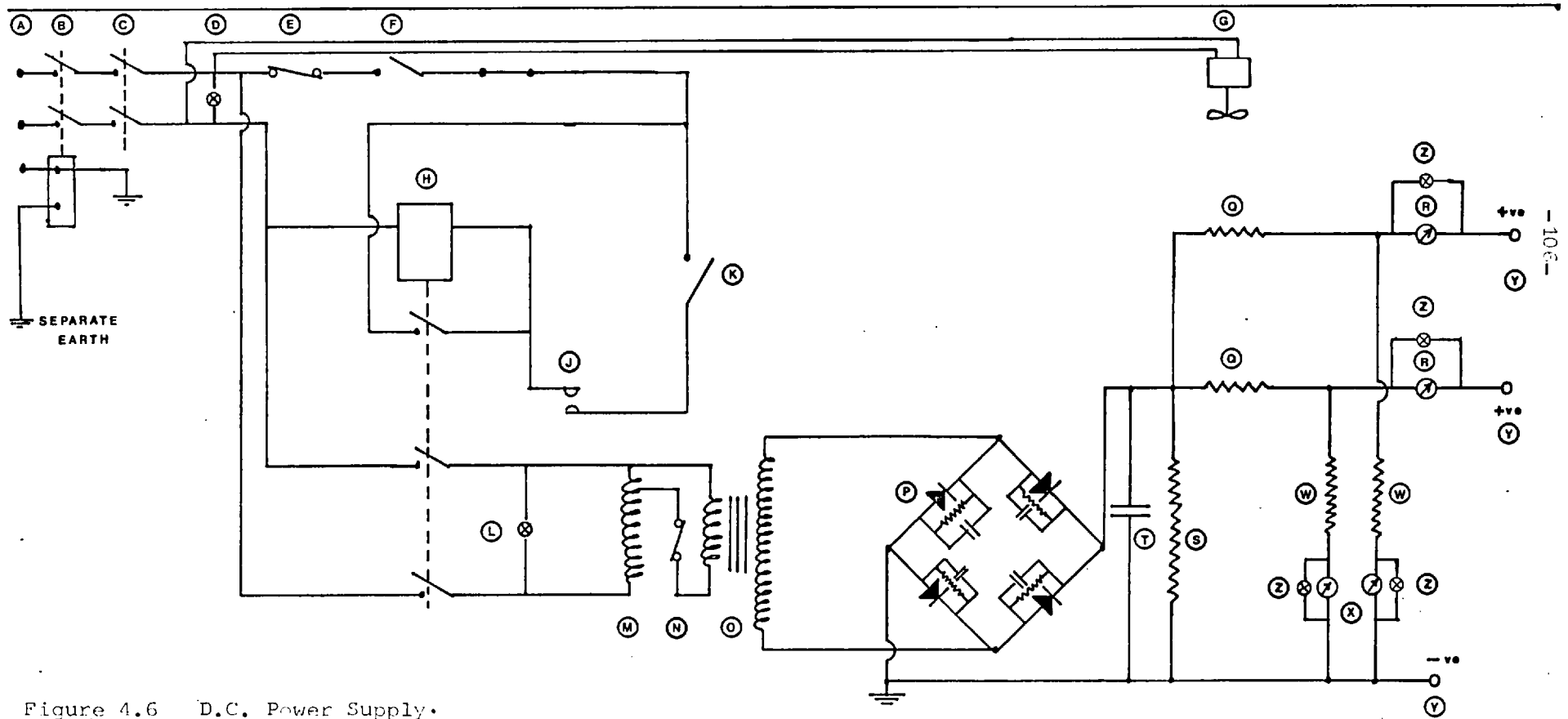
Figure 4.6 D.C. Power Supply.

SEPARATE EARTH
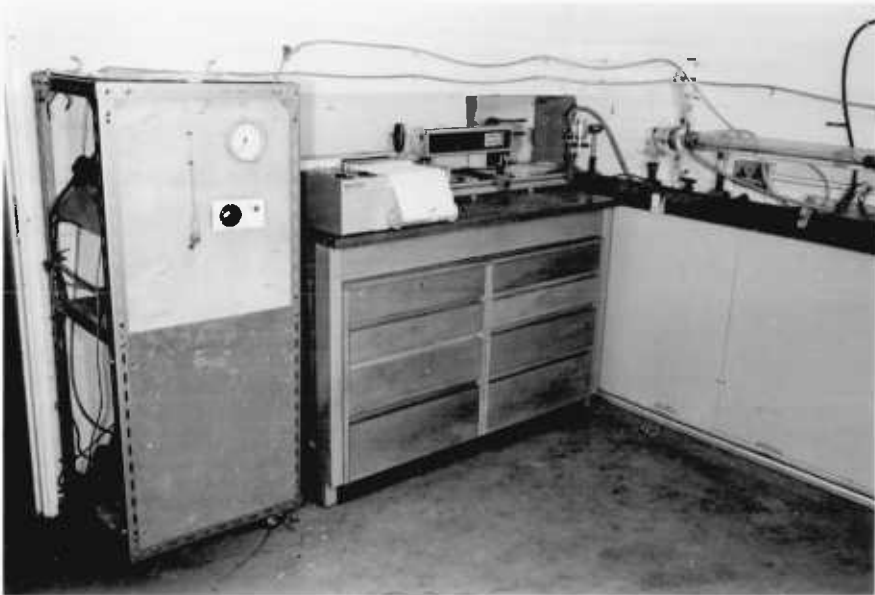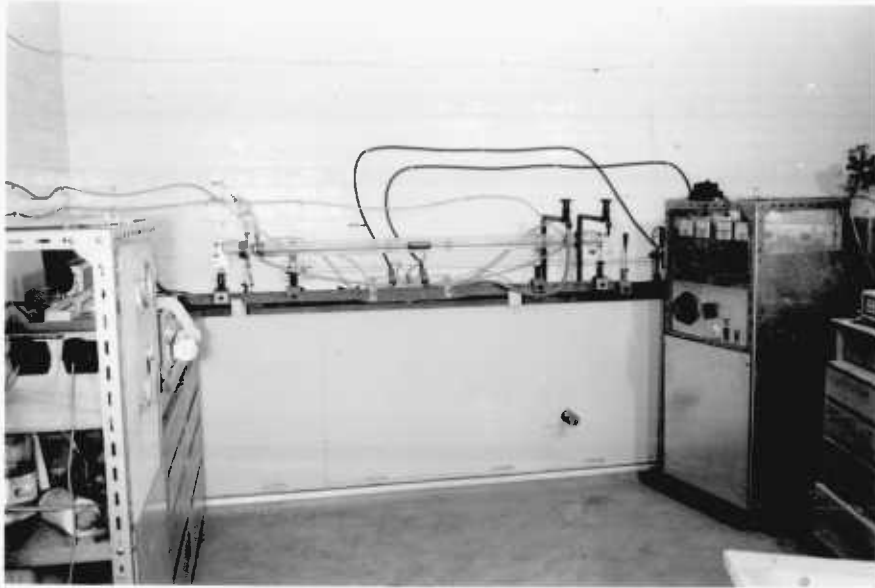
Plate 2   Apparatus - General view of the laser

CONDUCTIVITY METER

OUTPUT
WINDOW

BEAM
SPLITTER

LASER TUBE

APERTURE

DEIONISATION
RESIN COLUMN

IN

MAINS

OUT   WATER

RESERVOIR

PUMP

ICE BUCKET
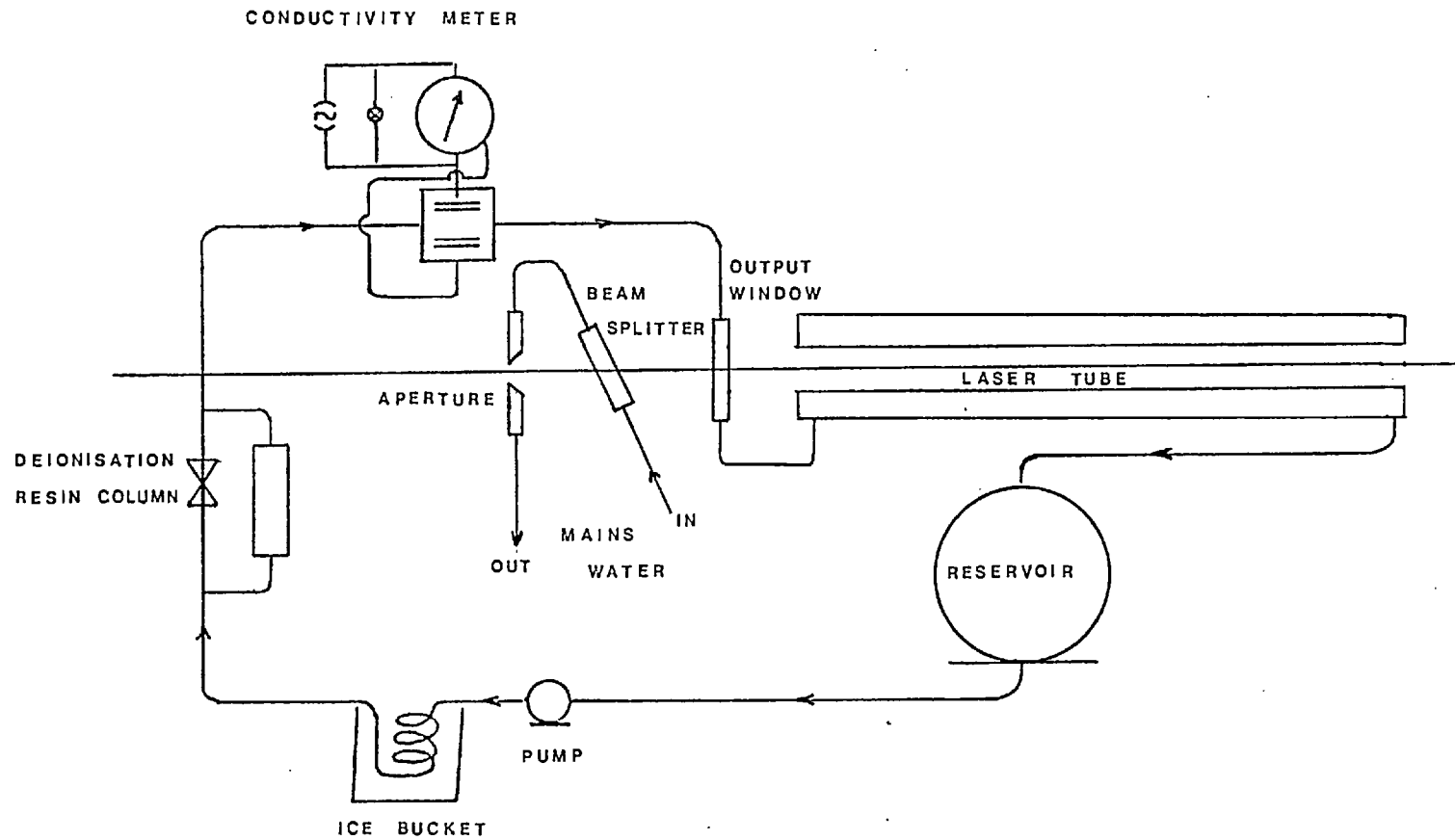
Fig 4.7   DEIONISED & MAINS WATER COOLING CIRCUITS

thermopile. (Griffin and George) used as a power monitor. The
signal from the thermopile was continuously recorded on a Smiths
servoscribe potentiometric chart recorder S2. The remaining 95%
of the beam power passed through an aperture and the aperture was
imaged by a sodium chloride lens onto a glass plate. Visual
alignment, but not focus, was obtained by feeding a beam of red
light (6328°A) from a He/Ne laser (Scientifica and Cooke 1mW) onto
the back side of the Ge beam splitter so that it was colinear with
the invisible infra red beam. The optical arrangment is shown in
figure 4.8 and photographs plates 1&2. The red beam from the other end
of the He/Ne laser was also used to monitor the position of the
total reflectance mirror during operation as shown in figure 4.8
and for aligning the laser mirrors after cleaning (section 5.1.1)

4.3.1   The Aperture

The aperture was watercooled, for the circular prints, but not
for the cross prints in which it was an aircooled 1mm thick mild
steel sheet painted matt black. The fuzziness of some of these
crossprints at the end of a long series of deposits suggested that
the hot aperture was aiding the formation of ghost images - (see
sections 7.2.3 and 8.13.)   -. So for the circular prints
a water cooled aperture was used. The aperture size (5mm diameter)
was such that it could be conveniently and reasonably reliably
totally covered by the beam.

4.3.2   The beam splitter

The beam splitter was a 3.8cm diameter, Germanium disc (ITT),
A/R coated both sides mounted in a kinematic mount with micrometer
adjustment screws made to our own design using some parts from the
SERL mirror mount drawings (No A4961 and C4961). The Germanium
disc was watercooled with a separate mains water supply. This
cooling was found necessary since with a prolonged run the Germanium
heated up. As the Germanium heats up so its absorptivity rises
reducing the output through the beam splitter and increasing the rise
in temperature. On some runs with an air cooled beam splitter there
was a complete power shut off due to this effect. Fortunately on
these occassions the laser was operating at low powers so the
germanium merely became very hot but did not crack or melt. This

TOTAL POWER
CALORIMETER

SERVOSCRIBE

THERMOPILE

SUBSTRATE   NaCl LENS   APERTURE

CO$_2$ LASER

COLINEAR
RED BEAM

He Ne LASER

THERMODOT INFRA RED
THERMOMETER

RED BEAM FOR ALIGNING THE REAR MIRROR
DURING OPERATION
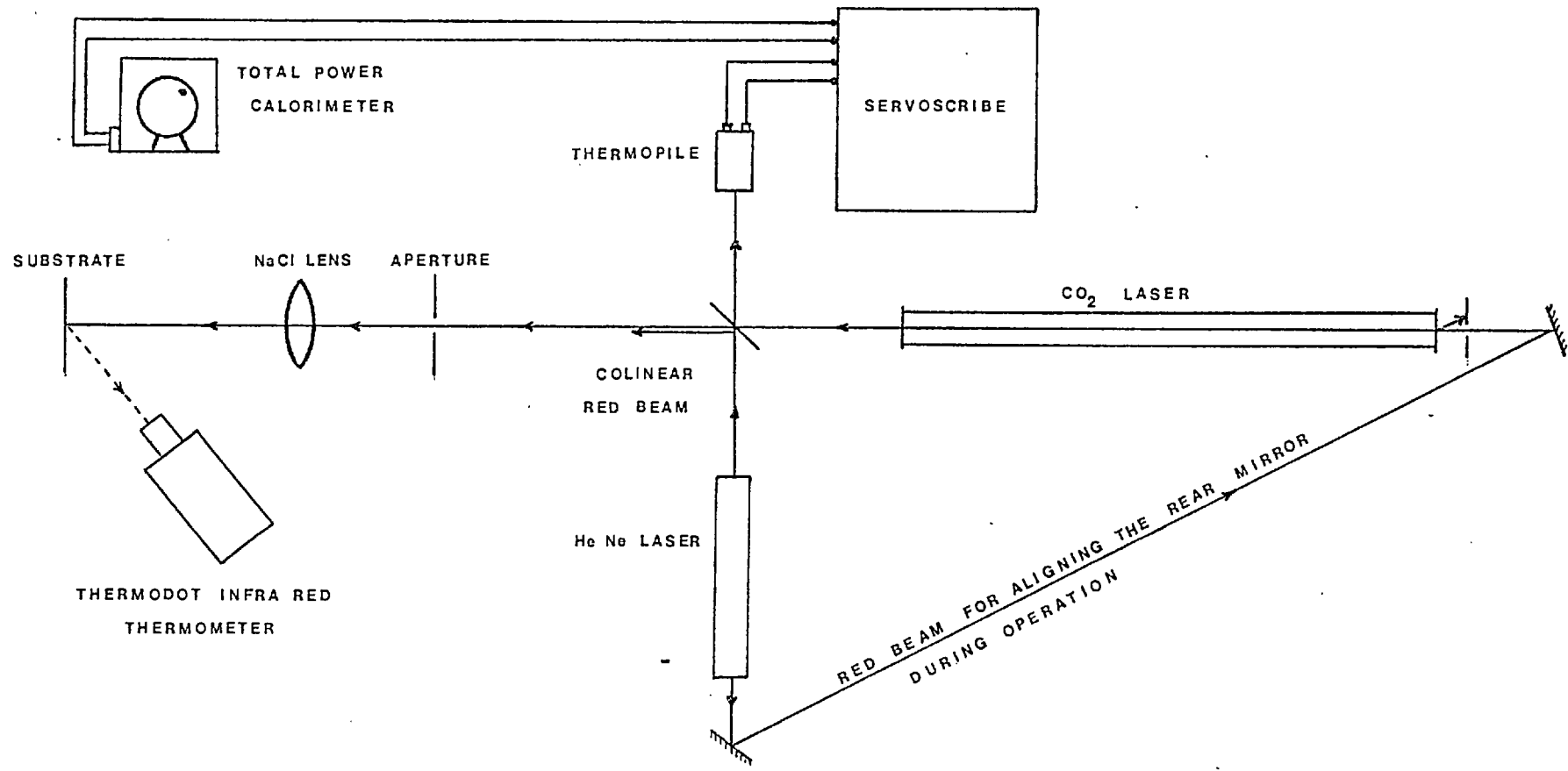
Fig 4.8   OPTICAL   ARRANGEMENT

property of germanium, known as the "thermal runaway" condition
has been studied by Horrigen et al (79) whose experimental results
are shown in figure 4.9 .
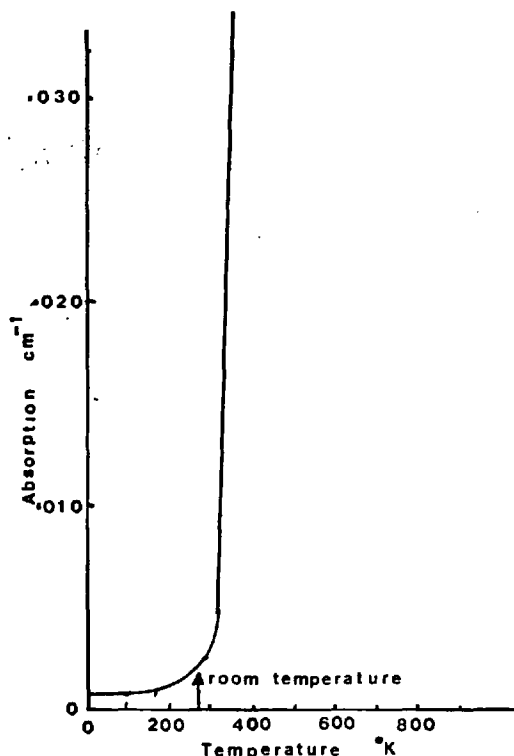
Fig 4.9   The variation   with temperature
of   the absorption   coefficient at 10·6 μ
for   Germanium (79)

Thus if the temperature of the Ge is allowed to rise above 40°C
then the increase in absorptivity is amply able to increase the
Ge temperature and so the temperature runs upwards until total cut
off or worse occurs. The optical data for Germanium are shown
in Table 4.1.

4.3.3. The lens
polycrystalline
      The lenses were made of/sodium chloride ground and supplied by
Optiglass Limited. They were of standard quality being all that was
required at this stage of the investigation. NaCl suffers from rapid
attack by water if the humidity exceeds 35% [80], unfortunately the
laboratory humidity usually exceeded this value and consequently
misting occurred towards the end of a long run. When this happened
the lens was gently cleaned with metal polish. The lenses were all
stored in a dessicator containing silica gel when not in use.
The optical properties of NaCl are shown in table 4.1

Table 4.1

Optically relevant properties of various lens materials

Material specification	optimised Ge	CdTe	ZnSe	GaAs	NaCl	KCl
Bulk absorption @ 27°C to 10.6μ cm^{-1}	0.018	0.002	0.006	0.02	0.002	0.002
Specific heat J/cm^3 °C	1.65	1.23	1.87	1.42		
Thermal conducitivity W/cm °C	0.60	0.07	0.21	0.46	0.07	0.07
Refractive index @ 10.6μ	4.0	2.64	2.4	3.3	1.50	1.50
Transmission range μ	2-23	1-30	.5-20	1-18	.2-21	.2-21
Flexural strength (rupture modulus) p.s.i.	13,500	3,200	8500	20,000	350	330
Density grm./cm³	5.323	5.86	5.27	5.32	2.17	2.00
Typical thermal distortion figure of merit⧸ (AR coated window 5mm thick @ 100W throughput)	0.018	0.023	0.015	0.031		

⧸ = Device absorption/(specific heat x thermal conductivity) low values being an advantage

Competitive materials for IR optics are: (optical properties
shown in table 4.1)

KCl Similar in most respects to NaCl having a low cost, excellent
transmission, and transparent to visible light allowing
alignment with a He/Ne beam. However, like NaCl, its thermal
properties are poor having a low thermal conductivity
and fracture strength. It is also quickly attacked by
water if the humidity exceeds 35%. There is little to
choose between KCl and NaCl.

Ge A costly material, subject to thermal runaway – see section
4.3.2 and a typical value of the thermaldistortion ; figure
of merit (device absorption/specific heat x thermal conductivity)
is 0.018 for an AR coated window with 100W throughput. This
value is similar to NaCl. The high refractive index (4.0
@ 10.6μ) is an advantage in making quality lenses since less
curvature is required.
An excellent material for the low powers used here but not
transparent to visible light giving alignment problems.

GaAs A costlier material than Ge, with greater strength and less
absorption, making it suitable for high power work.

ZnSe Transparent to visible light, and at present viewed as the
best material for high power laser optics. It is as costly
as GaAs.

CdTe A lower cost material than ZnSe but has a lower thermal
conductivity which is signfic ant only in very high power
application.

On the grounds of cost, availability and transparency to visible
radiation NaCl was chosen.

4.4 The Evaporator System
     Many materials could be deposited by this process – see
appendix 7. However, the problem of what to evaporate and deposit
was partially pre-empted by the work of G.J. Davies[41]; who, under
the author's supervision, established the mass transfer conditions

existing beneath a vertically impinging gas jet as a prelude to this present study.

Davies used cobalt acetyl acetonate (CoAcAt) and nickel carbonyl in his deposition work. It was found that the attraction of $Ni(CO)_4$, which allowed a wide range of concentrations, was outweighted by the extremely difficult experimental techniques required by safety considerations, and the fact that adherent plate deposits could not be formed from the more concentrated vapour. The comparative simplicity of working with relatively non-toxic cobalt acetyl acetonate at temperatures of about $120^{\circ}C$ was the reason the material was chosen.

Davies found a further benefit in using CoAcAt. If the chelate was decomposed in a mildly oxidising atmosphere CoO was deposited, which being partially transparent gave self profiling interference colour fringes. These Davies successfully used to measure his deposit thicknesses.

A note on Cobalt Acetyl Acetonate (CoAcAt)

a) Structure

Cobalt acetyl acetonate, $Co(C_5H_7O_2)_2$ is an example of an bidentate chelate compound. The crystal structure of this salmon pink metallic complex has been analysed by Bullen[81]. He found it to be a planar molecule with the cobalt atom lying 0.4×10^{-7} mm above the plane of the two ring ligands.
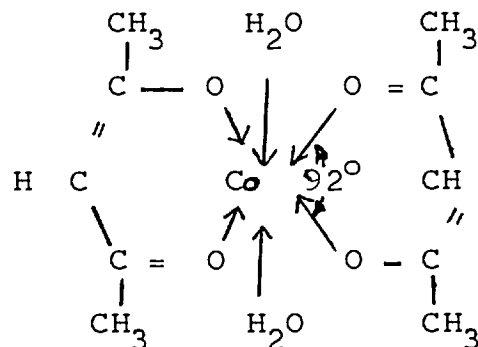
b) <u>Vapour pressure</u>

Vapour pressure data in the range $50^{\circ}C$ - $90^{\circ}C$ have been recorded by Van Hemert et al[82] and Berg and Truemper[83]. Due to pyrolysis an optimum vaporisation temperature of between 140 - $210^{\circ}C$ was identified by Charles and Haverlock[86] for CoAcAt in H_2 carrier gas.

c) <u>Thermal dissociation</u>

Thermal decomposition has been recorded as starting at $120^{\circ}C$ by Davies[41], $200^{\circ}C$ by Jablonowski[85]. The dissociation is found to be virtually complete and instantaneous above $300^{\circ}C$ (Hoene et al)[84], or $290^{\circ}C$ (Charles and Haverlock[86]) optimum substrate temperatures for the formation of plate deposits of cobalt have been suggested by Jablonowski[85] as 318-$352^{\circ}C$ and Charles and Haverlock[86] as 275-$300^{\circ}C$ both using a hydrogen carrier gas.

From this data it was seen that an evaporator system operating at around $140^{\circ}C$ capable of extended runs and using nitrogen carrier gas with an oxygen partial pressure in excess of 5×10^{-4} atmospheres (see section 6.3.4.5) was required*. The substrate temperature should be about $300^{\circ}C$ to produce good CoO deposits.

Several evaporator systems were tried:
(i) Davies' evaporator: this was a series of four packed beds of CoAcAt heated in an oil bath. It was wasteful of chelate due to the formation of the non volatile residue reported by Charles and Haverlock[86]. It also only allowed a uniform concentration for around 20 minutes before needing to be refilled. Refilling was time consuming and not suited to the temperamental laser power system which preferred an intensive experimental campaign.

(ii) A packed bed of glass beads heated in an oil bath and fed with preheated nitrogen carrier gas: the chelate was fed as an alcohol slurry. This design overcame the slow filling problem of design 1. The concentration of chelate, after the alcohol had

---

* Nitrogen was chosen instead of hydrogen after considering the experimental danger of firing a laser into a tank of hydrogen which might contain some oxygen.

blown over, was fairly steady. However it suffered from three main disadvantages:-

a) The oil bath took 5 hours to come to equilibrium.

b) the delivery lines had to be very long, and, although traced, condensation tended to occur in them sometimes causing blockages and chelate dust in the vapour.

(iii) The same glass bead packed bed heated eletrically (see figure 4.10) This design was built by A. Young. It was found to give an erratic output due to the low thermal inertia of the system.

(iv) A larger packed bed containing 500 grams of stainless steel balls heated eletrically with preheated gas and heated delivery lines designed and constructed by A. Young(see figure 4.11.) The higher thermal inertia was found adequate to give a steady vapour concentration for periods of up to 30 minutes between each slurry refill.

This was the evaporator system used on all recorded runs. The temperature at all stations shown in figure 4.11were recorded on a 12 pen recorded. In operation refills occurred more frequently than every 20 minutes.

4.5 Instrumentation

The operating parameters for the laser and evaporator had to be known for all runs. They weremeasured as follows and the methods used are discussed more fully in chapter 6.

Laser parameters:

(i) output power: 5% of the total beam power was deflected by a beam splitter into a Griffin and George thermopile (figure 4.8). The signal from the thermopile was continuously recorded on a Smiths Servoscribe recorder and calibrated against a spherical black body calorimeter.

(ii) tube current and voltage: these were measured by the meters shown in the circuit diagram (figure 4.6) Readings from these meters were taken intermittently.

Liquid feed — solution or slurry of chelate
in ethyl alcohol.

TC

TC

Evaporator

TC

Nitrogen and Chelate
Vapour out.

Nitrogen Preheater.

Firebrick insulation

GLASS BEADS

TC - thermocouple.

Column heaters.

TC

Nitrogen in.

Fig 4.10   EVAPORATOR 2.

liquid feed - solution or slurry of. chelate
in ethyl alcohol

TC

TC

TC

Nitrogen in→

→Nitrogen and Chelate
Vapour out

internal heater

packed column

S/STEEL BALLS

external heater

TC

TC
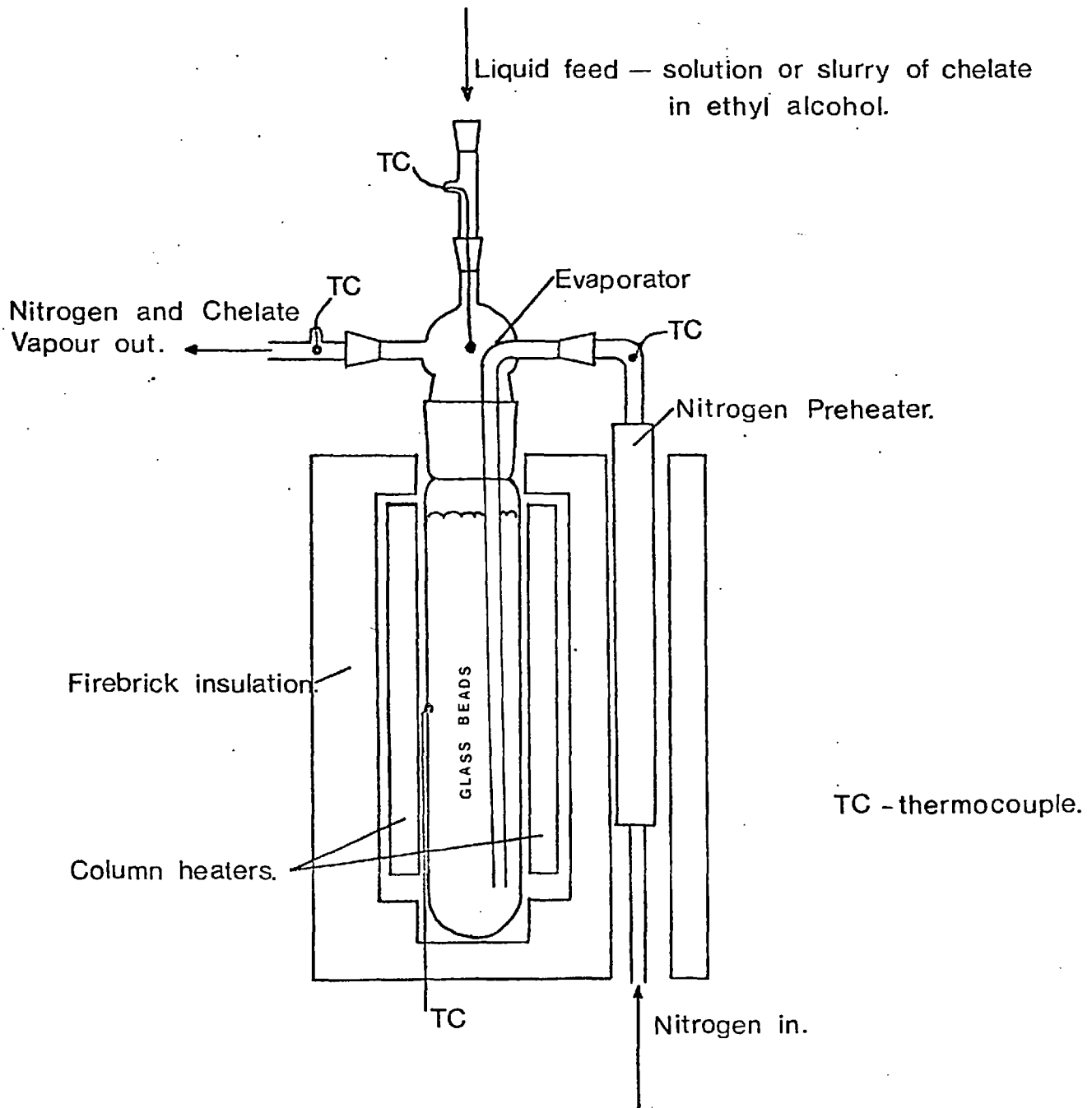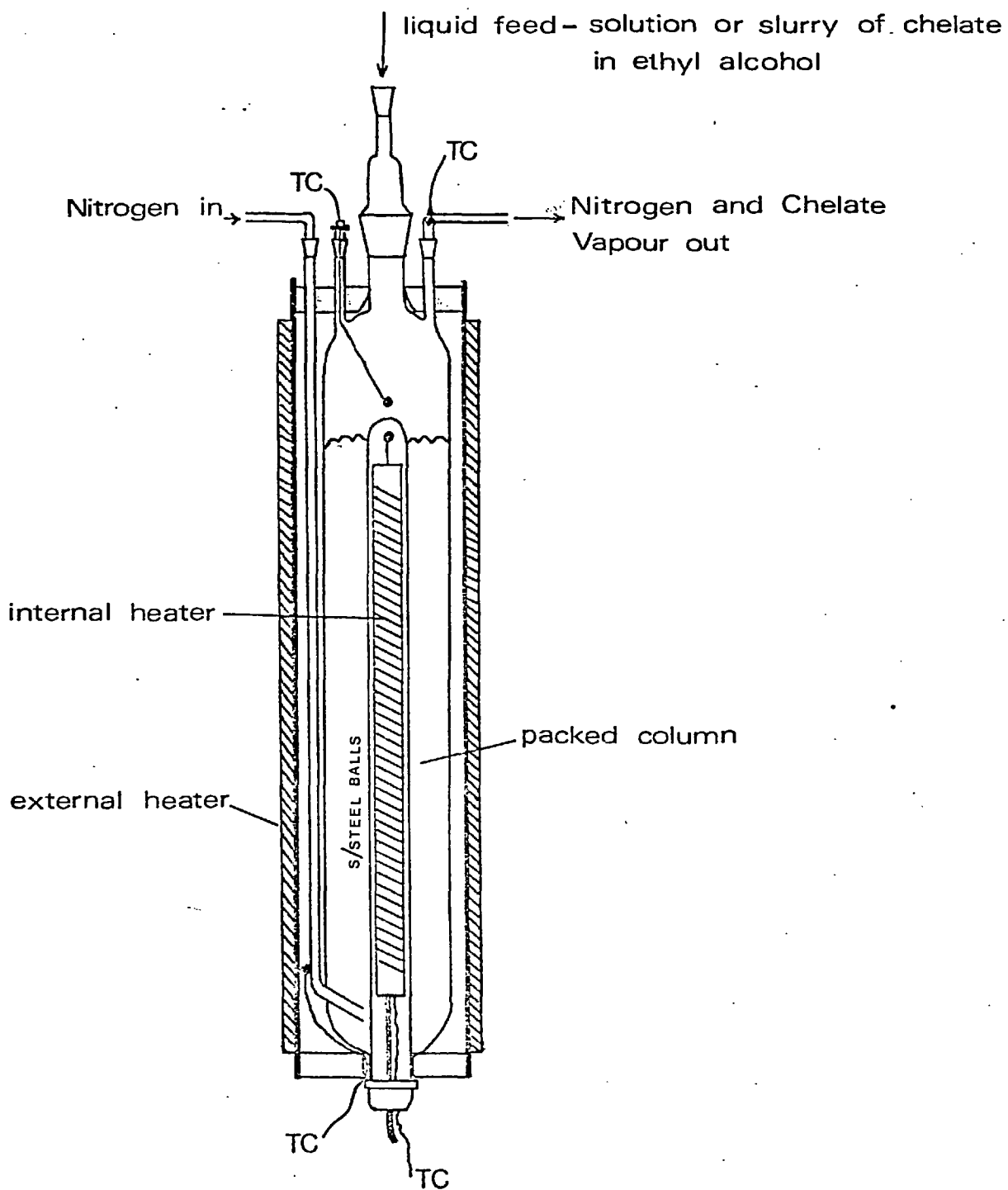
Fig 4.11 EVAPORATOR 3.

(iii)   tube pressure: this was measured on a pressure
        gauge (figure 4.5) readings were taken intermittently

Evaporator parameters:

(i)   temperature: readings from the thermocouples shown in
        figure 4.11   were taken continuously on a 12 pen chart
        recorder.

(ii)   gas flow rate: measured on a rotameter set in the
        cold nitrogen delivery line.   Readings were taken
        intermittently.

(iii)   Vapour concentration: the evaporator was calibrated by
        means of a bubbler system (section 6.3.12).   Also
        during runs, 8ml gas samples were taken from the
        delivery line and mixed with a 2cc sample of 10% H_2SO_4.
        The resulting cobalt solution was analysed for
        cobalt on an atomic absorption spectrophotometer (Perkin
        Elmer 290).   The results indicated the approximate
        concentration but chiefly they signalled if the
        evaporator had become exhausted.

Deposit Parameters:

(i)   Surface temperature: intermittent chart readings were
        taken of the surface temperature of the deposit and
        substrate by an IR industries thermodot TD17 infra
        red thermometer.

4.6   Choice of substrate

        A variety of substrates was tried.   Any moderately good
thermal conductor, such as stainless steel, titanium, etc could
not be heated sufficiently to cause deposition with the powers
available ($<$ 40W) (see section 8.2.9).   Also metallised
printed circuit boards could not be heated sufficiently.

        Thermo setting plastics, such as formica, charred.

Alumina, as supplied for microeletronic circuits by Materials Research Limited, was found to crack almost instantly upon heating, though sufficient temperature was obtained.

Glass microscope slides behaved very well and allowed optical fringe techniques to be used in examining the specimen shape, but suffered from cratering and localised cracking. Borosilicate glass, behaved similarly to glass.

Silica (Spectrosil) behaved similarly to glass, possibly with slightly less thermal damage effects, but required higher powers.

The substrates chosen were:-

		thickness
a)	Glass microscope slides	0.8 - 1.0mm
b)	" " "	1.2 - 1.5mm unannealed
c)	" " "	1.2 - 1.5mm annealed
d)	" " "	1.5 - 1.8mm unannealed
e)	" " "	1.2 - 1.4mm
f)	Silica(Spectrosil)	1.2mm

The choice being based on the reasoning:-
(i)   the deposition could be performed on glass
(ii)   glass slides were freely available
(iii) the surface of glass allowed optical interference methods for determination of shape.

CHAPTER 5

OPERATION OF THE EQUIPMENT

Prior to any fully instrumented runs the operation of the
laser and evaporator were investigated.

5.1   The Laser
5.1.1   Alignment
Before a sustained run the laser would be stripped down.   The
tube would be cleaned with a pull-through of acetone soaked cotton
wool.   The mirrors would be gently polished with acetone soaked
cotton wool to remove the dark sputter marks.   The Germanium
mirror was also, on occasions, lightly polished on a fine (1 micron)
diamond polishing wheel.   This effectively removed the staining
and did not appear to spoil the reflectance properties of the
mirror.

The cleaned parts were next assembled with a good vacuum seal,
no vacuum grease on the inside of the tube, and with the mirrors
perfectly parallel when under a vacuum.

The parallelism of the mirrors was achieved by placing an
aperture at either end of the tube.   The apertures were exactly
central to the tube bore.   This could be arranged either by having
the apertures mounted on the laser optical bench and centering
visually by looking down the tube; or by making the aperture
out of card; so that the card, which had a central hole in it,
fitted the circular mirror pockets at the ends of the plasma tube.
The Ge beam splitter (figure 4.8) was rotated through 90° so that
the He/Ne red beam was reflected into the output end of the tube.
The beam was adjusted to pass through both apertures and was thus
running along the tube axis.   A second red beam from the He/Ne
laser came either from another beam splitter placed just in front
of the He/Ne laser or from a mirror reflecting the weak rear out-
put beam as shown in the figure 4.8 .   This second beam was
reflected into the total reflectance end of the plasma tube and
made colinear with the first beam.

The total reflectance mirror was put in place. A glass flat
was placed over the other end, sealing the tube. A vacuum was
drawn. The micrometer adjustment screws and mount height were
set so that the first red beam was reflected down itself. The
point where the second beam,reflected from a small mirror.stuck
on the back of the total reflectance mirror, fell on the back
aperture was noted. That was the future reference point for
establishing that the mirror was approximately parallel with
the output window. This device saved many hours subsequently
if the alignment was lost.

The vacuum was released; the glass plate removed; and the
output mirror set in its water cooled mount at the end of the
tube. The vacuum was drawn again and the back reflection of the
first beam from the front face of the Ge mirror adjusted by means
of the mirror mounts to be colinear with itself. The parallelism
of the Ge slab was claimed by ITT to be very good...The micrometer
marks were noted for future reference. The back play in the
micrometers was sufficient to make these values not of great
importance. However, if alignment was lost they would usually be
adequate to get a lasing signal from which finer tuning could easily
maximise the signal.

The Germanium beam splitter was then rotated back through 90°
and the laser was ready for operation.

5.1.2 Output Power

The SERL papers [78,79,87] have shown that the laser power is
a function of gas pressure, gas flow rate, gas composition, tube
current, and tube temperature. It is also perhaps obvious, but
nevertheless important, to have a clean tube with properly aligned
mirrors. The performance of the laser used here against these
parameters is now discussed.

5.1.2.1. Effect of tube pressure on power output

Graph figure 5.1 shows the variation of total laser power after
passing through a lens with tube pressure. The scatter is probably
due not only to the variation in current, as shown, but also to tube

Fig 5.1 Laser performance as a function of
gas pressure

O TUBE CURRENT 50 mA

X " " 62 mA
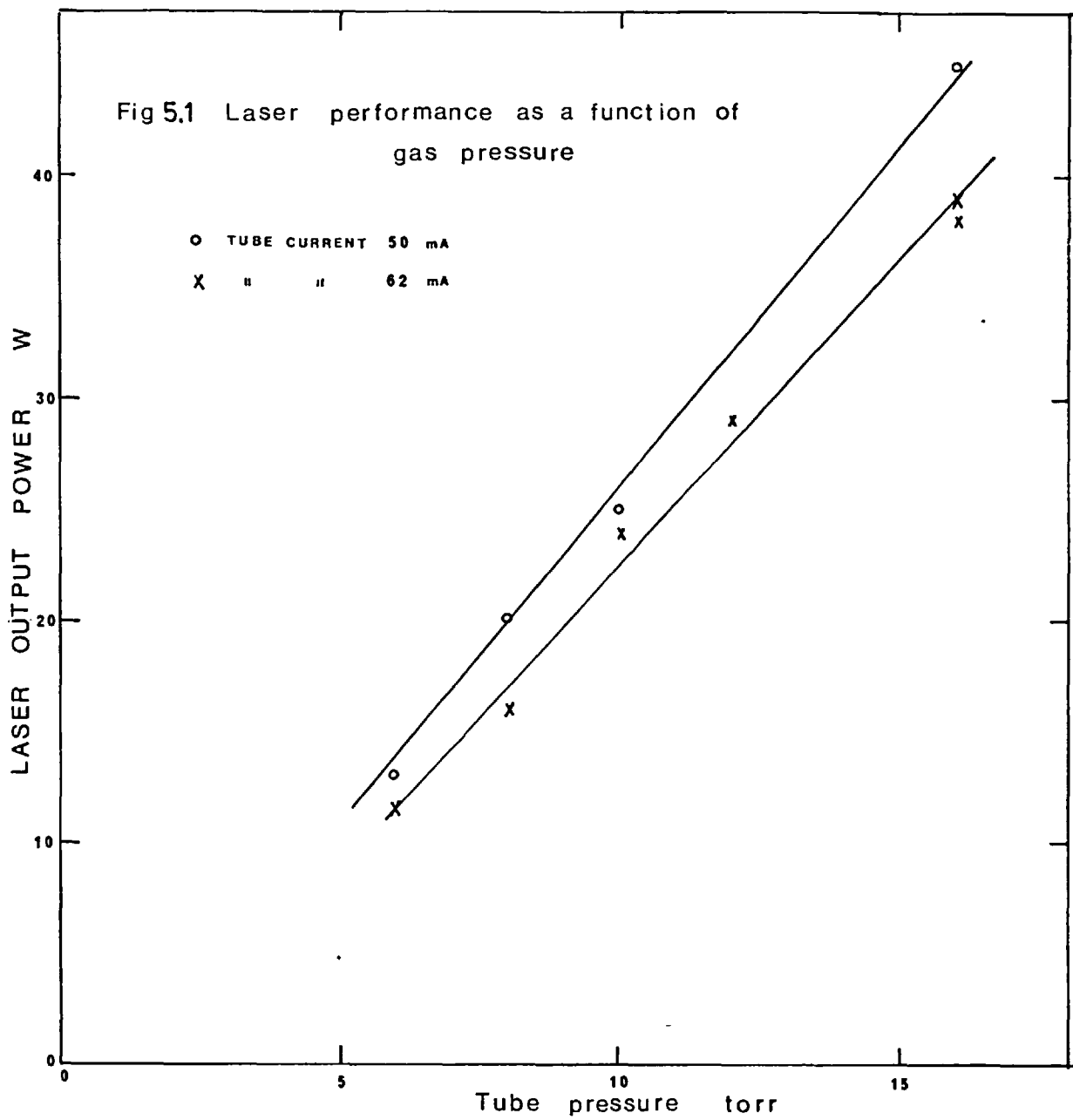
temperature and tuning. The strong correlation shown between pressure and power allowed the power to be controlled by the gas pressure.

5.1.2.2 Effect of gas flow rate

The piping and pump sizes prevented large gas flows. This almost certainly accounted for the low power output achieved for a laser of this length (40 W/m compared to 70 W/m). Flow rates were approximately 50 tube volumes/min. compared to the SERL lasers using 400 tube volumes/min.

The importance of the flow rate was simply seen by stopping the gas flow causing the laser power to fall to zero within $\frac{1}{2}$ - 1 minute.

5.1.2.3 Gas composition

Two gas mixtures were used - 82% He, 12.3% N_2, 5.7% CO_2 and 78% He, 13% N_2, 9% CO_2 - without any noticeable difference. This was in reasonable agreement with Wright[78,87]. However two disturbing abnormalities were observed:

(i) one cylinder was left standing vertically for 1 year and when it came to be used no lasing action could be obtained. This was considered due to either gas separation in the cylinder (Helium being much lighter than N_2 or CO_2) or the wrong mixture being supplied by BOC special gas division. The CO_2 was not considered to have liquified in the cylinder since the partial pressure would be approximately 4 atm which is to be compared with 35 atm required for liquifaction at $0^{\circ}C$.

(ii) The tube discharge sometimes varied in colour during a run, in fact slugs of colour could occasionally be seen slowly passing through the tube. These variations in colour were associated with a change in laser performance; the most successful lasing action being achieved when there was a bluish white discharge. This phenomenon suggested that a variable gas composition was being delivered from a continuously discharging cylinder, supporting the concept of gas separation in long standing premixed cylinders.

5.1.2.4 Effect of tube current

The observed slight effect of the tube current on laser power (graph 5.1) was more marked than was expected by comparison with the SERL results.

If the fall in power with increased current is due to a heating effect retarding the decay of $CO_2(01'0)$ to the ground state then the lower flowrate used in this work would be expected to cause a higher current dependence than with the faster flowrate of the SERL work.

The optimum current was that which gave a stable discharge with no power gain if increased. For example, at 15 torr it was around 40 mA. The optimum current, a function of the tube resistance, varied with tube pressure.

The power supply had a small voltage ripple in spite of the smoothing effect of the 30μ F condenser. This caused a power ripple from the laser, which was observable on a chart print made on a fast moving card. Peaks of charring occurred approximately at a 50 c/s frequency which is the same as the mains frequency.

5.1.2.5 The effect of tube temperature

Through out a long run the laser power output fell steadily. If the tube and cooling water system were allowed to cool the power level recovered almost to the initial value. This effect is most probably due to overheating together with a small amount of sputtering fouling the internal mirrors. The effect was not large enough, nor critical enough to this work, to warrant the installation of more efficient heat exchangers.

5.1.2.6 Cleanliness of cavity optics

Fouling of the cavity mirrors by sputtering necessitated cleaning about every 100 hours of operation (as described in section 5.1.1).

The effects of fouling were twofold; firstly, it caused a fall in power output and secondly, uneven fouling affected the power distribution within the output beam.

5.1.2.7. Foreign matter in the plasma tube

Certain materials in the tube seemed to cause severe loss of power if not actually preventing lasing action. This effect was loosely correlated with soft araldite, vacuum grease, and excessive moisture. Some moisture has been found to be beneficial — see appendix 5 — but near saturation vapours from wet tubing etc. would prevent lasing.

5.1.2.8. The effect of internal and external optical alignment on power output

A typical power output trace is shown in figure 5.2 trace (1). The trace shows a variation in power of the order of 15%. Trace (2), on the same figure, shows the comparison of the power signals, recorded by thermopiles, of the beam reflected from the beam splitter and that transmitted by the beam splitter. Although the correlation is good, and the scales are different for the two traces, it is apparent that there are fluctuations in the transmitted beam not seen by the reflected beam. This could possibly be due to the varying polarisation of the changing beam mode causing a variation in only the transmitted or reflected beam — see fig 5.3. Trace (,3) shows a comparison of the direct and reflected beams again but this time with the direct beam also passing through an aperture. The laser power is much greater than in trace (,2,) and the direct beam shows short sharp fluctuations not seen on the monitor trace, the sharpness of these fluctuations compared to the other traces is mainly due to the slower chart speed. The overall correlation is good, but not as good as trace (2) suggesting some of the wander is due to fluctuating alignment with the aperture.

There appear to be, therefore, three sources of fluctuations in power on the substrate surface:

(i) Fluctuation from the laser cavity
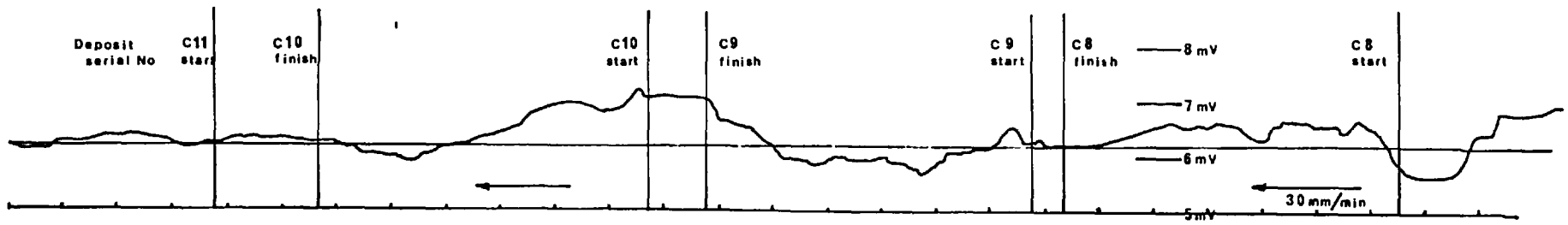
TRACE 1   TYPICAL OUTPUT TRACE FROM POWER MONITOR (A)
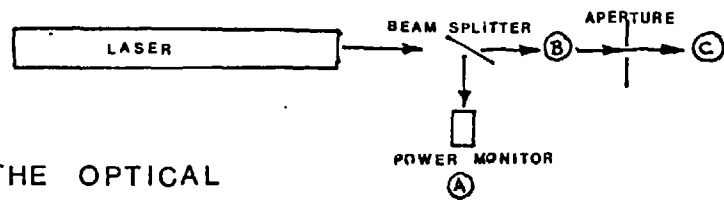
DIAGRAM OF THE OPTICAL
ARRANGEMENT
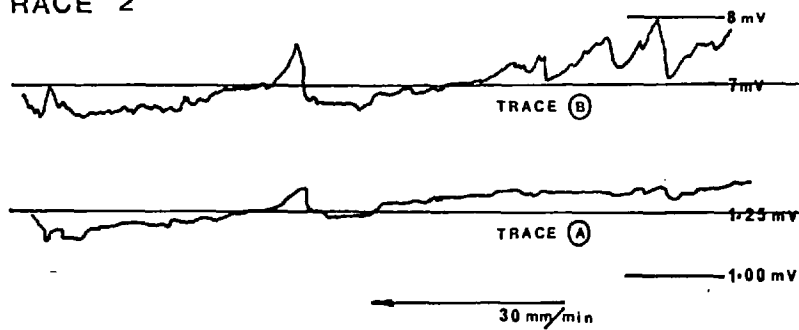
TRACE 2   TRACE 3
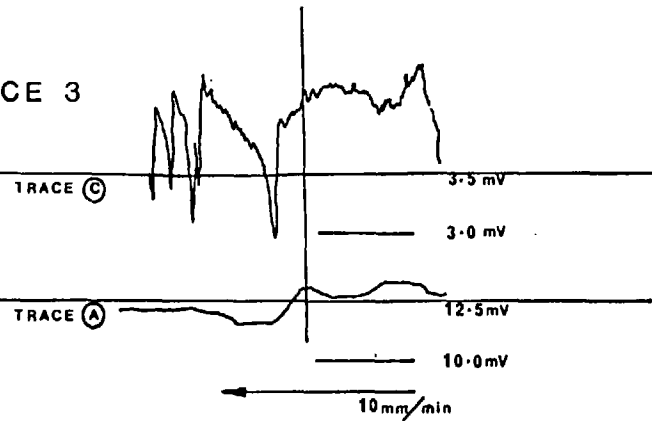
COMPARISON OF TRACES FROM :—

LOCATIONS A & B   LOCATIONS A & C

Fig 5.2

127

(ii) Varying transmittance at the beam splitter

(iii) Varying alignment with the aperture.

The main source of fluctuation is (i) only some 30% of fluctuation being accounted for by (ii) and (iii). Source (i) is considered due to thermal warping of the integral mirrors, slight movement of the mirror mounts due to heating etc., and variations in the optical density of the plasma. These operating together cause changes in the preferred mode of oscillation.

The effect is quite dramatically seen if the beam falls directly on a brick. The resulting glow pattern is seen to change ,rather like the northern lights.

As lasing in one mode proceeds it may cause variations in optical density or the gain factor which may cause a shift to another mode. Such fluctuation could be too fast to witness with the servoscribe and thermopile monitor used. Deshazer and Parks[88] have recorded a radial power distribution variation during the evolution of a 1ms single pulse. They correlate the extent of variation with cavity aperture size, smaller apertures giving steadier beams, presumably because they allow fewer modes to lase.

The longer term fluctuating component could often be corrected by realigning the mirrors, allowing the system to cool over night, or waiting for a particular slug of gas to pass out of the system.

The observed degree of fluctuation varied with each run and is recorded with the results in appendix 4.

5.1.3 Modes of Oscillation

5.1.3.1 Causes of Modes – theory

The resonant cavity defined by the mirrors of a laser has certain stable configurations of the electromagnetic field called modes. These stable configurations result in a variation in power both along the axis and radially. The extent of the power variation radially has been examined theoretically by several workers[89,14] notably Kogelnik[90,91], Fox and Li[92].

They consider the propagation of the resonating radiation to be satisfactorily described by Huygens principle. By this each point on a wavefront may be regarded as a source of secondary wavelets with an obliquity factor which gives the amplitude of the wavelet in any direction as being in proportion to $(1 + \cos \theta)$ - where θ is the angle between the optic axis and the ray in the direction of propagation. The total wavefront can then be computed from a Fresnel integral of the form:-

$$\psi_Q = \frac{jk}{4\pi} \int_A \psi_A \frac{e^{-jkR}}{R} (1 + \cos \theta) \, dA$$

where ψ_Q = field amplitude at the point Q

k = wave number

R = distance from the point A to Q

θ = angle between R and optic axis

j = $\sqrt{-1}$

A = area

The solution of this integral for cavity mirrors of infinite radius (i.e. no diffraction loss from the system) and with no variation in gain across the cavity has been shown[89,90] to give a Laguerre-Gaussian profile for an axi-symmetric system.

$$E(r,\theta) = E_o (\frac{\sqrt{2}r}{w})^\ell L_p^\ell (\frac{2r^2}{w^2}) \exp (-\frac{r^2}{w^2}) (\left\{ \begin{matrix} \sin \\ \cos \end{matrix} \right\} \ell\theta)$$

where $E(r,\theta)$ is the amplitude of the field in the transverse plane to the optic axis at a point, r, from the centre and angle, θ, from zero.

E_o is a constant amplitude factor, being the central amplitude

w is the beam radius, defined as the distance from the axis at which the amplitude is a factor of $\frac{1}{e}$ the axial value, assuming a Gaussian beam.

L_p^ℓ generalised Laguerre polynomial defined by:

$$L_p^\ell (x) = \frac{e^x \, x^{-1}}{p!} \frac{d^p}{dx^p} \left[e^{-x} \, x^{p + \ell} \right]$$

some low order Laguerre polynomials are:-

$$L_0^\ell (x) = 1$$

$$L_1^\ell (x) = \ell + 1 - x$$

$$L_2^\ell (x) = \tfrac{1}{2}(\ell + 1)(\ell + 2) - (\ell + 2)x + \tfrac{1}{2}x^2$$

From this solution it can be seen that the fundamental transverse electromagnetic standing wave - $TEM_{p,1,q}$ - is when $\ell = 0$, $p = 0$ (q refers to the longitudinal mode) and is

$$E(r,\theta) = E_o \, e^{-\frac{r^2}{w^2}}$$

This is known as the TEM_{ooq} mode and is seen to be a simple Gaussian power profile. Higher order modes $TEM_{p,1,q}$, have been calculated by Kogelnik[91] and the power distribution of some are shown in figure 5.3 for the cases of circular and rectangular symmetry.

The open resonator, having finite radius end mirrors, which is used in laser structures is inherently a multimode device. In general the laser oscillates simultaneously in several modes at the corresponding resonant frequency. The factors which determine which modes oscillate are the characteristics of the cavity in combination with those of the lasing medium.

The main resonator characteristics are those which define the relative diffraction losses of different modes. The higher order modes are those propagating at a slight angle to the axis of the laser system and hence suffer much by diffraction losses around the edges of the finite mirrors. This effect is quantified in the term "mode selectivity" M = power loss for TEM_{01}/power loss for TEM_{oo}. The value of M is determined by the resonator geometry, Fresnel number of the cavity, N, and the curvature of the mirrors. Figure 5.4 shows the variation.

131

Linearly polarised resonator mode configurations for square & circular mirrors.
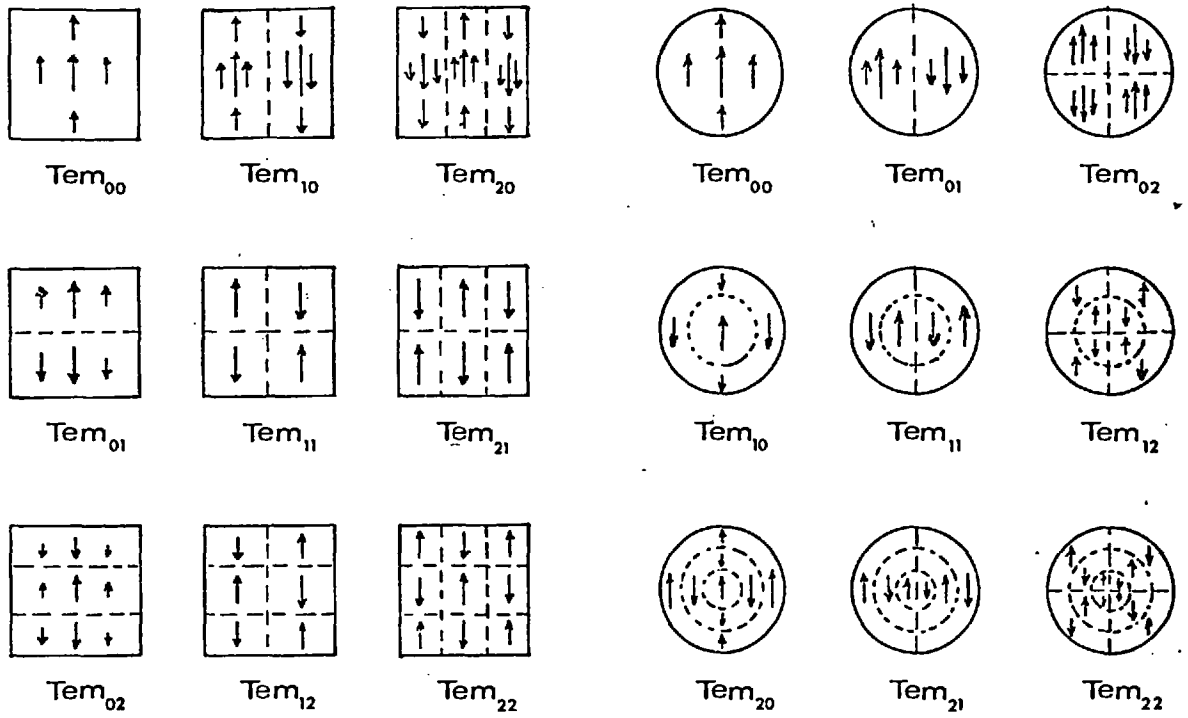
Mode patterns. (rect.symmetry) (circular symmetry)
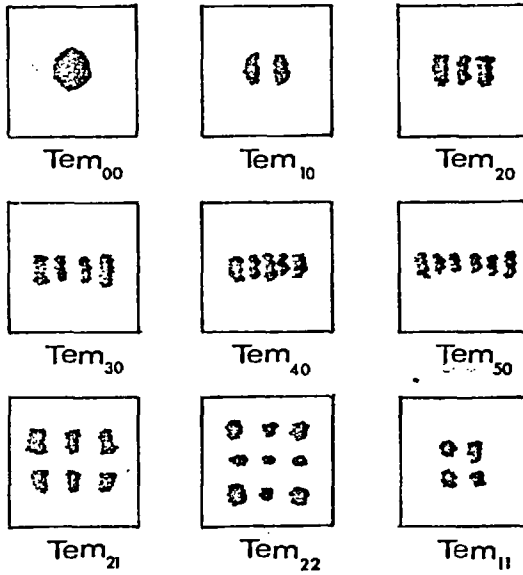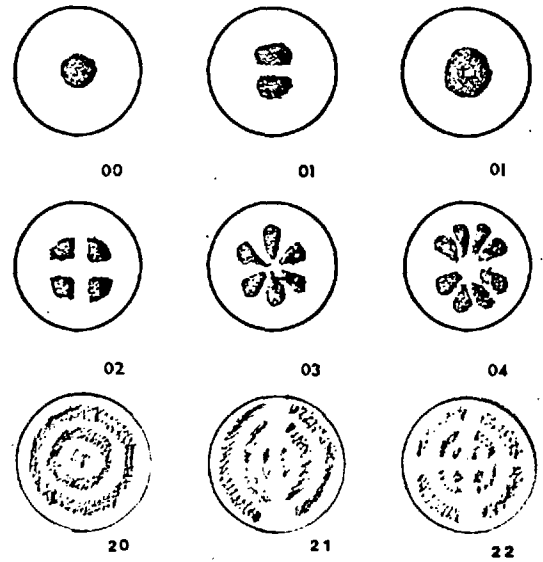
Fig 5.3
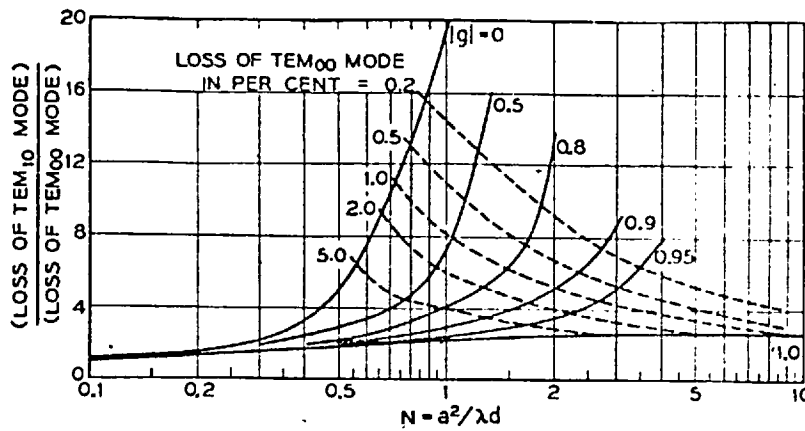
Figure 5.4 Ratio of losses per transit of the two lowest
order modes for resonators with circular mirrors
and $g_1 = g_2 = g = 1 - d/R$ (See figure 4.3) curves
for constant Tem_{oo} loss are shown dashed (90).

The main laser medium characteristics deciding the favoured
mode structures are the frequency band over which optical gain is
available, the amount of gain, the transverse variation of gain
(which could be high for a thick tube having internal thermal
gradients) and the non linear mode competition characteristics
of the medium.

The thick laser tube used here (2.54 cms diameter) had a Fresnel
number $N = \dfrac{a^2}{L\lambda} = 10.4$

where a = radius of the cavity mirrors = 0.0127m

    L = distance between cavity mirrors = 1.51m

    λ = lasing wavelength   = 10.6×10^{-6}m

For such a large fresnel number figure 5.4 suggests multi-
mode oscillation up to quite high order modes would be possible.
It was hoped that this would produce a broad reasonably uniform
power distribution sufficient to amply cover the object/aperture
without creating severe alignment problems.

5.1.3.2 Modes observed

A broad reasonably uniform beam was obtained. A typical char
print from the beam of the properly aligned laser is shown in

figure 5.5 print 1. Within this beam a structure could be detected by a carefully judged exposure of the card - around $\frac{1}{2} \rightarrow$ 5 seconds. This structure is shown in figure 5.5 prints 2, 3, 4. It displays a pentagonal matrix, print 2, or a hexagonal, print 4. This fine structure varied with time .as previously noted, Some of the other structures observed are shown as char prints in figure 5.5, prints 5-12.

It is possible to have rectangular symmetric modes in a circular symmetric system[14]. Hence striated structure such as print 5 having 5 stripes could be a TEM_{40} mode, of rectangular symmetry, uneven numbers of stripes being impossible with circular symmetry.

Print 11 shows similarities with a TEM_{10} or TEM_{11} while print 12 appears akin to a TEM_{12}.

However, the correlation of these observed prints with the theoretical modes is not obvious particularly in prints such as 8, 3, 4.

Some of these unusual modes, e.g. print 13, are possibly due to sputter marks on the mirrors distorting the output beam; while others may be due to an integral effect of several modes together. Movement of the card up or down the beam axis did not alter the mode structure, hence these power peaks were not considered to have anything to do with normal laser speckle patterns.

It will be noticed from figure 5.3 that the plane of polarisation is different for different mode peaks. Thus after passing through a beam splitter these peaks would be expected to be transmitted to different extents as already noted (p 126) which could account for the difference between prints 13 and 14.

5.2 The Evaporator System

The vapour concentration from the glass bead evaporator heated in an oil bath was reasonably steady for some 20 minutes after loading with an alcohol/chelate slurry and equilibrating over 10 minutes. However, if a dust filter was put near the jet nozzle a large fall of cobalt in the jet was recorded. This could have been due to either dust or condensation on the filter, probably

Fig 5.5 VARIOUS MODE PATTERNS OBSERVED AS CHAR PRINTS

1·55 cm

D24

1   2   3   4

D14

5   6   7

H12   H12   H12

8   9   10

C29

before   after
beam splitter

11   12   13   14
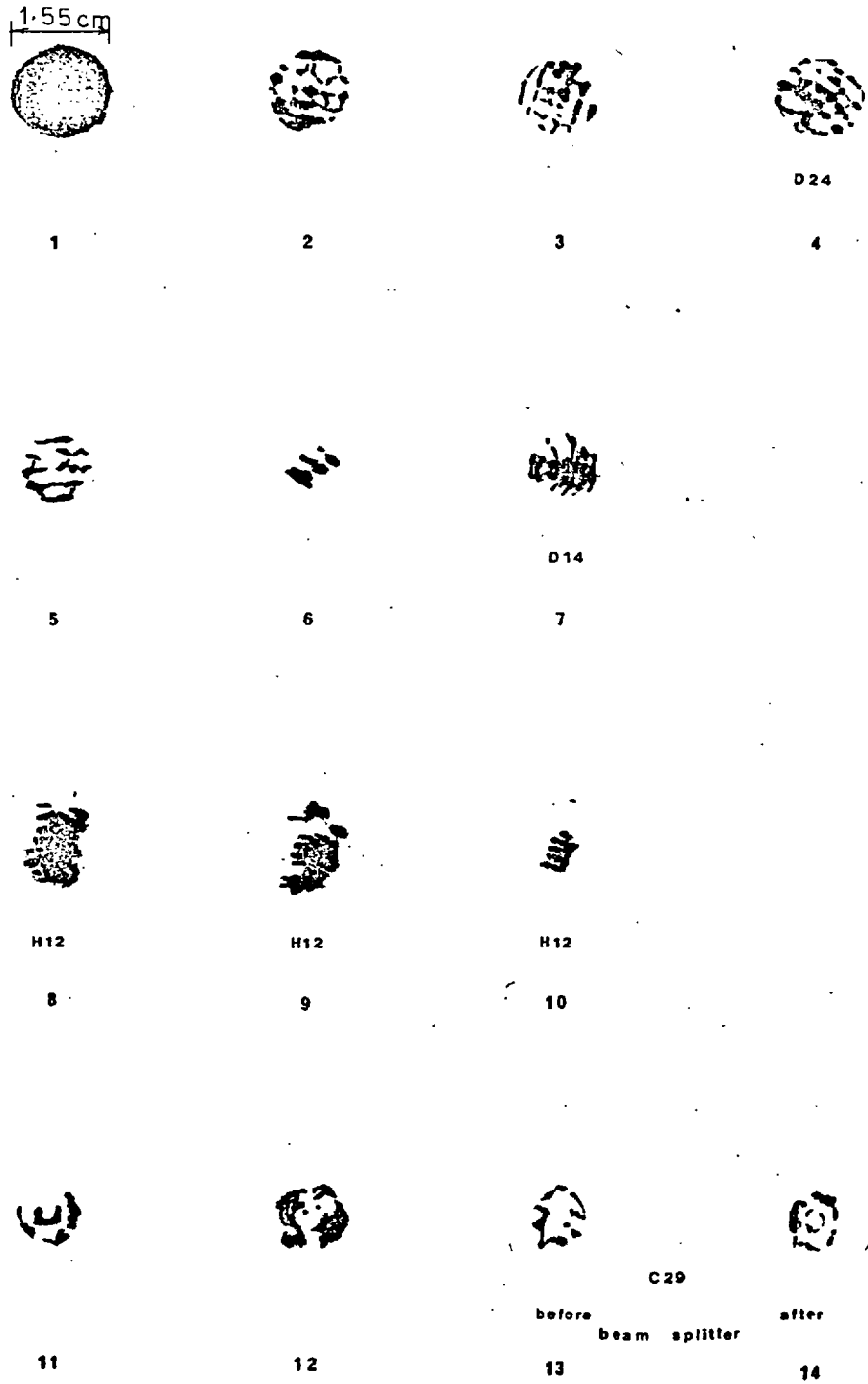
the latter due to the low concentration recorded. For this reason and those discussed in sec 4.4 this evaporator system was not used.

The performance of the electrically heated version with shorter delivery lines was also not satisfactory since the vapour concentration never achieved a steady state. Though the frequent addition of small volumes of slurry 2cc every 10 minutes produced a reasonably constant output concentration. However, it was doubtful if equilibrium was ever achieved with this system due to its low thermal inertia.

The large stainless steel packed bed evaporator (figure 4.11) gave a reasonably steady output with time as shown in graph 5.6 It was moderately easy to handle, and had very short delivery lines.

Graph 5.6 also shows a comparison of the readings from the two sampling techniques used, (see section 6.3.12) the bubbler and the syringe. These results indicated that the syringe method gave adequate accuracy to use as an on-line concentration check.

Fig 5.6   PERFORMANCE OF THE STEEL BALL EVAPORATOR
AND   COMPARISON   OF   THE TWO   CALIBRATION   TECHNIQUES

EVAPORATOR TEMPERATURE 120 °C

O   BUBBLER SAMPLES

▼   SYRINGE   SAMPLES

MEAN

VAPOUR CONCENTRATION   grm cm^{-3} x 10^6

TIME   min
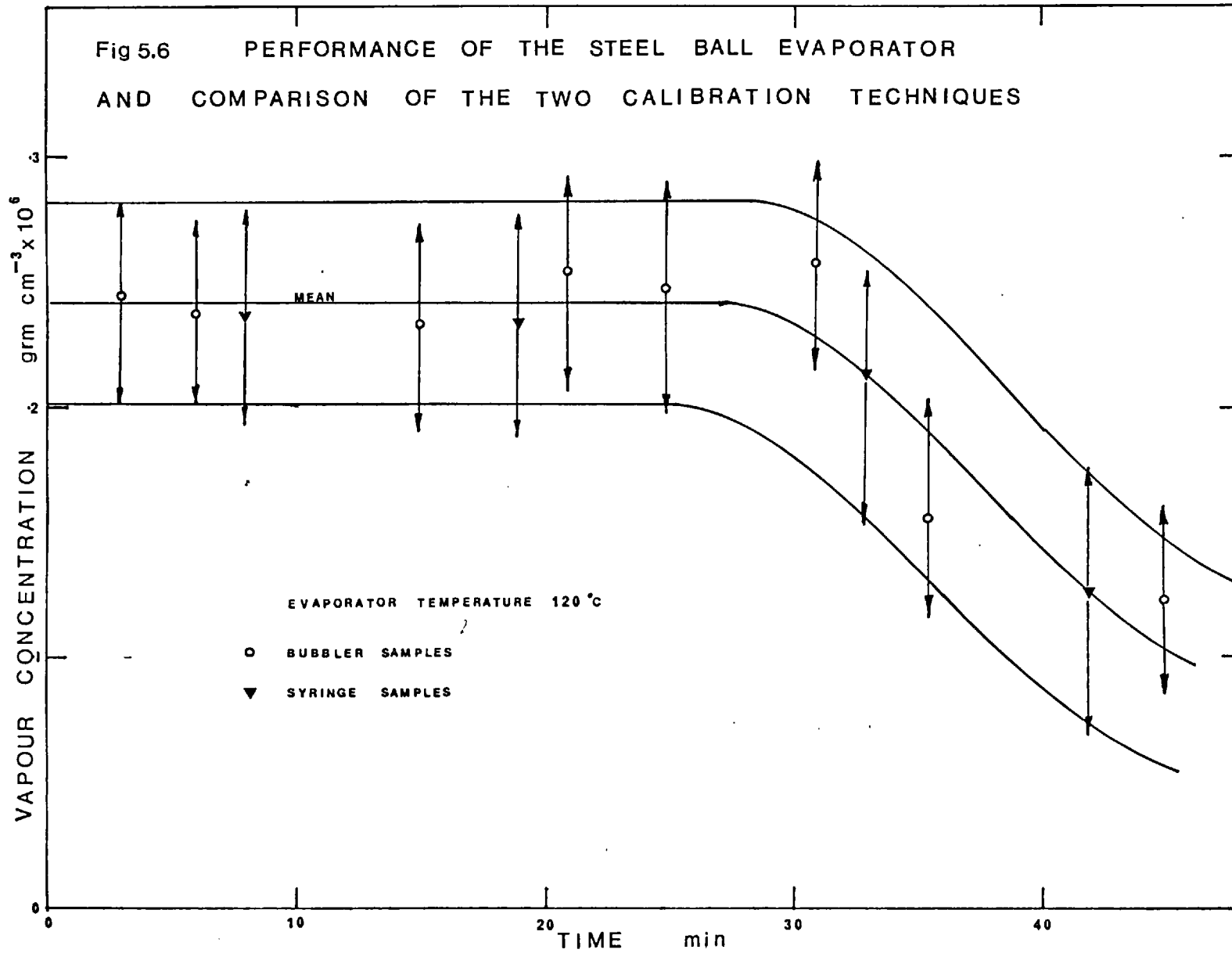
CHAPTER 6

EXPERIMENTAL METHODS

6.1 Experimental Strategy

The aims of these experiments were:

(1) To establish whether it is possible to print shapes in this manner.

(2) If so, to find what are the controlling parameters and what nature of influence they have.

The first objective was achieved in a series of image formation studies in which a unique shape "✤" was printed. The clarity of the print for such a shape was relatively easy to judge.,

The second objective was achieved by printing a circular image which could be mathematically modelled. These prints were made to study the rate of deposition and the extent of the deposit as a function of the identified process variables. The process variables were systematically varied as shown in table 6.1.

6.2 Experimental Procedure

Each deposition run required the monitoring of numerous process variables during the brief period of a run (approx: 2min/sample). The author is grateful to A. Young for his help in taking these readings.

The procedure was:-

(i)   Prime and start the evaporator; note the time.

(ii)   Pump down and start up the laser - align the optics with the help of the colinear red marker beam from the He/Ne laser.

(iii) Calibrate the power monitor thermopile for the optics to be used - see section 6.3.2.1.

(iv)   Reload evaporator and wait 5 minutes for it to achieve
         a steady output.

(v)   Take all readings on evaporator and laser - temperatures,
         gas flow rate, laser current, voltage, tube pressure
         and power monitor readings.

(vi)   Take syringe sample of gas from evaporator - see
         section 6.3.1.2.

(vii)   Check values of jet/plate distance, lens to aperture
         and lens to substrate distances.

(viii)   With brick blocking laser beam, place substrate in
         holder

(ix)   Remove brick and start timing the deposition (the jet
         was sufficiently hot that any condensation initially
         forming in the deposition area would be rapidly
         revolatilised; so if the brick was delayed in its
         removal the beam would not be striking unreacted
         chelate condensate).

(x)   Mark all charts - laser power, thermodot, evaporator
         temperatures.

(xi)   Take syringe sample of vapour from evaporator delivery
         line.

(xii)   Align the thermodot I.R. thermometer with hot spot
         and scan as required.

(xiii)   Check flowrates, laser power etc.

(xiv)   Replace brick at timed end of run, mark all charts,
         substrate sample, and syringe sample, take readings of
         laser and evaporator parameters, note process variables
         for run.

(xv)   Adjust deposition system for the next experiment and
         repeat from step (viii)

(xvi)   Reload evaporator every 15 minutes

(xvii)   At the end of series recalibrate laser power monitor

Series		lens used – focal length cm (i.e. beam diameter)	Power	Re	Lens/object distance (beam diameter)	Radial location	Jet/plate distance	Concentration vap.	Time of deposition	Substrate material	Substrate thickness	Object
A	1–13	29.5	✓									Vary power
	14–20	"	✓	✓								Vary power and Reynolds Number
B	1–15	"	✓					✓				Repeat A for reproducibility and different evaporator temperature to A
	16–20			✓								
C		"		✓		✓						Traverse of heated spot through jet impingement zone at various Re and new jet/plate distance to A and B series.
D		"	✓			✓						Traverse through focus of lens
E		"		✓		✓						Same as C but for a different beam diameter
F		"	✓				✓					Variation of jet/plate distance
G	1–14	5.3	A		✓		A					Transverse focus at two power levels and two jet/plate distances
	15–20		B		✓		B					
			✓				B	✓				
H	.	13.7	✓		✓							Traverse focus
I	1–15	13.7	✓								✓	Various thicknesses of glass substrate
	16–22								✓			growth studies
	23–27									✓		comparison with quartz substrate

Table 6.1

6.3 Measurement and Calculation of Parameters

Summary

The image formation studies were analysed phenomenologically
The interest in them being to identify the different types of
deposition effects, the main operating parameters and, in particular,
the general effect of these on the clarity of the prints. Few
other measurements were made.

The rate study results required the measurement of numerous
parameters. They were:-

Gas Flow parameters	(i) Jet exit Reynolds Number
	(ii) Vapour concentration
Laser Beam Parameters	(i) Laser power
	(ii) Beam diameter
Substrate Parameters	(i) Thermal diffusivity
	(ii) Surface Reflectivity
	(iii) Transmissivity to 10.6μ radiation
Deposit Parameters	(i) Thickness and shape
	(ii) Area and extent
	(iii) Radial position relative to jet axis
	(iv) Surface reflectivity
	(v) Chemical composition
	(vi) Temperature during deposition.

The way in which each of these was measured is now discussed
in turn.

6.3.1 Gas Flow Parameters
6.3.1.1 Jet Exit Reynold's Number

The significance of the jet exit Reynold's number on mass
transfer is discussed in (section 3.7.2.1) and on convective heat
transfer in (section 3.5.4.2.3)

The rotameter (size 35) measuring the quantity of cold
nitrogen feed to the evaporator was calibrated for the evaporator
system at 17°C. There was a 1cm Hg pressure drop from rotameter
to exit with a flow rate of 2.9 litres/min, which was accommodated
in the calibration.

The jet exit Reynolds number $Re_e = Re_i \sqrt{\dfrac{T_i}{T_e}}$ (see p59)

$$= \frac{\rho_i u_i D_i}{\mu_i} \sqrt{\frac{T_i}{T_e}}$$

$$= \frac{4 \rho_i Q_{cal}}{\pi D_j \mu_i} \sqrt{\frac{T_i}{T_e}}$$

where Q_{cal} = calibrated volume flow for gas at 17°C $m^3 s^{-1}$

ρ_i = density of N_2 @ 290°K = 1.18 kg m^{-3}

μ_i = viscosity of N_2 @ 290°K = 18.74 x 10^{-6} Ns m^{-2}[71]

D_j = jet diameter = 0.00508 m

T_i = 290°K

T_e = exit temperature, either 120°C or 140°C

i = inlet condition

e = exit conditions

Thus Re_e = 219 x Q_{cal}
    120°C

Re_e = 213 x Q_{cal}
140°C

6.3.1.2 Vapour concentration

The rate of deposition was expected to be linearly proportional to the vapour concentration[41]. Accordingly this significant variable had to be measured and held constant during deposition.

The evaporator system finally chosen was of such a size that it should have produced an equilibrium vapour of chelate in nitrogen; thus giving a constant output. However, it became exhausted after 20-30 minutes of operation at a flow rate of cold nitrogen of 2.9 litres/min.

The problem was to calibrate the evaporator to establish this constant vapour concentration as a function of evaporator temperature, and then to devise some simple technique to check on exhaustion.

The evaporator was calibrated by blowing the jet into a bubbler containing 10% H_2SO_4 (10% H_2SO_4 was proven quickly and completely to dissolve the CoAcAt by passing the gas through two bubblers in series, the first being very shallow. The second bubbler was found to contain no cobalt).

The vapour concentration was calculated from the volume of gas divided into the total quantity of cobalt blown over during the sampling time. The quantity of Cobalt = (concentration Co after blow – conc. before) x vol. sol^n in bubbler before. The concentration of Cobalt being found on an atomic absorption spectro- photometer.(Perkin Elmer 290). The accuracy of this method depended upon:

(i)   The calibration of the AA spectrophotometer, $\pm$ 10%, at these low concentrations.

(ii)   The successful backflushing to collect all the condensate in the bubbler internal pipe.

(iii)   Correct timing and volumes $\pm$ 0.05%

Due to the cummulative process in the bubbler a low reading on one test would lead to a high reading on the next producing an apparent oscillation in the evaporator output. This meant that

an error could affect all subsequent readings.

The melioration of this being that if this happened an easily observed oscillation would occur and so flag the event.

This bubbler technique could not be used during the deposition runs since it would mean disturbing the jet position and the expense of considerable time. This was not suited to the fluctuating power output from the laser.

Three simpler alternatives, to check on evaporator exhaustion, were tried.

(i) The jet was buried in cotton wool damped with 2mls of 10% H_2SO_4. This successfully collected all the chelate - which was easily condensed - but the hot jet evaporated an unknown quantity of liquid thus necessitating several weighings of the sample pot, or measuring the normality of the acid solution.

(ii) The jet was buried in dry cotton wool. This appeared to collect all the chelate. However it left some dust on the jet nozzle which could lead to large errors. Neither of the cotton wool condensers left the jet totally undisturbed.

(iii) A gas sample was taken by hypodermic syringe. In this a 10 ml hypodermic syringe was partly filled with exactly 2mls of 10% H_2SO_4. The needle was inserted through a silicone rubber bung into the gas delivery line adjacent to the jet. 8 mls of gas were drawn into the syringe so that it bubbled through the 2 mls of 10% H_2SO_4. The syringe was withdrawn, gently shaken and the sample ejected through the same needle, removing any condensate, into a sample pot for AA spectrographic analysis.

The simplicity of this technique, speed of operation, and lack of disturbance was excellent. The accuracy was checked against the bubbler and illustrated in graph 5.6. The comparison was within $\pm$ 10% the estimated experimental accuracy. Accordingly the concentration was monitored during deposition by this process mainly to check on exhaustion.

The effect of concentration was considered to be fairly well understood[41] and consequently it was not varied to any great extent. Two concentrations were used; that from the evaporator operating at 120°C and that for 140°C. Higher temperatures were tried resulting in evaporator breakages, rapid fouling within the evaporator, clogging of the jet nozzle and the formation of dust clouds from the jet. In view of these problems and the likely information to be gained these higher temperature regions were not explored further. Evaporator temperatures below 110°C gave insufficient chelate. The concentrations recorded during each run are shown in table 6.2:

Table 6.2

Series	Temp °C	No. conc: reading	Mean conc: ppm	Standard Deviation
A	140	8	.31	.08
B	120	15	.24	.10
C	140	9	.38	.08
D	140	21	.31	.13
E	120	5	.26	.12
F	140	9	.32	.10
G	120	10	.21	.10
H	120	14	.25	.08
I	120	21	.24	.08

Mean value for 120°C – 0.24 ± 0.04 ppm

for 140°C – 0.33 ± 0.06 ppm

6.3.2 Laser Beam Parameters

6.3.2.1 Laser Power

(a) <u>Thermopile</u> - during all runs the laser power was monitored by a Griffin and George thermopile exposed to $\pm$ 5% of the total beam via a reflection from a water cooled Germanium beam splitter. This thermopile was calibrated against a spherical black body calorimeter, described below, before and after every series of deposits for the particular optics used and for their particular state. (i.e. humidity pick up on the NaCl lens).

(b) <u>Black body calorimeter</u> - The calorimeter consisted of a hollow copper sphere, figure 6.1 , 75mm in diameter, and 0.5mm wall thickness, polished on the outside and anodised black on the inside. The sphere was supported on three pointed copper legs in an insulated, draught proof perspex box. The focussed beam was allowed to pass through a 3mm diameter hole in the sphere in such a way that the axis of the beam was at least 20° to the diameter through the hole.

The temperature rise of the sphere was measured with a chrome/ alumel thermocouple made of 0.03mm D wire. The fine wire being used to minimize conduction losses. The cold junction was attached to a block of copper, of about the same mass as the sphere (80g) mounted on the outside of the perspex box. The construction was similar to that of Wright's[78].

The calibration procedure was:-

(i)   Set up the optical system to be used for the deposition.

(ii)   Align the red marker beam and infra red beam using char prints by adjusting He/Ne laser and beam splitter.

(iii)   Turn off CO_2 laser, and place the calorimeter at the lens focus so that the red beam passes cleanly through the 3mm hole.

(iv)   Place a brick in the infra red beam path. Turn on the CO_2 laser, adjust to required power as observed by the thermopile

(v)   Start recording the calorimeter temperature on the servoscribe with it running at 120mm/min chart speed. Remove brick.

anodized black inside

polished outside

beam

NaCl lens

perspex box

copper sphere

TC

to servoscribe

cold junction

146
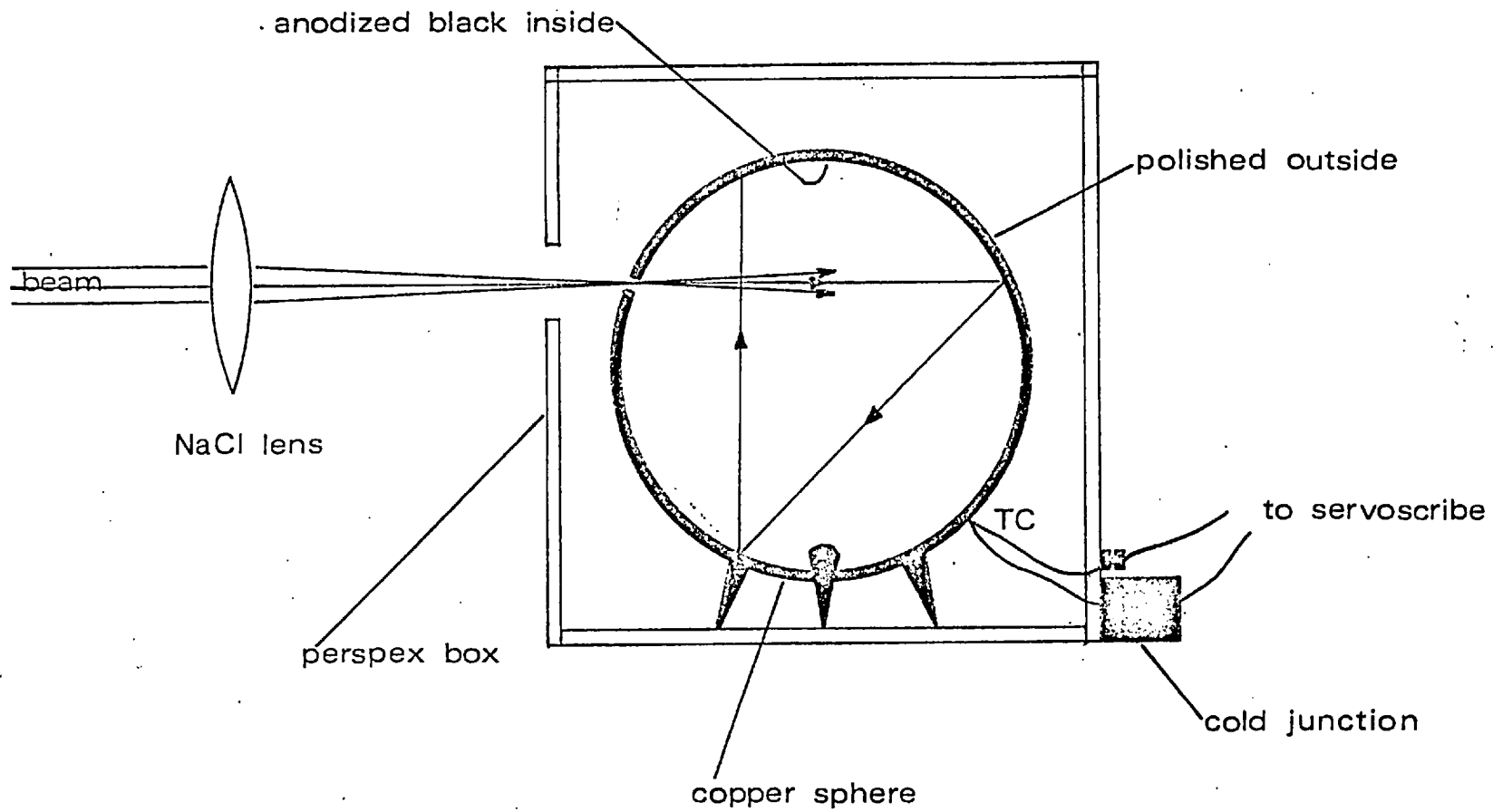
Fig 6.1   Calorimeter for absolute power measurement.

(vi)   When a long enough trace is achieved, replace brick,
        and continue recording the calorimeter temperature until
        it has cooled sufficiently ($\simeq$ 3/4 of total rise).

Figure 6.2   shows a typical chart record.

The power entering the calorimeter Q = heat gained + heat lost

$$= MC \left\{ (\frac{\delta T}{\delta t})_{heating} - (\frac{\delta T}{\delta t})_{cooling} \right\} \quad watts$$

The mass of the calorimeter M = 80.424 grams

The specific heat of copper C= 0.385 J/g$^\circ$C @ 27°C

$\left[from \quad C = a + bT + cT^{-2} \quad cal \; deg^{-1} \quad (93) \right.$

and for Cu   a = 5.41

                b = 1.50 x 10^{-3}

                c = 0.0

    atomic wt = 63.37

$$\therefore \quad C = \frac{5.41 + 1.50 \times 10^{-3} \times 300}{63.57} \times 4.18$$

$$= 0.385 \; J/g^\circ C \quad @ \quad 300^\circ K \simeq 27^\circ C \left. \right]$$

The possible errors in the system are:-

(i)   Fluctuating laser power causing uncertainty regarding
        power calibrated: The chart trace responded sensitively
        to this fluctuating power, in fact on one occasion
        a single heating of the calorimeter occurred under
        strongly fluctuating power levels and gave a varying
        slope in good correlation.   Thus the fluctuation,
        reported by Wright as reducing his accuracy to $\pm$ 6%
        was not considered nearly so significant here, since
        care was taken to measure the slope at a period of
        steady power.   The error from this cause was $\simeq \pm$ 1%

(ii)   Failure to trap all the infra red beam : the 3mm hole
        was some 10 times larger than the beam diameter at the
        lens focus making a miss or partial miss unlikely .
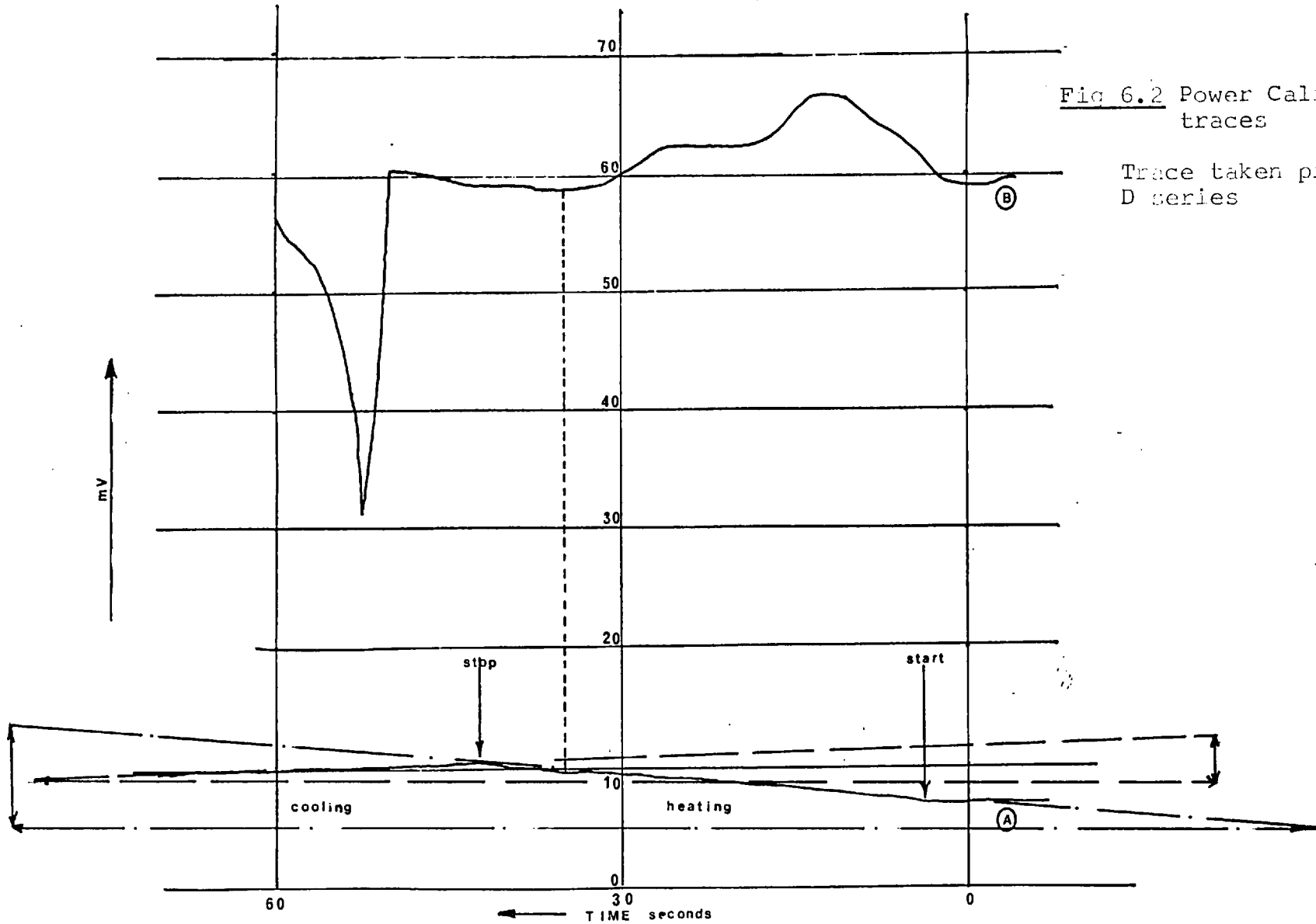
Fig 6.2 Power Calibration
traces

Trace taken prior to
D series

- 148 -

Trace A — Calorimeter thermocouple on 2mV full scale

Trace B — Laser monitor thermopile on 20mV scale

However, if the alignment had been very poor, or had it slipped subsequently, then a miss by the infra red beam resulted in a hole appearing in the Perspex or the smell of burning causing the error to be detected. This effect was considered so noticeable that it could be avoided.

(iii) Back reflection of a fraction of the beam out of calorimeter: this was avoided by the non alignment of hole diameter and optic axis, whereby at least 2 or 3 internal reflections on the black anodised surface would be required before loss from the calorimeter occurred. Therefore this effect was considered negligible.

(iv) The beam struck the spot where the thermocouple was soldered: this produced an odd trace with a step at the beginning and end. When this happened the calorimeter was moved.

(v) Conduction losses down the thermocouple wires: considered negligible due to the fine wire used and the way the calculations were balanced for heating and cooling.

(vi) Convection losses: minimised by the perspex box but even so the calculations were balanced for heating and cooling.

(vii) Absorption in the optics used: this was not a source of error since the power leaving the optic system and striking the substrate was to be measured. For interest the total laser power was established. In this case the absorption of the lens used had to be accounted and was measured by allowing a weak beam to fall directly on the thermopile to obtain a signal which was compared to the signal produced by the same beam after passing through the lens and striking the thermopile with the same diameter.

(viii)   Errors in reading the tangent from the chart: the
estimated accuracy was ± 5%

The overall accuracy was consequently estimated
as ± 6%.

6.3.2.2 Beam Diameter

It is very important to an understanding of the prints that
the beam spot size at the print position is known as accurately
as possible. In the theoretical section (page 73   ) it was
seen how the temperature could be represented in dimensionless
form by $T^* = \dfrac{T\pi k D_b}{P(1-r_f)}$, and that the intensity of heating was

described by the ratio, $P(1-r_f)/D_b$, when the main heat loss is by
thermal conduction into a semi-infinite block. In both cases it
is clear that any event dependent upon the spot temperature crucially
depends upon the spot diameter for a given power and substrate.

6.3.2.2.1. Previous methods of measuring

The problem of measuring the beam diameter is one that is
encountered in all laser power work, and has been approached by
others in various ways.

Most of these methods measure the contour of a single isotherm
as in the charring of card or heat sensitive paper, drilling of
holes[18],[15] in black paper or thin metal films or the formation
of glow images on thin asbestos sheet, or special fluorescent
screens. The simplicity of these techniques is their main
attraction. The inaccuracies are however, easily seen if a
convergent Gaussian beam is considered. When the beam is broad
sufficient power density is available for charring only at the
Gaussian peak, when the beam is narrow the same power is available
at the root. In either state the charring or drilling contour is
unlikely to coincide with the power contour having a power of 1/e
the central value – defined as the Gaussian diameter. This
argument is diagrammatically shown in the figure 6.3 and illustrated
by a graph from Cohen and Epperson[15] (figure 6.4) showing the
diameter of the hole drilled in a thin film of tantalum nitride
by a ruby laser focussed with a 2.54 cm focal length lens.

In this graph it is seen that the beam diameter apparently depends on power, particularly in the low power region – the expected error of this method.
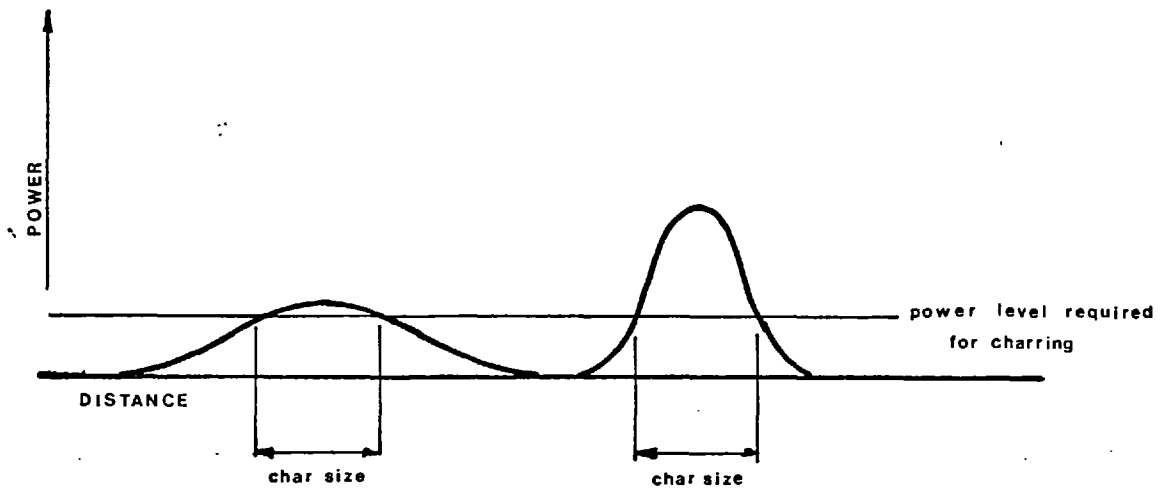
Figure 6.3 Showing the error in using an isothermal technique to measure the Gaussian beam diameter
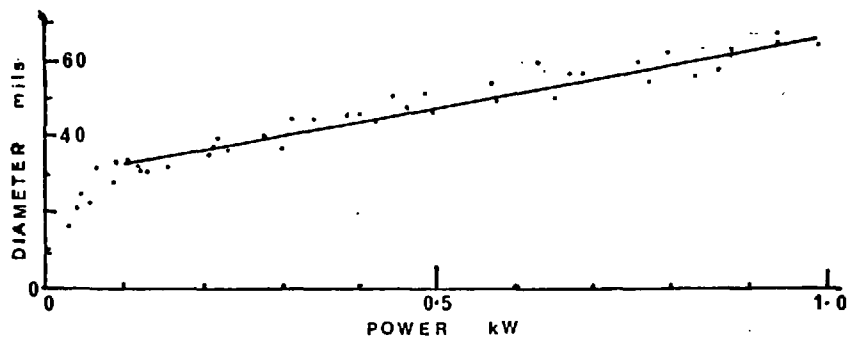
Figure 6.4   The apparent variation in beam diameter with power found by using an isothermal technique (15).

A further disadvantage of this technique, charring in particular, is that the recorded diameter is a function of the exposure time as shown in figure 6.5.

TIME

<u>Figure 6.5</u> The variation in the diameter
of char prints from the same
beam with the exposure time.

Multiple contour techniques yield an overall power vs radius
curve from which the correct Gaussian diameter can be calculated.
Such methods include the use of film as described by Waynant et
al[94] who used a photographic plate which responded linearly to
intensity. By this tiresome method they were able to plot intensity
contours and hence calculate the diameter at which the intensity
(as opposed to the amplitude $= \sqrt{\text{intensity}}$) falls to $1/e^2$ the central
value. This method was not suitable for 10.6μ radiation work since
it would require special film, liquid N_2 cooling etc.

Another multiple contour method is the photon drag detector
developed by Professor Gibson of Essex University. In this success-
ful device the drag of a photon avalanche through a single crystal
of Germanium creates a potential difference between the top exposed
surface and the bottom surface which can be amplified. By allowing
a scan of the beam to fall on the crystal the convoluted signal
of the intensity cross section can be displayed on an oscilloscope. ⊃
Unfortunately the Germanium needs a higher powered beam than used
here to drive it (> 2-300W).

A different approach altogether is to fit observations to a
mathematical model and back calculate. Cohen and Epperson[15]
measured the fusion depth in their welding experiments and back
calculated via a model to obtain the beam diameter that was required
to cause the fusion.

In this work a form of back calculation is suggested based upon
the observed thermal rise times. This technique is of much use for
large 'slow' heating spots.

Finally, it is possible to calculate from optical theory the beam diameter.

From these possibilities it was decided to calculate the beam diameter theoretically, to get the overall beam shape and then scale this shape to fit observations from the thermal rise time of the heated spots.

6.3.2.2.2 Theoretical calculation of beam diameter

There are four effects operating to decide the beam diameter

(i)   The effect of diffraction on a Gaussian beam.

(ii)   The effect of truncation at the aperture on (i)

(iii) The effect of non Gaussian modes

(iv)   The effect of spherical aberration in the lens used.

The overall beam shape is described by (i) the others can be handled as a scale factor[95] on (i) which will here be decided experimentally. Each of these aspects will now be discussed.

6.3.2.2.3

(i) Diffraction limited beam geometry

It has been observed on page 128 that the fundamental $TEM_{o\,o}$ mode from a laser has a Guassian profile defined by:-

$$P(r) = \frac{P_{TOT}}{\pi\,w^2}\,e^{-\frac{r^2}{w^2}}$$

where w = radial distance at which the power falls to 1/e of the central value.

It is, therefore, not unreasonable, as a first approximation, to assume that the beam power is Gaussian. If it is further assumed that truncation effects at the aperture and spherical aberration within any lens are negligible; then it is possible to apply standard optical techniques to calculate the diffraction spread of the beam.

These techniques are:-

(i)   Ray transfer matrix methods described by Kogelnik and Li[91].

(ii)   Analytical solutions of the Laguerre - Gaussian functions described by Boyd and Gordon[96] and Dickson[101].

(iii)   Geometrical solutions described by Deschamp & Mast[97] and Laures[49], and Sinclair and Bell[98].

The geometrical solution is not only the simplest to use but yields a pictorial representation of the beam propagation which is useful in this analysis.

6.3.2.2.4   <u>Propagation circle method for Gaussian Beams</u>:

The output beam shape coming from an optical confocal cavity - that is a cavity having equal radius of curvature mirrors set at one radius apart - can be calculated by this method. It directly calculates the radius of curvature of the wavefront, R, and the beam parameter, b', which is related to the spot size by:-

$$b' = \frac{\pi w^2}{\lambda}$$

Where w = beam radius

λ = wavelength of radiation

b' is also related to the confocal radius, b,
(where 'b' is the distance between the confocal mirrors) by:

$$b' = \left[\frac{b/2^2 + z^2}{b/2} \right]$$

The radius of curvature of the wavefront, R, is also related to b, by:

$$R = \left[\frac{(b/2)^2 + z^2}{z} \right]$$

These equations come from the analytical solution of the wave functions. The propagation circle construction proceeds to calculate these terms as follows:

Consider a confocal cavity of length, b, as shown in figure 6.6.
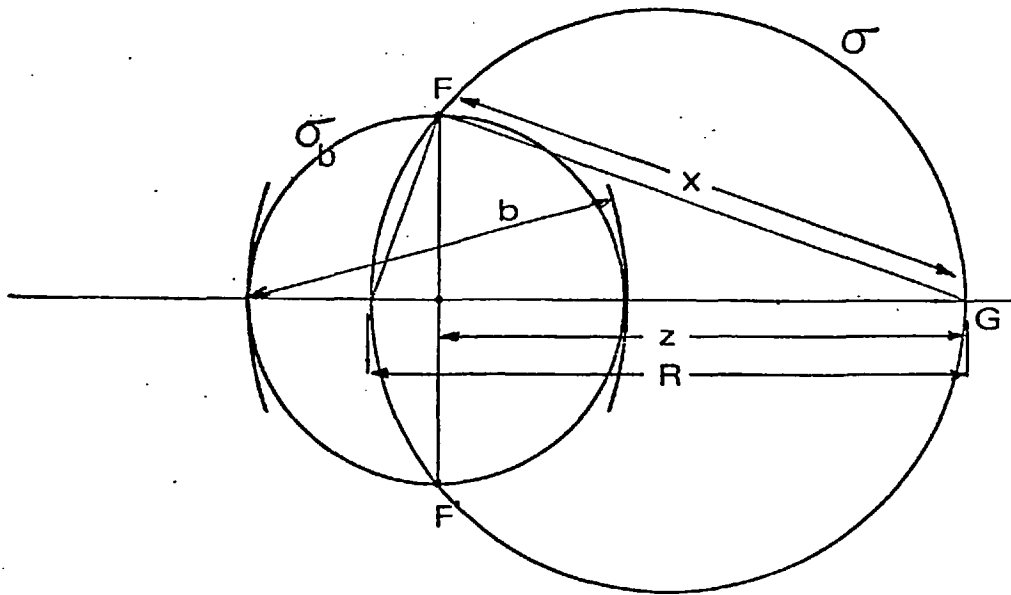
Fig 6.6   Construction of σ circles.
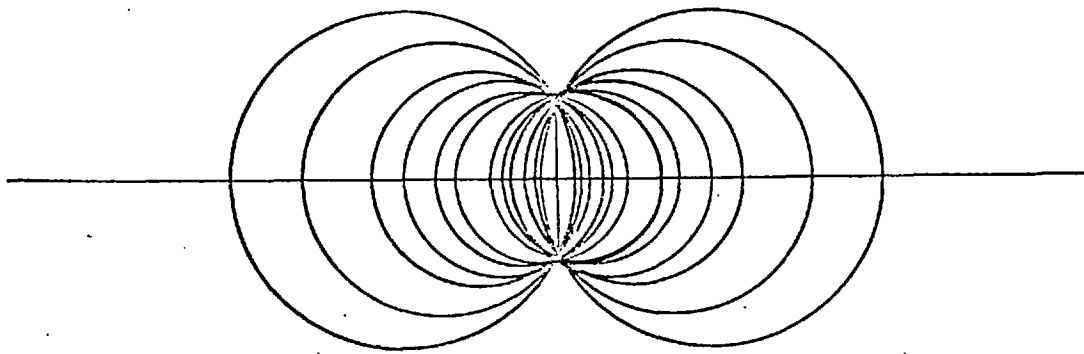
Fig 6.7   Wavefronts in a confocal cavity.

Construct a σ_b circle centred on the point $z = 0$ having a diameter equal to the radius of curvature of the confocal mirrors. Construct a vertical line through $z = 0$ to intersect the σ_b circle at F and F'. These points are called the "lateral focal points" of the confocal cavity.

Construct a circle, σ, passing through the lateral focal points and the axial point, G, a distance, z, away from the vertical line FF'. The diameter of this σ circle is equal to the radius of curvature of the beam at the point G. This is simply shown by observing that:

$$x^2 = (\tfrac{b}{2})^2 + z^2 \quad \text{and} \quad \frac{R}{x} = \frac{x}{z}$$

and $\therefore$

$$R = \frac{(b/2)^2 + z^2}{z}$$

which is the same as the equation from the analytical approach. Figure 6.7 illustrates the wavefront thus calculated as it is generated within a confocal cavity.

The beam parameter, b', is found by constructing a further circle, a π circle, (see figure 6.8) which passes through the lateral focal point F and is a tangent to the optic axis at the point G. The diameter of this circle is b'.

For

$$x^2 = (b/2)^2 + z^2$$

and

$$\frac{b/2}{x} = \frac{x}{b'}$$

$\therefore$

$$b' = \frac{(b/2)^2 + z^2}{b/2}$$

From this value of b' the spot size at z can be calculated from the relation :

$$w = \sqrt{\frac{b' \lambda}{\pi}}$$
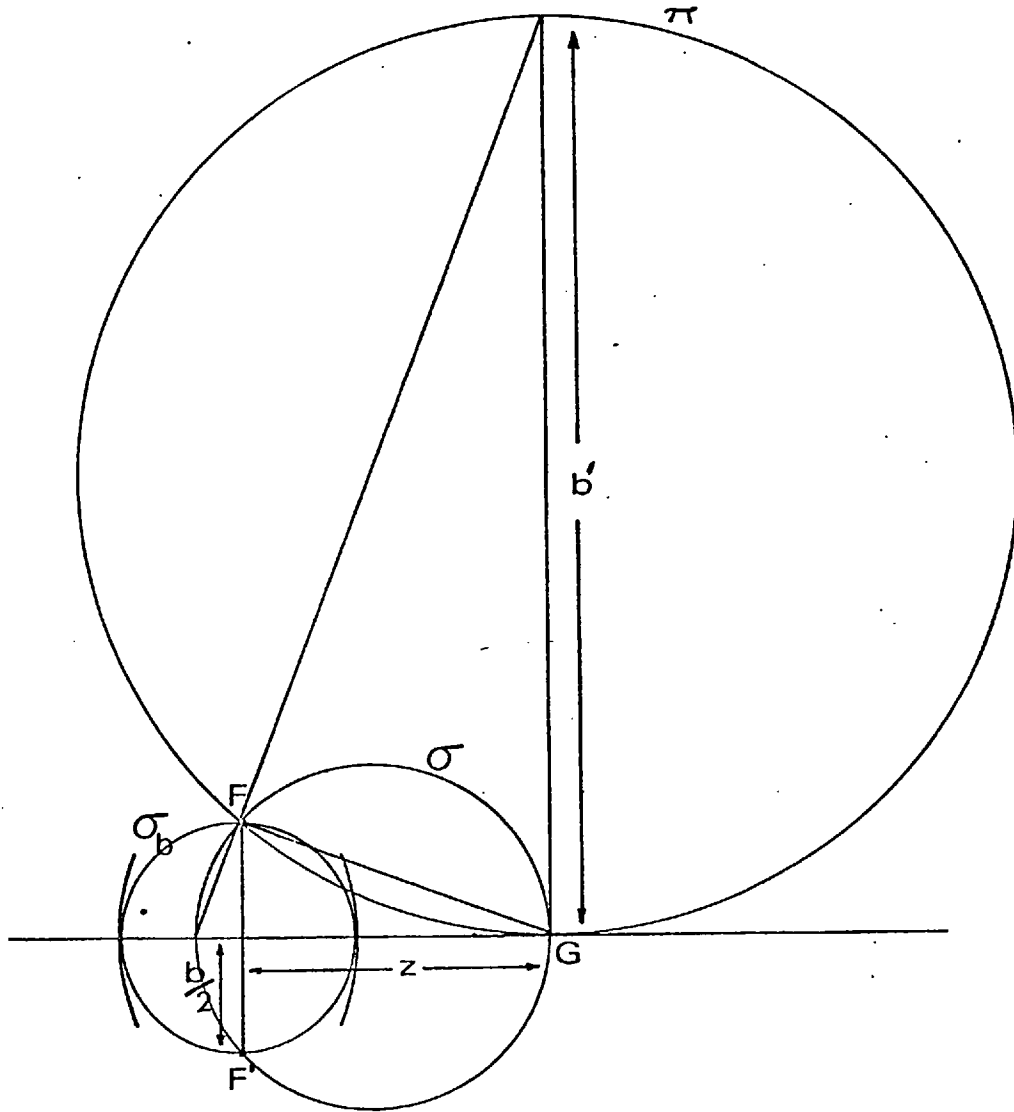
Fig 6.8   Construction of π circles

Although the lasing cavity used in this work was not a
confocal one. It is possible to calculate the confocal equivalent
cavity, by observing that within the cavity the wavefront which is
oscillating must conform with the mirror surfaces at each mirror,
and so finding the lateral focal points from the intersection of
the projected wavefronts from each mirror (see figure 6.9).
Thus given the lateral focal points FF' the radius of the wave-
front at any position, z, away from this line can be found, as
previously described.

Using an 8m radius of curvature total reflecting mirror and
a plane 80% reflectance Ge mirror as in these experiments would
yield the confocal equivalent radius of b = 6.3m as shown in the
figure below:
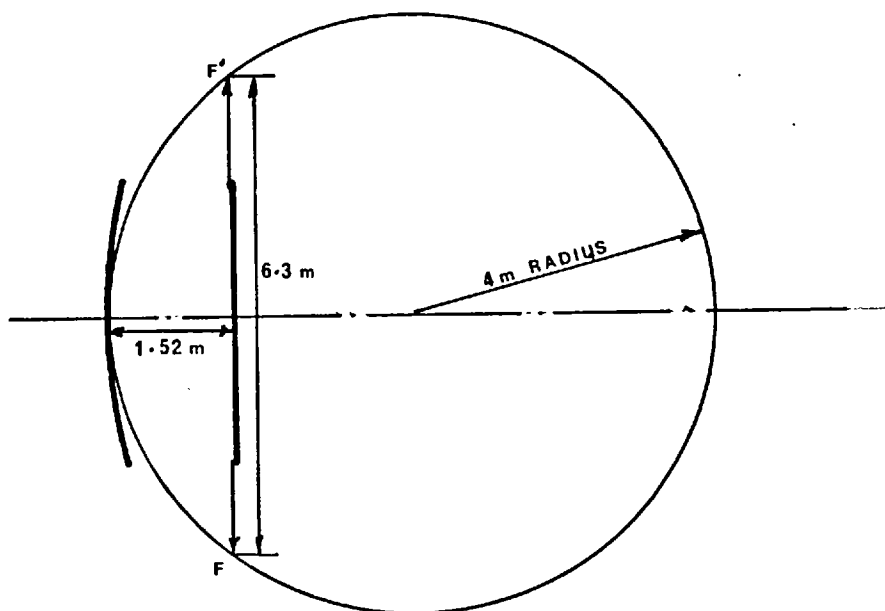
Figure 6.10   Calculation of the confocal equivalent
               of the cavity used.
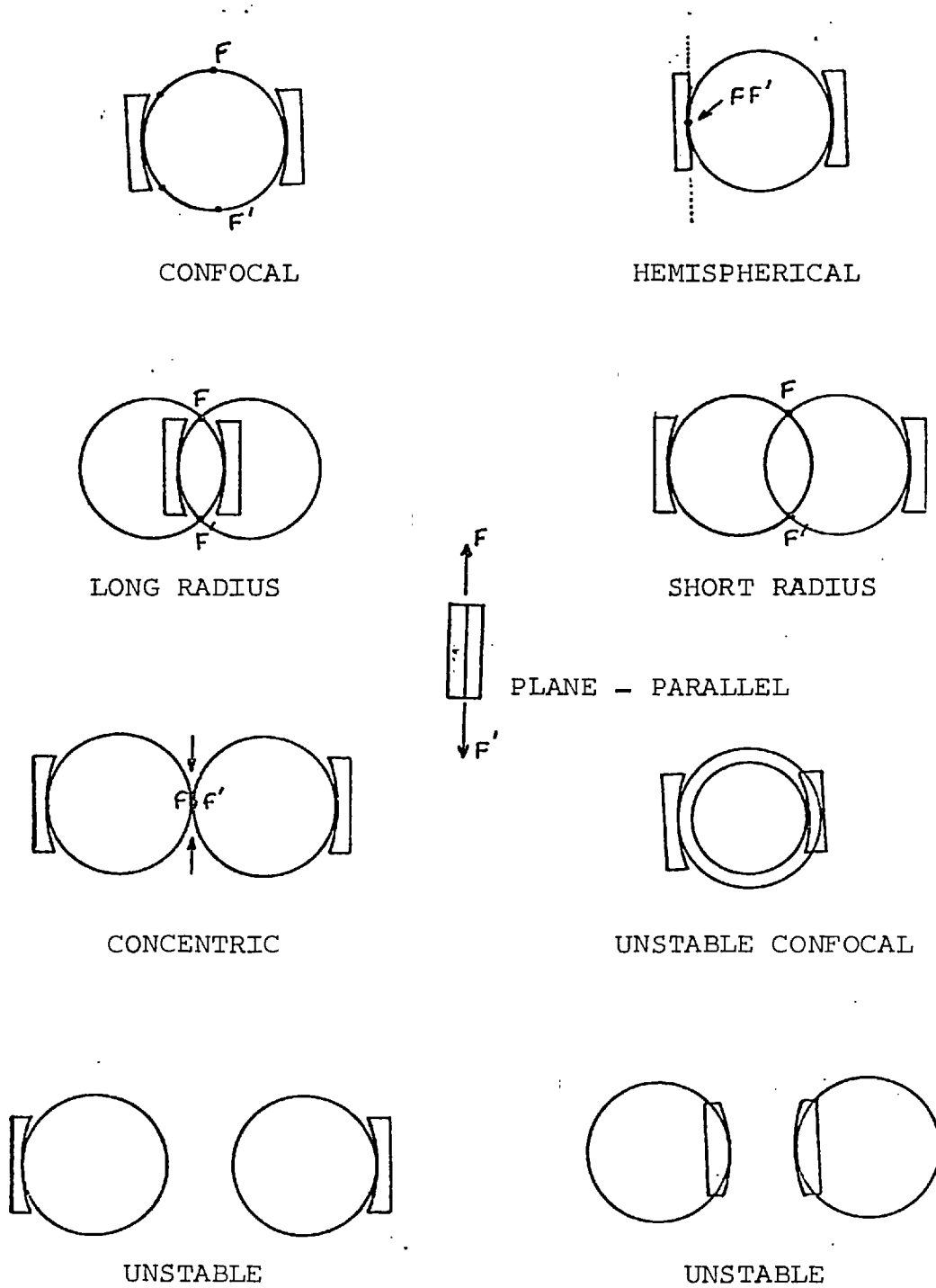
FIGURE 6.9   Various types of curved-mirror cavities

Also the figure has identified the location of the lateral focal points FF' and by constructing π circles at various distances from FF' the beam shape can be constructed. Figure 6.11 shows such a construction for the cavity used and various other cavities considered for these experiments - see section 4.2.2.2 laser construction.

After leaving the laser the beam first passes through an aperture sited 60 cms from the output window for all experiments. This will create truncation effects which are discussed later (section 6.3.2.2.6 page 164). For this part of the analysis the object/aperture would have a scaling effect on the beam size. For the laser cavity optics used figure 6.11 (8m line) shows the Gaussian beam size to be 6.68mm at the 5mm diameter aperture. Thus the scaling effect, ignoring diffraction effects related to truncation, would be 5/6.68 = 0.75 = M. This assumption is discussed further in the sections on truncation and modes.

After the aperture the beam arrives at a lens. If the lens is considered 'thin' and not to cause spherical aberration then the radius of curvature, R_1, of the wavefront arriving at the lens is related to the radius of curvature of the emergent wavefront, R_2, by:

$$\frac{1}{R_1} + \frac{1}{R_2} = \frac{1}{f}$$

where f = focal length of the lens.

A thin lens would not alter the beam diameter within the lens, and thus would not alter the beam parameter, b'. Thus the beam emerging from the lens would have a wavefront of radius R_2 and a beam parameter unaltered of b'. The intersection of the wavefront σ circle (of diameter R_2, passing through the centre of the lens) and the π circle of diameter, b', tangential to the same point in the lens reveals the new lateral focal points for the Gaussian beam subsequent to the lens. The construction is shown in Figure 6.12 . The new lateral focal points are used as before to find the wavefront and beam diameter at any point subsequent to the lens simply by drawing the appropriate σ and π circles
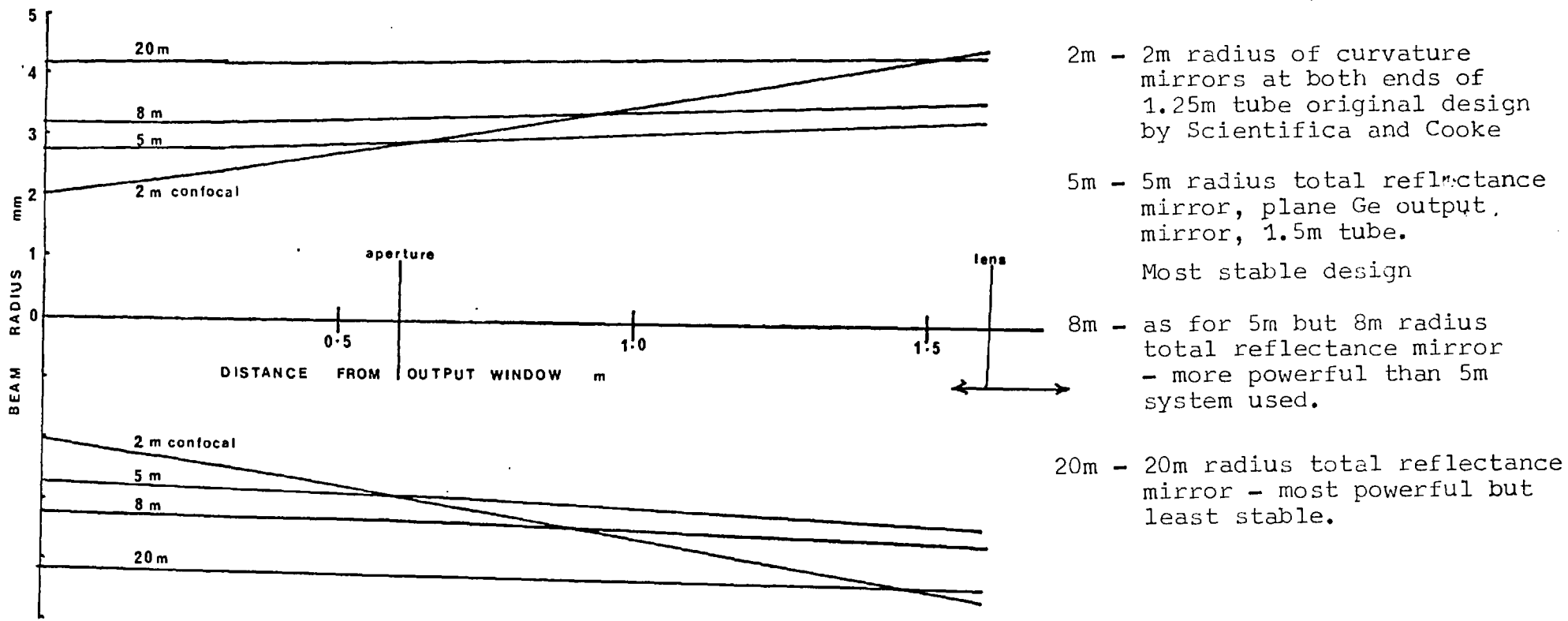
fig 6.11 The diffraction limited emergent beam geometry as a function of cavity optics.

2m – 2m radius of curvature mirrors at both ends of 1.25m tube original design by Scientifica and Cooke

5m – 5m radius total reflectance mirror, plane Ge output, mirror, 1.5m tube.

Most stable design

8m – as for 5m but 8m radius total reflectance mirror – more powerful than 5m system used.

20m – 20m radius total reflectance mirror – most powerful but least stable.

which yield $b'_1 = \dfrac{\pi\ w^2}{\lambda}$. The minimum spot diameter is

$$D_{min} = 2 \times M \times \sqrt{\dfrac{b_1\ \lambda}{2\pi}}$$

where $b_1 = F_1F'_1$ the distance between the lateral focal points.

Although figure 6.12 illustrates the construction for finding the lateral focal points of the beam after the lens the scale is such that it is difficult.to measure F_1F_1'. Thus this had to be calculated.
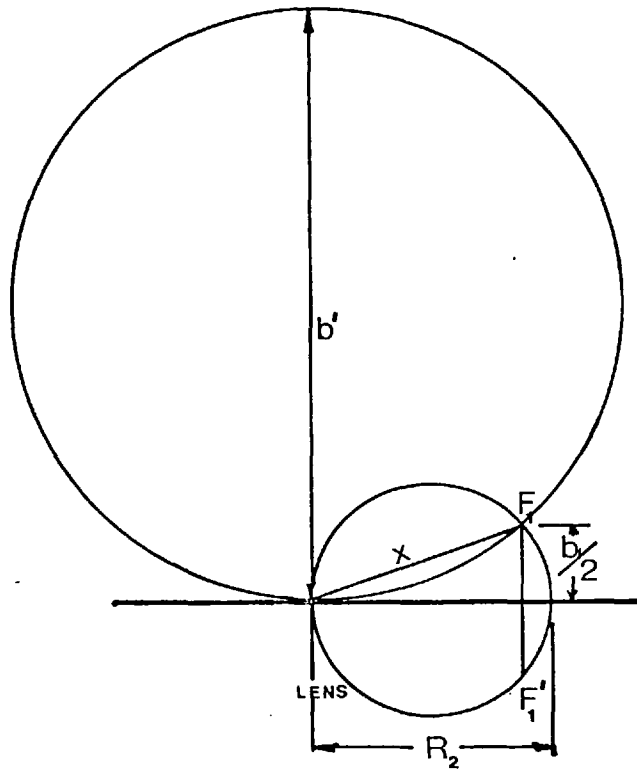
Figure 6.12 Construction to find the lateral focal points subsequent to the lens

$$\dfrac{b'}{x} = \dfrac{x}{b_1/2} \qquad \text{by similar triangles}$$

$$x^2 = (\frac{b_1}{2})^2 + (R_2 - \delta R_2)^2 \doteq (\frac{b_1}{2})^2 + R_2^2 \qquad \text{by pythagoras}$$

$$\therefore b' = \frac{(\frac{b_1}{2})^2 + R_2^2}{b_1/2}$$

$$\therefore b_1 = \left(2b' \pm \sqrt{4b'^2 - 16R_2^2}\right)/2 = F_1F_1'$$

(if δR_2 is seen from a construction to be significant a correction to R_2 is simply made).

Knowing the position and size of F_1F_1' the beam geometry can be calculated as before by calculating b_1' as shown in figure 6.13

Figure 6.13

Construction to find beam radius at the location Z_1 distant from lens.
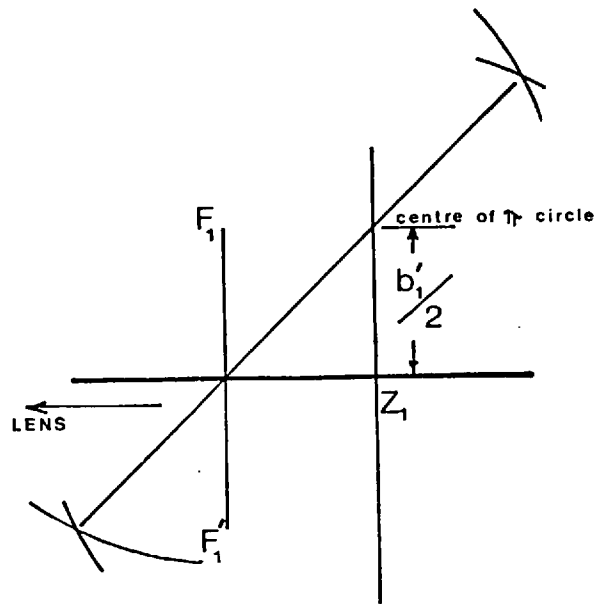
From the value of b_1' the beam diameter, can be calculated:

$$D_b = 2 \times M \times \sqrt{\frac{b_1' \times \lambda}{\pi}}$$

6.3.2.2.5 <u>Calculations for the lenses used</u>

The focal length of the lenses used for 10.6μ radiation was established as discussed in section 6.3.2.2.11, page 178 Using these focal lengths with the laser cavity optics noted on page 158 , the propagation circle method established the beam shapes for all the experimental series. These are shown in graphs 6.14 - 17. The spot size for series A, B and C were calculated as shown in table (6.3) which acts also as an example of the calculations used in plotting the graphs.

The effect of different cavity optics on the beam shape after the lens is shown in graph 6.17 for interest.

6.3.2.2.6 <u>The effect of truncation</u>

So far the beam shape has been discussed for a beam having a Gaussian power profile governed solely by refraction and diffraction.

At the aperture a truncation was noted. This would produce a non Gaussian beam having side lobes in the far field pattern and structure within the main lobe in the near field. These patterns have been studied by A.L. Buck[99] and Campbell et al[100]. They found the truncation effects were important when the aperture radius was less than twice the Gaussian spot radius. Dickson[101] calculated that truncation at the 1/e power radius (in his paper $1/e^2$ intensity radius, which is the same thing)gave an increased spot size of > 50%.

Thus an increased spot diameter would be expected due to this effect.

It is interesting to note further that the axis intensity would be expected to oscillate with increasing distance from the aperture up to one Rayleigh distance.

The Rayleigh distance = $2a^2/\lambda$

where a = aperture radius λ = wavelength
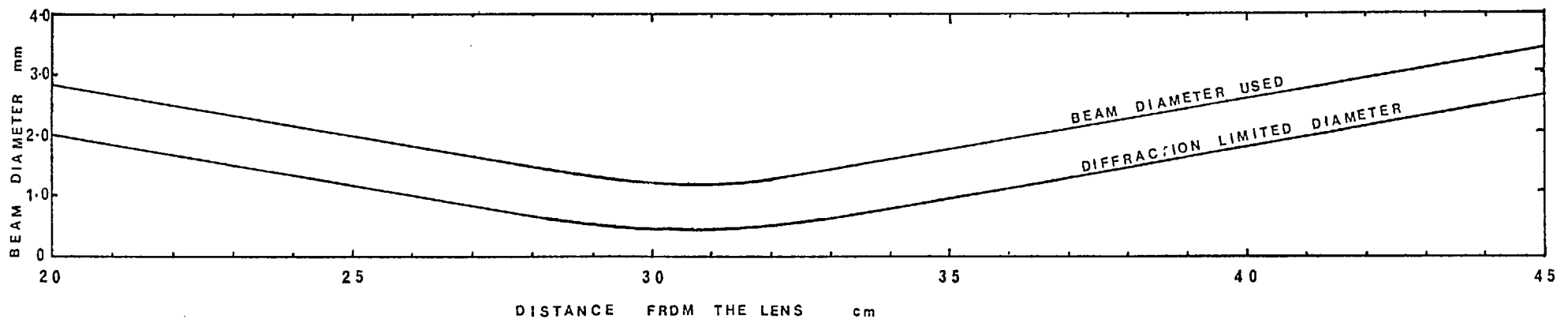
Fig 6.14   Beam shape calculated   for   the 29·5 cm   lens   as in series D E & F
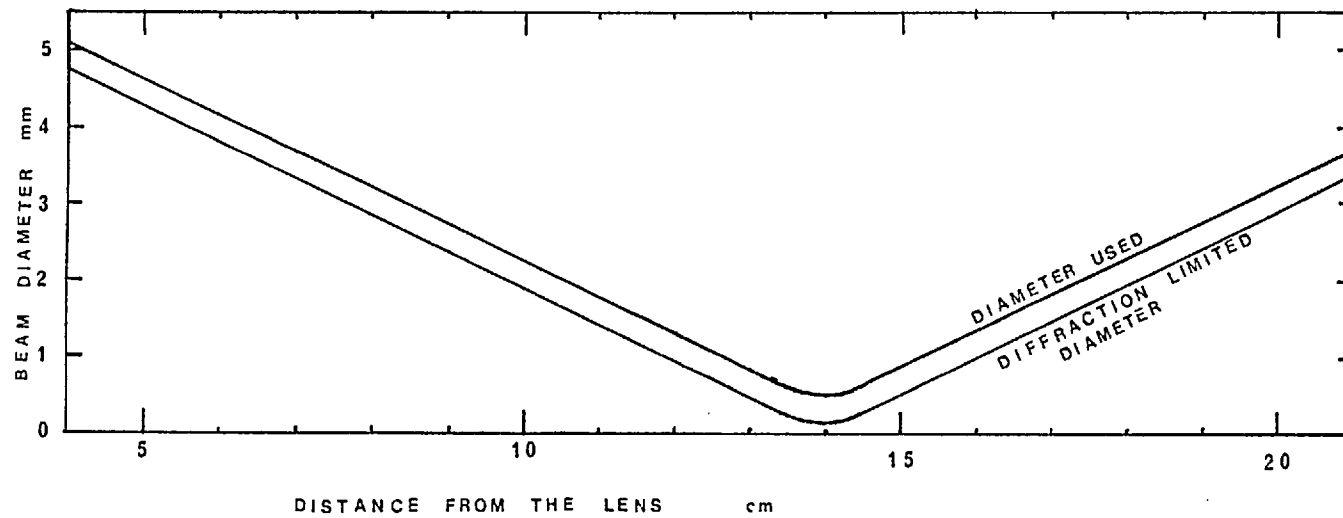
Fig 6.15 Beam shape calculated for the 13·7 cm lens as in series H & I
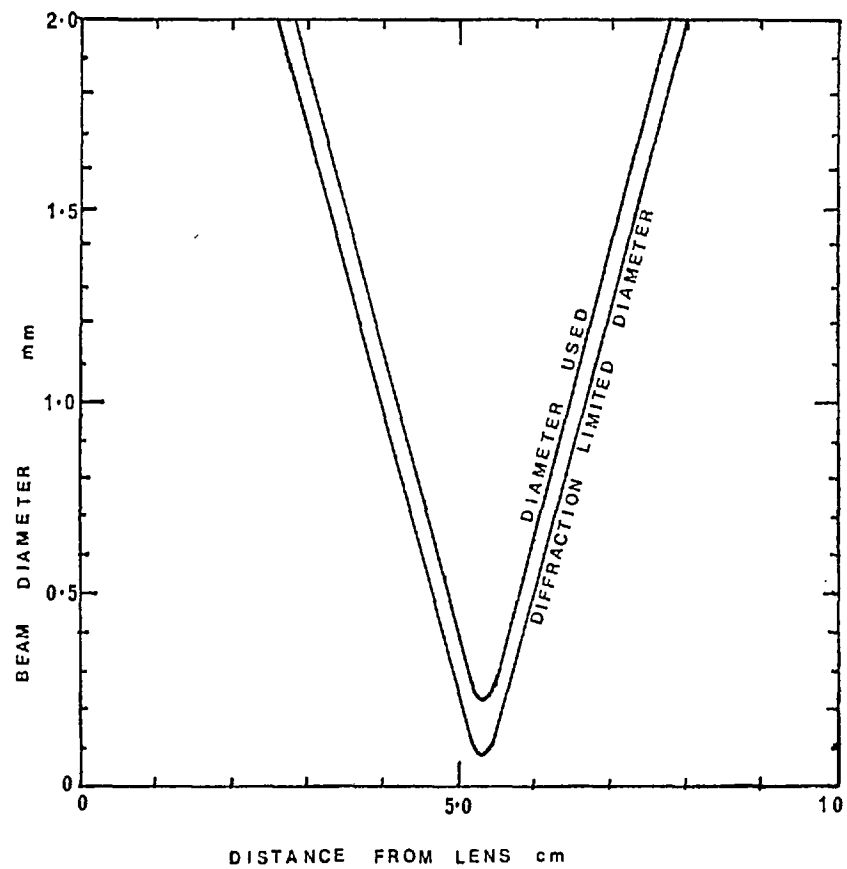
Fig 6,16 Beam shape calculated for the 5·3 cm lens as in series G

Aperture 60cm from output window

Lens   100cm "   aperture

Focal length 29.5cm

SYSTEM A   20m radius curvature
                 total
                 reflectance mirror, plan
                 output

SYSTEM B   8m

SYSTEM C   5m

SYSTEM d   2m radius confocal
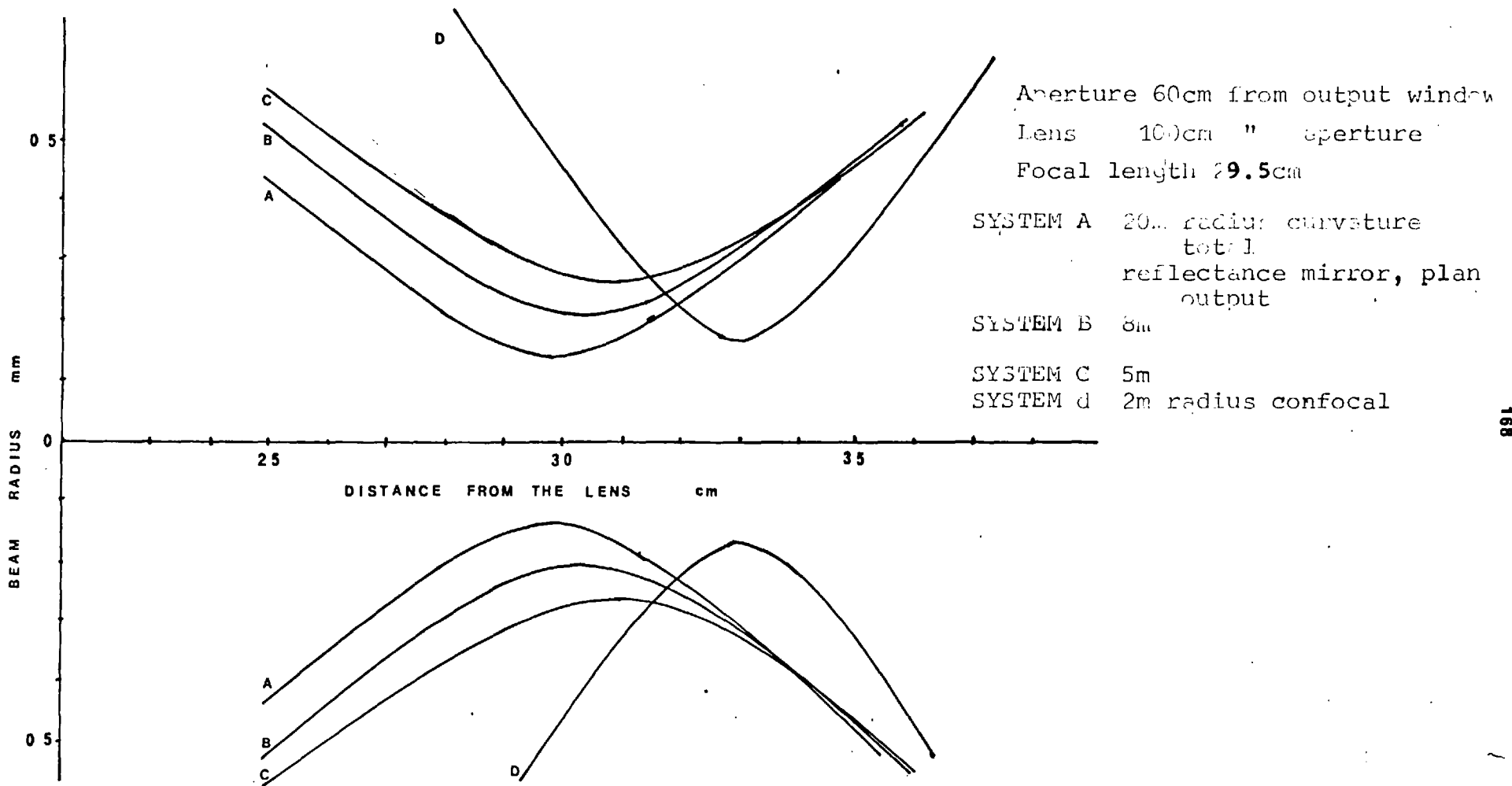
Fig 6.17   Variation of beam shape with cavity optics of the laser

Expt Series	Radius of total Refl. Mirror m	FACTOR M				LATERAL FOCAL POINTS F_1F_1'						BEAM DIAMETER		
		Position of aperture m	Diam σ circle at aperture m	Beam radius at aperture mm	M for 5mm diam aperture	focal length f cms	aperture/lens distance	R_1 wave-front at lens m	R_2 wave-front leaving lens m	Diam π circle at lens m	F_1F_1' m	lens/image distance cms	Diam π circle b'_1 cms	Spot diam. mms.
A,B	8	0.60	3.3	3.34	0.75	29.50	73.66	8.9	.3051	3.75	0.050	33.02	5.3	0.63
C	8	0.60	3.30	3.34	0.75	29.50	74.3	8.9	0.3051	3.75	0.050	35.2	13.1	1.0

Table 6.3

Example of Beam Calculations

After this distance, .the "far field" is achieved in which the intensity falls exponentially. This is shown in figure 6.18 taken from Deshazer and Parks[88]

beam radius = w   axial distance = R

aperture radius = a

Figure 6.18 Centre line intensity for truncated Gaussian beams vs distance from the aperture.

The experimental region is seen to lie within this distance and thus spots would be expected to suffer from detail within the main lobe. This detail is a complexity added to the detail due to multimode output from the laser. However, since w/a for the experiments was 1.25 and the experimental region was short, figure 6.18 shows that this effect will not be large.

6.3.2.2.7 The effect of mode structure

For circularly symmetric beams the power distribution would be approximately described by a Laguerre – Gaussian function as noted on page 128 et seq. That is a Gaussian distribution in the TEM_{00} mode, and a more diffuse distribution in higher order modes due to the radial multiples from the Laguerre polynomial.

For example the TEM_{01} mode would have a distribution given by:-

$$P = \frac{P_{tot}}{\pi w^2} \frac{\sqrt{2}\, r}{w} e^{-(r^2/w^2)} \sin \theta$$

This amplitude distribution is compared to that for the TEM_{00} mode with varying degrees of truncation at the output window – measured as the cavity Fresnel No,N, in figure 6.19– from the work of Fox and Li and discussed in Allen and Jones' book[89]. An increase in some 20% of the beam radius is noted. Thus the effect of higher order modes will be to further enlarge the spot size. Marshall[95] allows for this by a constant multiplier for higher modes.

6.3.2.2.8 Effect of Spherical aberration

Spherical aberration is the deviation of the radiation from the diffraction limited route due to refraction or reflection at a spherical surface. It is dependent on the curvature of the surface; thus any reduction in lens curvature (R_1 and R_2), due to increased focal length, f, or increased refractive index of lens material (n) $-\frac{1}{f} = (n-1)\left[\frac{1}{R_1} - \frac{1}{R_2}\right]$ – results in less spherical abberation.

Spherical surfaces are used because they are cheaper to make and easier to align than parabolic surfaces. For minimum spherical aberration the surface radii should be related according to the equation :

$$\frac{R_2}{R_1} = \frac{2n^2 + n}{2n^2 - n - 4}$$

where n = refractive index.
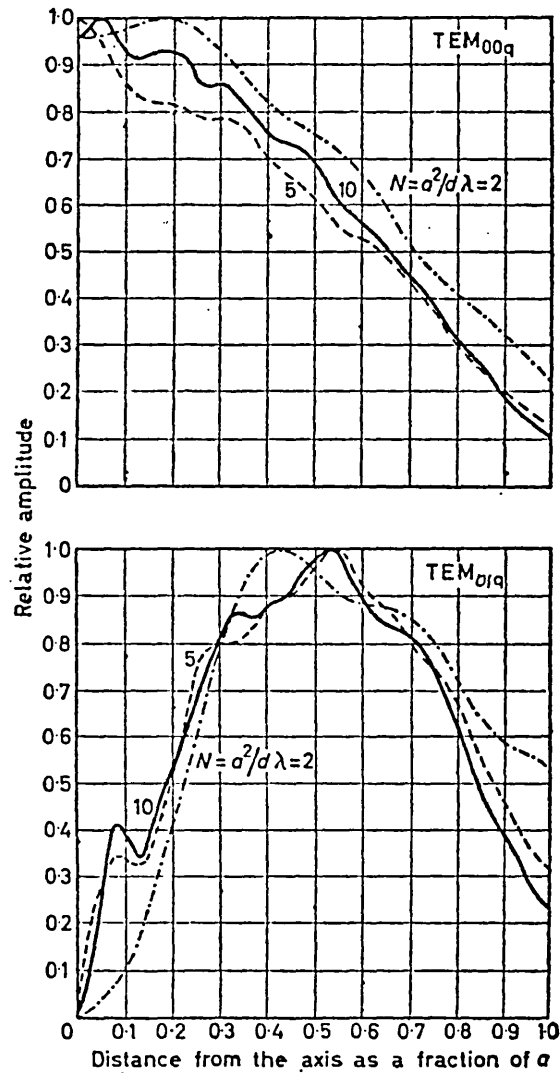
Figure 6.19 Amplitude distribution of radiation across a circular mirror for TEM_{00q} and TEM_{01q} modes, plotted for various values of N. (89)

For such a lens some 35% increase in spot size could be expected with an F1·5 lens having a refractive index of 1.5. But above an F7.0 spherical aberration becomes negligible compared to truncation effects.

The lenses used were equiconvex and therefore not designed for minimum aberration, but even the shortest focal length lens used had an F No $>$7.0 ($\simeq$10.0). Hence spherical aberration effects would be expected to be negligible compared to truncation effects.

6.3.2.2.9 Experimental evaluation of beam scale factor

The previous sections have established the overall beam shape, and have shown that the beam size calculated from diffraction theory is substantially smaller than that expected at the substrate. This is found to be the case; for by using the theoretical spot size in the mathematical model unreasonably high temperatures are predicted, $\sim$1500°C in some cases. In these cases:-

a) The spots were not seen to glow white or even red.

b) Thermodot I.R. readings suggested temperature nearer 300 - 400°C.

c) The deposition rates observed were far lower than those predicted from these higher temperatures.

d) The time taken for the spot to reach thermal equilibrium was much slower than predicted.

Based on the observation of point (d) it is possible to evaluate quantitatively the order of scale factor required as described in the next section .

6.3.2.2.10 Thermal rise time calculations

Traces figure 6.20 show the variation of spot temperature with time as recorded by the thermodot TD17 I.R. thermometer fitted with special 3.5 - 5" focal length optics.

To obtain these traces the thermodot was centred on the spot, which was invisible, by maximising the thermal signal. This was done by careful movement of the thermodot on an x-y platform. For the trace C32 shown, the thermodot was correctly centred from the start of heating, but not for C17 (the peaks on the rise of C17 are due to centering checks).

The target size of the thermodot was

$$\left(\frac{3 + \text{distance from target to the front of objective lens in inches}}{300}\right)$$

$$\times \ \frac{1}{\cos{(\theta)}} \quad \text{inches}$$

where θ = angle between normal to substrate and thermodot optic
axis

The objective lens was 4" from the target and θ was 60°. Thus the target area was:-

$$\left(\frac{3 + 4}{300}\right) \times 2 \times 2.54 \text{ cms. square}$$

$$= 0.12 \times 0.12 \text{ cms square}$$

The diameter of the spots in the traces shown were $\simeq$ 0.2 cms and the calculated diffraction limited beam diameter was $\simeq$ 0.10 cms. Thus the theomodot was viewing as far out as $R^* \geq$ 1.0 and possibly $R^* = 2.0$.

Considering the theoretical curves (figure 3.8 et seq) it is seen that 90% of equilibrium is achieved at the spot centre after a time given by $\theta^* \simeq 34$, at $R^* = 1.0$ the time is $\theta^* = 35$, while at $R^* = 2.0$ the time is $\theta^* = 62$. Thus depending upon the
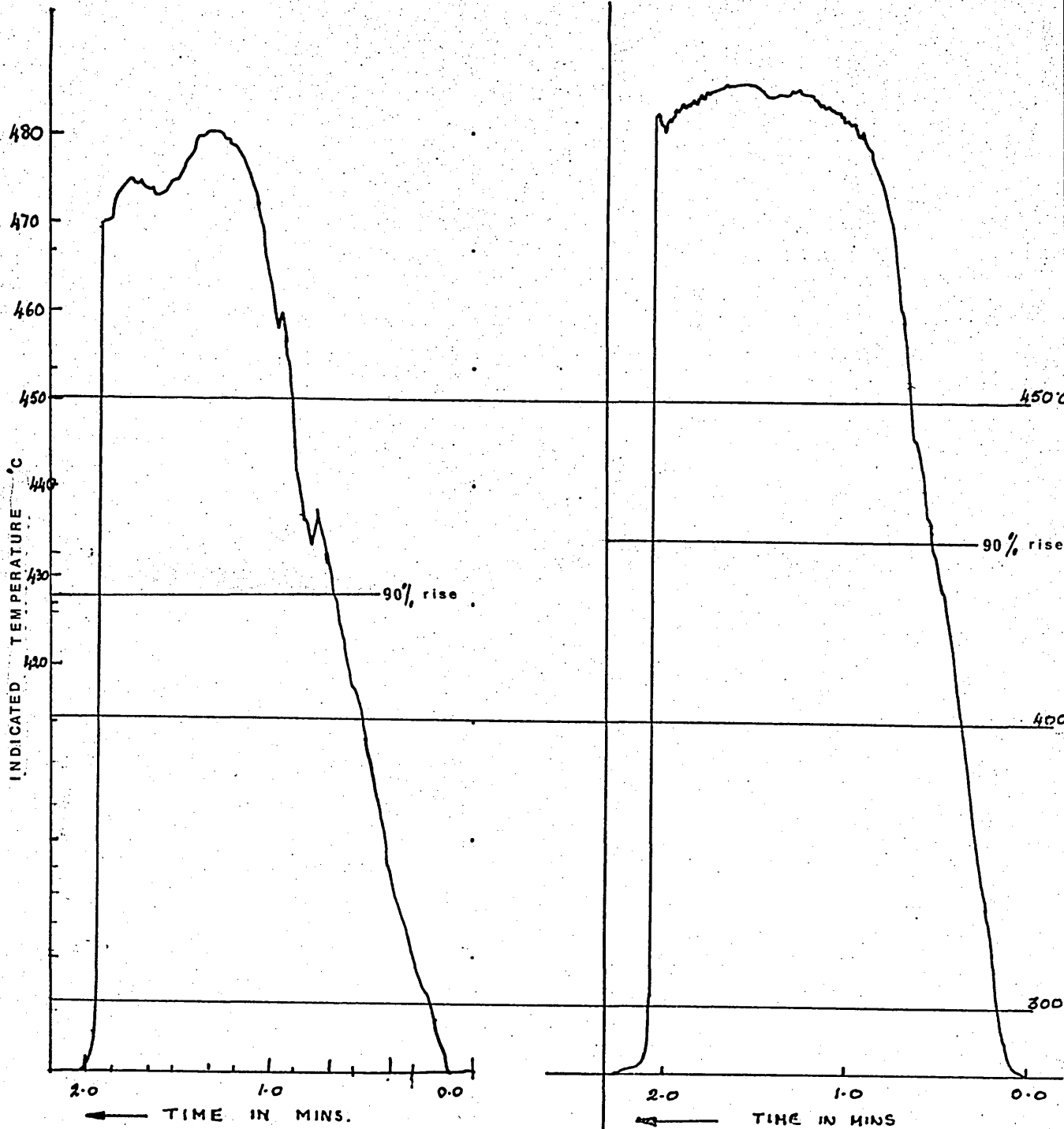
SAMPLE C17

A 'mound' deposit
inner diam 1.27mm

SAMPLE C32

A peak deposit with black
inner diam 1.44mm

Figure 6.20   Thermodot traces showing average central
spot temperatures taken over an area of
1.2mm x 1.2mm

precise view from the thermodot 90% equilibrium should be achieved between $\Theta^* = 35$ and $\Theta^* \stackrel{\sim}{=} 55$. The area weighted average is approx. $\Theta^*_{90\%} = 49$. Assuming the thermal diffusivity $\alpha = 0.29 \times 10^{-6}$ m^2/s and recalling that, $\Theta^* = \frac{16\alpha t}{D_b^2}$

It is possible to state that: $D_b = 2\sqrt{\dfrac{4\alpha t_{90\%}}{\Theta^*_{90\%}}}$ from which table 6.4 was calculated using various rise time traces.

The error in this method is mainly from the uncertainty in the appropriate value of Θ^* – fortunately D_b is dependent to the power of $\frac{1}{2}$ on Θ^* – $\pm$ 16%. A further error is introduced in the estimation of the 90% time which will be approximately $\pm$ 5% (allowance must be made for the non linear thermodot scale) and the value of α $\pm$ 2%. The response time of the thermodot is given as 0.3s to 95% full scale which would introduce a further error of $\pm$ 1%.

The estimated overall accuracy will be around 25%. This rather large number is to be compared with the difference between observed and calculated diameters of 200%.

The results for the D series, shown in table 6.4, for which the spot size was variable, indicated that the concept of a multiple on the geometric beam diameter for all positions after the lens was likely to be incorrect. The picture presented was of an almost constant addition to the beam diameter. This also results in a more sensible appearance of the beam than would be the case with a constant multiple. This constant addition has been calculated as 2.0 times the minimum geometrically calculated spot size and is illustrated in graphs (6.14-17).

Since this multiple is caused almost entirely by beam mode and truncation effects the same multiple would be expected for all lenses. The thermal rise time of the G, H, and I series were too fast and the spots too small for a reliable trace to be obtained and hence this assumption could not be fully checked.

Table 6.4

Diameter Estimation Based on Thermal Rise Time

Run	$t_{90\%}$ Time to 90% Max: Temp	$2\sqrt{\dfrac{4\alpha}{\Theta^{\bullet}}}$ $t_{90\%}$ $(ms^{\frac{1}{2}})$	Rise Time Diameter cm	Geometric Diameter cm	Ratio $\dfrac{\text{Rise Time Diam}}{\text{Geom Diam.}}$	Difference Rise time Diam − Geom. Diam
D5	70	.0003077	.257	.15	1.71	.107
D20	37.5	"	.188	.125	1.50	.063
D21	12	"	.106	.050	2.12	.056
D22	24	"	.151	.070	2.15	.081
D23	18	"	.131	.044	2.97	.087
D24	12	"	.106	.048	2.21	.058
C17	45	"	.206	.10	2.06	.106
C18	43	"	.201	.10	2.01	.101
C32	35	"	.182	.10	1.82	.082
C33	49	"	.215	.10	2.15	.115
C34	43	"	.202	.10	2.02	.102
				MEAN STD DEV	2.06 0.369	.087 .021

The experimental conditions for each deposit are shown in Appendix 4

6.3.2.2.11 <u>Establishing the focal length of the NaCl lenses</u>

<u>using 10.6μ radiation</u>

The beam calculations displayed in table 6.3 and discussed in section 6.3.2.2.5, page 164 require the focal length of the lens to 10.6μ radiation. It is expected that this focal length would be considerably longer than that for visible light, and there lies the problem. The beam calculations are fairly sensitive to the exact focal length yet to establish the clearest image from a focussed laser beam is well nigh impossible - see figure 7.1 (-+- series). Accordingly this problem was solved by a three pronged approach:

1) Establish the visible light focus by standard thin lens techniques and use a constant multiplier to find the focal length for 10.6μ radiation.

2) Perform a series of char prints and estimate the beam waist. From the beam waist back calculate via the diffraction theory beam calculations to find the focal length.

3) Observe the ordering of the thermal damage effects noticed in the deposits as a result of variation in the focal length.

<u>Approach 1 - From visible radiation focal length</u>

The filament of a lighted lamp set 1m from the lens was brought to a focus on a card the two distances, image to lens (s) and lens to lamp (o), were measured. The focal length to visible radiation was found from the thin lens equations:-

$$\frac{1}{s} + \frac{1}{o} = \frac{1}{f}$$

The lens was fairly obviously not thin, being 0.5 cms thick. However, the only requirement is an estimate of the focal length for visible light.

The results were:-

Lens No	Series for which lens was used	visible radiation focal length cms	value x 1.08 cms
1	A,B,C,D,E,F	27.3	29.5
2	G	4.9	5.3
3	H,I	12.7	13.7

Table 6.5

The refractive index for NaCl to visible radiation is approximately 1.54 while at 10.6μ it is reported to be 1.50[103,104]. This dependence with wavelength is illustrated in figure (6.21) taken from Harry's book[103].
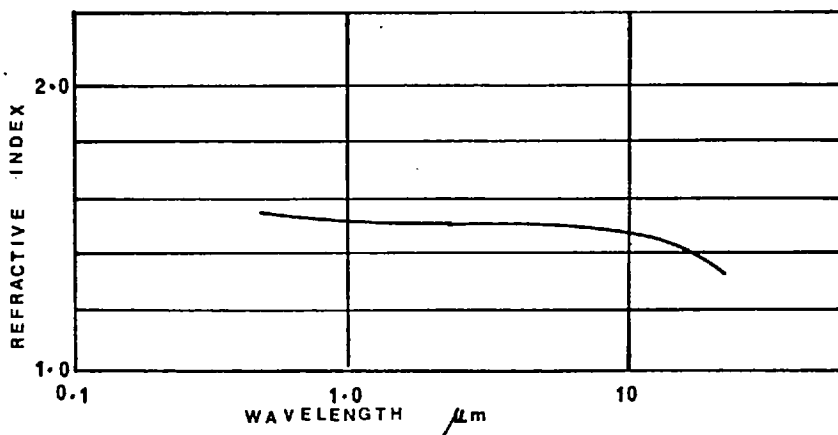
Figure 6.21   Variation of the refractive index of sodium chloride with wavelength

Now for a thin lens the focal length (f) is a function of the refractive index (n):

$$f = \frac{1}{(n-1)} \frac{1}{(\frac{1}{R_1} - \frac{1}{R_2})}$$

for a thick lens this becomes:-

$$f = \frac{-R_1 R_2}{(n-1)(R_1 - R_2 - (n-1) t/n)}$$

where t = lens thickness   cms

R_1, R_2 = radius of curvature of front and back surfaces.

In either case:-

$$f \propto \frac{1}{(n - 1)} \quad \text{to a first approximation}$$

and therefore :-

$$\frac{f_{10.6\mu}}{f_{vis}} = \frac{0.54}{0.50} = 1.08$$

using this multiplication factor approach 1 yields values for
the focal lengths at 10.6μ shown in table 6.5 . The estimated
accuracy being ± 5%.

Approach 2 - from char print beam waist

The weakness of an argument based on char prints for finding
the focal length of a lens has been pointed out (page 150   et seq).

However, an indication of the beam waist position can be
found this way. Graph 6.22   shows the results of
numerous char prints using lens 1. The beam waist is seen to
lie between 26.6 cms and 31.7 cms, with a preference towards 30cms.

Beam calculations (see figure 6.14) reveal that the beam
waist for a 29.5 cm focal length lens, placed 60 cm from the plane
output window of a laser having an 8m radius total reflectance
mirror -as for these char prints - would have a beam waist
at 30 cms from the lens.

Thus this approach gives values as follows:-
(the estimated accuracy being ± 10%).

lens 1 - 29.5 cms focal length to 10.6μ
lens 2 -   5.3 cms   "   "   " . "
lens 3 - 13.7 cms   "   "   "   "

Figure 6.22   DIAMETER OF CHAR PRINTS VS DISTANCE FROM
                         LENS FOR LENS 1

Lens/aperture distance - 73cm
Laser/aperture distance - 60cm
Laser cavity 1.5m long with 8m radius
total reflectance mirror and plane
output windown.
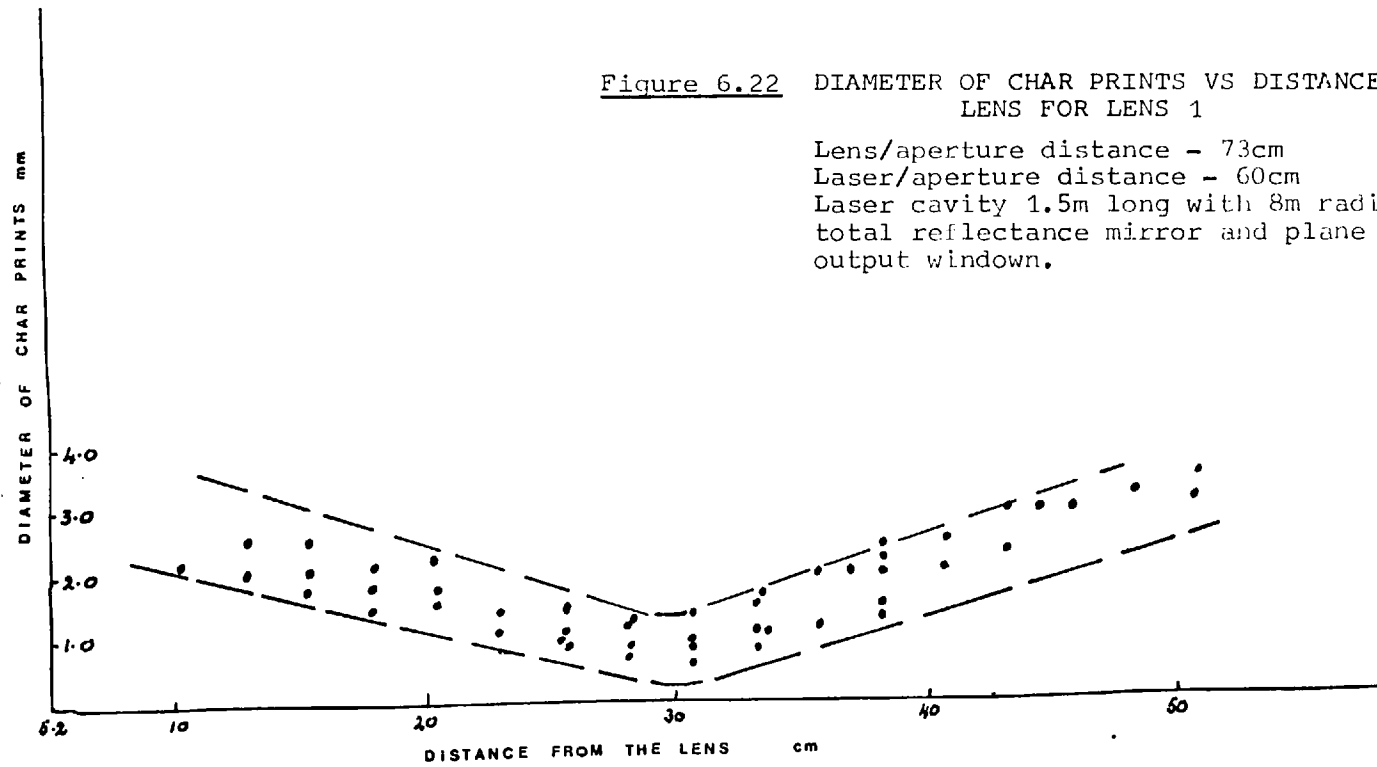
Approach 3 - from ordering of thermal events

It would be expected that craters and cracks would be more likely to form under intense heating. It would therefore be an indication of the correctness of the estimated focal length if these events correlated with measured values of power/beam diameter

Table 6.6 shows how the D series is only sensibly sorted according to the above criterion if the focal length is around 29.5cm. Likewise the H series is suited by a focal length of 13.7cm and the G series by a focal length of 5.3cm.

Conclusion

All three approaches yield a similar focal length of:

$$
\begin{array}{lll}
\text{lens 1} & 29.5 & \pm \ 1\text{cm} \\
\text{lens 2} & 5.3 & \pm \ 0.2\text{cm} \\
\text{lens 3} & 13.7 & \pm \ 0.5\text{cm}
\end{array}
$$

These values have been used in the relevant calculations.

6.3.3 SUBSTRATE PARAMETERS

6.3.3.1 Thermal properties

The substrates chosen were soda glass and spectrosil silica.

The glass chosen was that from Chance Propper microslides and Axa Limited. It turned out on investigation that both of these suppliers obtained their thin sheet glass from the same Belgian supplier* and consequently all the glass is of the same composition within the range of normal manufacturing fluctuations. The Belgian supplier was contacted by Chance-Propper and gave the properties of their glass as those in table 6.7.

---

* Société anonym citalo

Table 6.6

Assumed focal length

	24.92 cm			26.67 cm			29.5 cm			30.15 cm			32.0 cm	
P/D_b	Speci-men	Shape	P/D_b	Speci-men	Shape	P/D_b	Speci-men	Shape	P/D_b	Speci-men	Shape	P/D_b	Speci-men	Shape
5	D1	—	5.4	D1	—	7.5	D1	—	6.5	D1	—	7.4	D17	—
5.7	D2	—	6.1	D2	—	8.7	D2	—	7.5	D2	—	7.5	D1	—
6.08	D3	—	6.6	D3	—	9.6	D3	—	8.3	D3	—	7.8	D12	no deposit
7.5	D20		8.6	D20		10.2	D17		8.3	D17		8.9	D2	
8.1	D4		9.1	D4		12.9	D12	no deposit	10.3	D12	no deposit	9.0	D16	
8.2	D25		10.3	D5		13.0	D16		10.5	D16		9.4	D15	
8.6	D22		10.7	D22		13.5	D15		10.13	D13		10.0	D13	
9.0	D5		10.7	D25		13.7	D4		11	D15		10.2	D3	
9.7	D18	cr	11.7	D17		13.6	D13		12.4	D4		10.8	D1	
10.0	D21	cr	12.3	D19		14.4	D20		12.9	D14		11.7	D12	
10.4	D19		12.5	D21	cr	15.8	D14		12.9	D20		11.7	D11	cr
11.0	D6		12.9	D6		16.2	D5		15.2	D5		15.2	D4	
11.8	D24	cra	13.05	D18	cr	20.6	D11	cr	16.7	D11	cr	18.1	D20	
13.4	D7	cra	15.4	D24	cra	20.7	D10		16.9	D10		18.7	D5	
13.6	D23	cr	16.8	D7	cra	21	D22		21-24	D22		23.8	D25	
15.6	D17		18.2	D16		22.3	D25		21	D6		29.7	D9	cr
16.2	D9	cr	18.9	D15		23.2	D6		23	D19		30-40	D9	cr
16.3	D8	cra	18.9	D23	cr	24.7	D19		30	D21	cr	33	D6	
22.7	D11	cr	22.2	D9	cr	26-34	D21	cr	35	D25		34	D23	cr
22.9	D10		22.5	D8	cra	32.1	D24	cra	36.3	D7	cra	34	D24	cr
28	D16		25.7	D14		33	D18	cr	39	D18	cr	39	D18	cr
29	D15		26.8	D12	no deposit	36.3	D7	cra	51	D24	cra	39.6	D19	
48	D14		28-30	D13		38.6	D23	cr	68	D23	cr	42	D22	
55-58	D12	no deposit	44.6	D11	cr	43.4	D9	cr	89	D9	cr	48	D7	cr
70.8	D13		45.0	D10		43-58	D8	cr	90-120	D8	cr	50	D21	cr

Values of D_b used here are the diffraction spot sizes before allowance for truncation etc.
cr = cracked   cra = crater

TABLE 6.7a

Thermal Properties of the Soda Glass
Microscope Slides Used

Property	Ref.	Value	
Density @ 23°C	manuf	2.5 gm/cm^3	
Thermal Conductivity at normal temps.	manuf	8.15–9.3×10^{-3} J/cr °Cs	
at melting point	"	17.4–23.2×10^{-3} J/cm °Cs	
Specific Heat at normal temps	105	0.50 J/g °C	
Thermal Diffusivity " " "	manuf 105	0.0066 cm^2/s	
Strain Point	manuf	between 470–490°C	
Tempering Lower Temperature	manuf	535°C	
Transformation Temperature	manuf	558°C	
Softening Point ("Melting Point")	manuf	585°C	
Melting Temperature	105	~1400°C	
Youngs Modulus E @ 23°C	manuf	68.6 N/mm^2	
Coefficient of Expansion	manuf	°C^{-1}	% expansion
from 23 to 100°C		7.54×10^{-6}	.058
23 to 400°C		8.14×10^{-6}	.307
23 to 558°C		8.48×10^{-6}	.456
23 to 585°C		9.02×10^{-6}	.507
558 to 585°C		19.84×10^{-6}	.053

Table 6.7b

Thermal Diffusivity Data on Glasses (General)

Material	Thermal Cond: J/cm °C sec	Specific Heat J/g°C	Density g/cm^3	Diffusivity cm^2/s	Ref.
Quartz	110×10^{-3} axis				K&L
	65×10^{-3} axis				K&L
Silica glass	13.8×10^{-3}	0.75	2.2	0.0083	S
	8.3×10^{-3}			0.007	F
	11.84 @ 41°C	0.71		0.0075	C
Glass	8.5×10^{-3} flint	0.5	2.70	0.0063	K&L
	5.5×10^{-3} extra dense flint		4.78	0.0023	K&L
	12.44×10^{-3}	0.753	4.78	0.00447	F
		0.67 crown			
Pyrex	11×10^{-3}	0.78	2.23	0.00632	K&L
(80% SiO$_2$ 14% B$_2$O$_3$ 4% Na$_2$O 2% Al$_2$O$_3$	11.34×10^{-3}	0.25	2.35	0.0193	S

K&L Tables of Physical and Chemical Constants GWC Kaye and TH Laby, Longmans, 1966
S Smithsonian Physical Tables, Forsythe, 1964, 9th revised edition.
F Handbook of Engineering Mechanics, Higge, McGraw Hill, 1962
C Handbook of Physical Constants, S.P. Clark, memoir 97, Geological Society of America, 1966

Notes on Table 6.7 (ref. (105) Morey Glass handbook)

Strain point is the temperature at which the viscosity
$= 10^{14.5}$ poise and the stress is relieved in
a reasonable time, i.e. hours.

Transformation temperature = temperature at which glass has
viscosity of 10^{18} poise.

$\left\{\begin{array}{l}\text{Softening point} \\ \text{annealing point} \\ \text{melting point}\end{array}\right.$ = the temperature at which the viscosity is
approximately $10^{12.2}$ poise and glass sags under
its own weight.

Melting temperature = the temperature at which the viscosity
is 10^2 poise and the glass is fluid enough to
pour and cast.

It should be noted that for this study the precise values of these properties, the most important of which is the thermal diffusivity, are not required; hence the manufacturer's values, being in good agreement with those found in the literature,are sufficient.

However, a deceptively simple technique for checking the thermal diffusivity of the precise glass used was available. The technique was that of flash diffusivity measurement described by Susumu Namba et al[106] with the theory developed by Parker et al[107] and subsequently amplified for small diameter disc sources by Donaldson[108].

The theory is described in Appendix 6. The apparatus is shown in the figure (6.23)
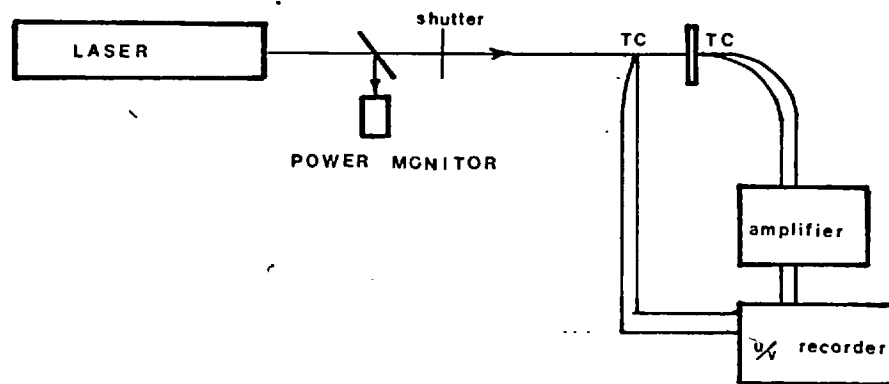
Figure 6.23   Experimental arrangement for the flash
               method of measuring the thermal diffusivity

The experimental procedure was:-

1) Fix a thermocouple with sellotape to the back surface of the substrate to be examined, ensure a good thermal contact between the thermocouple and substrate by a small dab of silver paint.

2) Place a second thermocouple immediately in front of the substrate, but not touching, and in the line of the beam.

3) Attach both thermcouples to a U/V recorder, the back face thermocouple being attached via a 5000X amplifier.

4) Fire a short pulse of 10.6μ radiation at the substrate. The time must be short enough that it is small compared to the time taken by the heat to pass through the substrate, but long enough to give a signal.

5) Note the time to rise to $\frac{1}{2}$ full value $t_{\frac{1}{2}}$ and the three values of t_x and the value of t_f - see diagram of actual trace from a Chance Propper microscope slide (figure 6.24)

6) Calculate diffusivity, as from Appendix 6 in which it is shown that:-

$$\alpha = \frac{1.38 \ L^2}{\pi^2 \ t_{\frac{1}{2}}} \qquad\qquad D1$$

$$\text{or} \qquad \alpha = \frac{0.48 \ L^2}{\pi^2 \ t_x} . \qquad\qquad D2$$

$$\text{or} \qquad \alpha = \frac{0.40 \ L^2}{\pi^2 \ t_F} \qquad\qquad D3$$

The results for the substrates used are shown in table 6.8. The values obtained from $t_{x_{finish}}$ using equation D2 and t_F using equation D3 are in fair agreement with the literature value. However there is an unpleasant ambiguity as to which value of t_x it is fair to take. Theoretically the input pulse should be instantaneous and so the problem should not arise. Practically by this method, the value of $t_{x_{finish}}$ dwindles to zero or even negative with long pulses on brass samples which makes a nonsense of the most successful value.

Material	Thickness cm	Chart Speed mm/s	Pulse Time s	t_x start s	t_x mean s	t_x finish s	$t_{\frac{1}{2}}$ s	t_F s	α_{tx} finish cm^2/s	$\alpha_{t_{\frac{1}{2}}}$ cm^2/s	α_{t_F} cm^2/s
Microslide	.1205	75	.16	.28±.02	.20±.02	.12±.02	1.61±.05	.10±.02	.0059±.001	.00216	.0058±.001
"	"	"	.215	.33±.04	.24±.04	.13±.04	1.34±.05	.12±.06	.0054±.002	.00152	.0049±.0025
"	"	"	.33	.44±.04	.29±.04	.13±.04		.12±.04	.0054±.002		.0049±.002
"	"	"	.60	.66±.05	~ .32 peak off chart	.20		.13±.04	.0035±.003		.0045±.002
Chance–Propper Slide	.129	400	.18	.28±.02	.20±.02	.134±.02	.515±.03	.11±.01	.0060±.001	.0045	.0061±.0006
"	"	75	.13	.28±.02	.20±.02	.135±.02	.56±.04	.12±.01	.0060±.001	.0041	.0056+.0006
Silica Spectrosil	.128	75	.16	.24±.02	.16±.02	.10±.02	.96±.2	.08±.02	.0084±.002	.00237 ±.002	.0083±.0016
	.128	400	.087	.185	.145	.10	.975	too poor trace	.0084±.002	.00233	--

Table 6.8

Flash Diffusivity Results

Fig 6.24 Tracing of chart record
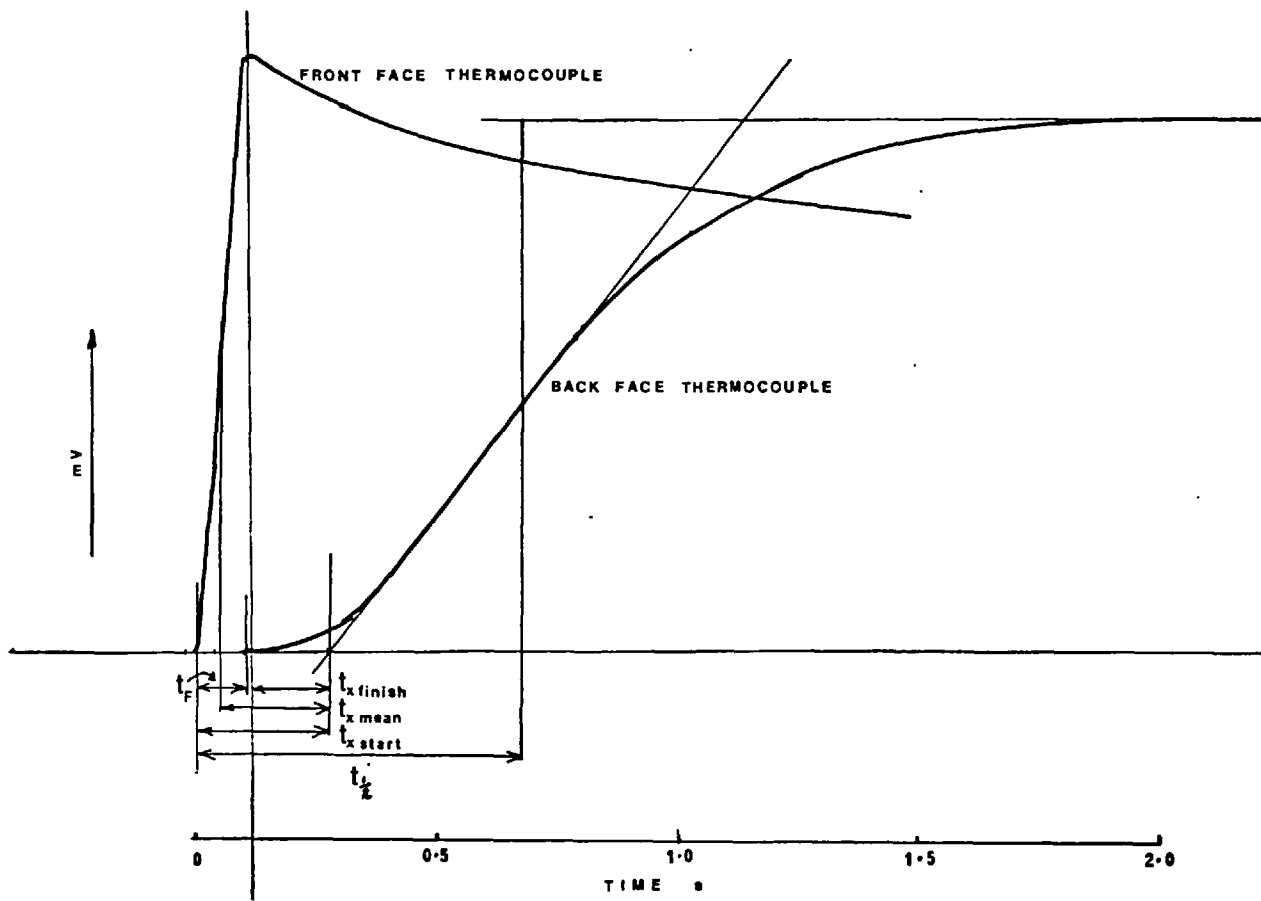
To overcome this problem of the finite duration of a pulse, which was necessary for an adequate signal, the equations for t_F were calculated as discussed in the Appendix 6. t_F successfully gave reasonable readings for brass, but the measurements were too small to be very accurate.

An alternative was tried using the 100 ns 25kW pulse from a YAG laser. Since glass is transparent to the 1.06μ radiation from the YAG laser the surface was coated with carbon black. This attempt failed for three reasons:-

a) Insufficient power was available, even at 2.5 J/pulse to give a reasonable signal using the Southern Instruments U/V recorder and a 5000X amplifier.
Namba et al used a 1ms 2 joule pulse (2kW) so the pulse should have been adequate and the problem may have been in the amplifier.

b) Interference between the acousto-optic Q switch RF circuit and the amplifier led to a poor signal and limited the possible amplification.

c) The carbon black coating could have given erroneous readings.

In conclusion very strong pulses are most suited to this technique but it is possible to obtain approximate values from the t_F readings.

Apart from introducing the concept of t_F into this technique this work had a further advantage in that it showed that the microslide and heat resistant Chance slides were very similar, a fact subsequently corroborated by the supplier.

Conclusion

The experimental values being in reasonable agreement with the literature value, the latter were taken.

The values used in the calculations were:-

	Density g/cm^3	Thermal Cond: J/cm ^{o}Cs	Spec ht J/g ^{o}C	Thermal Diffusivity cm^2/s
Glass	2.5	8.28x10^{-3}	0.5	0.0066
Silica (Spectrosil)	2.2	13.8x10^{-3}	0.75	0.0083

6.3.3.2 Transmissivity

By recording simultaneously the output from a thermocouple placed in front of the substrate and one place behind the substrate when a 10.6μ laser beam passes down the line between them - as in the thermal diffusivity experiments - it was observed that no radiation passed through a 1.2mm thickness of glass - see figure (6.24).
This is in agreement with the extrapolated % transmission of glass and quartz quoted in the literature[103] and shown in figure 6.25.
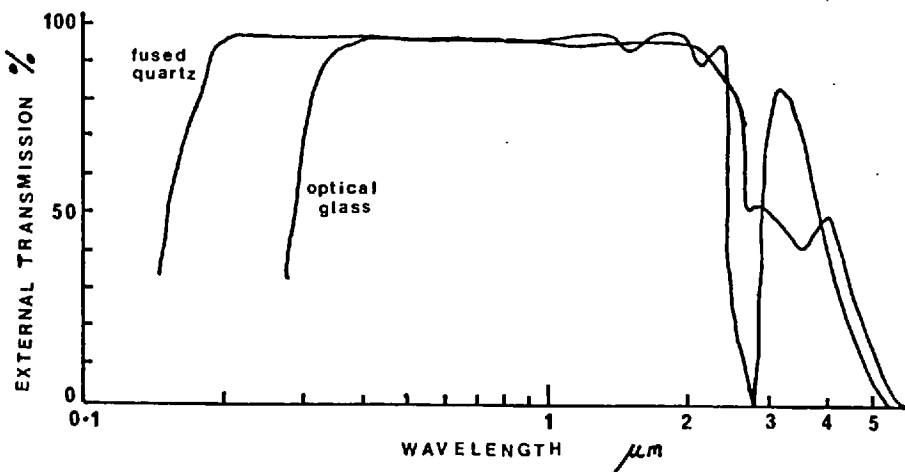
Figure 6.25   % transmission through a 2mm thick slab
as a function incident wavelength (103)

6.3.3.3 Surface Reflectivity

The surface reflectivity of glass and quartz to 10.6μ radiation for varying angle of incidence was measured. The incident power was measured by a thermopile, B, (figure 6.26) placed in the direct beam stopped down by an aperture. The thermopile, B, reading was correlated with the reading of the monitor thermopile, A. The thermopile, B, was then moved so that it received the reflected radiant power from a sample of the substrate. Thus the reading from thermopile, A, gave the thermopile, B, reading of the incident power via the correlation. The ratio of this reading to the reflected power reading also measured on thermopile B gave the fraction of power reflected or the reflectivity. The experiment was repeated for various powers and angles of incidence.
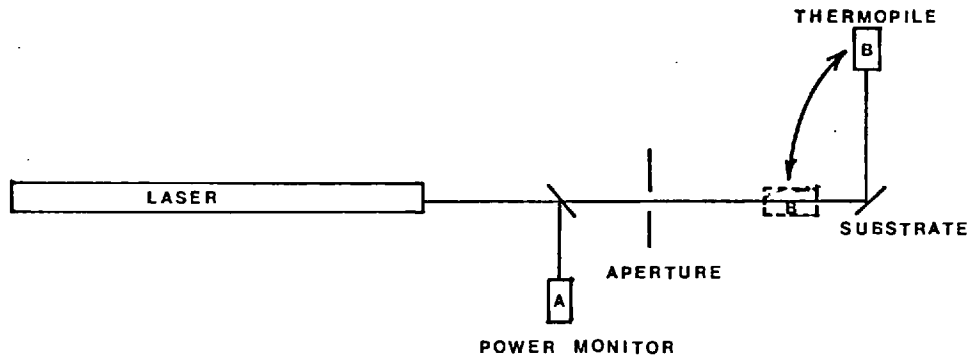
Figure 6.26 Experimental arrangement for measuring
reflectivity to 10.6μ radiation

The results are shown in graph fig 6.27 . The reflectivity as expected[103] increases at large angles of incidence.

Some dependence of the reflectivity on substrate temperature might be expected. In that Bramson[109] gives the expression -

$$r_f(T) = 0.365 \ (\frac{\mathcal{C}(T)}{\lambda})^{\frac{1}{2}} - 0.0677(\frac{\mathcal{C}(T)}{\lambda}) + 0.006 \ (\frac{\mathcal{C}(T)}{\lambda})^{3/2}$$

Fig 6.27   Variation of substrate reflectivity

to   10·6 μ radiation

with angle of incidence
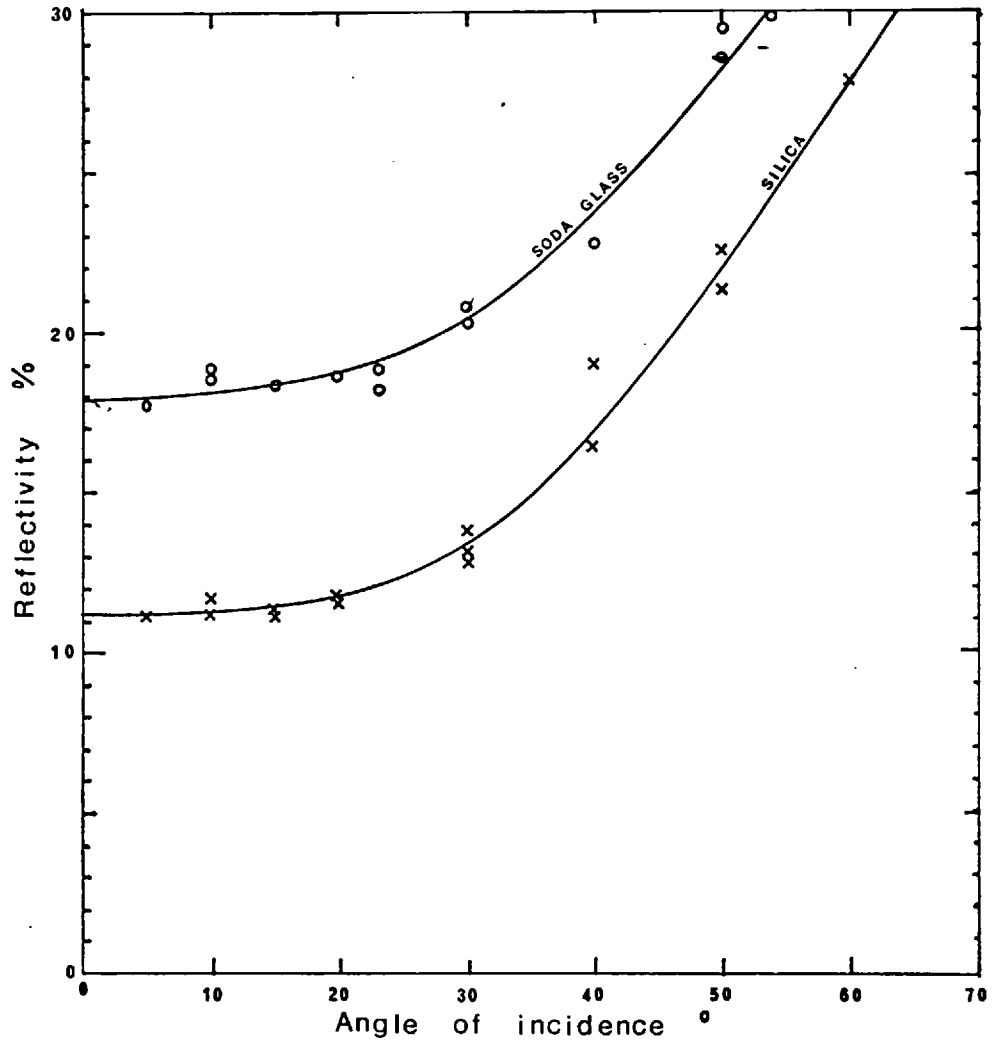
where: $r_f(T)$ = reflectivity

$\rho(T)$ = resistivity

λ = wavelength

This represents a very small to negligible effect for the temperature experienced, and no variation in reflectivity was noted with incident laser power – below the thermal damage level.

6.3.4 Deposit parameters

6.3.4.1 Thickness

The cobalt oxide deposits did not in all cases produce self profiling colour fringes as Davies[41] found for his deposits of CoO on copper. So alternative methods had to be devised.

These were:

    a) A interferometric method

    b) Talysurf

    c) Colour fringe measurements

    d) Holography

These are now discussed in sequence.

6.3.4.1.1. Double beam interferometric method

Various optical interference methods are available for measuring surface shapes. They are reviewed by F. Herzog[110].

The double beam method described here has the advantage of simplicity of operation, but the disadvantage of complexity of interpretation. The interpretation problem was   solved and hence this technique could be and was used.

The optical arrangement is shown in the schematic diagram.
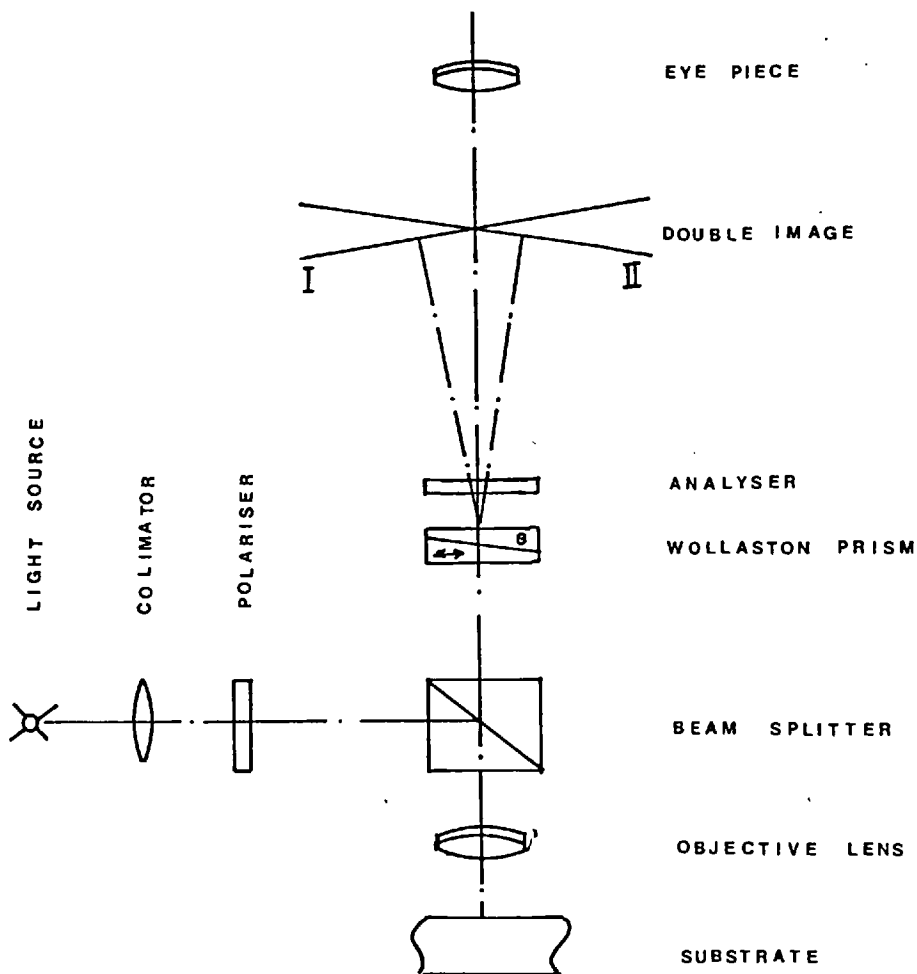
Fig 6.28   Optical   arrangement   for   double   beam
interference

The Wollaston prism designed by Normanski consists of two wedge shaped parts of a crystalline quartz which have the same thickness at the centre and which are cemented together to form a parallel plate. The optical axis in the two prisms are perpendicular to each other. If a linearly polarised beam of monochromatic light falls on the undersurface of the Wollaston prism such that the plane of polarisation is $45°$ to the optic axis of the prism the beam is split symmetrically due to the optical properties of the crystal' into two separate beams which are linearly polarised perpendicular to each other and whose axis are inclined at an angle 'ε' to each other. The angle ε is related to the prism angle α by the equations $\varepsilon = 0.0182 \tan \alpha$. A further polarisation filter with the plane of polarisation perpendicular to the polariser allows the intensity of the two light beams to be so controlled that they interfere with each other noticeably.

The monochromatic light required for clear interference pictures was made by placing a sodium filter in front of a tungsten lamp. Shear images such as plate 3 are produced.

The interpretation of these images is complex due to the overlapping of the images, and the author's understanding of the beam optics as described by Herzog[110]. From the optical arrangment, figure 6.28, it would appear that all the deposits are hollows, and not mounds, as described in figure 6.29. Such an image inversion is possible if the strongest multiple reflection comes from the substrate/film interface and not the film/air interface. This is discussed by Hill[111]. However gold plating the sample gave no change in the shear image, so this elaborate explanation was not the cause.

The talysurf record gave indisputable proof that the deposits were mounds of various shapes and thus the sense of the interpretation suggested in figure 6.29 is wrong for the optic system of the Reichard microscope used.

INTERFEROGRAM

SHEARED DOUBLE IMAGE
OF A SMALL HOLLOW
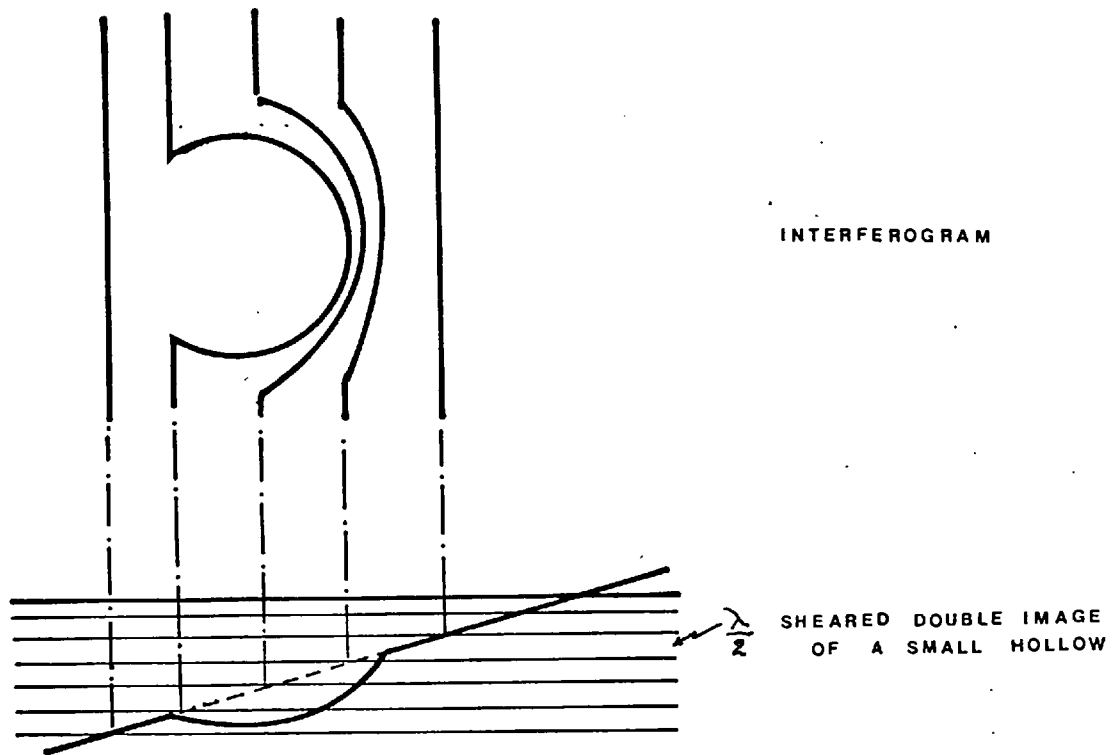
Figure 6.29   Interpretation of shear images according to the
optical path described by Herzog (110) illustrated
in figure 6.28

The interpretation of the interferograms was as follows:

a) Draw lines along fringes to show the undisturbed position

b) Draw line of shear passing through peak of deposit

c) Measure, from dust or characteristic mark, the shear
distance.

d) Measure displacement on shear line of first fringe displaced.

e) Move up from fringe (d) towards the peak centre along the
shear line the shear distance.

f) Estimate displacement at this point and add to displacement
measured in (c).

g) Continue in this manner until deposit centre is reached.

Plate 3   illustrates this.

SHEAR DISTANCE

DIRECTION OF SHEAR
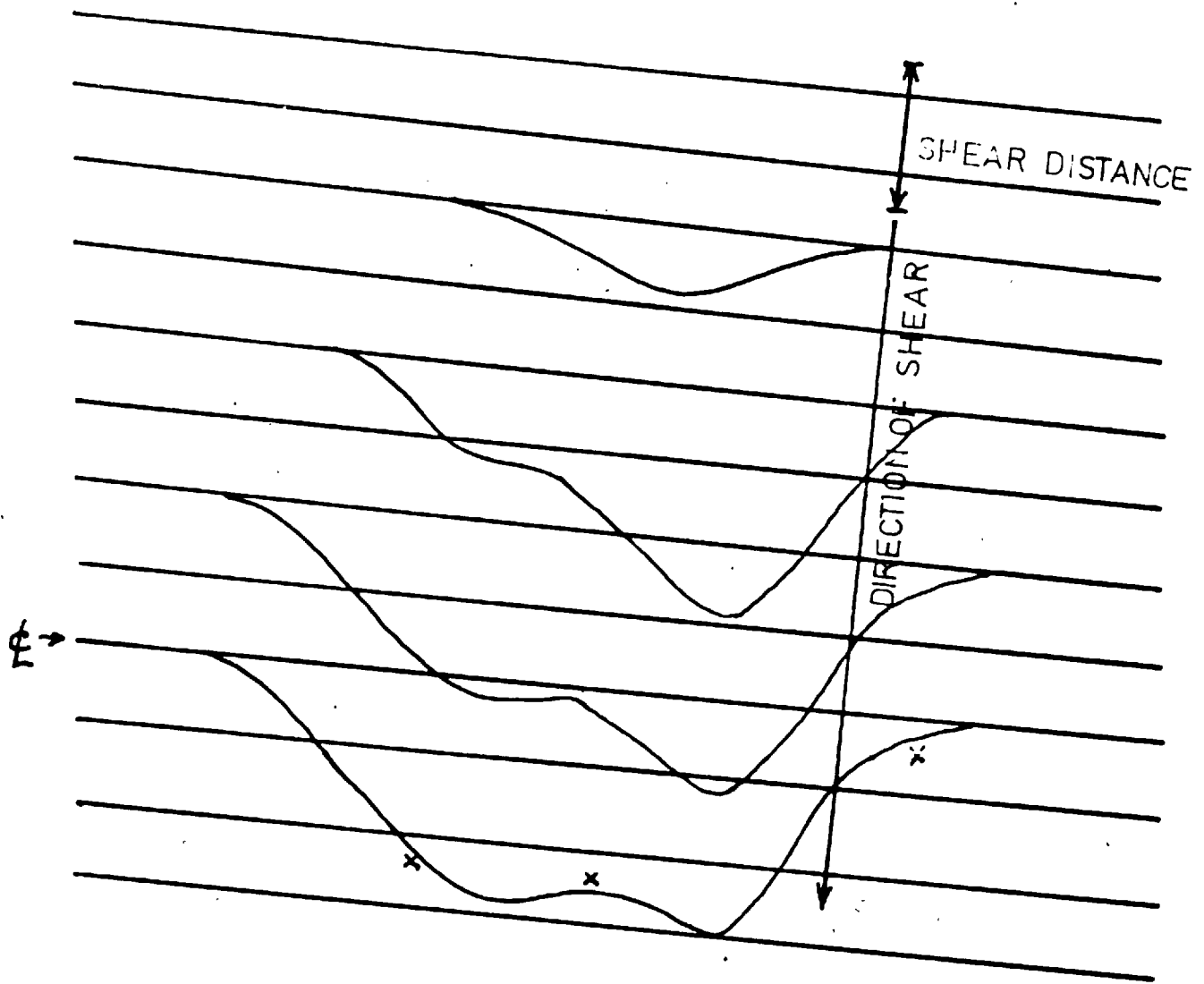
✗ Talysurf reading

Maximum displacement
= 3·3 fringes = 0·97 μ

PLATE 3: THE METHOD OF INTERPRETING THE
SHEAR IMAGES — SAMPLE D22

The fringe system observed is due to the interference between
the two sheared images, as illustrated in figure 6.29.   Thus if
a higher order fringe cuts across the undisturbed line of a lower
order fringe then the substrate surface has risen by a depth of
$\lambda/2$ at that point relative to a point on the surface of the
substrate one shear distance away.

In the example plate 3 it is estimated that the maximum displacement
at the mound peak is 3.3 fringes.   Thus the height of the mound
is

$$3.3 \ \times \ \frac{\lambda}{2} = 0.97 \ \mu$$

since λ for sodium light is 5890 $\overset{\circ}{A}$.

It was usually possible to check this tedious estimation against
a talysurf reading, or even a colour fringe value.   The expected
error of this method varied with the quality of fringe system.
If as in plate 3 it would be of the order of $\pm\frac{1}{2}$ fringe $\simeq .1\mu$.

PLATE 3: THE METHOD OF INTERPRETING THE
SHEAR IMAGES — SAMPLE D22

The fringe system observed is due to the interference between
the two sheared images, as illustrated in figure 6.29. Thus if
a higher order fringe cuts across the undisturbed line of a lower
order fringe then the substrate surface has risen by a depth of
$\lambda/2$ at that point relative to a point on the surface of the
substrate one shear distance away.

In the example plate 3 it is estimated that the maximum displacement
at the mound peak is 3.3 fringes. Thus the height of the mound
is

$$3.3 \times \frac{\lambda}{2} = 0.97 \ \mu$$

since λ for sodium light is 5890°A

It was usually possible to check this tedious estimation against
a talysurf reading, or even a colour fringe value. The expected
error of this method varied with the quality of fringe system.
If as in plate 3 it would be of the order of $\pm\frac{1}{2}$ fringe $\approx$ .1μ.

6.3.4.1.2 <u>Talysurf</u>

A model 3 'Talysurf' surface measuring instrument was also used to measure the surface profile of the deposits. This instrument operates by traversing a sharply pointed diamond pyramid stylus across the surface. The up and down movement of the stylus relative to a trailing flat tungsten carbide skid is converted into a corresponding change in an electric current by a variable inductance unit. This current is amplified and used to control a rectilinear plotter using a spark marking system operating at 600 volts D.C. The magnifications of $2-0.04\mu/$ scale divisions are possible. A typical trace is shown in figure 6.30. The sense of the talysurf was checked on an engraved plate, trace 1. The procedure was as follows:

i) The skid was carefully adjusted to be parallel with the surface. Failure to do this meant that comparison was being made with a point on the surface as opposed to a mean surface level, giving erratic results. (Figure 6.30, trace 2).

ii) The sample was carefully cleaned, by wiping with ethyl alcohol and lined up on the line of travel of the stylus. If the chelate condensate was not removed this affected the comparator reading on the skid making interpretation very difficult.

iii) Suitable magnification selected.

iv) Traverse made

Most traces were straight forward to interpret. The magnifications available were x1000, x2000, x5000, x10,000, x20,000, x50,000, when each division on the chart paper was equivalent to 2.5μ, 1.25μ, 0.5μ, 0.25μ, 0.125μ, 0.05μ. The main source of error was due to missing the centre of the deposit with the traverse. This was particularly so for the G series in which the deposits were very small. But even if this happened a reading was usually recorded by the skid trace passing over the deposit. This was found to be comparable to that given by the stylus when the stylus was properly aligned (figure 6.30, trace4).

FIG 6.30 Operation of the Talysurf

TRACE 1

Engraved glass
surface showing the
direction of a signal
for a **depression**

1 division = 0.5μ

SURFACE

TRACE 2

Showing effect of
poorly adjusted **skid**

stylus   skid

1 division = 0.5μ

Sample B19

TRACE 3

A correctly adjusted
skid

stylus   skid

1 division = 0.5μ

Sample B19

stylus   skid

TRACE 4

Showing **that even if**
the stylus should miss
the deposit a reading
may be given by the
skid.

1 division = 0.5μ

Sample D7

The accuracy of this method depends on two features:

a) Whether the specimen was traversed centrally

and

b) Whether the skid was resting on the original substrate surface.

Point (a) was known by a comparison of stylus rise and skid fall traces.

Point (b) was estimated from the trace smoothness.

For a good trace, as in D25 (Plate 7) the estimated error is of the order of ± 1 division i.e. ± 0.25μ.

6.3.4.1.3 Colour Fringes

Those deposits which showed colour fringes were photographed on the Reichart microscope by illumination from a mercury vapour lamp incident normal to the specimen surface.

An example is shown in plate 8

The deposit thickness in the fringe region can be calculated from interference theory.
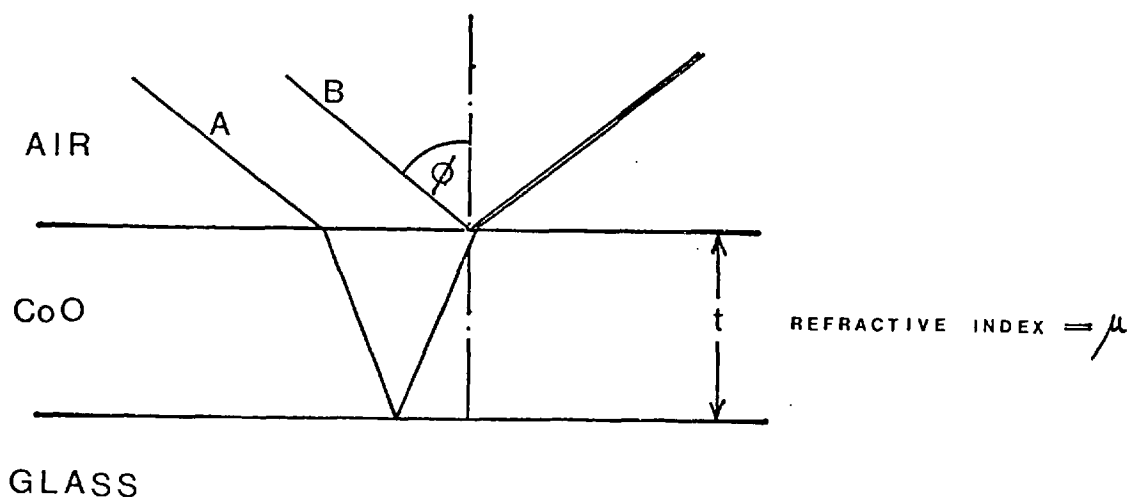
Figure 6.31 Ray diagram showing thin film interference

The optical path difference between ray A, which undergoes refraction through the transparent CoO, and reflection at the glass/CoO interface and ray B, which is reflected from the surface of the CoO layer is equal to $2\mu t \cos \emptyset$.

Ray A has also undergone a reflection at the CoO/glass interface which introduces a π phase change.

Thus for constructive interference between ray A and B

$$2\mu t \cos \emptyset = (n + \tfrac{1}{2})\lambda$$

where n is an integer from zero.

However due to the similarity of the refractive indices of CoO and glass (1.7 and 1.5 respectively) the π phase change will be affected by a small amount θ.

Thus now:-

$$2\mu t \cos \emptyset = (n + \tfrac{1}{2} + \theta)\lambda$$

For normal incidence, as used here, $\cos \emptyset = 1$ and so

$$2\mu t = (n + \tfrac{1}{2} + \theta)\lambda$$

The values for: λ for Hg vapour light, were taken from the standard tables

n was found from a count of the fringe system

μ for CoO, was taken 1.73 ± 0.15 from Davies (41) who measured it by a Brewster angle method.

θ was found by observing that the red band of first order spectrum coincides with the violet band of the second order spectrum: Thus:

$$(n + \tfrac{1}{2} + \theta)\lambda_{red} = (n + 1\tfrac{1}{2} + \theta)\lambda_{violet}$$

for n = 1 and θ = -0.085 $\therefore$ t = $(n + 0.415)\lambda/3.46$

from which table 6.9 was drawn up.

Table 6.9

Showing Deposit Thickness in °A
At Different Order Colour Fringes

n/λ	Violet	Green	Yellow	Red
0	486	655	693	829
1	1655	2233	2364	2825
2	2825	3811	4034	4821
3	3994	5389	5705	6817
4	5164	6968	7375	8813
5	6334	8545	9046	10810

Interpretation of the higher order fringes was difficult due to the overlapping of the different coloured systems. Even so this method gave a useful check on the depth readings obtained from methods (a) and (b) for samples which had not undergone serious diffusion.

The estimated accuracy was a function of fringe order and was around 10%. It was rare to obtain a central reading this way, due to the blurring of the central fringes by diffusion or masking by black centres or craters.

6.3.4.1.4.   Holography

Holographic interferometry   (113) offered the possiblity of observing, and measuring the growth of a deposit with time. If that could be done a great deal would be learnt about the growth mechanism of these deposits.

Initial experiments were performed to obtain holograms. Special fine grained film sensitive to 6328°A radiation (SCIENTIA 10E 70)

was used. The technique is discussed further in the author's
paper (114). Holograms of various objects were obtained in
this way. However, it was decided that the results were not
clear enough, the procedure too complicated, and the chance of
success on growing deposits slender. The reason for the last'
criticism was the private communication from A. Ennos (NPL) who
showed the author a holographic interference photograph of a
corrosion pit. No fringes were visible in the pit because of
the lack of point to point correspondence between the interfering
surfaces.

Summary on methods of measuring thickness

The agreement between the double beam interferograms, the
talysurf and the colour fringe methods of thickness measurement
was well within the expected experimental error ($\simeq \pm$ 10%).

So all three methods were used since some specimens were more
suited to one technique and some to another. Plates 7 and 8 show a
comparison of the three techniques in one sample.

There is, of course, the possibility that the glass had
moved and so what is being measured is thermal distortion and
not the deposit thickness. This error is not likely to be found
in the colour fringe readings, (PLATE 10) since they are a direct reading
of film thickness but unfortunately not all deposits showed good
colour fringes probably due to diffusion into the glass. The
correlation between colour fringes and the other methods for
low (P/D_b) deposits was good. Hence, thermal distortion for
lower values of P/D_b (< 12 W/cm) was considered unlikely. For
higher values there was obvious distortion shown by cratering.
To try and measure the deposit thickness, inspite of this, some
samples were photographed from beneath using the double beam inter-
ference method. The pictures àgain showed the deposit surface,
but inverted. No noticeable reflection occurred at the glass/CoO
surface for light coming from the glass side.

Thus 'thickness' measurements at high values of (P/D_b) almost
certainly contain an element of thermal distortion.

6.3.4.2 Area and Shape

6.3.4.2.1 Diameters

When printing the image of a circular aperture circular deposits were formed. The diameters of these deposits were measured using a Pye Unican two dimensional microscope 6147/M and double checked on a conventional Olympus microscope with a cm scale in the eyepiece.

Four different diameters were observed and recorded:
(a) "Outer diameter" of the edge of very thin skirt region
(b) "Inner diameter" of the edge of the bulk of the deposit
(c) "Burnt diameter" of the edge of central black zone
(d) "Blue diameter" of the edge of central blue zone.

The accuracy of these readings depended upon the definition of the edge of each zone and the circularity of the deposits. An average estimated figure being $\pm$ 5%.

The outer diameter is identified as the outer extent of the deposit which exhibits superior reflection to white light or superior absorption to transmitted white light. It is closely, if not precisely, the physical limit of the deposit.

The inner diameter is identified as the radial location within the spot at which the deposit thickness starts to grow quite abruptly.

The 'burnt' diameter is identified as a centrally placed dark black zone.

6.3.4.2.2. Area

An attempt to overcome the inaccuracies due to the irregular nature of some of the deposits was made by measuring the area directly on the Quantimet QTM (102, 115) and then back calculating to obtain a mean diameter.

The Quantimet is an instrument of considerable potential in mineral analysis. However, on these samples viewed both by transmitted and reflected light (transmitted was preferred), spurious effects were noted. For example, in regions showing a

good colour fringe pattern alternate dark and bright
rings would show on the Quantimet screen with the consequence
that only the dark rings would count in the deposit area.
Similarly, all cracks were recorded as though they were deposits,
and only the thicker parts of thin deposits were recorded. In
particular, "outer diameters" could rarely be measured, and
perhaps most disconcerting, the amount of "outer diameter" measured
varied with the contrast setting on the Quantimet screen.

The correlation between the Quantimet and the travelling
microscope was not satisfactory these measurements were ignored.

6.3.4.3. Radial position relative to jet axis

Where the hot vapour of the jet struck the substrate there
was usually an area free of condensed chelate. The centre of this
area was considered to be the jet axis. The distance of the
deposit centre from this point was measured by a travelling micro-
scope and recorded as the radial location of the deposit.

The accuracy depended mainly on establishing the centre of
the condense free zone and is estimated at $\pm$ 1mm.

6.3.4.4 Reflectivity of Deposits

Method of measurement

The reflectivity of the deposit surfaces was measured in the
same way as was the substrate reflectivity. The added difficulty of
locating the small deposit with the narrow invisible 10.6μ beam
was overcome by careful alignment with a red marker beam. The I.R
beam was stopped down by an aperture and lens so that it was small
enough to be totally reflected from only the deposit without
damaging it.

The results

The results are shown in table 6.10. Only a few deposits
were large enough to reliably accommodate the beam.

For thin shiny deposits, no significant increase in reflectivity
was observed; though one sample had a 3-4% increase in one location

Sample	Laser Incident Power Relative Units	Reflected Power from deposit Relative Units	Reflected Power from substrate Relative Units	Relative Reflectivity $\left[\dfrac{\text{Deposit}}{\text{Substrate}}\right]$	Reflectivity,
Thin shiny films					
17	59.7	13.7		1.20	.23
- substrate	62.1		12.0		.19
17	65.6	12.5		1.08	.19
"	64.2		11.5		.179
19	72	12.9		.99	.18
"	69		12.3		.179
18	59.7	11.0		1.01	.185
"	64.2		11.7		.182
Mound showing colour fringes 17B	53	8.0		.85	.150
substrate	56		9.9		.175

Table 6.10

Deposit Reflectivities

not found in an alternative location on the same deposit.

A deposit showing fringes gave a reliable drop in reflectivity of around 3%. This was not due to optical scatter or surface warping since the red marker beam was reflected without aberration.

There was no black spot large enough to be measured.

Discussion

The reflectivity would be expected to vary with deposit thickness and surface structure.

D. Hacman (ref. 116) reports the application of reflectivity measurements to the continuous monitoring of metal film thickness during deposition. His work shows how the reflectivity of different metals varies with thickness rising steeply with increasing thickness up to some $300^{\circ}A$ after which a fairly steady value was obtained.

The results collated from the literature and confirmed by Hacman's own work are to quote Hacman, subject to "production conditions"

However, after 0.05μ thickness the overriding effect would be expected to be the "production conditions" or infact the deposit surface structure.

It appears that CoO deposits on glass show no rise in reflectivity with increasing thickness up to $\sim 0.1\mu$ after which the reflectivity falls by some 3-4% as mound growth takes place up to $\sim 1.0\mu$. At greater thicknesses the precise surface formation is crucial in deciding the reflectivity. In particular, black centres would be expected to show a large fall in reflectivity due to the observed roughness of the surface.

6.3.4.5 Composition

The pyrolysis of cobalt acetyl acetonate in an inert or reducing atmosphere should result in the deposition of cobalt with the evolution of acetyl acetone and other organic compounds, including carbon as found by Jablonowski (85):

$$Co(C_5H_7O_2)_2 + H_2 \longrightarrow Co + 2C_5H_8O_2$$

$$Co(C_5H_7O_2)_2 \longrightarrow Co + C_5H_8O_2 + 2C + C_3H_6O + H_2O \quad \text{etc.}$$
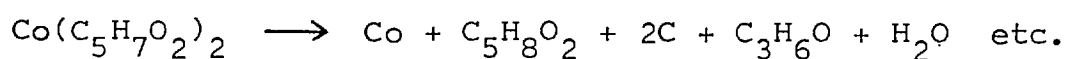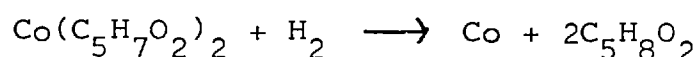
In the present work there was a small partial pressure of oxygen in the deposition zone due to entrainment of the surrounding atmosphere by the jet. Accordingly, the finely divided and very reactive cobalt film deposited would be expected to be oxidised, as found by Davies (41). (Davies found this to be so for oxygen partial pressures as low as 5×10^{-4} atmos. in a basically reducing atmosphere of hydrogen).

The transparency of the deposits required to reveal the colour finges observed was far greater than would be possible if the deposits were made of cobalt metal.

The electrical resistivity of the deposits was found to be approximately infinite as expected for cobalt oxide but not cobalt metal.

Accordingly, it was concluded that the deposits were made of a cobalt oxide. Cobalt produces three oxides, CoO, Co_3O_4 and $Co_2O_3 \cdot H_2O$, the latter existing only as a monohydrate which decomposes at $300^{\circ}C$. . Most deposits were formed at higher temperature than $300^{\circ}C$ and so $Co_2O_3 \cdot H_2O$ is ruled out as a possibility.

Electron probe analysis of the deposits indicated the presence of cobalt and oxygen in the deposit — the oxygen count rate being higher on the deposit than that on the surrounding glass ruled out the possiblity of this reading being a background from the glass showing under the thin film — the films were too thin to allow the determination of an accurate value of Co/O ratio.

X-ray diffraction to elucidate the crystal structure and thus find which oxide also failed. The x-ray diffraction was arranged to be done by forward reflection to limit the depth of penetration. No discernable diffraction pattern was given, suggesting the crystallites, if any, had not developed to a sufficient size.

The deposits were also too small for accurate chemical analysis. Infact any chemical analysis to determine the Co/O ratio would be complicated by the ability of both CoO and Co_3O_4 to absorb oxygen into their molecular lattice, in the case of CoO this can occur even

at room temperature. (.73). . Spot analysis showed that thin deposits dissolved readily in dilute nitric or sulphuric acid as expected for all cobalt oxides (26).

However, thicker deposits could not be dissolved in boiling nitric acid (the skirt region dissolved readily). This suggested that the more severe heating required for thicker deposits allowed some diffusion into the glass.

Thermodynamic data is available for CoO and Co_3O_4 formation (41); for

$$2Co + O_2 = 2CoO$$
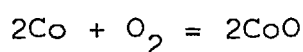
$$\Delta G_T^O = - RT \log_e(p_{O_2}) = -113,820 + 1.38T \log_{10}T + 32.06T$$

and

$$\frac{3}{2} Co + O_2 = \frac{1}{2} Co_3O_4$$
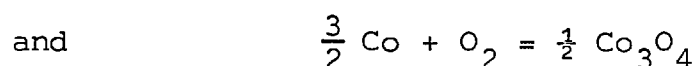
$$\Delta G_T^O = -RT \log_e(p_{O_2}) = -103,650 - 1.15T \log_{10}T + 45.28T$$

Since the Co/Co_3O_4 equilibrium ΔG_T^O is always less negative than the Co/CoO the production of Co_3O_4 directly from cobalt is not possible and so Co_3O_4 would be produced only via the monoxide CoO.

The oxygen potential diagram (figure 6.32) suggests that this subsequent oxidation would take place since the CoO/Co_3O_4 line lies below the oxygen potential line for oxygen partial pressures greater than 5×10^{-4} atmospheres – a partial pressure considered reasonable for the jet/plate distances used.

Whether this predicted equilibrium event occurs or not depends to a certain extent on reaction kinetics, and the precise oxygen partial pressure. Davies (41) found this prediction did not occur possibly due to the slower formation of Co_3O_4.

There is also the effect, if any, of the glass lattice on the equilibrium for these thin films, some possible diffusion having already been noted.

Fig 6·32 <u>OXYGEN POTENTIAL DIAGRAM</u>
<u>FOR THE CoO DEPOSITION</u>
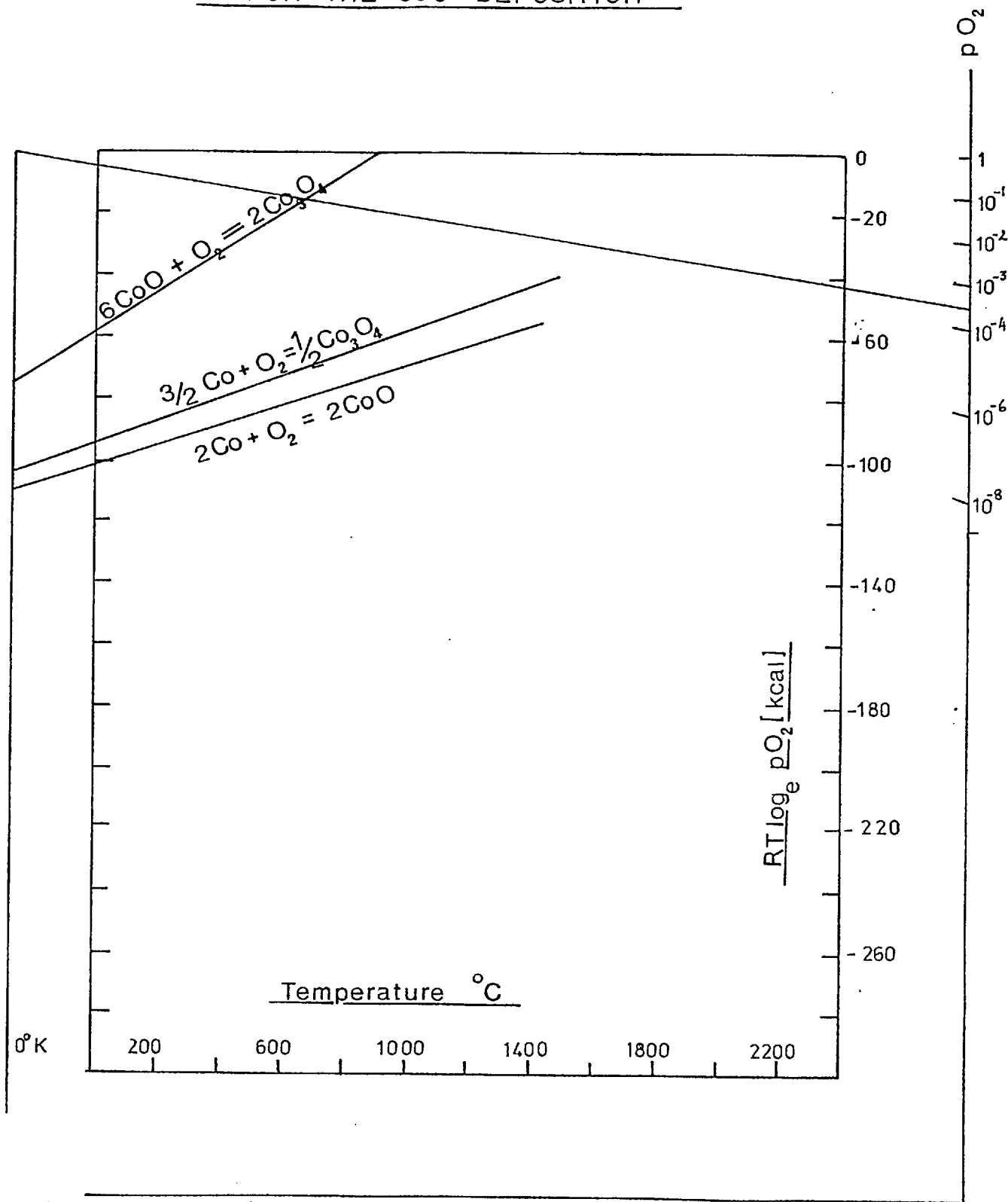
Fortunately for this study the fact that theCo/O ratio is of the order of 1:1 or 3:4 is adequate information.

A possibility exists, however, that the deposit is chemically inhomogeneous, having a variable Co/O ratio across the surface, due to variations in temperature across the surface. If this is so, then inhomogeneous optical properties might be expected. Brewster angle measurements with polarised light and analyser did not show any variation of refractive index across the surface, implying the deposits were homogeneous or the difference optically between CoO and Co_3O_4 were not discernible.

In conclusion, it was considered that the deposits were composed of CoO or Co_3O_4. The exact oxide could not be determined though the indications favoured CoO. The deposits formed at higher temperatures showed signs of some interdiffusion with the glass substrate.

6.3.4.6. Temperature During Deposition

Deposit temperatures during deposition were measured by a Thermodot TD17 infra-red thermometer mounted on an x-y table as shown in plate (1).

The signal recorded was a function of the radiant power entering the objective lens of the IR thermometer in the $2.15 - 2.25\mu$ wave band. All 10.6μ radiation was filtered out, thus avoiding errors due to diffuse reflections. (massive reflection of 10.6μ radiation into the objective lens would heat up the lens, giving an erroneous reading).

The target from which this radiation came could be seen in the eye piece, its size ($\sim 1.0mm$ x $1.0mm$) is discussed on page 174.

The accuracy of this instrument was given by the manufacturer as $\pm 6^{\circ}C$ with a response time of 0.3s for 95% full scale deflection. This accuracy is, of course, decreased by uncertainties in the emissivity of the substrate surface. Only relative temperatures were needed in establishing thermal rise times and thermal contours so for these measurements this accuracy problem did not exist.

Indicated temperatures, using an emissivity setting of 1.0, were comparable to expected temperatures.

CHAPTER 7

THE EXPERIMENTAL RESULTS

7.1 <u>Summary</u>

The experiments were arranged as far as possible so that groups of deposits had all controlled parameters constant except for the one being investigated. There were too many parameters for a full orthogonal set of experiments.

The experimental conditions and measurements taken on all rate of deposition deposits are given in appendix 4.

Numerous observations from these results were made.They are discussed in the following sequence:

A) <u>Image formation studies</u> (sections 7.2)

    (i)   Effect of variable object area

    (ii)   Effect of focal position

    (iii)   Effect of a hot aperture

    (iv)   Effect of a non-uniform heating

    (v)   Effect of extended heating

B) <u>Rate of deposition studies</u> (sections 7.3)

    (i)   Deposit structures

    (ii)   Effect of incident power/beam diameter on thickness and extent of deposit

    (iii)   Effect of radial location within jet on thickness and extent of deposit

    (iv)   Variation of thickness and extent with time

    (v)   Effect of Reynold's number

    (vi)   Effect of jet/plate distance

    (vii)   Effect of varying the vapour concentration

    (viii) Effect of varying the jet temperature

    (ix)   The effect of varying the substrate properties

    (x)   The effect of varying the modes from the laser

    (xi)   Temperature profile of the heated spot, profile of deposit

    (xii)   Variation of spot temperature during deposition

FIG 7.1

0·7 cm

CONTACT PRINT
OF APERTURE

4 3 2 1 0 1 2 3 4
DISTANCE FROM MINIMUM SPOT   cm
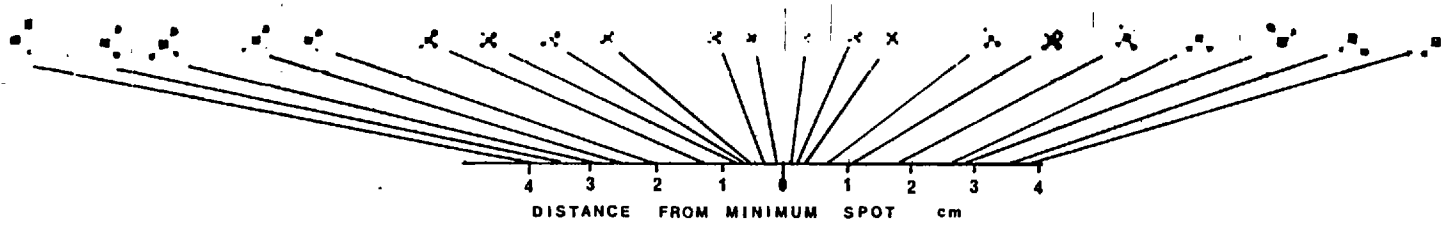
Char prints at various distances from the focus of the 13·7 cm lens

0 1 2 3
DISTANCE FROM MINIMUM SPOT   cm
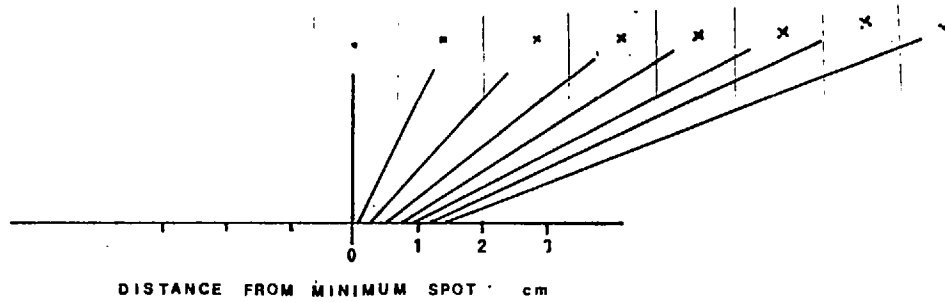
Char prints at various distances from the focus of the 5·3 cm lens

7.2 Image formation studies

Plate 4 show a selection of prints in CoO on glass of the dumbbell cross aperture whose shape is shown in figure 7.1

Plate 4 shows that imaging is possible by this method though the printed image may not be identical in shape to that of the object/aperture.

7.2.1. Effect of variable object area

The larger heated areas become hotter than the smaller areas. Sample AC shows cratering in the larger heat zones, while in sample AK only the larger zones have been printed. In sample AL the thin connecting lines between the end dots are printed relatively thinner than in the original.

7.2.2. Effect of focal position

No detectable effect of focus on image clarity was noticed If such an effect existed it was completely masked by (P/D) effects since the image size also varied with focal position. However the series of char prints figure (7.1) illustrate fairly convincingly that for the parallel beam used a clear heat image existed over most, if not all, the distance behind and in front of the lens.

7.2.3. Effect of a hot aperture

It was noticed that a film deposit formed someway outside the heat image zone at the later stages of a run as in samples AM and AN.

The temperature of the aperture (1mm thick mild steel) at these times was estimated as 150-200°C. It was only air cooled.

It is suggested in section 8.13 that the heat load from the aperture was partly responsible for this blurring of the image.

7.2.4. Effect of non uniform illumination of the aperture

The beam diameter from the laser and diameter of the aperture were comparable. Smaller apertures required higher laser powers than were available to produce a print. Consequently

non uniform illumination of the aperture was common. Char
prints confirmed that the non uniform appearance of, for
example, sample AD and AL was due to the heat image not the
printing.

7.2.5. Effect of extended heating

Most deposits in this section were formed in 1 minute.
Sample AQ, however, was formed in 6 minutes, resulting in a
considerable blurring of the print, particularly in the in curvate
region of the print pattern.

7.3 Rate of Deposition Studies
7.3.1. Deposit Structures

Nearly all the deposits could be considered to belong to
one of five structural groups as is noted against each deposit
in the results shown in appendix 4.   These groups were:

(a)   Flat thin plates less than 0.1μ thick

(b)   Mounds

(c)   Raised horseshoe cracks

(d). Peaks

(e)   Craters

The appearance of each group is now discussed in turn in
the sequence above.

7.3.1.1. Thin Plates

These deposits are thin flat sheets.   When viewed in white
light they are noticeably opaque with a shiny metallic appearance.
They can be divided into two subgroups according to the
appearance of the deposit edge.

7.3.1.1.1. Hazy edged deposits: Example plate 5 (a) and (b)

A scanning electron micrograph of a similar deposit A1 did
not show any surface detail.   It appeared that the deposit
was laid down as a thin plating film and was as featureless
as the conducting gold film required by the SEM technique.

7.3.1.1.2. Clear edged deposits: Example plates 5 (c), (d),(e) & (f).
Scanning electron micrographs of sample F14 show some
surface features . Notably:-

(i) Black dots in the central deposit area

(ii) A "beach" zone some 30-40μ wide also   containing black
dots plus fragments of sheet material.

Sample F14 also shows a lack of overall circularity. This
non circularity was found on several other deposits. When
it occurred it would print reproducibly and show up on char
prints. It is thus considered a feature of the beam mode and
not a feature of the deposit mechanism.

The black dots were found on many other deposits between
the inner and outer diameters, a region considered to have a
temperature between 150-350°C (see discussion secs 8.2.11 & 8.2.2.7)
They did not appear to be holes in the deposit but regions
of poor illumination under the SEM.

7.3.1.2. Mounds

These are round or flat top deposits of over 0.5μ thickness.
When viewed in white light they appear shiny and metallic with
colour fringes. They were more opaque than the thin plates,
and exhibited an inner region surrounded by a 'skirt'. The
inner region was identified by the start of a coloured fringe
system or some other coloration. In many samples the colour
fringes faded in the central region suggesting the deposit had
diffused into the glass substrate. The general shape is shown
in the figure 7.2.
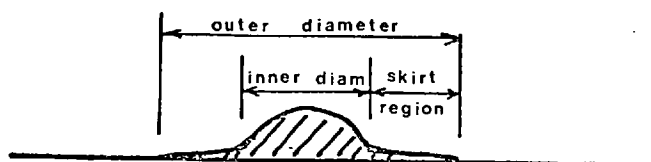
Figure 7.2 Cross-section of a
            'mound' deposit

7.3.1.2.1 (a) and (b) Plates with a small central mound: Example D10
plate. 6 / These feature a "beach" zone and possibly a region
of central roughness.

7.3.1.2.2 Thick flat plates: such as F10,&A2:plates 6(c,d,e,f,g)
The talysurf trace of F10 shows the flat top. The interfero-
gram shows a skirt zone and a clear edge. A scanning electron
micrographs of A2 shows a clear edged, rough central zone
covered in small lumps. This roughness could account for its
black appearance. There is a skirt region, but this does not
show any features, and a"horseshoe" crack, which appears to
have formed on cooling or subsequently since it was not filled
with any deposit.

7.3.1.2.3 Smooth round mounds: Example D25 and B22 plates 7,8 &9
Scanning electron micrographs of D25 show small lumps as
previously found on sample A2. These lumps appear to be of
two types - see plate 7(d) - small and sharp and larger and
less convex. In plate 7(e) some deposit has flaked off exposing
a cross section of a less convex lump and it is seen to be a
blister. However plate 7(f) shows a lump with its top removed
and it appears quite solid. Thus although some lumps are
blisters others may be overgrown sharper lumps which in turn
may have resulted from a nucleation problem. The small sharp
features were only found in the edge zone - i.e. a reduced
temperature zone.

    The SEM general view of B22 shows two "beach" zones (also
exhibited on plate 11 / corresponding to the "inner" and "outer"
diameter previously noted   . The central region
shows a random roughness, unlike that associated with peaking,
(see section 7.3.1.4) lumps were not found. The outer "beach"
zone shows black dots of various sizes and small platelets as
for thin plate deposits.

7.3.1.3 <u>Raised Cracks</u>: Example E1 plate 10.

The vertical edges apparent on talysurf traces of several deposits are due to a partial cone fracture undercutting the deposit.

The crack system is clearly visible from the underside and could hence be seen to have formed both during deposition, and immediately afterwards.

The crack lifts upwards presumably due to residual tensile stresses in the surface (see section 8.2.1.3.1).

7.3.1.4 <u>Peaks</u>: Examples B18, D9 plates 11 and 12

In this series of experiments this was a relatively rare type, possibly due to peaking being converted to cratering for a very small increase in power (see section 8.2.1.2.1 on stress analysis). The group is distinguished by showing relatively sharp peaks on a basic mound shape, and usually a black centre.

Sample D9 talysurf trace shows this quite clearly. The black centre is shown in the interferogram. The SEM pictures (plate 11) show the central peak to be due to a folding of the deposit as though drawn to a point. The roughness of this region (plate 11) would explain its dark appearance. The vertical sides seen on the talysurf are found in SEM plate 11 to be due to cracks, where partial filling is seen to have occurred proving that the raised crack occurred relatively early in the deposition. The mound away from the peak showed the small lump formation previously noted, plate 7 .

plate 12
Sample B18/talysurf trace suggests either a double or triple peak or a peak just dissolving into a crater. The black centre is more distinctive than in sample D9.

SEM photographs show: a craze crack pattern, a double "beach" structure, systematic wrinkles near the peak region (plate 12) and on the central peak region (plates 12) and black dots in certain areas of the outer "beach" zone.

7.3.1.5 <u>Craters</u> . Examples G4, F13 - plates   13,14.

The general structure of a crater is shown in the diagram:
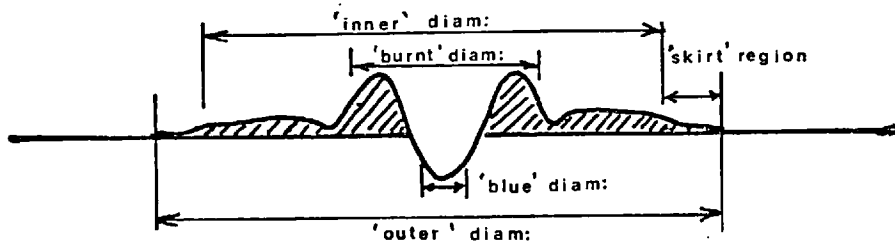
<u>Figure 7.3</u>   Cross section of 'crater'
deposit

The 'crater' or depression below the substrate surface, occurred, in all cases studied, in the centre of a mound or flat plate deposit.   The deposit sometimes having a "beach" zone,which often exhibited black dots   .   The crater bottom and sides were smooth - plate 13(e,f.). In places a small depression on the outer edge of the crater ridge could be seen - plate 13f .   Wrinkling of the deposit, as in the peak structure, was not observed except vaguely on the outer ridge roots - plate 13d .   Some craters exhibited a transparent blue centre,plate.15f.

The crater could be a single symmetric one, as in G4, or it could be lopsided having a ridge on one side only, or it could be peaked in the centre, producing the effect of a double crater as on the talysurf trace of F13 plate 14.

The SEM studies of F13 show it to be a multiple peaked deposit and not of the more fluid appearance of the G4 type crater.   F13 shows strong wrinkling in the central region - plate 14(d,e) and a flat plate formation in the outer region - plate 14f   Extensive cracking can be seen both in the inte :- ferogram and the plate 14(b,d) taken of one of the edge peaks.

PLATE 4

PLATE 4

Image Formation Studies

lens used:-   5.3cm focal length
gas flow rate:-   Re = 1000
jet/plate distance:-   2.54 cm
power measured in relative units (RU)

4(a) Sample AL
power 35-40 RU:
deposition time
1 minute;distance
from lens 5.8 cm

4(b) Sample AC
power:- 40 RU
deposition time: 1 min
distance from lens 5.8cm

4(c) Sample AK
power:- 28 RU
deposition time:
1 minute distance
from lens 5.8 cm

4(d) Sample AD
power:- 25 RU
deposition time: 1 min
distance from lens: 5.8 cm

4(e) Sample AM
power:- 30-35 RU
deposition time:
1 minute, distance
from lens 5.48 cm

4(f) Sample AN
power:- 30-38 RU
deposition time: 1 min
distance from lens: 5.38 cms

4(g) Sample AQ
power: 30 RU
deposition time:
6 minutes, distance
from lens: 5.95 cm
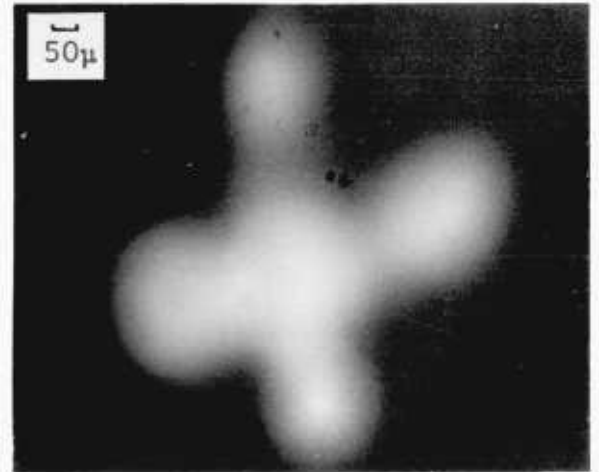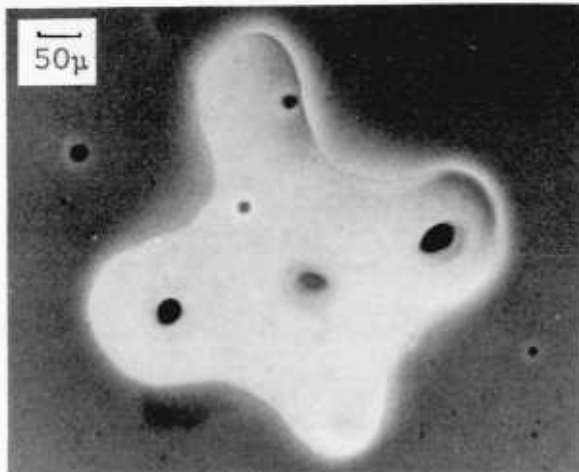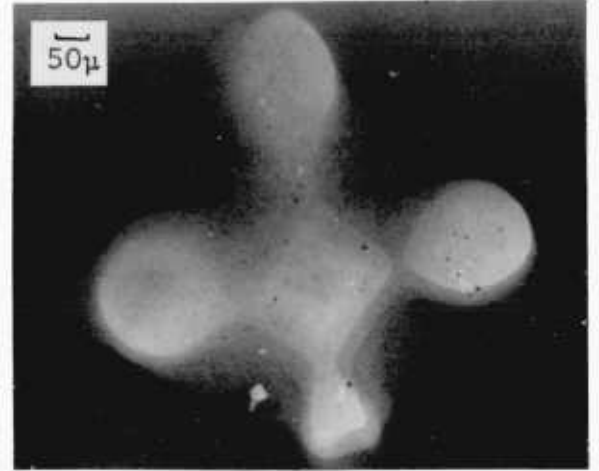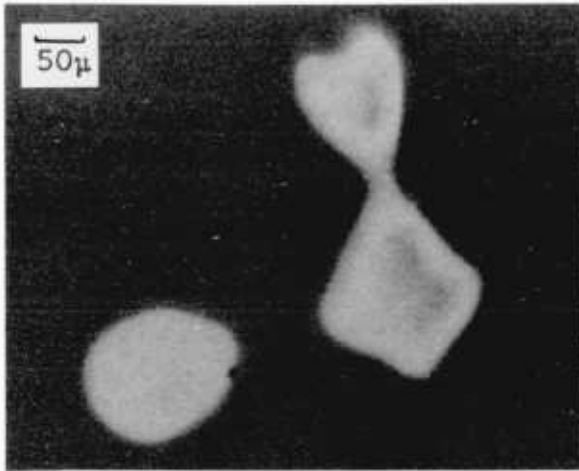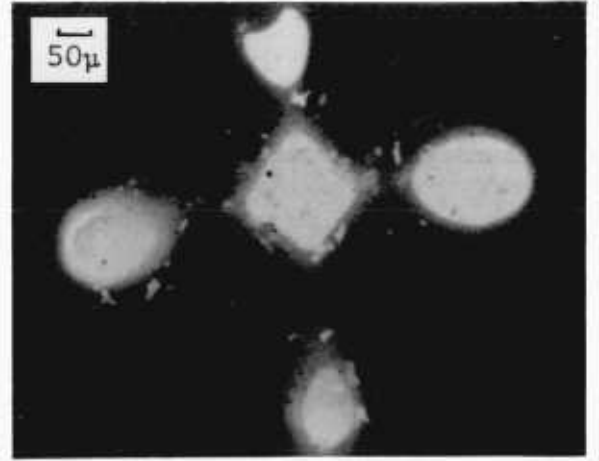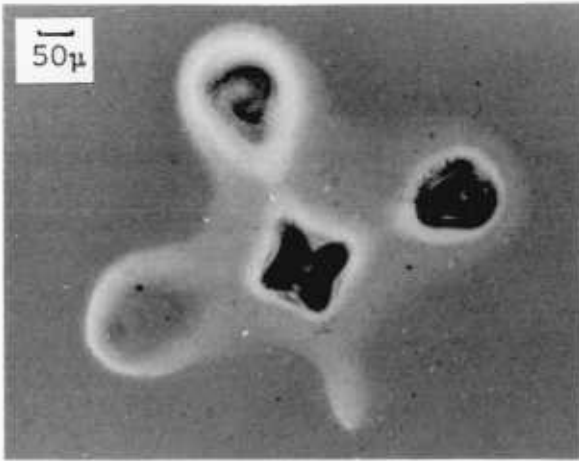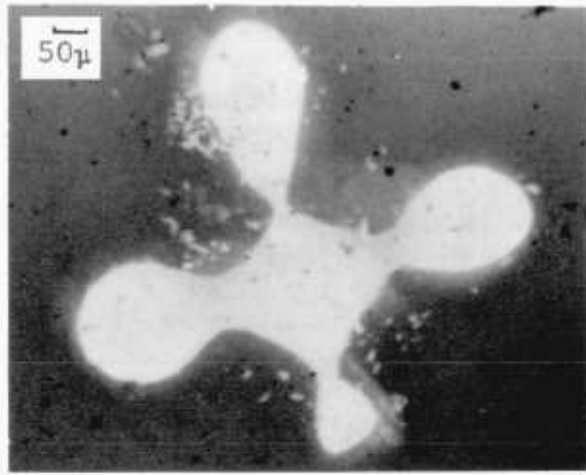
PLATE 5

PLATE 5

Examples of Plate Deposits

5(a)
Sample D2 talysurf
trace, thickness
scale = .25μ/division
0.7 of a division
= 0.17μ

5(b)
interferogram
sample D2
0.4 total fringe
displacement = 0.12μ

5(c)
Sample E27 interferogram

5(d)
Sample F14

5(e)
Scanning electron micrograph
of sample F14, general view
of deposit showing the 'beach'
zones

5(f)
Sample F14
showing central
black spots and
'beach' zones
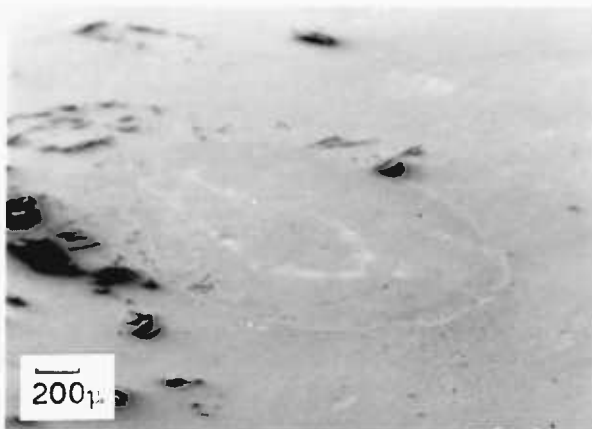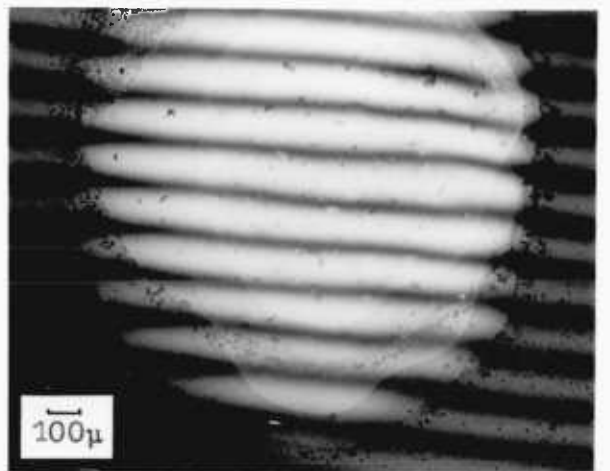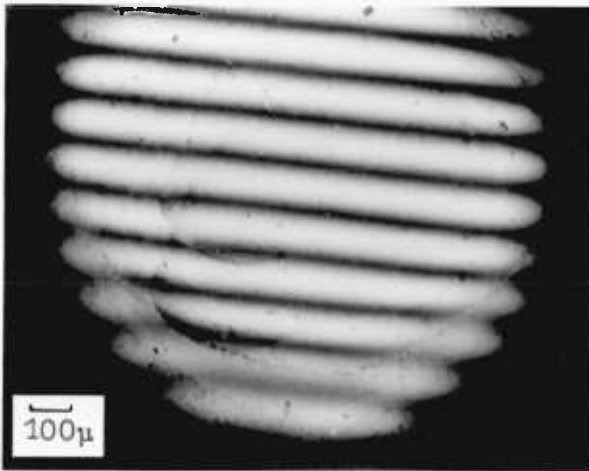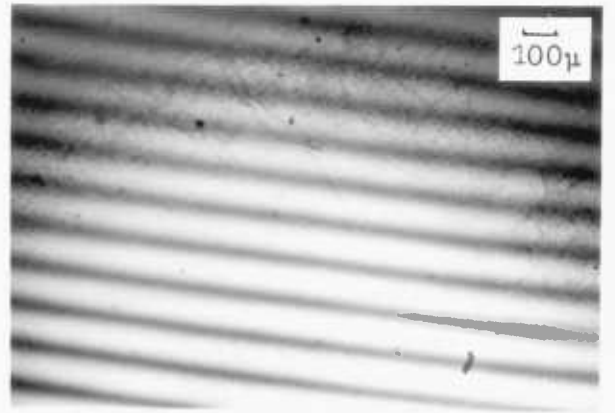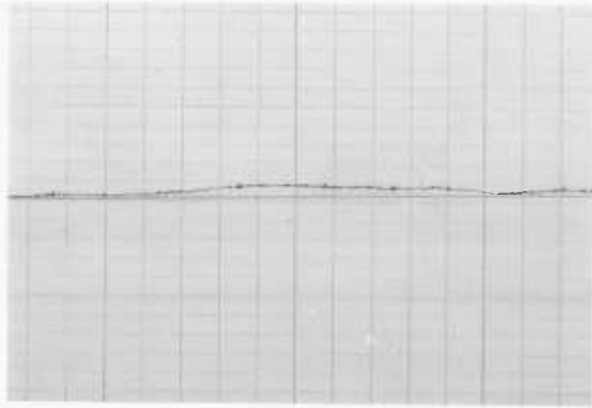
PLATE 6

PLATE 6

Examples of Mound Deposits

6(a)
Sample D10
talysurf trace
scale 0.25μ/division
0.25μ thick

6(b)
Sample D10
interferogram
showing small central
mound 0.9 fringe displace-
ment = 0.26μ thick

6(c)
Sample F10
talysurf trace
scale 0.25μ/division
skid = 0.74μ   stylus = 0.37μ
thick
example of a 'thick' flat plate

6(d)
Sample F10
interferogram

3.1 fringe displace-
ment = 0.9μ thick

6(e)
sample A2
general view by SEM
a thick flat plate sample
showing the clear edge

6(f)
Sample A2
showing rough central
zone

6(g)
Sample A2
Close up of the clean
edge with a microcrack
formed after deposition
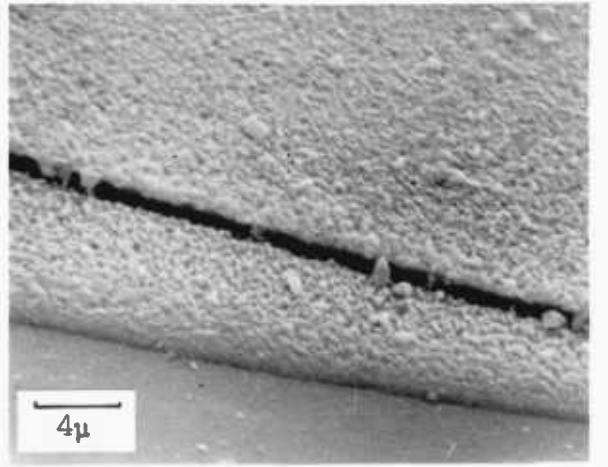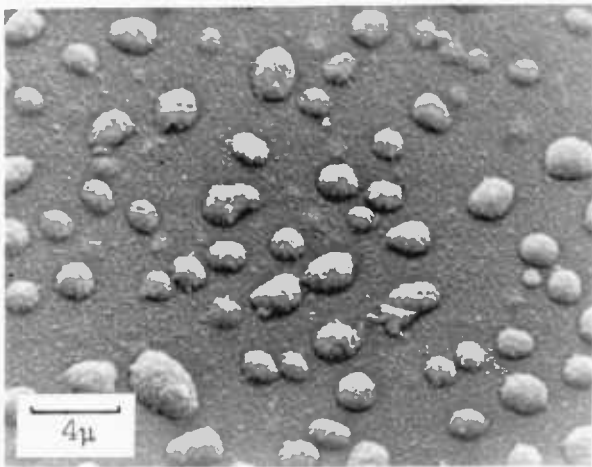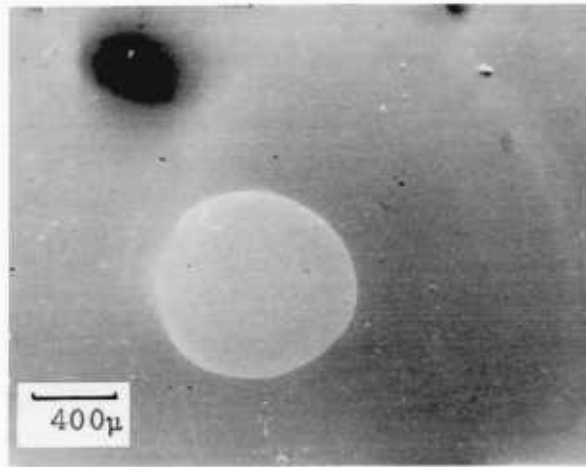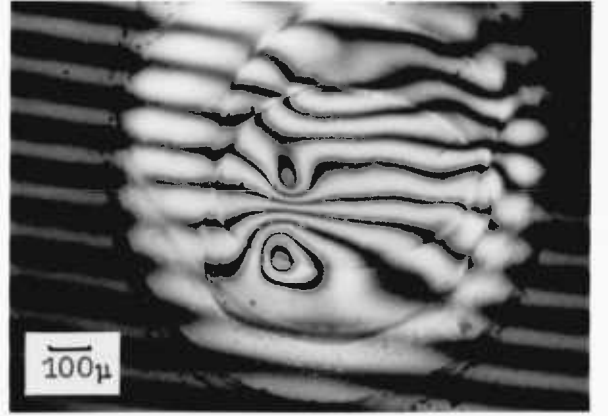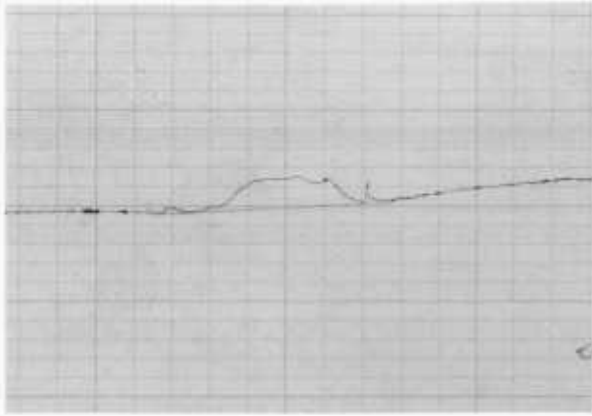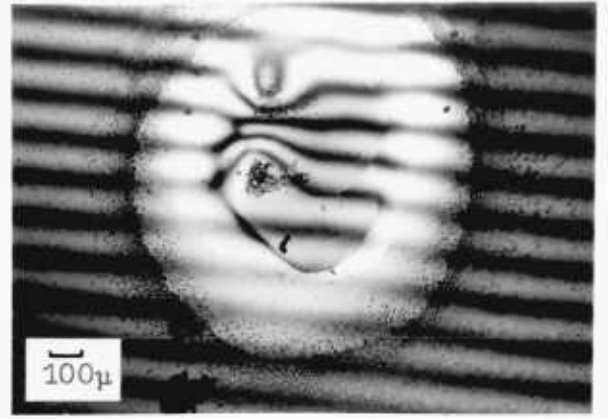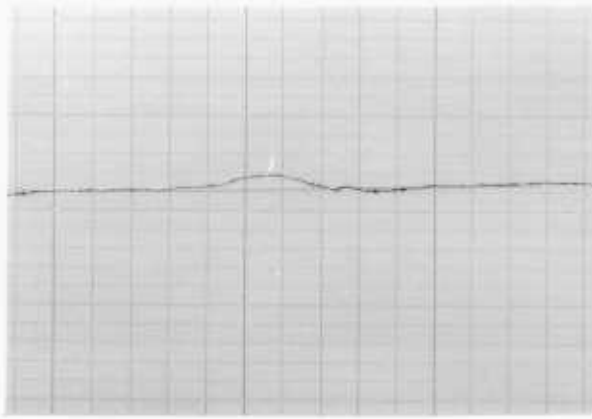
PLATE 7

PLATE 7

Example of a Mound Deposit

Sample D25

7(a)
talysurf trace
scale - 0.25µ/div-
ision, stylus = 0.53µ
skid = 0.88µ

7(b)
inteferogram
3.15 fringe dis-
placement = 0.93µ

7(c)
long view of 'skirt'
region

7(d)
Edge of deposit
showing large and
small lumps

7(e)
central region showing
a blister under a lump

7(f)
central region
showing a decapi-
tated lump which
does not appear to
be a blister

stylus

skid

100μ

20μ

2μ

2μ

1μ
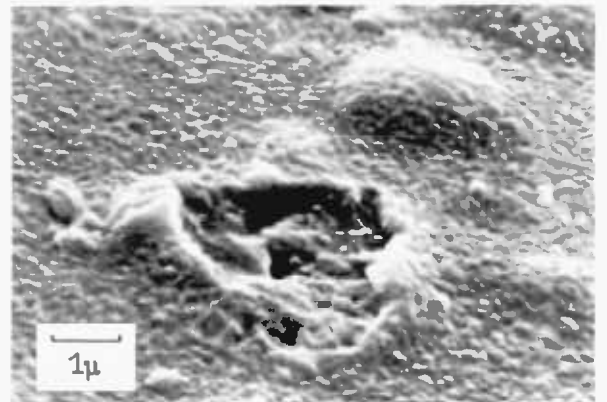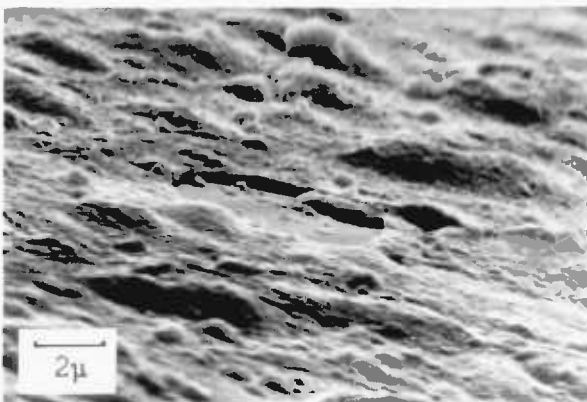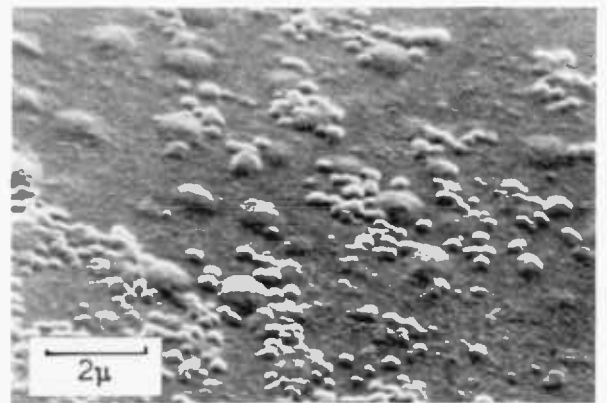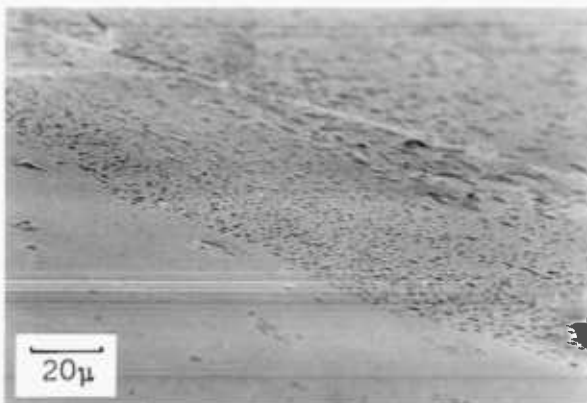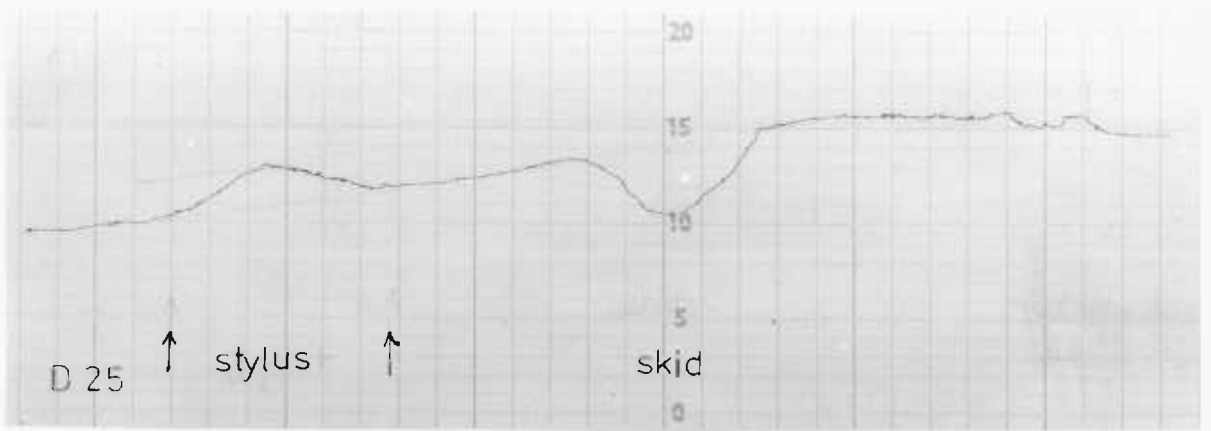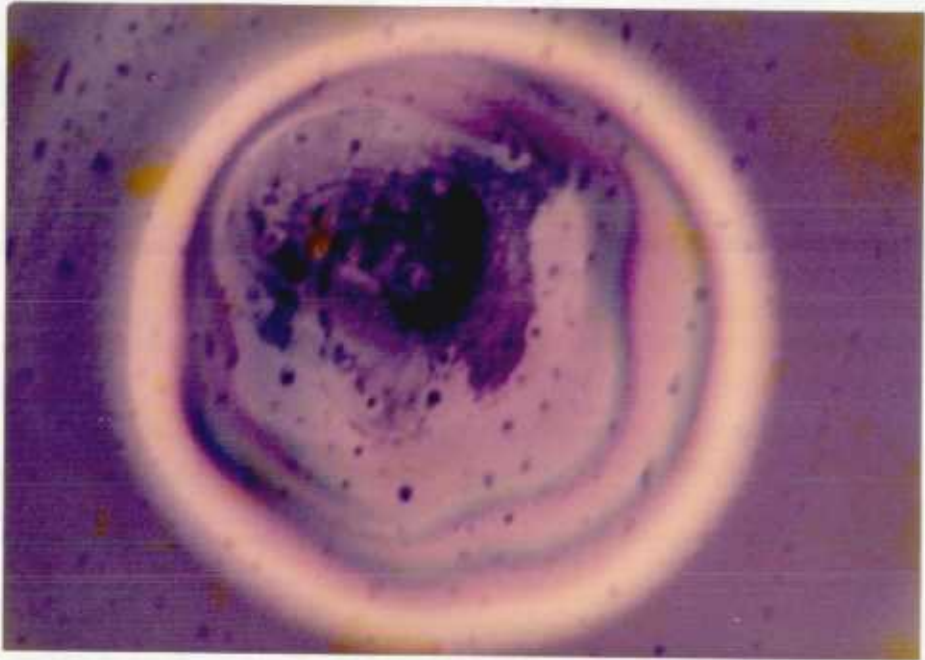
PLATE 8

Colour fringes shown in sample D25
under mercury vapour illuminsation
fringes $\risingdotseq$ 3 red fringes
= 0.9μ thick

PLATE 9

PLATE 9

Example of a Mound Deposit

Sample B22

9(a)
talysurf trace
scale 0.25μ/division
thickness ≃ 0.37μ

9(b)
interferogram
1.25μ fringe total dis-
placement = 0.36μ thick

9(c)
SEM general view

9(d)
SEM central area

9(e)
SEM skirt region
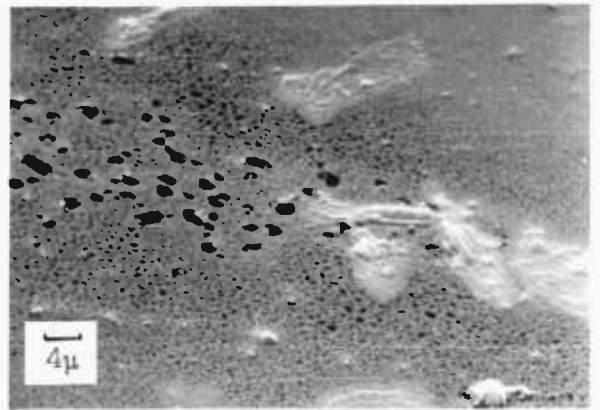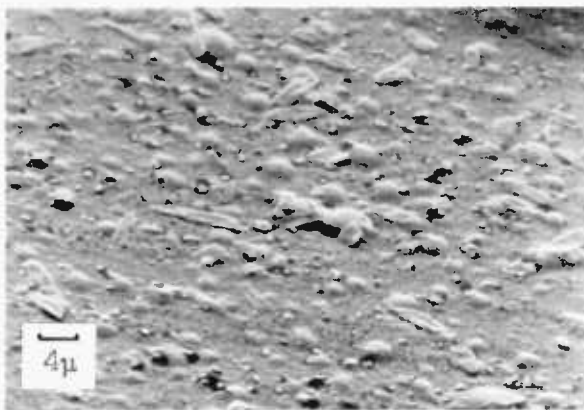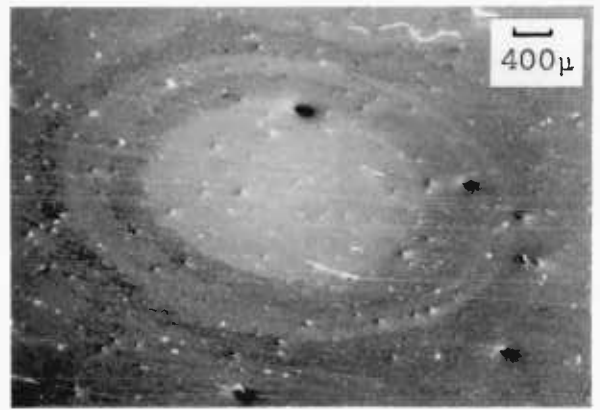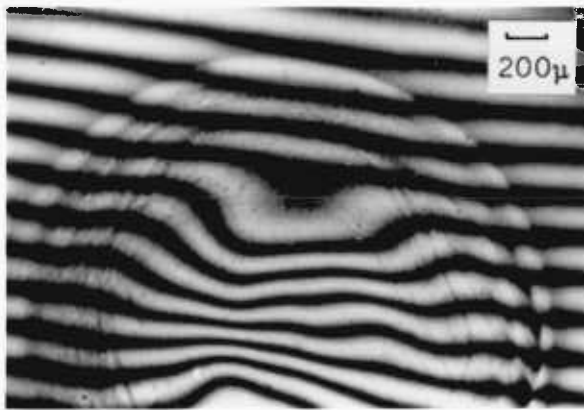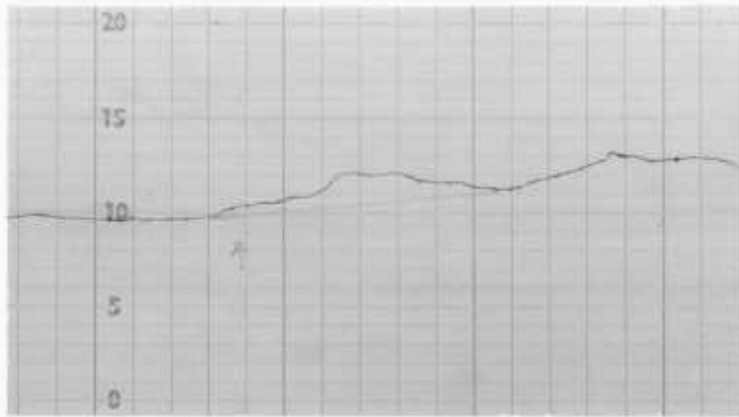
PLATE 10

PLATE 10

Example of a Raised Crack

Sample E1

10(a)
talysurf trace
showing raised
crack scale 0.5μ/
division ≃2.7μ high

10 (b)
Double beam interferogram

10(c)
colour fringe interferogram using
Hg vapour illumination

200μ
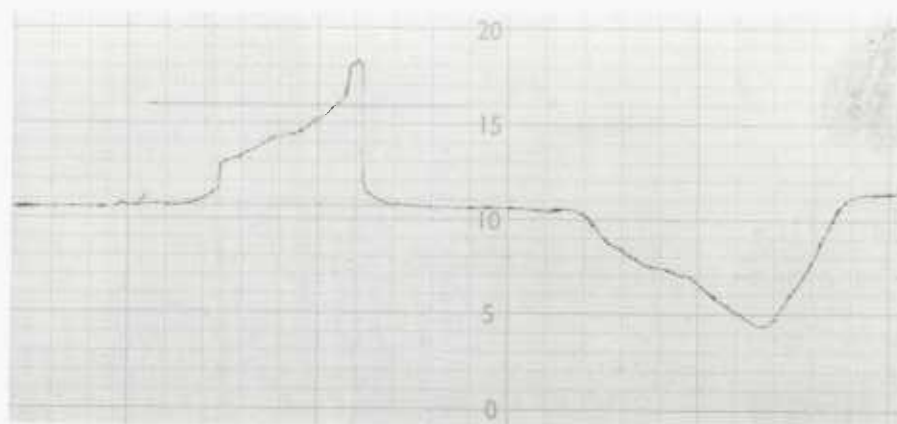
PLATE 11

PLATE 11

Example of a Peak Deposit

Deposit D9

11(a)
talysurf trace
scale 1.25µ/division
plateau   3.75µ
peak   7.25µ

11(b)
interferogram

11(c)
SEM the central peak

11(d)
SEM close up of the
peak

11(e)
SEM the horseshoe crack
showing some filling

11(f)
the plateau region
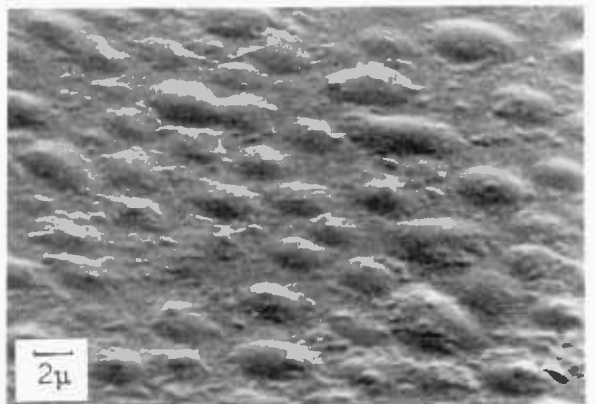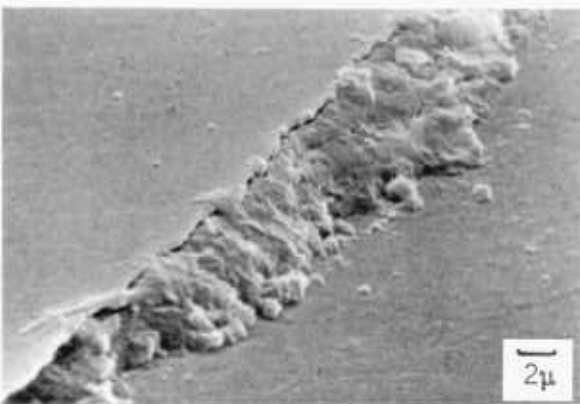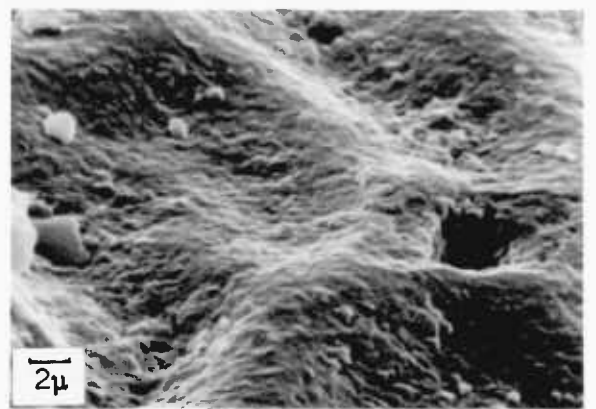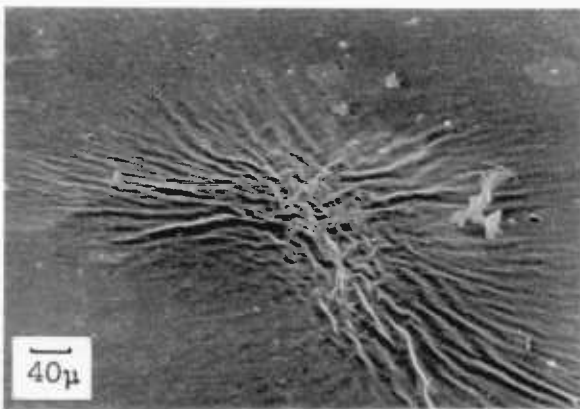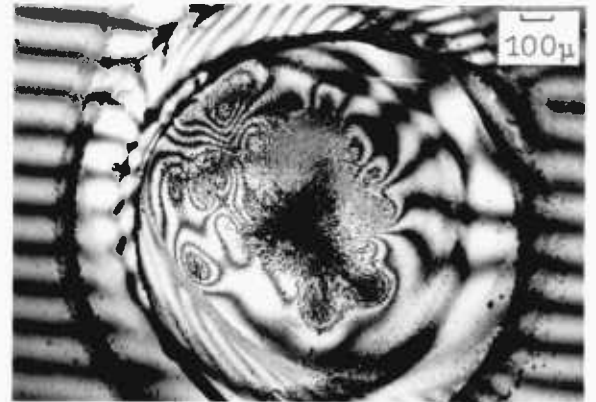
PLATE 12

PLATE 12

Example of a Peak Deposit

Sample B18

12(a)
talysurf trace
scale 0.5μ/division
peak   5.8μ high
pl ateau = 3.3μ high

12(b)
interferogram plateau
2.9μ high

12(c)
SEM general view
showing a double
"beach" zone

12(d)
SEM sample central zone
showing a craze crack
pattern

12(e)
SEM ripple pattern
near the peak region

12(f)
SEM the peak

12(g)
SEM "beach" zone
showing black dots
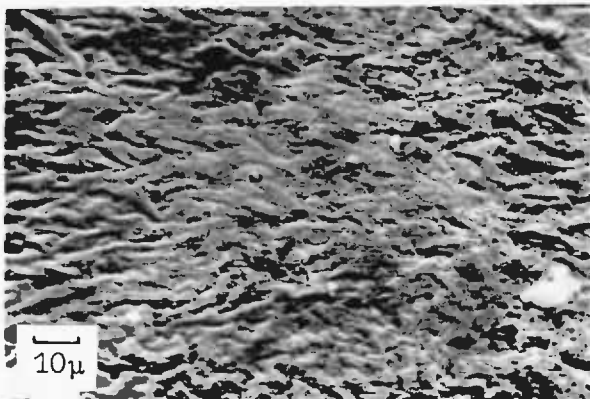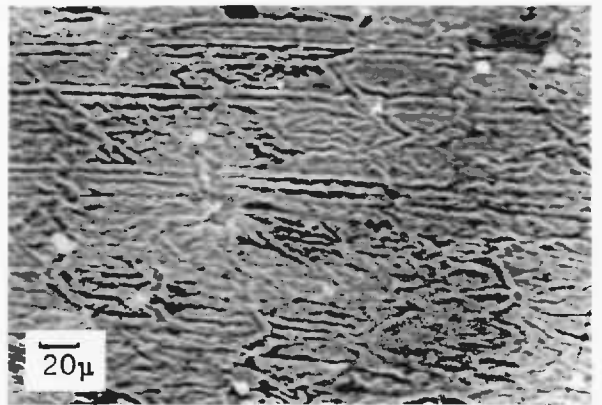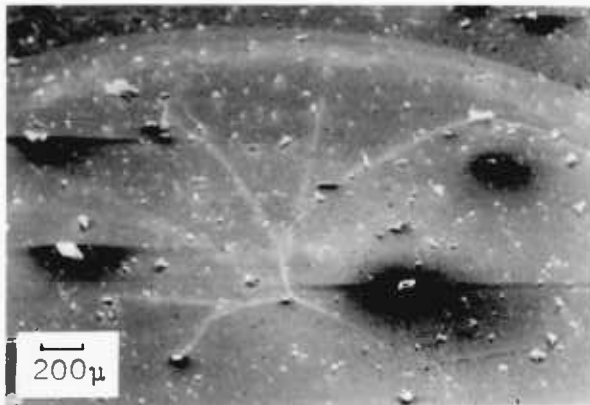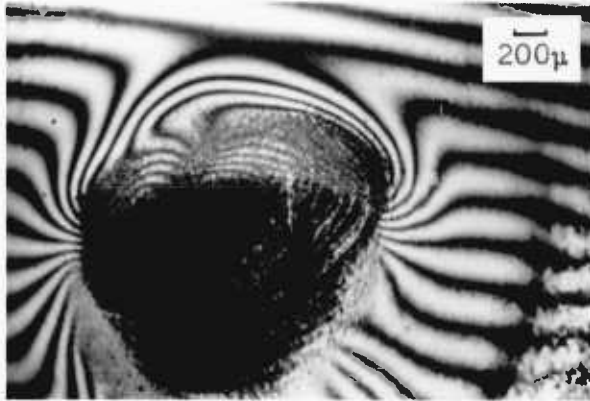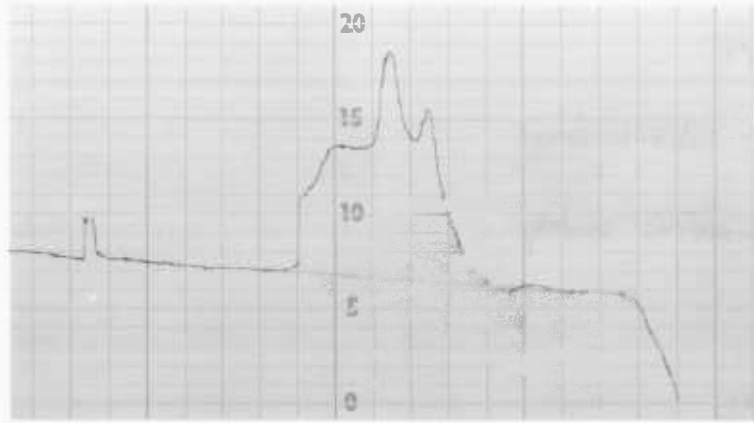
PLATE 13

PLATE 13

Example of a crater deposit
Sample G4

13(a)
talysurf trace
scale 1.25µ/division
15µ high

13(b)
interferogram

13(c)
SEM
general view

13(d)
SEM
detail of the
outside edge of the
crater showing a crack

13(e)
SEM
centre of the
crater

13(f)
SEM
detail of outer
edge of crater poss-
ibly showing a small
depression

100μ

100μ

4μ

10μ

4μ
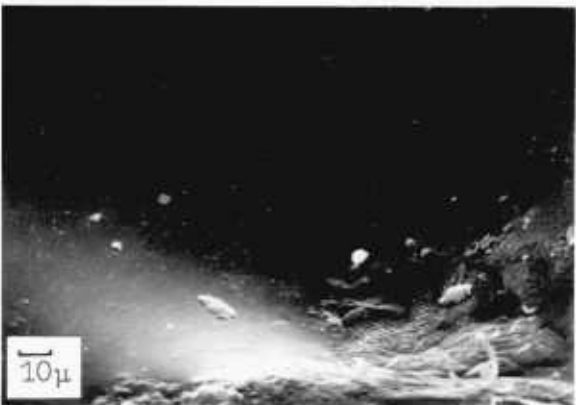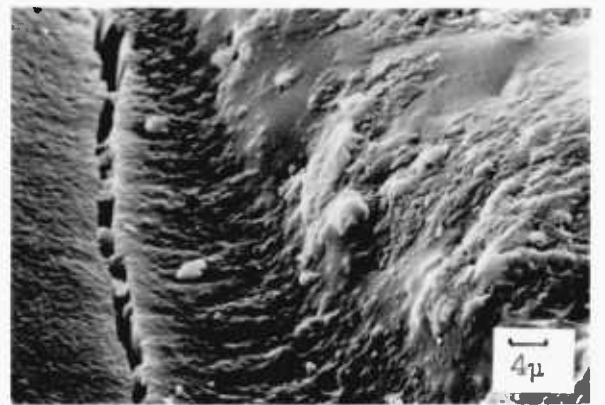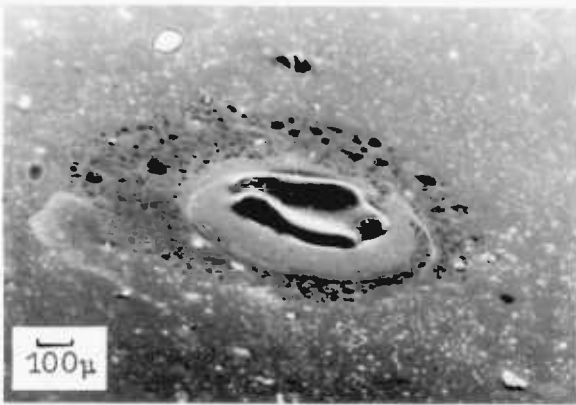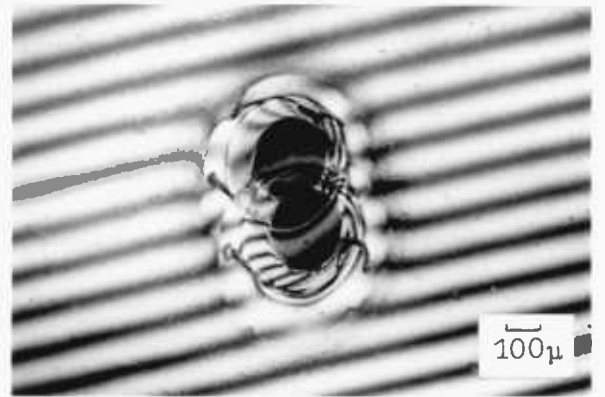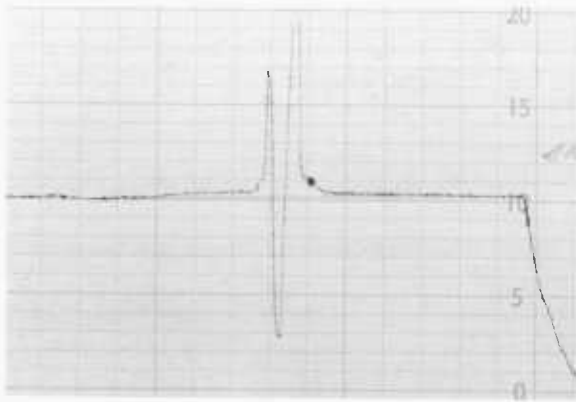
PLATE 14

PLATE 14

Example of a Multiple Crater Deposit

Sample F13

14(a)
Talysurf trace
scale 1.25μ/division
10μ high

14(b)
double beam inter-
ferogram

14(c)
SEM general view

14(d)
SEM detail of one of
the peaks, showing
random roughness on
the right and syste-
matic wrinkling on the
left

14(e)
SEM detail of systematic
wrinkling

14(f)
SEM outer edge of
deposit
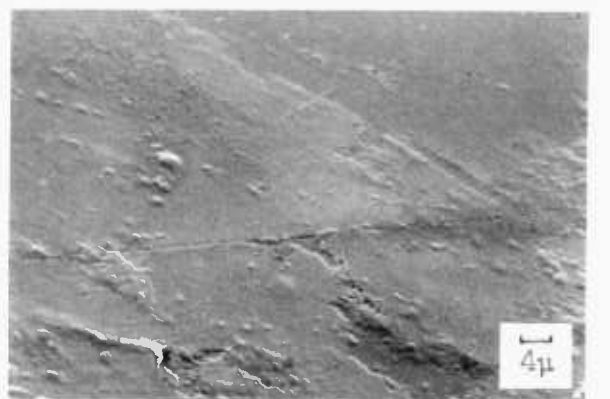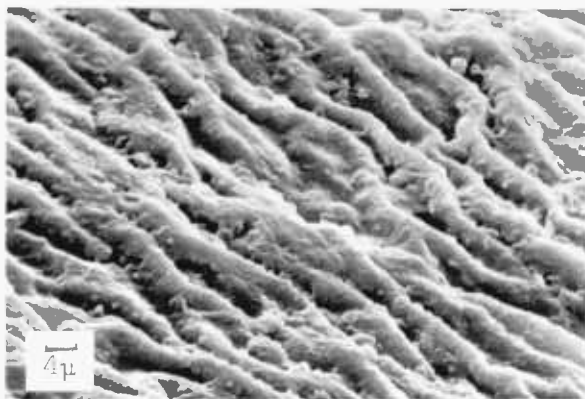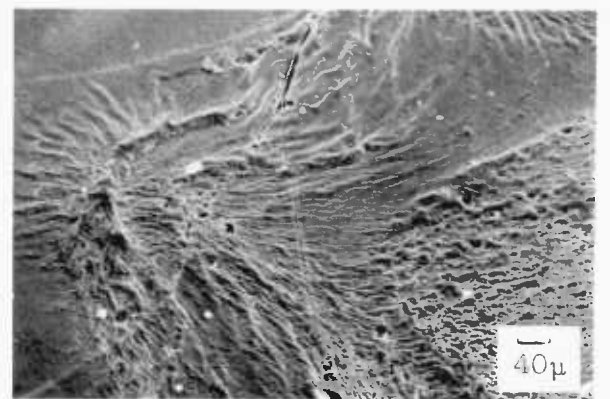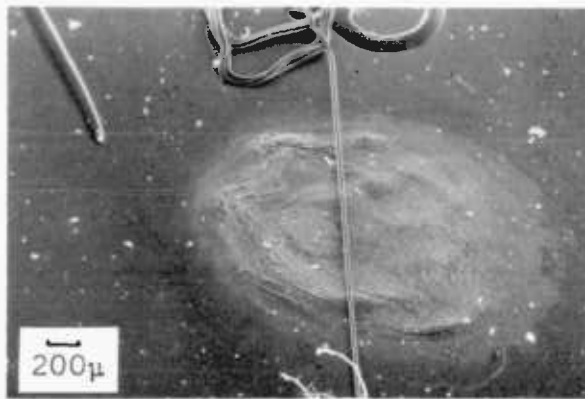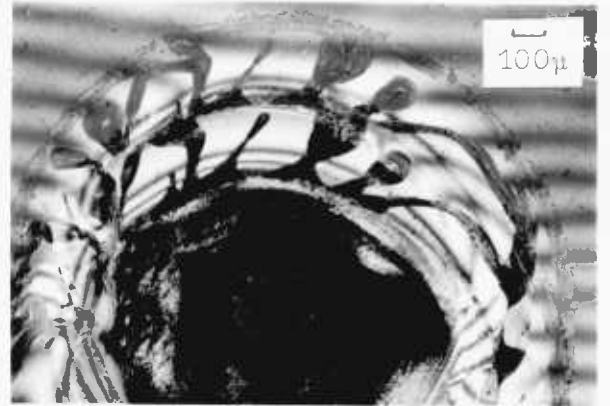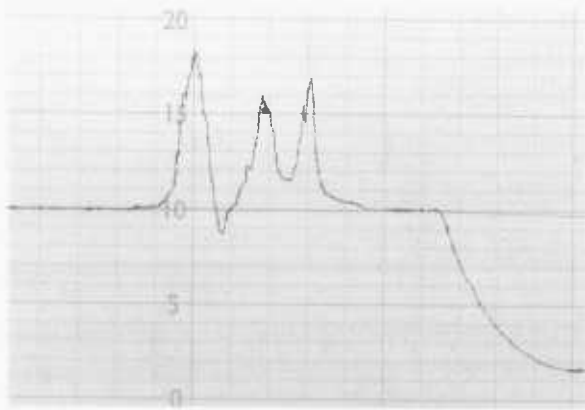
PLATE 15

PLATE 15

Examples of unusual deposit shapes and beam char
prints

15(a)
Sample C23

15(b)
Char prints
associated with
C23

15(c)
Sample H10

15(d)
Char print
after H10

15(e)
Sample H11

15(f)
Colour photograph of the blue central zone
observed in some deposits
Sample I

Sample C23

before
beam splitter

after
beam splitter

Char prints before C23

Sample H10
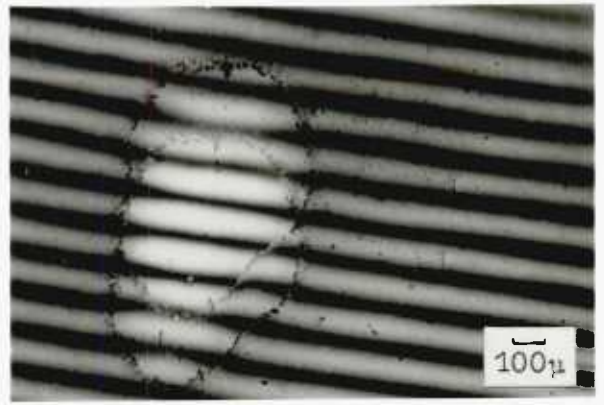
Sample H11

Char print after H10

PLATE 16
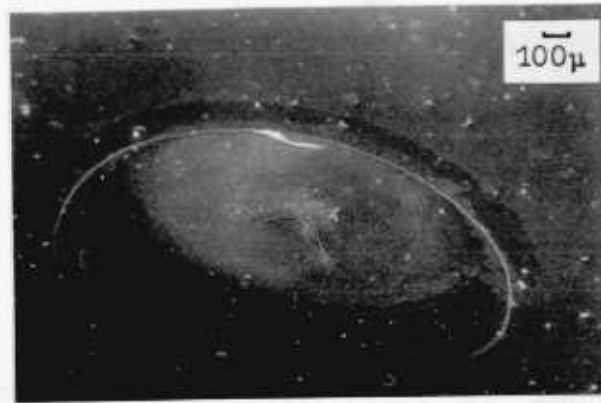
16(a)
Sample D9 illustrating a horseshoe crack –
Herzian type cone fracture-occurring mainly
during deposition
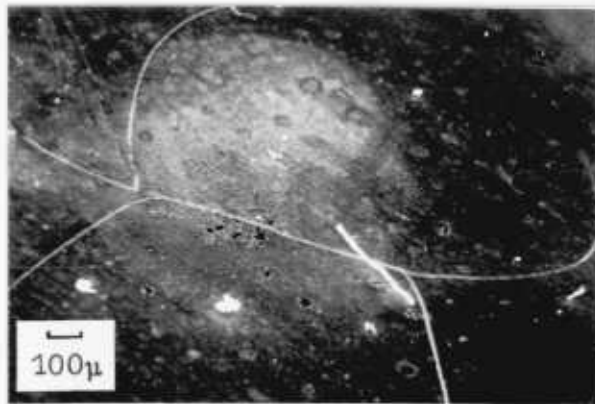
16(b)
Sample D25 illustrating an 'H' type fracture
mainly occurring after deposition

7.3.1.6. <u>Summary of deposit structures</u>

1) The deposits could be arranged into five structural groups

a) thin flat plates   (i)   showing no features

                                  (ii)   showing black dots and platelets

b) mounds   (i)   with a small central mound and outer region as in a(ii)

                                  (ii)   Thicker plates with a clear edge, pimples in the thicker region and a horseshoe ., herzian type, crack around the thicker ‑ zone.

                                  (iii) Smooth round mounds: with pimples in thicker region, black dots in thinner region. Central region could show random roughness and some cracking.

c) raised cracks   deposit lifted out of surface by warping of a Herzian type fracture.

d) peaks   as for (b) but with a wrinkled zone producing an exceptionally high signal on the talysurf . trace.

e) craters   a depression into the substrate surface surrounded by a smooth ridge at the centre of a type (b) deposit.
An alternative was a multiple peak creating a hollow which penetrated the substrate surface.

7.3.2 <u>Effect of (incident power, P/beam diameter, D_b)</u>

7.3.2.1 <u>On Deposit Thickness</u>

Graph 7.4   shows values of deposit thickness vs (P/D_b) for a deposition time of two minutes, jet exit Reynolds number of 2079, chelate concentration of 0.306ppm, jet exit temperature of 120°C, and jet/plate distance of 3.81 cms. Also shown on the graph are the thermal conduction model predictions discussed later (section 8.2.2.1).

Fig 7.4 DEPOSIT THICKNESS AFTER 120s AS A FUNCTION OF P/D_b AND D_b.

THEORETICAL CURVES $Re = 2079$ $\rho_E = 0.306$

EXPT: POINTS D & F SERIES

NO LOSS $D_b = 0.00096$ m

0.00048 m

0.00096 m

0.00192 m

0.0022 m

DEPOSIT THICKNESS μ

P/D_b W/cm
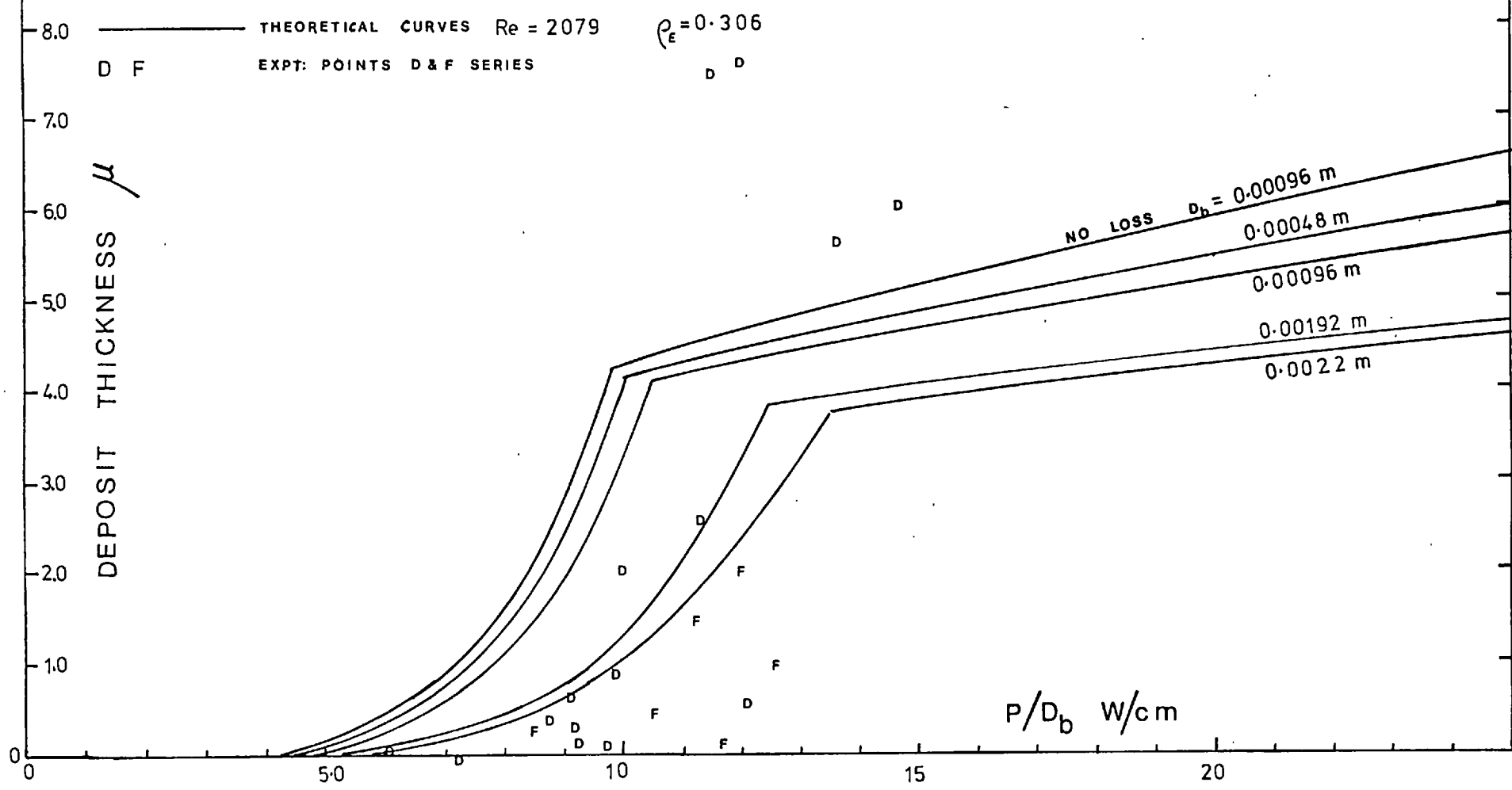
It is clear from graph 7.4 that (P/D_b) is one of the most important parameters. To emphasise this point graph (7.5) was plotted which includes all centrally placed deposits formed in two minutes regardless of any third parameter. This is more spread than in graph 7.4 but nevertheless a clear overall trend. Also plotted on graph 7.5 (which has a broken scale) are the regions for the formation of the five structures just noted. From the slope of the lines separating the structural regions it appears that the difference between formation of mounds and plates is not a strong function of P/D_b but mainly the state of growth; an observation supported by the growth sequence (section 7.3.4). On the other hand the formation of craters is highly dependent on (P/D_b) with less dependence for peaks and crack formation.

It is the uncertainty in the precise value of (P/D_b) for each deposit which could account for the observed scatter in graph 7.4 . This uncertainty is due in part to the observed fluctuation in power during deposition ($\pm$ 10%) and in part to the value taken for the beam diameter, D_b (possible error $\pm$20%).

These values give a variation in (P/D_b) given by :

$$d(\frac{P}{D_b}) = \frac{dP}{D_b} \pm \frac{P}{D_b^2} dD_b$$

$$\therefore \quad \frac{d(\frac{P}{D_b})}{\frac{P}{D_b}} = \frac{dP}{P} \pm \frac{dD_b}{D_b} = \pm 30\%$$

7.3.2.2 Variation of deposit outer diameter D_o with P/D_b

Graph 7.6 shows the variation of the D_o plotted as (D_o/D_b) for the conditions stated. Also shown on the graph 7.6 are the predictions from the thermal conduction model of the location of the 150°C isotherm for various beam diameters.
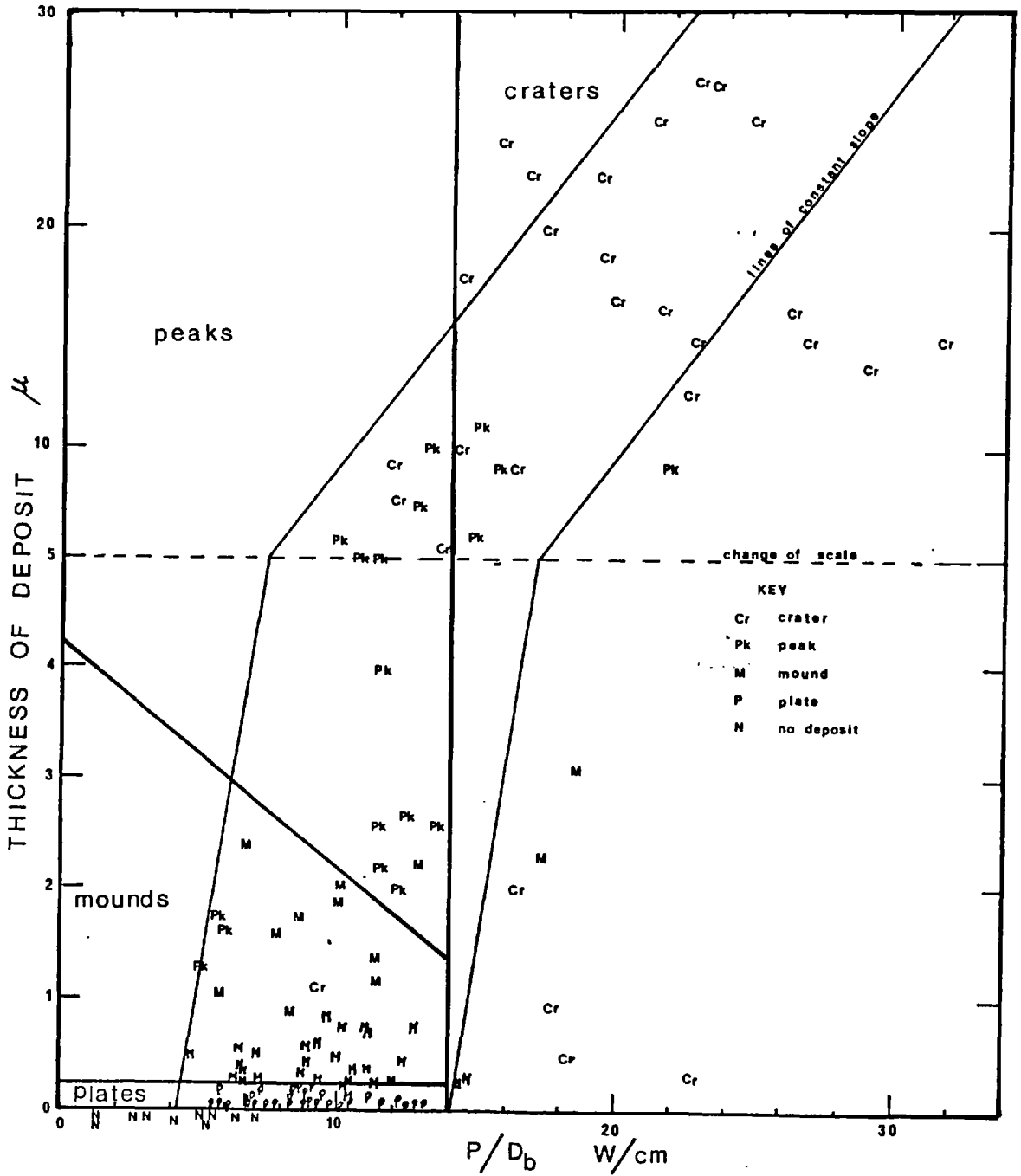
Fig 7.5   Deposit thickness as a function of P/D$_b$ for all runs of 120s

Fig 7.6 VARIATION OF OUTER DIAMETER WITH (P/D_b) FOR VARIOUS BEAM DIAMETERS D_b
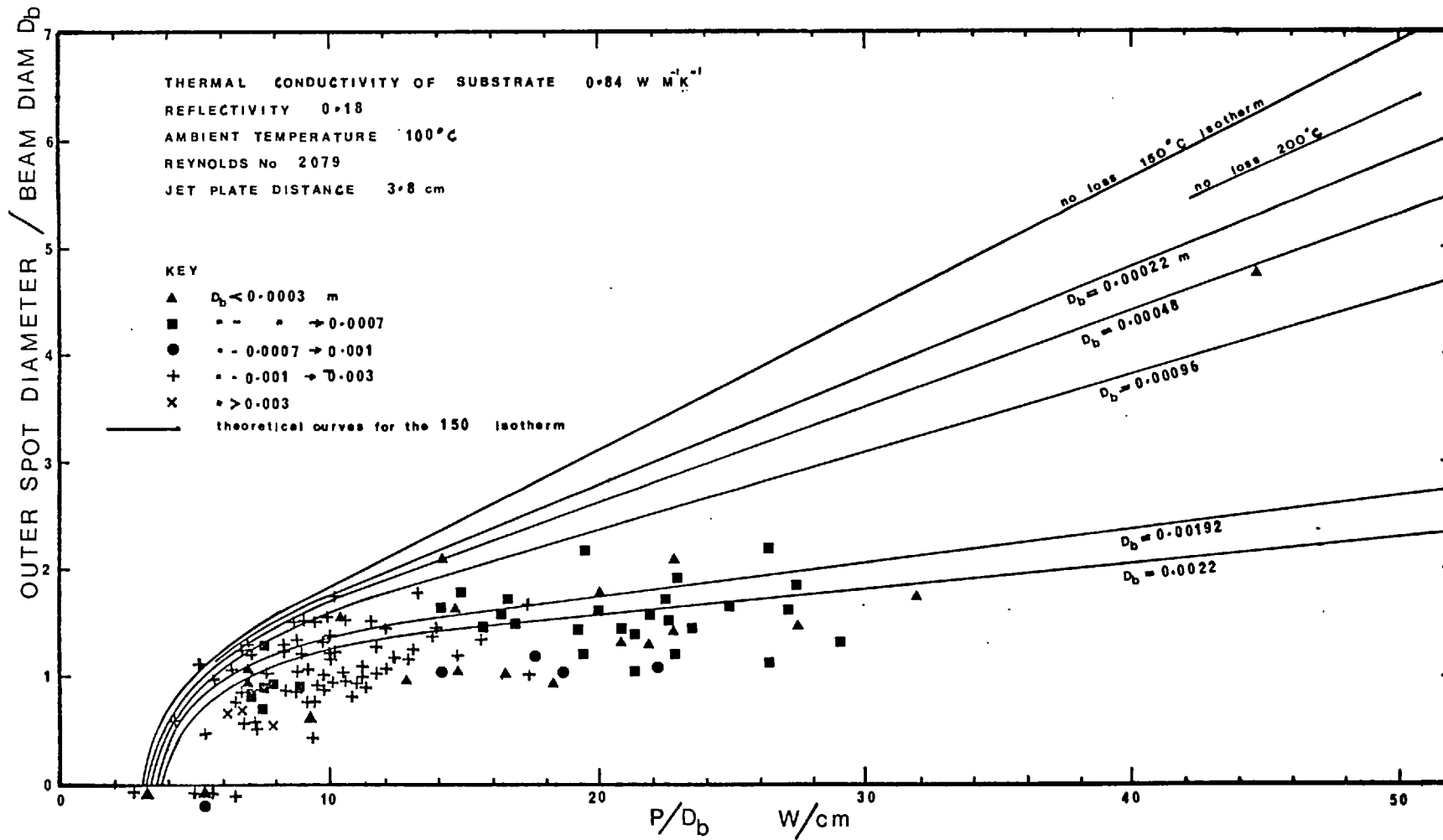
The observed scatter in this graph and the other diameter·vs power graphs   are not only due to the uncertainty in the value of P/D_b, previously noted, but also in the measurement of the outer limit of the deposits. A further point is that the outer visible limit may not be the outer limit of the deposits.

The uncertainty in the value of the beam diameter is not so critical here as in the growth results since it affects the values on both axes. A variation in D_b would move a point on the graph almost parallel to the isothermal lines. It does however, affect the heat loss expected and hence the theoretical curve to which it is related.

7.3.2.3. Variation of inner deposit diameter D_i with (P/D_b)

The inner diameter, D_i, has been noted under the description of mounds (page 217) and craters (page 220). The dimensionless inner diameter, (D_i/D_b) is plotted against (P/D_b) in graph 7.7 . The results are compared to the theoretical predictions for the locations of various isotherms.

7.3.2.4. Variation of 'burnt' diameter D_{BR} with (P/D_b)

The 'burnt' regions are centrally place black zones, seen under the scanning electron microscope to be regions of roughness. They have been noted to occur with peak and crater formations.   These regions normally had clear edges allowing a reasonably accurate measurement of the 'burnt' diameter, D_{BR}.

The dimensionless form of the 'burnt' diameter, (D_{BR}/D_b) is shown plotted against (P/D_b) in graph 7.8   and compared to the prediction of the location of the $500^\circ C$ isotherm.

7.3.2.5 Variation of the crater diameter with P/D_b

The measurement of the crater diameter was difficult due to the poor definition of the edge of a crater, and uncertainties in distinguishing between a black centre and a crater. Only

Fig 7.7   VARIATION OF INNER DIAMETER WITH (P/D_b)

Thermal conductivity of substrate 0.84 W $M^{-1} K^{-1}$
Reflectivity   0.18
Ambient temperature $100^\circ C$
Reynolds No 2079
Jet Plate Distance   3.8 cm

KEY
    D_b 0.0003 m
    "   "   0.0007
    "   0.0007   0.001
+   "   0.001   0.003
x   "   0.003

———   theoretical curves for the 150 isotherm

no loss 227°c
no loss 234°c
no loss 254°c
no loss 388°c
no loss 400°c

354°c isotherm
$D_b = 0.002$ m

INNER DIAMETER / BEAM DIAMETER

P/D_b W/cm
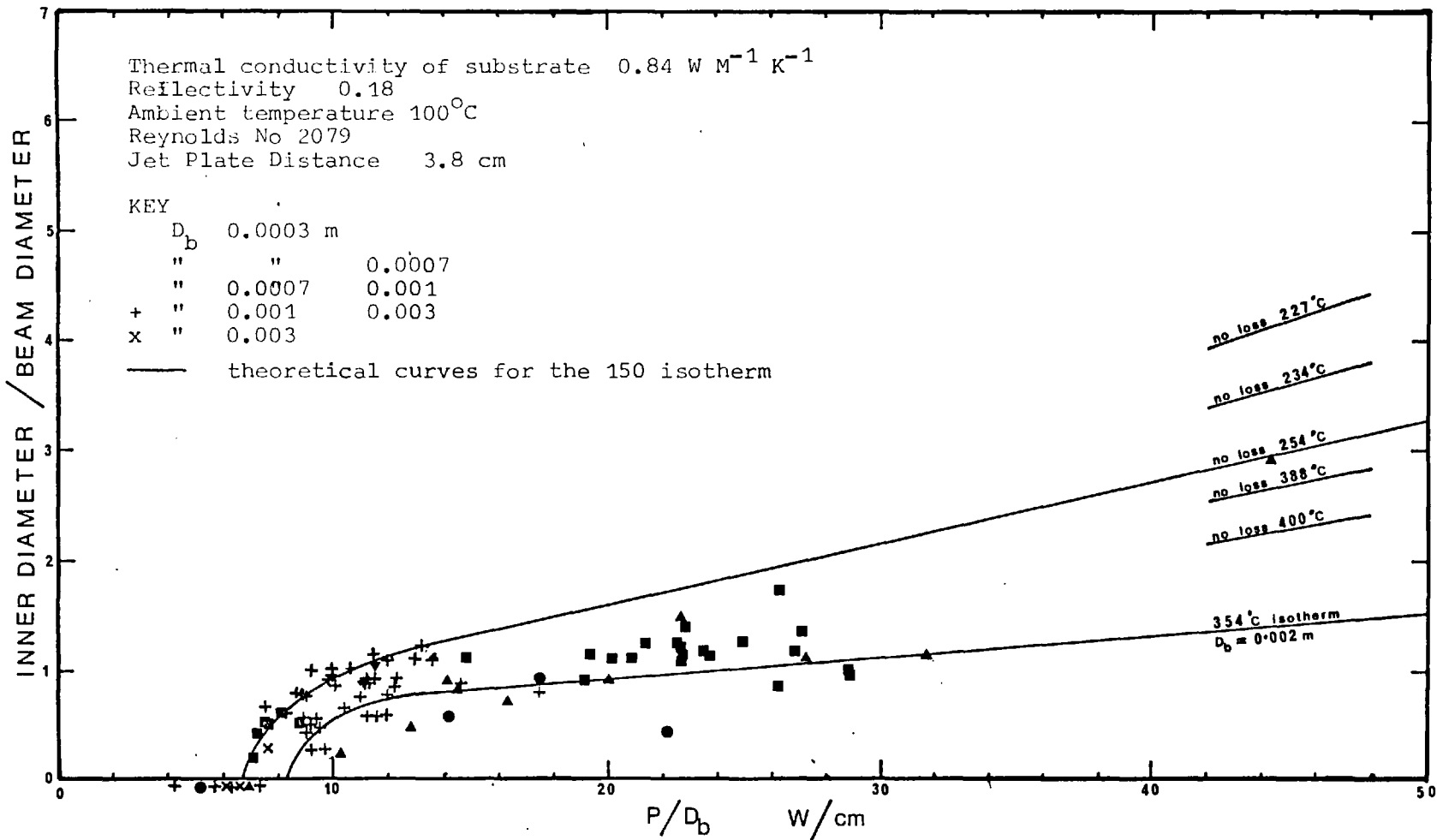
Fig 7.8   VARIATION OF 'BURNT' DIAMETER WITH (P/D_b)

Thermal Conductivity of Substrate 0.84 W M^{-1} K^{-1}
Reflectivity 0.18
Ambient Temperature 100°C
Reynolds No 2079
Jet Plate Distance 3.8 cm

KEY
    D_b 0.003 m
    "^{b} "   " 0.0007
    "   " 0.0007 0.001
+   " 0.001 0.003
x 0.003

——   theoretical curves for the 150 isotherm

500°C Isotherm no loss
500°C Isotherm $D_b \approx 0.002$ m

'BURNT' DIAMETER / BEAM DIAMETER

P/D_b W/cm

228

Fig 7.9   VARIATION OF THE CRATER DIAMETER WITH (P/D_b)

Thermal Conductivity of Substrate 0.84 W M^{-1} K^{-1}
Reflectivity 0.18
Ambient Temperature $100^{\circ}C$
Reynolds No 2079
Jet plate distance 3.8 cm

KEY
  D_b 0.0003 m
  ,,^{b} 0.0007
        0.0007   0.001
  +   0.001   0.003
  x   0.003

——   theoretical curves for the 150 isotherm

700°C isotherm no loss

700°C isotherm $D_b = 0.002$

229

relatively deep craters, showing clearly on a talysurf trace,
or by focal effects within a microscope, were recorded as
craters in graph 7.9 . This graph shows the variation of
dimensionless crater diameter with (P/D_b), together with the
theoretical prediction of the $700^{\circ}C$ isotherm, which was considered
to fit the experiments best. Craters were not observed for
values of (P/D_b) less than 14 W/cm

7.3.2.6 The formation of blue zones - example Plate (15f)

Blue centres to some cratered deposits were observed. The
lowest value of (P/D_b) at which a blue centre was observed was
19.3 W/cm (sample I1) a value supported by 20.0 W/cm and 21.4 W/cm
for I9 and I3. respectively

Numerous deposits did not show
any blue centre when formed with values of $(P/D_b) \simeq 18$ W/cm.

Bearing in mind that it is quite reasonable that some deposits
may have formed a blue centre which was subsequently covered due
to a fall in power, or that the blue centre became black due
to further dissolution of cobalt into the glass (see section
8.2.1.3., page 264) it is possible that some blue product
formation may have been missed. In consequence the lower limit
of power required for the formation of a blue centre is
probably less than that observed. However, it appears that the
lower limit is of the order of 19 W/cm.

7.3.3. Effect of radial location within jet on deposit size

In series C and E the lens was turned slightly between
samples so moving the hot spot across the substrate but allowing
the bulky jet and evaporator to remain fixed. For the small
deflections involved ($\pm$ 7°) and the narrow beam from the aperture
striking the lens (~ 0.5 cm D) the variation in beam diameter
due to coma formation was considered negligible. Likewise the
variation in power absorption with the small changes in lens
thickness was neglibible compared to the normal power fluctuations
observed.

For series C the ratio (P/D_b) was kept at 6.0 $\pm$ 1.0 W/cm and for series E at 11.0 $\pm$ 1.5 W/cm.   In both series the third parameter changed was the jet Reynolds number.

7.3.3.1. Deposit thickness

The C series formed only thin plate deposits while the thickness of the E series deposits as a function of radial location is shown in graph 7.10 .   It is not possible to draw a decisive curve of Sherwood's number vs diameter from this graph. However it can be seen that the deposition rate is reasonably constant within the jet stagnation zone $(R/D_j \lessapprox 0.6$ i.e. 0.3 cms (ref 41)). Beyond this, in the transition and wall jet regions, the rate of deposition steadily falls with distance.

7.3.3.2. Deposit diameter

By contrast the deposit outer diameter, as shown in graph 7.11 was virtually independent of radial location. The inner diameter, though likewise independent, fell rapidly after a certain distance almost certainly due to the lack of sufficient growth to build up a visible inner region. Graph 7.12.

7.3.3.3. Deposit shape

The opacity of the deposits showed a thicker edge towards the jet for the deposits formed at the more distant locations. The effect could not be seen on interferograms due to the extremely thin deposits formed in these remote places.

7.3.4. Variation of the thickness and extent of deposit with time

The series I16 – 22, taken over a period of unusually steady beam power, shows a linear growth rate with an induction period of approximately 10s – graph 7.13   .

The variation of the outer, inner, and 'burnt' diameters with time is shown in the log/linear plot of graph 7.14 where it is compared with the theoretical predictions.

Fig 7.10   EFFECT OF THE DEPOSIT POSITION RELATIVE TO THE   JET   AXIS

$P/_{D_b} = 14.0$

$Re = 1842$

Lines are drawn connecting points on the
same run sequence. Zones are marked as
found by Davies (41).

Jet Diam D_j = 0.508 cms

$$\frac{B}{D_j} = 7.6$$

Vapour cone $\sim$ 0.3ppm

STAGNATION ZONE

TRANSITION   ZONE

$P/_{D_b} = 12.0$

$Re = 1842$

$P/_{D_b} = 13.0$

$Re = 840$

$P/_{D_b} = 12.2$

$Re = 1092$

DEPOSIT THICKNESS $/\mu$

RADIAL   POSITION R/D_j
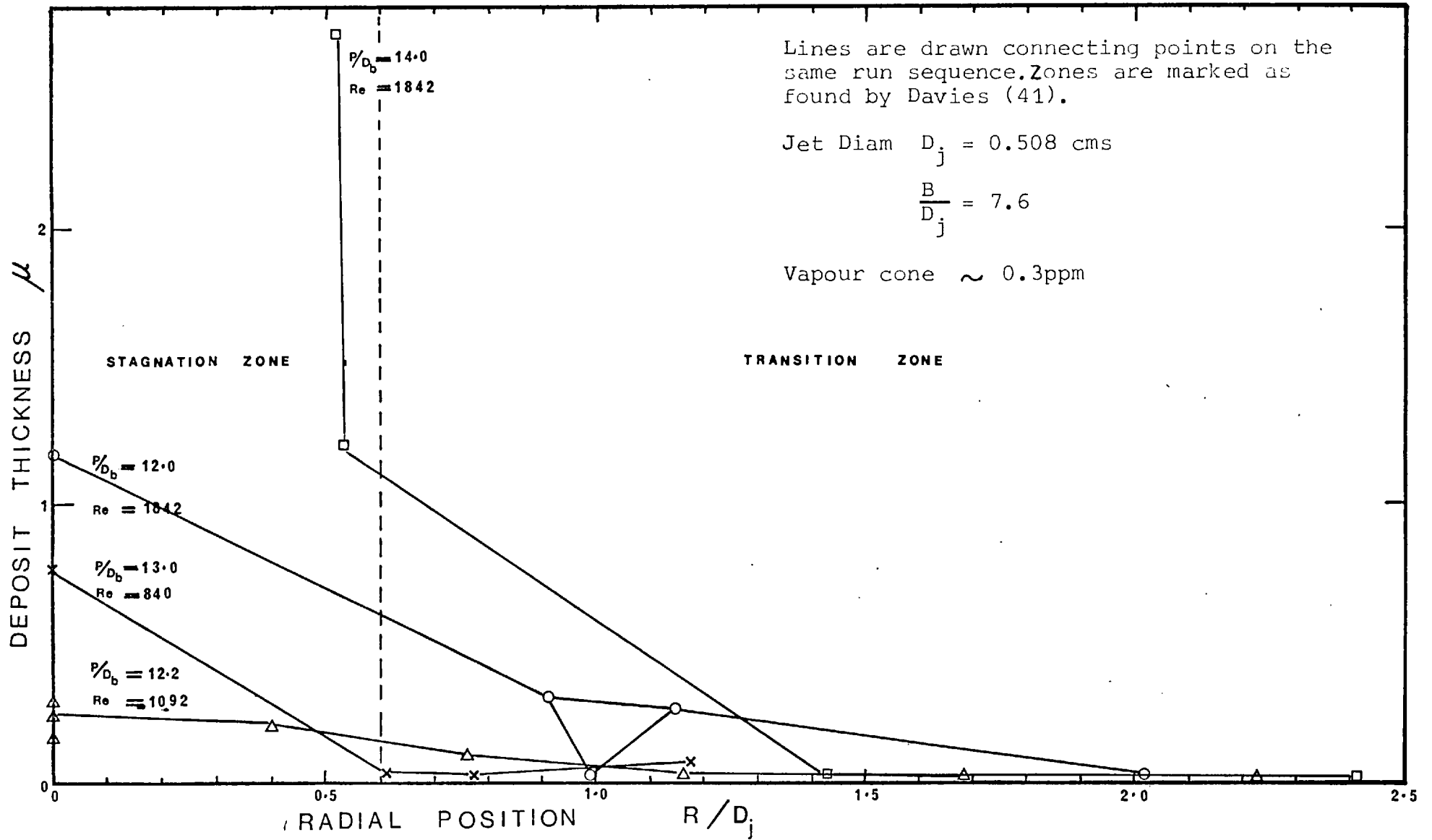
Fig 7.11 VARIATION OF THE OUTER DIAMETER, D_O, WITH RADIAL LOCATION WITHIN THE JET

	P/D_h, W/cm	jet plate distance, B, cm	vapour conc , ppm	time s
E Series	~11	3·81	~ 0·26	120
C Series	~6	2·54	~ 0·38	120
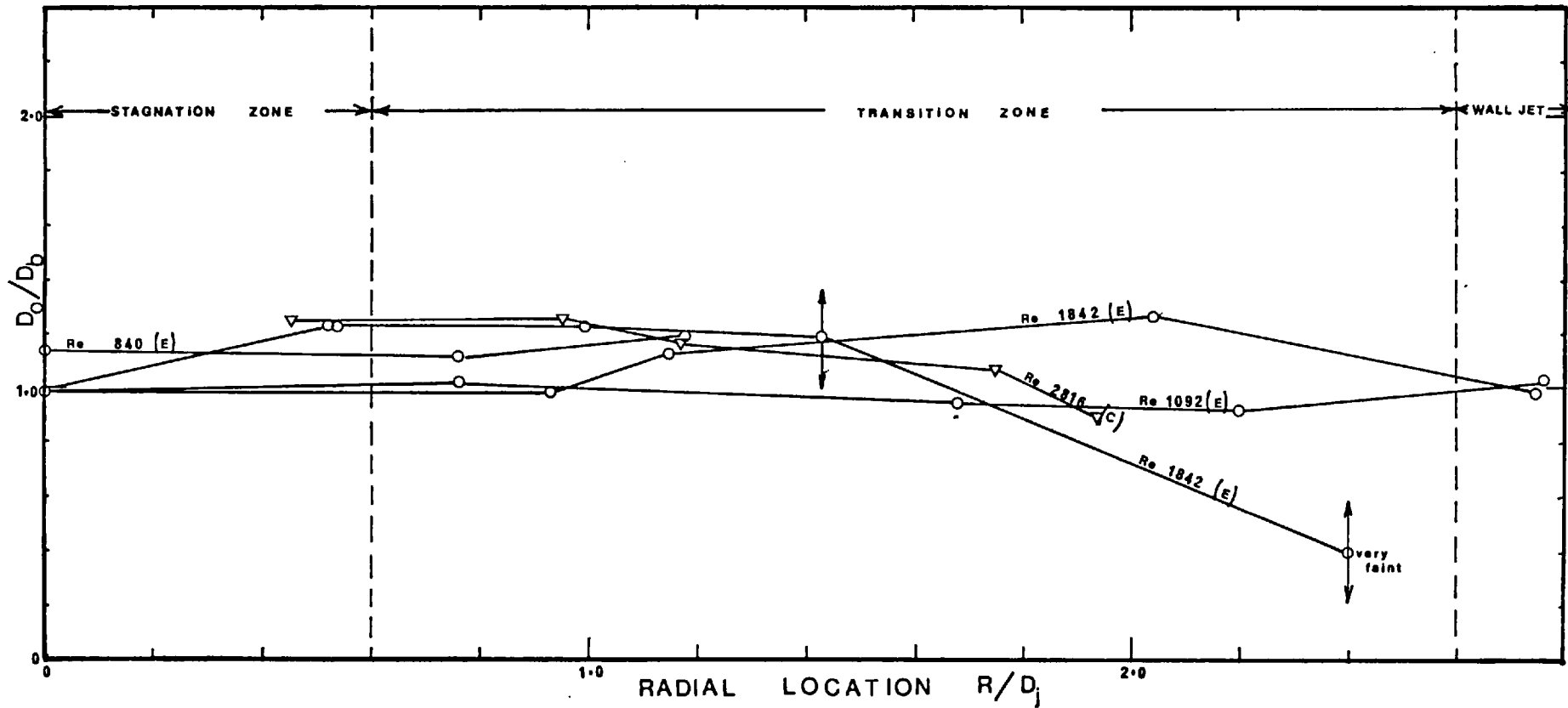
Fig 7.12 VARIATION OF THE INNER DIAMETER, D_i, WITH THE RADIAL LOCATION WITHIN THE JET

	P/D_b W cm^{-1}	jet plate distance, B, cm	vapour conc, ppm	time, s
E series	~ 11	3·81	~ 0·26	120
C series	~ 6	2·54	~ 0·38	120
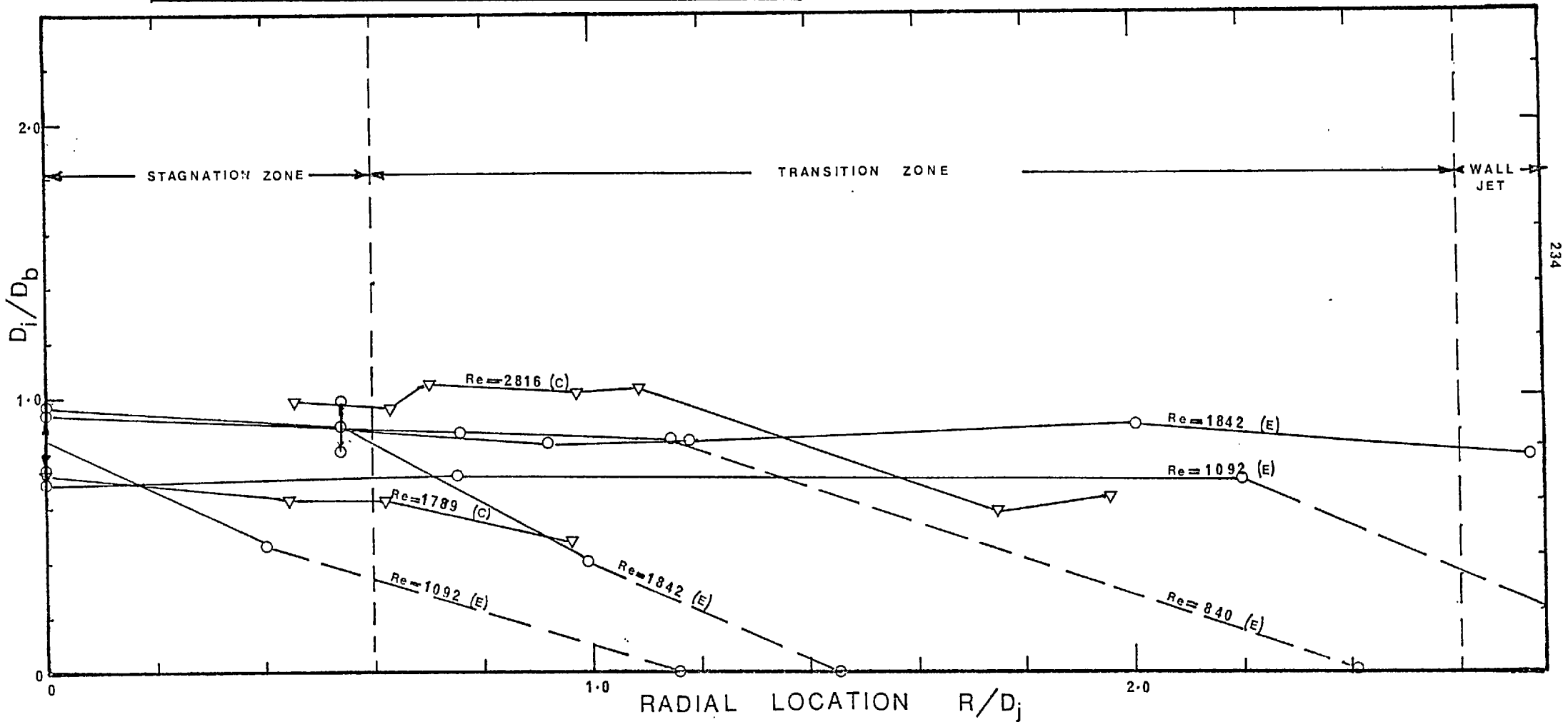
Fig 7.13 GROWTH RATE CURVES
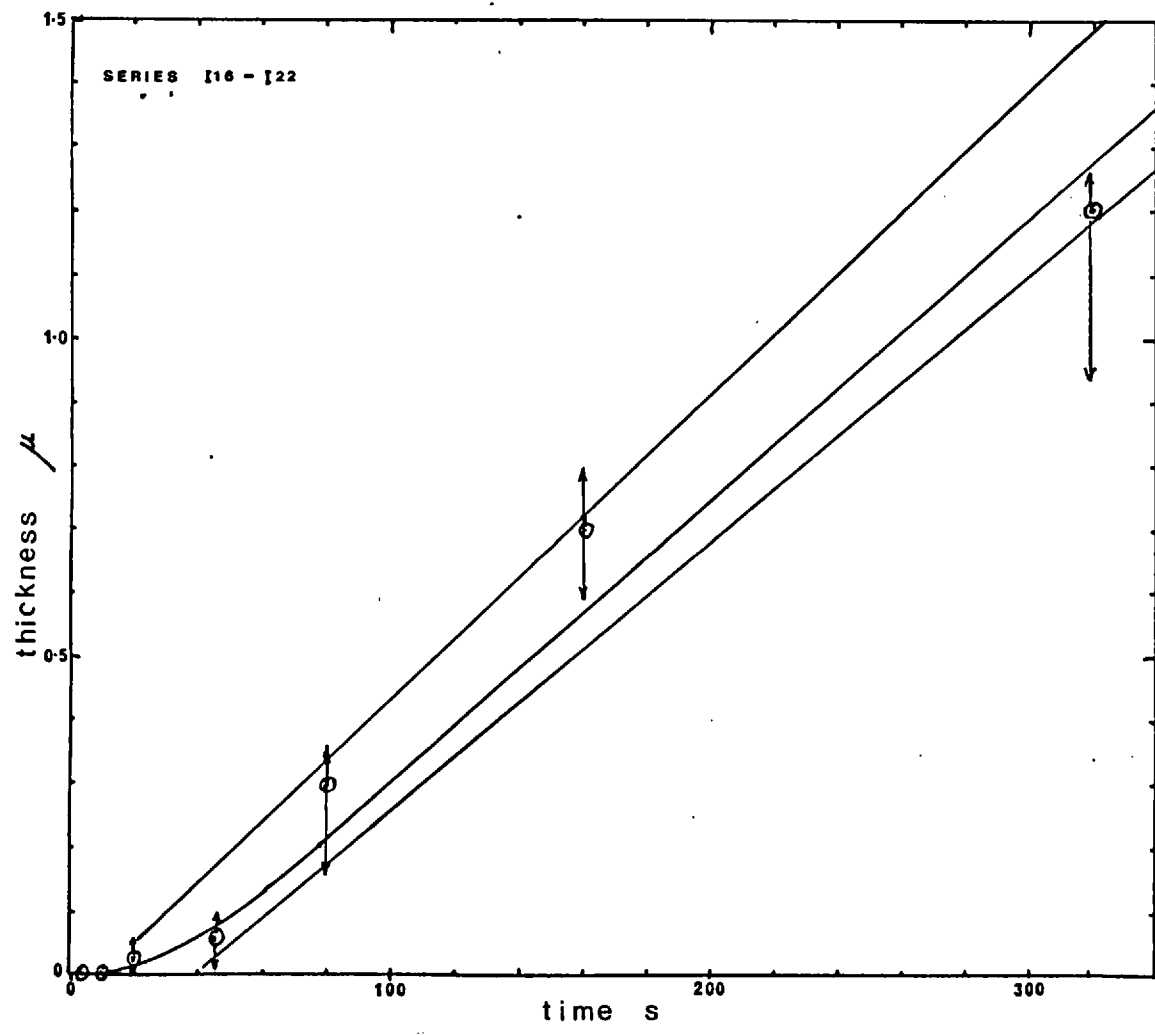
Fig 7.14   SPOT DIAMETER vs TIME
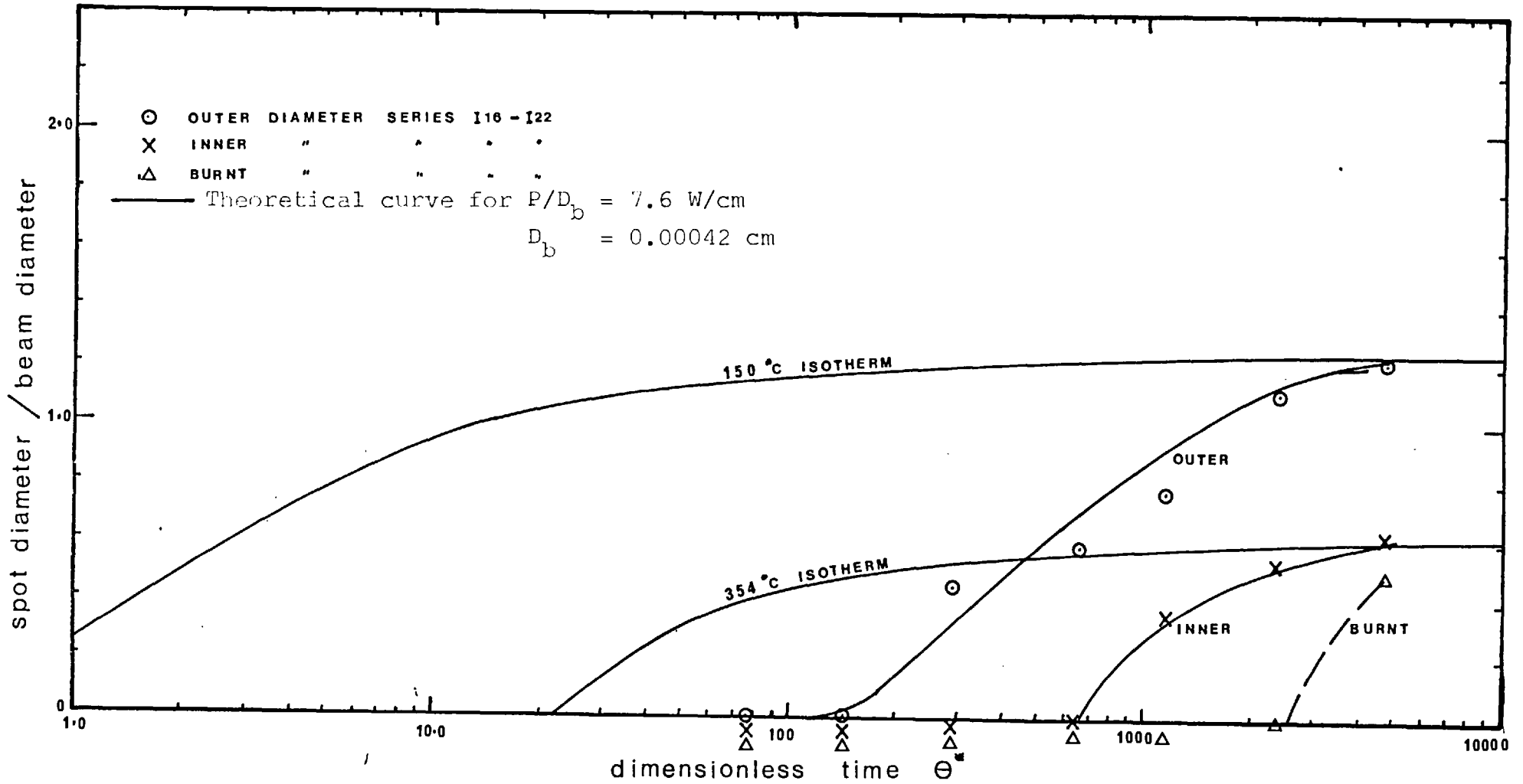
7.3.4.1. Variation of spot temperature during deposition

Thermal rise time curves have been discussed in section 6.3.2.2.10 page 174 and illustrated in figure 6.20 page 175

There are three principal observations from these curves:

(a) The long time, $\sim 50s$, taken to reach thermal equilibrium: (a fact which has been used to establish the beam diameter).

(b) The very low thermal inertia of the spots: the temperature fluctuations after equilibrium are thought to be due to power fluctuations in the laser beam. (The maxima seen on the rising part of the curve for C17 are due to checks on the centring of the thermodot.)

(c) The lack of any noticeable break in the curve suggesting a change in reflectivity: with the formation of a black centre in C32 an increased temperature or rate of rise would be expected. Such an event occurs but is not very remarkable. The increased slope observed is partly accounted for in the non linear temperature scale. Also on thin plate deposits no sharp rise, falling early, but continuing to rise slowly was found. This would be expected if there was a significant rise in reflectivity.

7.3.5 Effect of varying jet Reynolds number

Graph (7.15) and graph (7.16) and graph (7.17) all show the minimal expected and observed influence Re has in determining the deposit thickness and shape within the limited range of Re employed.

7.3.6. Effect of varying the jet/plate distance on deposit size

The jet/plate distance, B, was measured by a spacer block, as the distance from the jet tip to the centre of the impingement zone on the substrate.

Fig 7.15 EFFECT OF THE REYNOLDS NUMBER ON DEPOSIT THICKNESS
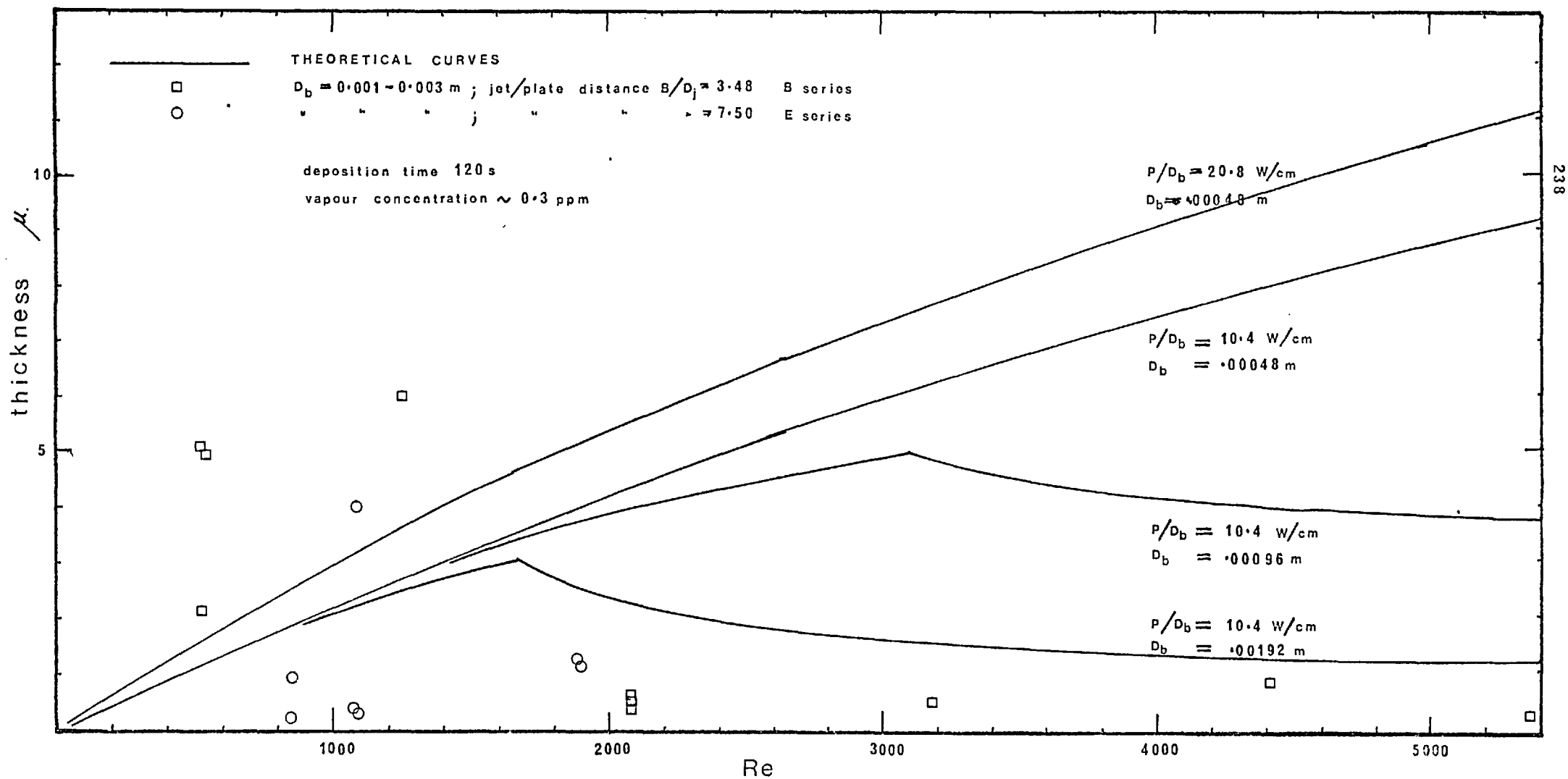
Fig 7.16   OUTER DIAMETER   vs   Re
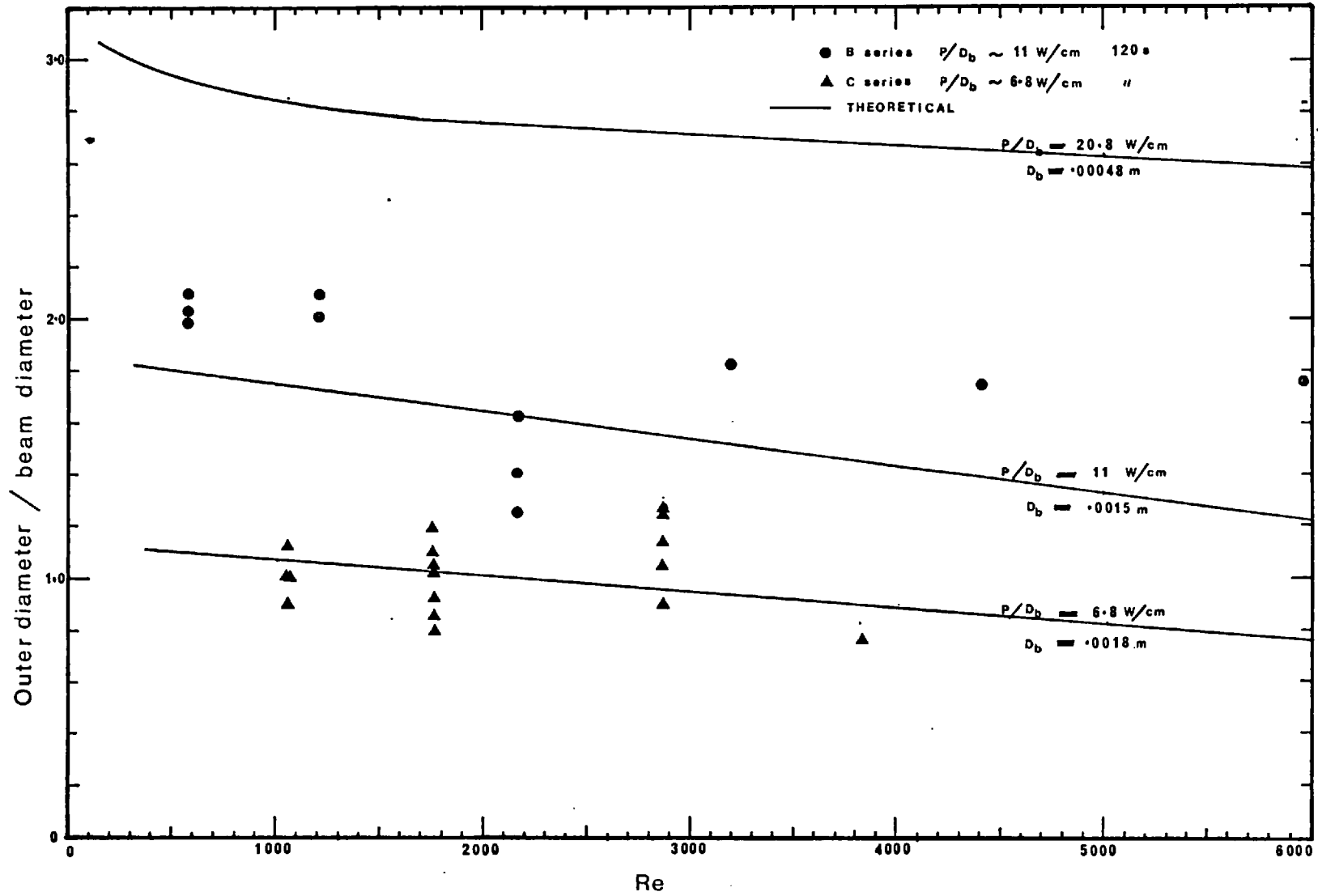
Fig 7.17   EFFECT OF Re ON INNER SPOT DIAMETER

THEORETICAL CURVE FOR $D_b=0.0015m$ $P/D_b=11.0$ W cm

B series
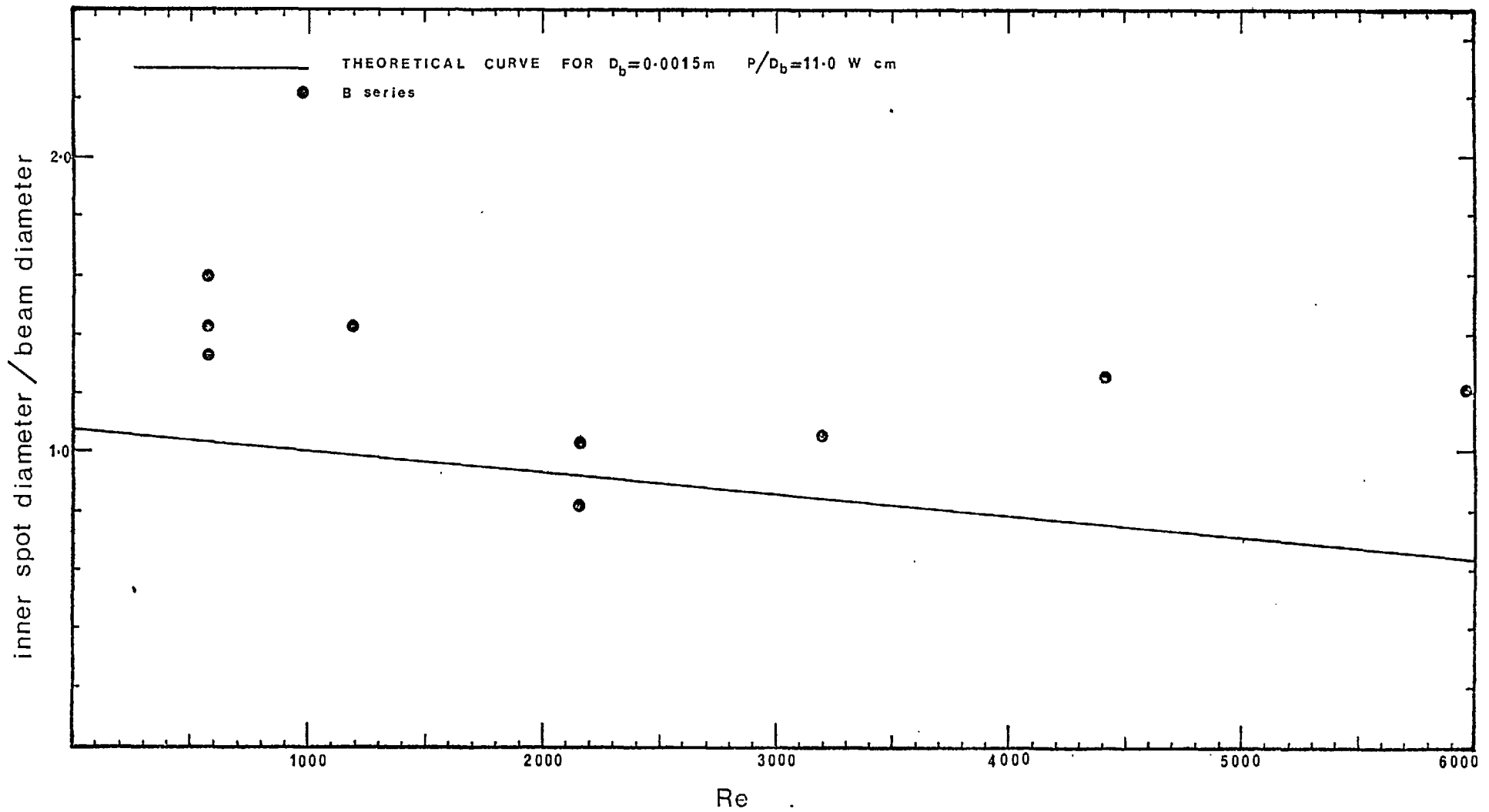
Initial qualitative experiments gave the experimental range of (B/D_j) for the apparatus used as $7.5 > B/D_j > 2.5$. Above 7.5 there was condensation of the chelate in the jet before striking the substrate, below 2.5 the laser beam was blocked by the heated jet tip.

Within these limits the F series of experiments was run to test the effect of jet/plate distance on deposition. To get the full range of B/D_j the jet was angled more steeply ($65°$ to the normal instead of $45°$ as with all other runs). Unfortunately some of this series were spoilt by humidity effects on the lens (shown by the effect of cleaning the lens). The variation of deposit diameters was however less affected and is shown in graph 7.18 together with the theoretical predictions.

Further experiments were made in the G series which agreed with this observed minimal dependence of deposit diameters on B/D_j.

7.3.7 Variation of deposit size with vapour concentration

The gas temperature and vapour concentration were not independent variables for the evaporator system used. All deposits were formed under one of two evaporator conditions: vapour concentration $\sim$ 0.27ppm and $120°C$ jet exit temperature or vapour concentration $\sim$ 0.31ppm and $140°C$ jet exit temperature.

A variation in concentration would not be expected to alter the extent of the deposit only the rate of growth.

Unfortunately the growth results, being an integral event, show far more scatter than that predicted, see figure 7.19. where series A and B are compared.

A larger variation in concentration at the deposition zone is found in the deposits formed with varying radial locations within the jet. These results are shown in graphs 7.15, 16, and 17, but they too will   differ in the local gas temperature.

Fig 7.18   DEPOSIT DIAMETER vs JET/PLATE DISTANCE
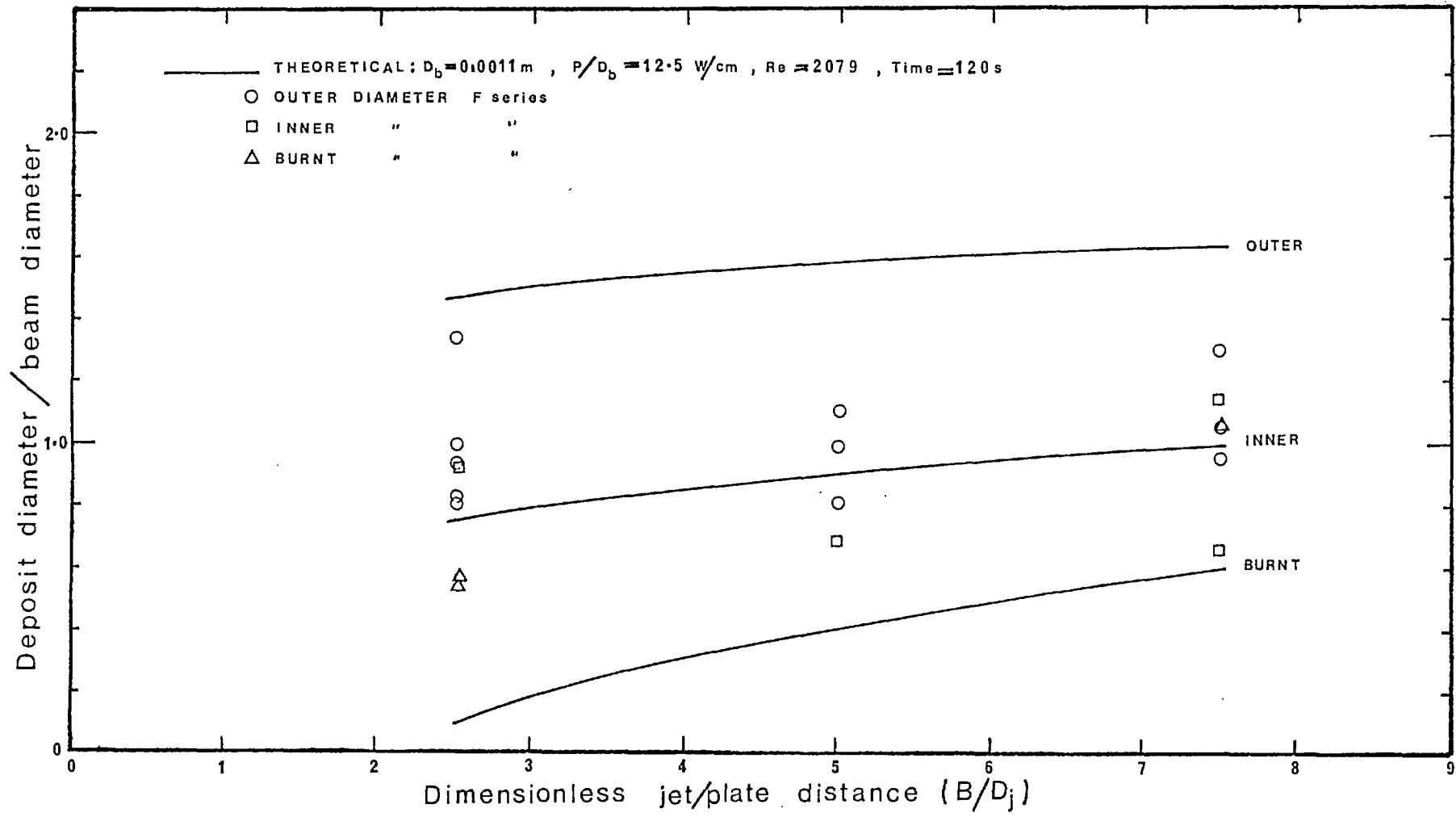
Fig 7.19 EFFECT OF VARYING JET TEMPERATURE

THEORETICAL CURVES: Re~2079 ; D_b-0·00192 m; T_a~100 °C ; B/O_j~7·5 ; time 120s

A   A series: conc~0·31 ppm   jet exit temperature 140°C

B   B series: conc~0·24 ppm   ·   ·   ·   120°C

conc: ·306 ppm

conc: ·256 ppm

Deposit thickness μ

P/D_b W/cm
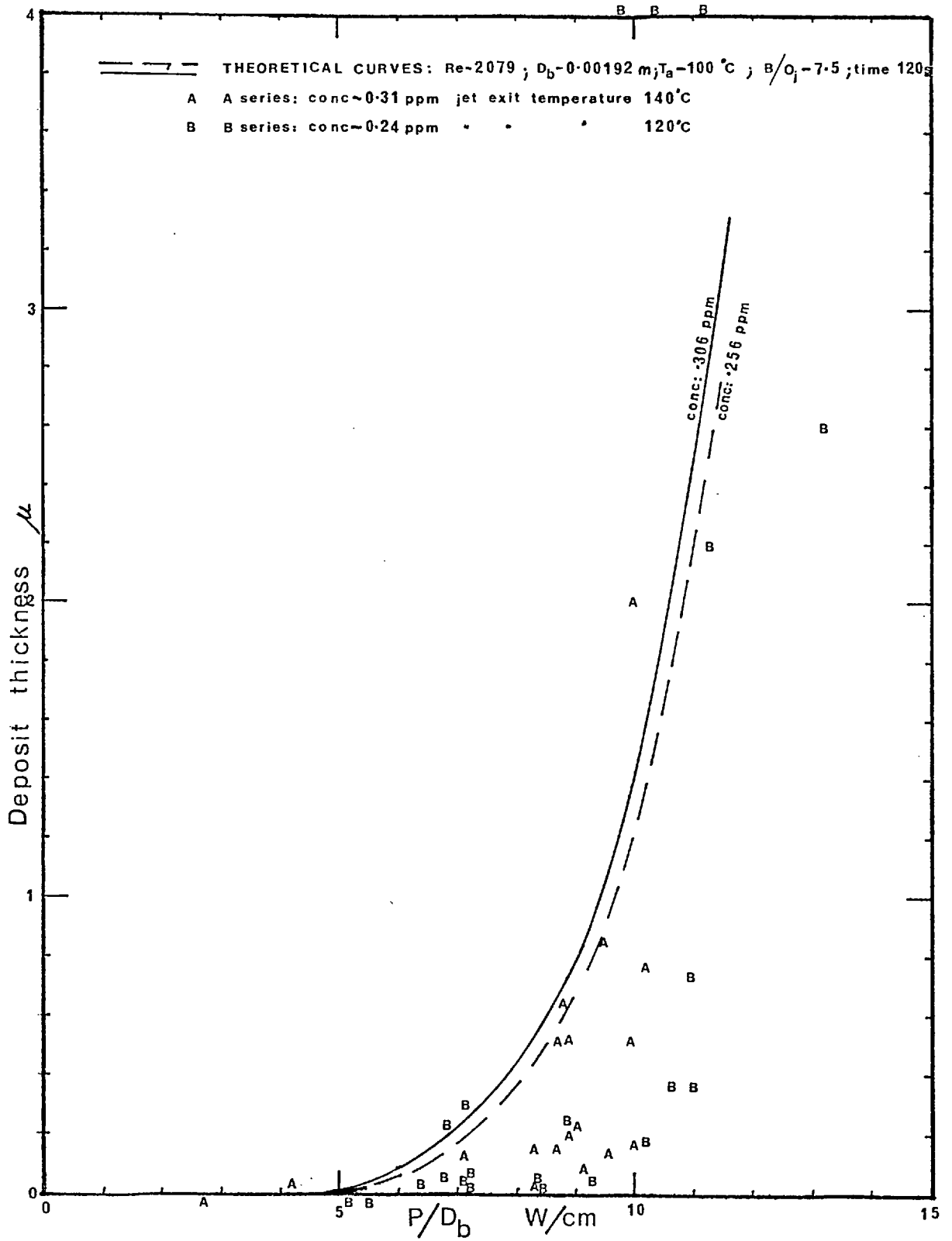
7.3.8 Variation of deposit size with Ambient Temperature

It follows from 7.3.7 that any observed variation in outer diameter between A and B could be due to variation in the ambient temperature and not likely to be due to the different concentration (though note section 8.2.4.1 - rate of growth).

The two jet exit temperatures used (120° and 140°) suffered some cooling in the free jet measured as $8^\circ C/cm$, for Re = 2079 by a thermocouple placed in the freely expanding jet. The initial drop in the jet core zone was smaller $\sim 2^\circ C/cm$. The core zone extended a distance of 4 x D_j.

To reduce this jet cooling, series A and B were run with the jet as close to the substrate as possible without blocking the laser beam.

A comparison of the outer diameters of the deposits from these two series as functions of P/D_b, graph 7.20, shows no significant effect due to the small temperature change used.

Fig 7.20   VARIATION OF JET EXIT TEMPERATURE
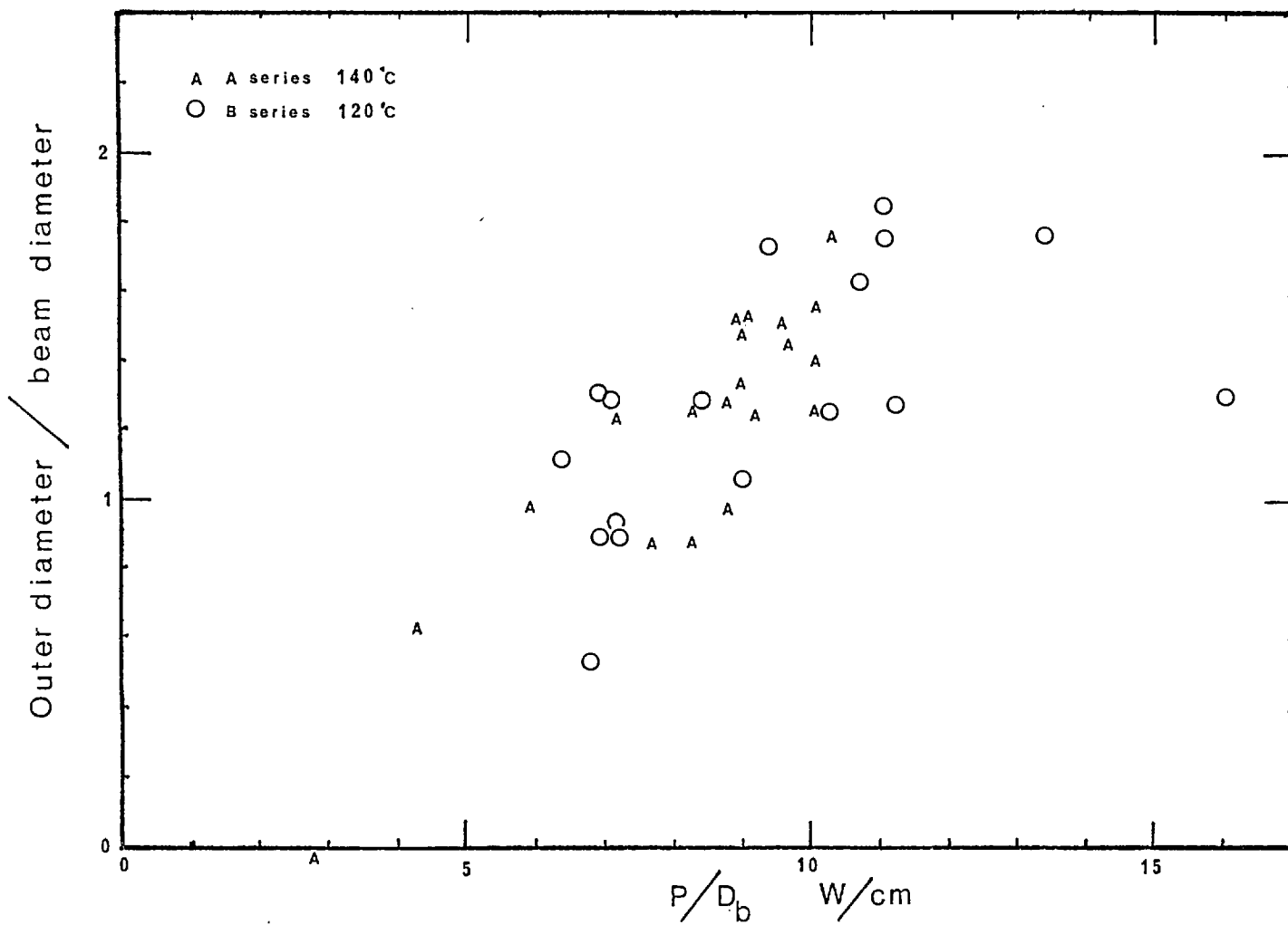
7.3.9 <u>Variation of deposit size with substrate properties</u>
Various substrates were tried:

(a) Copper: no deposit could be formed on copper foils
                0.1mm thick, with the power available. In
                fact it was noticed that even the chelate
                condensate which formed on the copper could
                not be evaporated at (P/D) values of less
                than 40 watts/cm.

(b) Alumina: Sheets of pressed alumina powder from
                Materials Research Limited were tried but
                shattered nearly every time a deposit was
                attempted.

(c) Glass: Deposits formed readily on glass, most runs
                were consequently performed on glass. The
                glass used is described in section 6.3.3.

(d) Silica (Spectrosil) A short series of deposits (I23-27)
                were formed on silica.

(e) Silvered glass: Glass, as in (c), was plated with $\sim$ .1μ
                of silver by vacuum evaporation. Deposition
                on the silver was attempted. No deposit formed
                until the silver was damaged.

A wider variety of substrates would have been possible
if more power had been available.

Comparing the soda lime glass and silica (spectrosil)
results. Graph 7.21 shows the slower growth of deposits on
silica and that they required approximately 10 W/cm for
deposition to start, whereas glass required only 6 W/cm.
These figures are dependent upon the correct calculation of
the beam diameter and power for the I series (and consequently
hold an error of $\pm 30\%$). But since the same optical arrangment

Fig 7.21   TREND IN DEPOSIT THICKNESS VS   P/D$_b$ FOR   GLASS & SILICA

SUBSTRATES
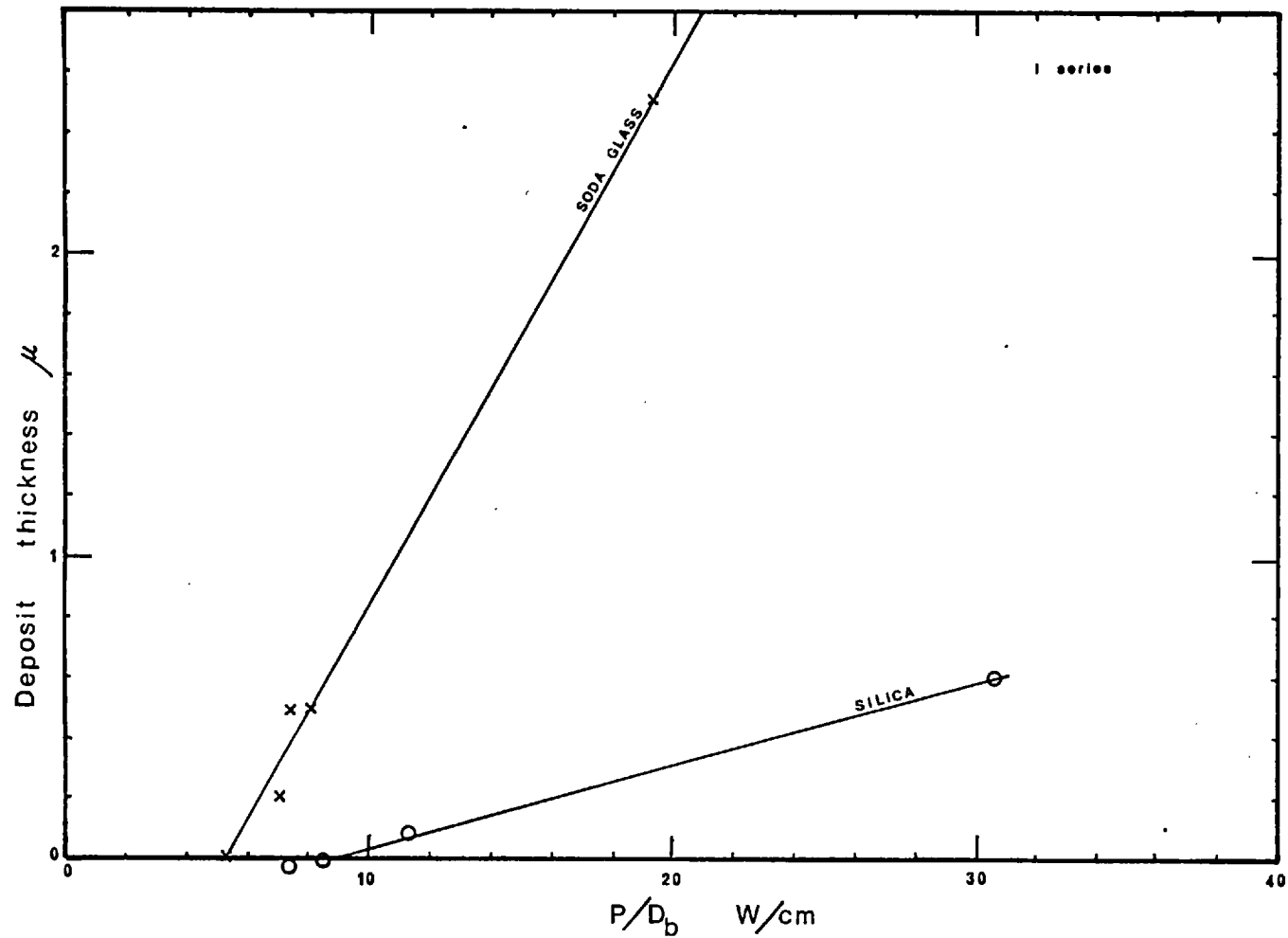
Fig 7.22 GRAPH SHOWING EFFECTS OF SUBSTRATE THICKNESS AND MATERIAL
ON DEPOSIT OUTER DIAMETER
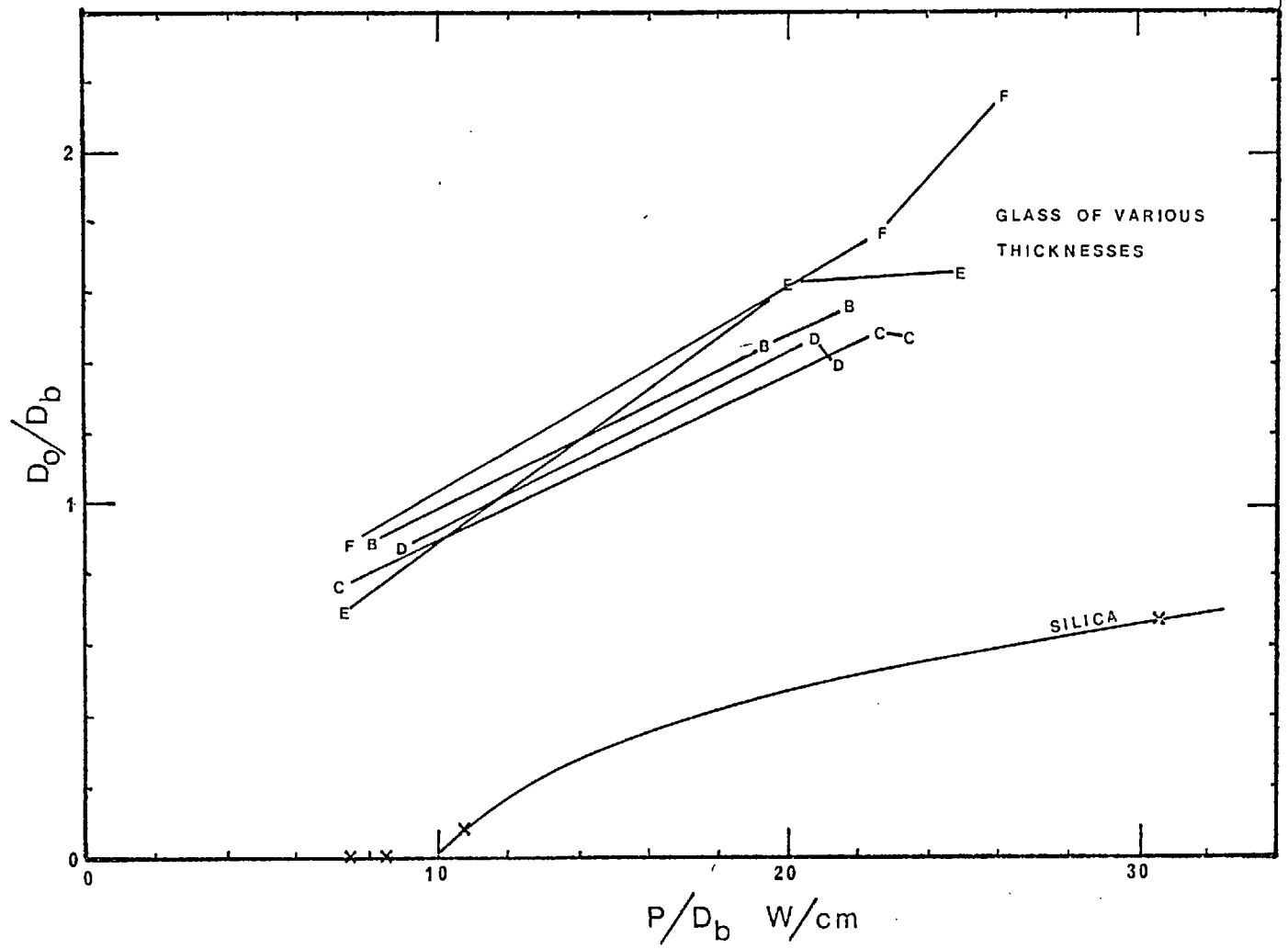
SYMBOL	THICKNESS	
B	1·2 - 1·5	mm
C	1·5 - 1·8	,
D	1·2 - 1·5	,
E	1·2 - 1·4	,
F	0·8 - 1·0	,
X	1·2	,

248

was used for both the relative power requirements of silica:
soda glass is 10:6 with an estimated error of ±10% due principally
to the power fluctuations.

Graph (7.22) shows the smaller size of deposits
formed on silica for a given value of (P/D_b).

The width of the skirt, [(outer - inner diameter)/beam
diameter], on the silica sample showing an inner diameter, I25,
was 0.39. Under similar conditions on glass the skirt width
was 0.23 (I1), 0.50 (I9) and 0.44 (I10).

7.3.10 Effect of laser modes

The non circularity of some deposits, such as C23 and H11
see plate 15 and the unusual formation of others, such as
the double peak of H10 - plate 15 , could be correlated with
asymmetric mode patterns from the laser as observed on char
prints.

Under these conditions an irregular power distribution
emerging from the aperture would be expected. As an example;
a highly striated mode pattern in the beam, was observed before
and after sample H10 was formed see plate 15. Two of these
striations would be expected to pass through the 0.5 cm diameter
aperture and could consequently explain the twin peaks found
in sample H10.

A detailed analysis of this phenomenon was not attempted.
some 'mode' printing has been shown to occur by A. Young under
the author's supervision.

7.3.11 Variation of spot temperature during deposition

The time dependence of the central spot temperature has been discussed in section 6.3.2.2.10.

The temperature profile was examined by transversing the thermodot TD17 IR thermometer across the forming deposit. The resulting convoluted temperature signal showed a near Gaussian profile, not in obvious disagreement with the theoretical predictions of the temperature profile.

CHAPTER 8

DISCUSSION

CHAPTER 8

DISCUSSION

8.1. Image Formation Studies

8.1.1. Effect of variable object area

The larger areas of an image showed signs of having been hotter than the smaller areas.

If the aperture/object is uniformly illuminated then the power density over the area of the image will also be uniform, regardless of the size of the area, neglecting truncation and lens aberration effects.

It might be expected that the power density, measured as watts/cm^2, would decide the temperature of the region. So with a uniform power density the varying sections in the image would print uniformly. Sample AK (plate 4) shows that this does not happen.

The theoretical model has shown that $T^* = \dfrac{\pi k T D_b}{P(1 - r_f)}$ is the parameter defining the temperature. In particular it was seen (page 73) that $T^* = 1.77$ for the case of no surface heat loss and at infinite time. Thus (P/D_b) not $(P/D_b{}^2)$ is the prime variable defining temperature on a given substrate. This was interpreted as being due to the heating effect being dependent on the total incident power which is $\alpha\ D^2$, but the volume heated by thermal conduction $\alpha\ D^3$ i.e. $P \times D^2/D^3$ crudely represents the thermal balance.

The dot sections at the ends of the dumbell cross measured 2.0mm diameter and the connecting bars measured 0.5mm in width. Thus the temperature difference between these regions would be expected to be about 4. Since neither section is totally circular the actual factor would be less than 4. Such a difference in temperature is quite sufficient to explain why craters formed only in the larger areas of AC (plate 4) or why printing only occurred

in the larger areas of AK (plate 4   ).

There are two principal conclusions to be drawn:
a) The parameter (P/D_b) is of more relevance to this work, and related spot heating phenomena than $(P/D_b{}^2)$.

b) To print a particular shape the object/aperture will not necessarily have the same shape, but should have areas dependent on D rather than D^2, in fact something resembling an outline is required.

8.1.2 Effect of focal position

A parallel beam of light passing through an aperture will not behave as the light from an aperture radiating according to Lambert's law. The parallel beam will remain effectively parallel except for truncation and diffraction effects. A parallel Gaussian beam is self propagating (101). So on passing through a lens the size of the beam pattern will alter as the focal point of the lens is reached after which the beam is inverted but keeps the same pattern. This is simply shown by ray tracing. The diffraction and truncation effects would get progressively more significant with increasing distance from the aperture. Lens aberration effects would be minimal at the focal point of the lens. Thus, due to the very small divergence angle of the beam from the aperture no particular effect is expected at the point of focus of the image of the aperture. In fact any small sharpening of the image at that point compared to that at locations nearer the lens would be lost due to the increasing diffraction spread with distance.

The char sequences figure 7.1   thus come as no surprise. But the location, if any, of the clearest image becomes complex. This is discussed in sec 8.16   under the general subject of image clarity.

8.1.3. Effect of a hot aperture/object

Towards the end of a series of experiments blurred deposits were sometimes formed with material being deposited at a distance from the heat image, (plate 4 AM, AN).
This led to the speculation that a significant heat flux was falling on the substrate from the focussed image of the hot aperture plate.

Unlike the parallel laser radiation passing through the aperture and striking only a localised spot on the imaging lens, the hot aperture plate would behave as a Lambert's law radiator from which the radiant flux would strike the lens as a whole. The magnitude of this flux would be given approximately by the Stefan-Boltzmann equation:

$$q_{A \to L} = \sigma \ T_A^{\ 4} \ A_L \ F_{LA}$$

where subscript L refers to the lens,
    subscript A refers to the aperture,
 and the matt black aperture is considered to have an emissivity of 1.0.

The area of the lens, A_L = 11.3 cm^2. The view factor of the aperture from the lens $F_{LA} \approx$ 0.01 (from the F factor chart in Perry's Chemical Engineers handbook, 4th edition, page 1037, graph 10.19. For two parallel discs 52cms apart with the smaller diameter/distance apart = 0.073.)
From which:-

$$q_{AL} = 0.64 \ x, 10^{-12} \ x \ T_A^4 \quad \text{watts}$$

For a maximum possible temperature of the metal around the aperture of 300°C = 573°K

$$q_{AL} = 0.07 \ \text{watts}$$

The image size was reduced by a factor of 10 giving a value of P/D of the order of:-   0.18 W/cm.

This is the extreme value of P/D from this source and on its own is insufficient to cause deposition. However, added to a region bounded by a hot image on three sides as in AM and AN it could be crucial being 2-4% of the heat required for deposition to start.

To avoid a risk of this effect entering the rate studies two precautions were taken:

a) Long object/lens distances were arranged
b) A water cooled aperture was used.

8.1.4 Effect of nonuniform illumination of the aperture

This is the same as having a different shaped aperture.

8.1.5 Effect of extended heating
(see section 8.2.2.2. on spot diameter - varying with time)

For complex shapes as in sample AQ the effect of extended heating will be more marked for incurvate shapes due to the thermal inputs of the region. An infinitely long heating period of a finite slab would eventually heat the whole slab and, depending upon natural convection, could well raise the whole slab above the deposition temperature. The deposit shape under such circumstances would be defined partly by the variable mass transfer field from an impinging jet, - in fact a circular deposit as described by Davies (41) - and partly from the temperature profile which would still be present.

8.1.6 Clarity of Prints

The 'clarity' of the prints is defined as the sharpness of the print edge. It depends on the flow of heat within the substrate generating a certain thermal profile, and on the temperature dependence of the rate of deposition. For really clear images either or both of these should be a step function; however, since that is not physically possible an approximation as near as possible is sought.

Thus to achieve sharp prints:

1) The edge of the temperature profile should be as steep
    as possible within the substrate. The factors affecting
    this are:-

    a) Low thermal conductivity substrates (see section 8.2.9.)
    b) Low ambient temperature (see section 8.2.8.)
    c) Cool aperture (see section 8.1.3.)
    d) Steep power profile (see figure 3.6   and note further
        that the steepest profile for a given distribution is
        at the focal point of the lens).
    e) Short heating time or pulsing.

2) The location of the deposition isotherm should coincide
    with the steepest part of the thermal gradient. This would
    be possible on most occasions by a suitable choice of jet
    Reynolds number (see section 8.2.5).

3) The growth rate should be as fast as possible subsequent
    to the deposition temperature being achieved. This means
    a high vapour concentration (see section 8.2.7).

4) The central region of the hot spot should have a uniform
    temperature, if a uniform deposit is to be achieved. As
    discussed in section 8.1.1. this would involve a specially
    designed aperture to ensure a uniform value of (P/D_b) over
    the region.

8.2 Rate of Deposition Studies

8.2.1 Deposit structures

The formation of circular deposits by pyrolysis on a variable
temperature zone results in a number of structural features.
They are:-

    a) The outer, inner and burnt diameters
    b) crater formation
    c) blue spot formation

d) cracking of the substrate

e) peaking

f) thin film formation

g) diffusion into the substrate.

These will now be discussed in sequence.

8.2.1.1 Outer, inner and burnt diameters

The outer, inner and 'burnt' diameters defined in section 7.3.1 can be associated with various isotherms as discussed in sections 8.2.2.2, 8.2.2.3 and 8.2.2.4.

The outer diameter is associated with a temperature of approximately $150°C-200°C$ the temperature at which CoAcAt starts to decompose (41,85).

The inner diameter is associated with a film temperature of approximately $500°K$ which, for the vapour concentration used, is the isotherm at which the rate of decomposition starts to increase rapidly with a small rise in temperature. The 'burnt' diameter is associated with a temperature of around $500°C$. At around this temperature boundary layer control of the deposition process would be expected to become rate determining and also the glass substrate would be expected to start to move due to thermal stresses.

The inner and outer diameter phenomenon can be predicted from the theoretical model as illustrated in figure 8.1 showing the theoretical section through a mound deposit.

8.2.1.2 Craters

It was found that craters were formed in specimens subject to a (P/D_b) value in excess of 16 ± 3 W/cm. In order to check that this value was not a function of either the chelate decomposition process (i.e. a surface tension effect etc.) or the jet blowing on the surface (i.e. pressure effects etc.), tests were made on glass with no chelate or jet blowing, in fact with only the focussed laser beam on the glass substrate.

Fig 8.1   THEORETICAL   DEPOSIT   PROFILE

$\Theta^* = 25.5$

$\Theta^* = 10.7$

$\Theta^* = 0.94$

P/D_b — 41.5 w/cm
Re —— 1671
D_b — .24 mm
T_a — 100 c
C_o — .306 ppm

OUTER RADIUS

INNER RADIUS

Thickness $\mu \times 100$

Dimensionless   radius R^*

0.5   1   1.5   2

258
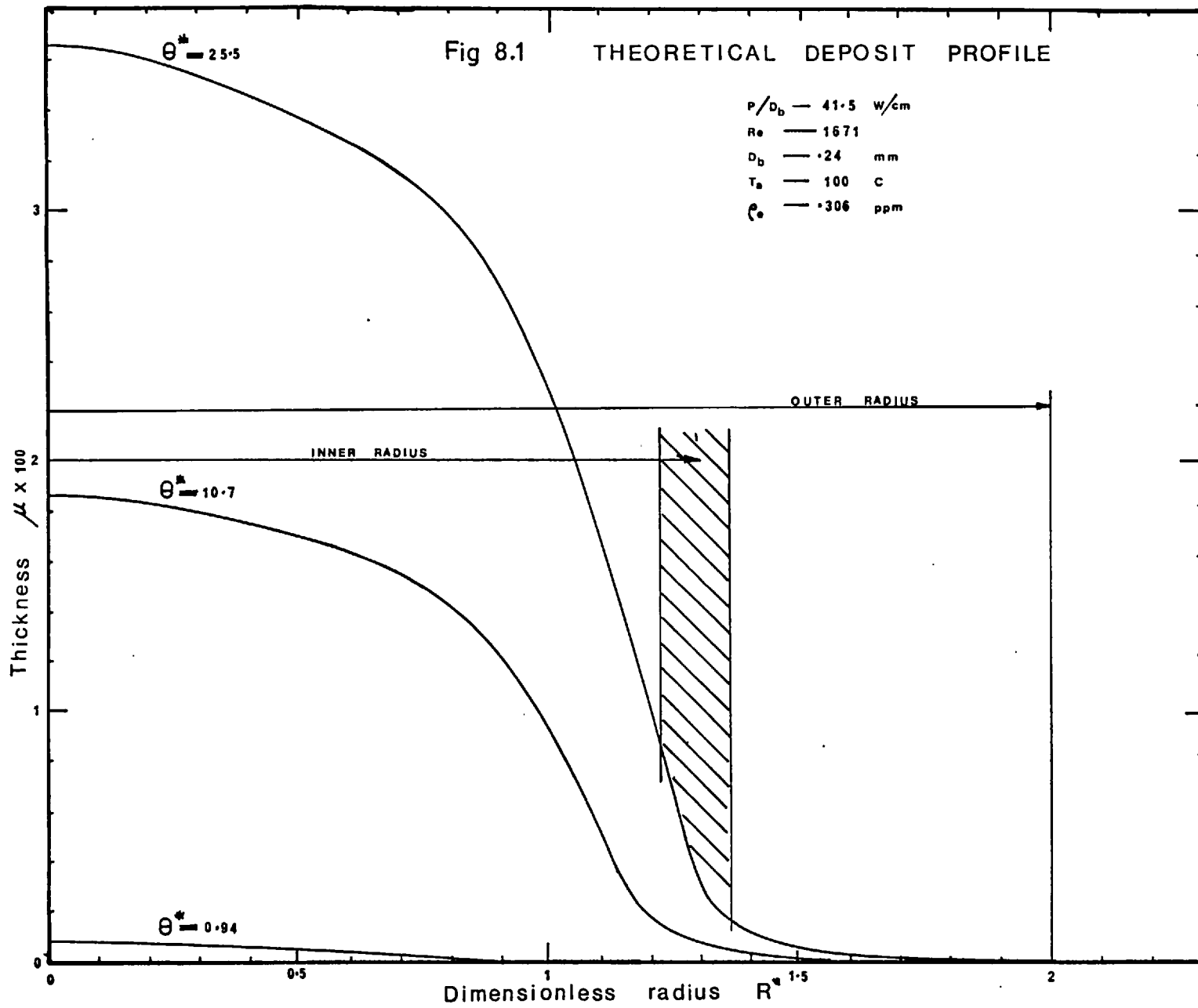
Tests were also made with a jet blowing but with no chelate. The results are shown in table 8.1 .

Sample	(P/D_b) watts/cm	Whether cratered ($\checkmark$=cratered)	Expt Conditions	Minimum P/D_b for cratering mean value
1	26	$\checkmark$	No jet	
2	21	x	or	
3	28	$\checkmark$	chelate	
4	23	$\cancel{\checkmark}$		20.0
5	28.5	$\checkmark$		— 17.5
6	20.0	$\cancel{\checkmark}$		= 18.7 ± 2
7	10.5	x		
8	10.0	x		
9	17.5	$\cancel{\checkmark}$		
10	16.0	x		
11	12.0	x		
12	25.0	$\checkmark$	with	
13	24.0	$\cancel{\checkmark}$	140°C jet	
14	20.0	$\cancel{\checkmark}$	Re=3895	20.0 ± 3
15	10.0	x	$B/D_j = 10.0$	
16	16.0	x		
17	17.5	x	no chelate	

Table 8.1

The onset of cratering was 15-20 watts/cm. A value of (P/D_b) of 15 watts/cm for a typical spot size of 0.042 cms would result in central temperatures of the order of $700^{\circ}C$.

Thus, it is surmised that a minimum temperature of the order of $700^{\circ}C$ is needed before cratering occurs.

The cause of cratering is neither jet pressure nor chelate surface effects and must therefore be due specifically to thermal causes. One of which could be evaporation of the glass, as in standard laser drilling, but such an event requires temperatures in excess of $2000^{\circ}C$ with possible plasma formation, both highly visible activities which were not noticed nor predicted by the theoretical model.

Another possible thermal cause which would result in cratering is thermal stressing. This is now considered further.

8.2.1.2.1 Thermal stress analysis of a hot spot

Over the past twenty years or so considerable attention has been paid to thermal stresses in welded sections which has led to a series of theoretical and experimental papers on thermal stresses due to spot heating reviewed by Masubuchi (120).

The foundation work was done by Watanabe and Sato (118) and H. Kihara and others (121), who studied this process comprehensively for a disc source on a thin plate by using Mises yield criterion. Otani (122) had previously developed a graphical solution for a similar problem using Tresca's yield criterion. Masubuchi (117) working from Watanabe and Sato's paper develops graphs for the thermal and residual stresses due to spot heating a plate. In the present experiments on deposition the isotherms could be considered almost spherically symmetric whereas in the model discussed by Masubuchi and similarly by Kihara (119) a cylindrically symmetric system is assumed. This is equivalent to a line heat source through the substrate as opposed to a surface disc source. However, the

results given by Masubuchi show qualitatively the variation in stress expected in the thin glass slides used here. A check on this was made by calculating the stress distribution expected in a non-uniformly heated sphere as discussed by Timoshenko and Goodier (123) it showed reasonable similarity. Hence Masubuchi's results were used qualitatively in the following arguments.

Masubuchi assummed:

1) radial symmetry with only radial,σ_r,and tangential,σ_t, stresses.

2) mean invariant values of the modulus of elasticity, yield stress,σ_y, & coefficient of linear expansion.

3) no stresses held in material above 700°C.

4) the stress strain curve is:
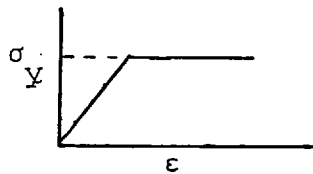
5) there is instantaneous plastic flow.

6) the initial temperature distribution is shown in figure 8.2

7) the stress in the plate was zero before heating.

By a numerical method of adding the stresses generated during small time steps to the stresses present before the time step the thermal and residual stresses shown in figures 8.3 & 8.4 were calculated for a mild steel plate.

From this analysis three regions can be identified.

(i) Region I ($0 \leq r \leq r_1$). The central region where non elastic deformation occurs during heating and also during cooling.

(ii) Region II ($r_1 \leq r \leq r_2$) an annular region around region I where plastic deformation occurs during heating but strains after cooling remain elastic.

(iii) Region III ($r > r_2$) a region where plastic deformation does not occur during the thermal cycle.
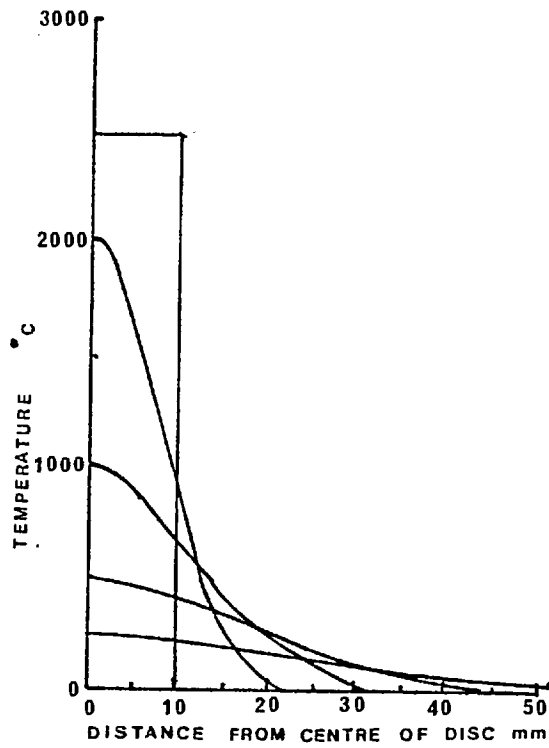
fig 8.2 Assummed initial temperature distribution
and subsequent profiles
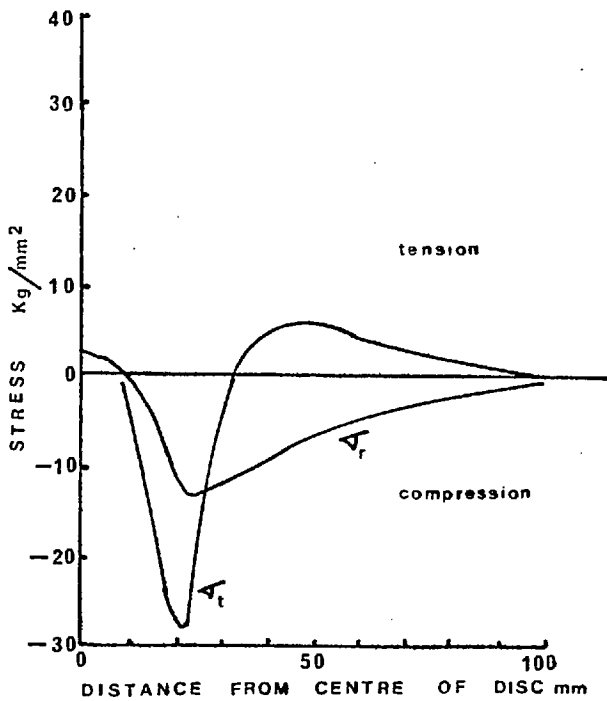
fig 8.3

fig 8.4

Stress distributions when centre temperature has fallen to:

600 °C

0 °C
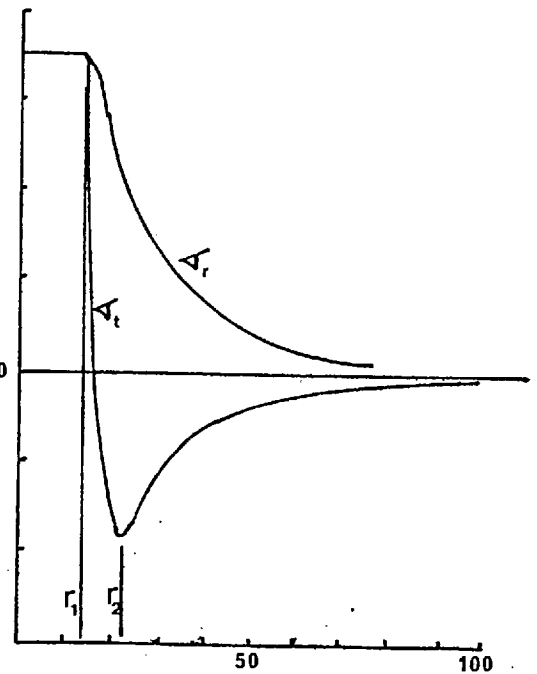
i.e. residual stress

Qualitatively the same stress pattern must occur in glass as
in the mild steel example of Masubuchi with the values of r_1 and r_2
being functions of the beam diameter and power. In the case of
heating a large hollow sphere it can be shown (123) that σ_r
is a minimum at $(a \sqrt{3})$ where a = radius of the hollow centre (or,
in the analogy, the plastic or molten centre). The minimum shown
by Masubuchi is approximately that relationship to the plastically
deformed zone, which corresponds to the value of r_2.

From this it appears that an annular region between 'a' and
approx: '2a' is subject to compressive plastic deformation - creating
an annular ridge - the region less than 'a' flows plastically under
a tensile force during and after heating forming a hollow. However,
it is to be noted that the ridge or crater forms during heating when
the compressive stress is a maximum both tangentially and radially.

Whether this plastic strain is to be expected in glass subject to
values of $(P/D_b) \geq 15$ watts/cm or rather with central spot temper-
atures of around $700^{\circ}C$ is the next question.

The manufacturers of the glass used give a value for the
softening point as $585^{\circ}C$. That is to say, that at this temperature
internal stresses in the glass are relieved within minutes. Thus,
a temperature of $700^{\circ}C$ would be expected to allow plastic flow within
the two minutes allowed for most deposits, with the consequent
formation of a crater as described.

For lesser values of (P/D_b) the heating would not be sufficiently
intense to cause a region I. Under these circumstances the central
region will be under compression during heating both tangentially
and radially. Plastic flow can occur within hours above the strain
point, which is given as $470-490^{\circ}C$. Thus, provided this temperature
is exceeded some inward plastic flow would occur. If this happened
after a deposit had been formed or partially formed the deposit
would be wrinkled into a 'pinch' formation as in sample D9 and F13
and result in a 'peak'. (see plates 11, 14)

8.2.1.3 Blue Zones

Blue centres were observed in some samples (e.g. I1-I10) The lowest value of (P/D_b) recorded for blue centred deposits is that for I1 at 19.3 ± 2.7 W/cm.

Such a value of (P/D_b) would be expected to give a central temperature of $956^{\circ}C \pm 150^{\circ}C$, since $T_{o8}^{*} \simeq 15.7$ for the I series.

Glass becomes truly fluid above $1400^{\circ}C$, and consequently for blue centred deposits the centre would have been quite fluid.

Under these conditions cobalt oxide will dissolve in glass forming $(CoO_4')^{2-}$ groups linked through the four O' ions to the (SiO_4') groups as structural building units with two alkalii or one calcium ion in close association to ensure local neutrality. The $(CoO_4')^{2-}$ ion gives a vivid and strong blue colour. Even very small concentrations of cobalt in glass can completely block the passage of red light. Larger concentrations of cobalt will appear black (124).

8.2.1.4 Cracks

Three fundamental crack patterns were observed:

TYPE I   A Herzian type cone fracture, example Plate 16a which was horseshoe shaped on the surface cutting into the surface at an angle of around 45°. Such a fracture is typical of a point load. In this case a point tensile load.

TYPE II   A Herzian type again but with numerous radial branches, example F13 plate 14 .

TYPE III An 'H' style fracture; example D25. Plate 16(b)

Considering the negligible strength of glass to a tensile load, and the calculated fact of significant tensile stresses both during heating and upon subsequent cooling cracking is to be expected.

The Herzian types I and II are expected from the stress analysis which reveals a stress pattern over the heated region similar to a point tensile load. The type III double horseshoe or 'H' fracture is

possibly more involved. In particular, sample D25 is known to
have cracked in this way several days after the deposition.
The cracking would consequently be expected to depend on the
residual stress distribution, triggered possibly by a knock, the
talysurf needle or some other cause. The residual stress
distribution is qualitatively shown in figure 8.4   in which high
central tensile stresses are apparent.

8.2.1.5 Peaks

Quite abrupt peaks were observed on some deposits for
example D9 and B18. ^{plates 11,12} The appearance of D9 suggests some movement
of the substrate rather than a new deposition mechanism and such
a theory is supported by the reasoning on crater formation.

An alternative possibility is that, as mass transfer control
takes over, preferential growth would occur on points rising into
the concentration boundary layer. These points would not only
grow faster because of the enriched vapour but also because their
thermal contact with the substrate is weaker, and the rough surface
created lowers the reflectivity and so they become hotter which in
turn increases their rate of growth.

It is the abruptness of the peak and the patterned structure of
the wrinkles which are not explained by this alternative. For, if
the temperature rose the increased deposition rate is not very large
under boundary layer control (see figure 3.19 page 87   ) and if the
reflectivity fell from 0.18 to 0.0 little difference in temperature
is expected (see section 8.2.10). If direct pinnacle heating
occurred then random pinnacles and spikes would be expected, not
ridges and patterned wrinkles as observed.

So it is concluded that peaking, as distinct from black central
zones, is due to the movement of the substrate under thermal stresses
It is the condition just prior to cratering.

8.2.1.6 Thin Film Formation

Deposits formed using a low value of (P/D_b) seemed to grow quickly and then stop and remain as very thin flat plates.

It seemed possible that a thermal cut off occurred due to a rise in reflectivity and thus the deposits automatically grew to a certain thickness (reflectivity) and then stopped. Accordingly, the reflectivity of these deposits to 10.6μ radiation was carefully measured (page 205) surprisingly there was no significant rise noted, and certainly not enough to cause any temperature change sufficient to halt deposition.

An alternative explanation is that the opacity of CoO is good and hence the deposit appears to form after a few molecular layers have been deposited; while in actual fact deposition continues, with no obvious change in appearance, at the very slow rates appropriate to the low value of (P/D_b).

8.2.1.7 Diffusion into the substrate

As reported in section 6.3.4.5, some deposits would not dissolve in boiling dilute or concentrated nitric acid. Had they been made of CoO, Co, or Co_3O_4 they would have dissolved readily.

Those that did not dissolve had been subject to the more severe heating. The less highly heated specimens dissolved quickly.

Diffusion into the glass was suspected. So a sample was sectioned but no penetration observed.

The diffusion of cobalt into glass follows analogous equations to the flow of heat into glass. The diffusion coefficient for Co in glass should be of the order of 10^{-9} cm^2/s @ $600°C$ by comparison with the value of copper given by Doremus (125). On the other hand the thermal diffusivity of glass is around 2.9×10^{-3} cm^2/s.

The thermal penetration of the $150°C$ isotherm is found from the theoretical model to be approximately a factor of 0.35 of the spot diameter after two minutes.

Thus for a large 2mm diameter spot the thermal penetration of the 150°C isotherm is around 0.7mm. The rate of penetration is proportional to the diffusivity and hence the depth is also. Thus the maximum possible depth of diffusion is of the order of

$$\left[\frac{0.7 \times 10^{-9}}{2.9 \times 10^{-3}}\right] \text{mm} = 0.24 \times 10^{-3} \text{ microns}$$

It is not surprising that no penetration was observed since only a few atomic layers would have been penetrated. This is sufficient for chemical refractoriness but not sufficient to be seen by optical microscopy. It is also sufficient to explain the firm adherence of the deposits.

It is interesting to observe at this point that the diffusivity is a strong function of the temperature. So the thermal field considered here represents a diffusion cage. Diffusion can not proceed in a finite time beyond certain isotherms. Thus this spot heating technique could be used for controlled depth diffusion.

8.2.2   Effect of P/D_b

8.2.2.1. Effect of (P/D_b) on deposit thickness

Graph 7.4 page 222 shows the fit between the theoretical prediction of deposit thickness as a function of (P/D_b) with the experimental results.

The theoretical curves show the sensitive dependence of growth on temperature in the chemically rate controlled region and the less dependence in the region whose rate is controlled by boundary layer gradients. They also show the effect of beam diameter. This, perhaps unexpected dependence, is due to heated spots having a convective and radiant heat loss proportional to their area (i.e. beam diameter squared) causing larger spots to run comparatively cooler. A further effect is due to larger spots heating up slower causing a significant reduction in available deposition time. (approx: 20s in a 120s run using a 2mm diameter beam).

The experimental fit is reasonable in the chemically controlled zone bearing in mind the complexity in calculating the beam diameter, the unavoidable power fluctuations from the laser during most runs, and the fact that the jet was not vertical as assumed in the theoretical model. Growth is an integral event and so every power fluctuation adds to an accummulated deviation. For this reason, it is not so surprising that the small dependence on beam size is not observed.due to the experimental scatter.

The expected fall in growth rate as the boundary layer gradients become rate determining was not observed. It has been argued on page 260 that thermal distortion of the substrate is likely to occur when the central spot temperature rises to around $700^{\circ}C$ or when the value of (P/D_b) is around 15 watts/cm. This happens to coincide with the expected change in controlling mechanism. Hence the thickness for values of $P/D_b > $ 15 W/cm or so is likely to be partly made up of thermal distortion and partly of deposition. Measuring the crater rim as the deposit thickness an almost linear dependence of thickness on (P/D_b) is observed - (graph 7.5   ).

8.2.2.2   Effect of (P/D_b) on the size of the outer spot diameter

The variation of outer spot diameter with (P/D_b) is shown in graph 7.6   . It is seen that deposition starts at values of (P/D_b) of around 4 watts/cm equivalent to a central temperature of $150^{\circ}C$ - $200^{\circ}C$. This value is in agreement with Davies (41) and Jablonowski (85) for the onset of thermal decomposition of CoAcAt.

The theoretical prediction for the location of $150^{\circ}C$ isotherm is also shown in Graph 7.6   . All the comparable experimental results fall below the no loss isotherm line. This could be due to one or all of three effects:-

(i)   Under reading of the outer diameter, due to the difficulty in observing monomolecular or very thin layers.

(ii)   Decomposition is only significant at higher temperatures.

(iii) There is significant heat loss which must be allowed in the theoretical calculations.

It is very unlikely that invisible layers would extend some two beam diameters beyond the visible limit of the deposit as required by explanation (i).

To achieve a fit between a no loss theoretical line and the experiments, a no loss isotherm of 350-400°C is required by explanation (ii). Such a temperature will only start to be achieved for values of (P/D_b) greater than 9.0 watts/cm yet deposits are formed down to a value of 4.0 watts/cm. To suggest decomposition starts at temperatures of 350°C is in contradiction to the findings of others.

This leaves the third effect: including heat loss by surface convection and radiation in the theoretical calculations produces the fan of theoretical curves also shown in Graph 7.6.
The fit is quite good for the larger beam diameters of 0.001-0.003m and $>$ 0.003m. The smaller spot sizes show a greater scatter, partly due to power fluctuations since

$$d(P/D_b) = \frac{\delta P}{D_b} - \frac{P}{D_b^2} \delta D_b$$

the small power fluctuation yields a larger variation in P/D_b for small spots in some cases $\pm$ 10 watts/cm. The error due to miscalculation of D_b will be much less significant than in the thickness calculations since D_b occurs on both axis. A variation in D_b for a given deposit causes a diagonal movement on the graph similar to the slope of the theoretical curves.

In conclusion; it has been seen that deposition starts around 150°C - 200°C. That the outer diameter is associated with this isotherm. That the theoretical model has to include a surface heat loss effect and that by so doing sufficient correlation with the experiments justifies the assumption that the deposition phenomenon is described by thermal conduction within the substrate.

8.2.2.3 <u>Effect of (P/D_b) on the size of the 'inner' diameter</u>

An "inner" diameter event is predicted theoretically (see graph 8.1 page 258). It is seen there to be due to the abrupt variation in deposition rate in the chemically controlled region. For the vapour concentrations used this occurs at or near a film temperature of $500^{\circ}K$ such a film temperature is achieved with the surface temperature equal to $354^{\circ}C$ if the ambient gas temperature is $100^{\circ}C$.

Shown on graph 7.7 page 227 are the experimental results together with the $354^{\circ}C$ isotherms for the "no loss" and $D_b=0.002m$ cases. The fit is remarkably good considering the points made in (8.2.2.2). To see just how good, further "no loss" isotherms are included. It seems clear from this that the "inner" diameter is associated with a surface temperature of $350^{\circ}C \pm 50^{\circ}C$ and that the hypothesis for the inner diameter is justified.

8.2.2.4 <u>Effect of (P/D_b) on the size of "burnt" and "crater"diameters</u>

The average minimum value of (P/D_b) found to cause a black centred deposit is seen in graph 7.8 page 228 to be around 10.0 watts/cm. Such a value gives a central spot temperature, based on $T^*_{\infty_o} = 1.77$, of $500^{\circ}C$. A surface temperature of $500^{\circ}C$ together with an ambient gas temperature of $100^{\circ}C$ gives a film temperature of $573^{\circ}K$. This is the temperature at which boundary layer control becomes rate determining (graph 3.19 page 87). The variation of "burnt" diameter vs P/D_b is shown in graph 7.8 compared to the $500^{\circ}C$ surface temperature isotherm. Most of the results fall in the expected zone though the scatter is sufficiently large to have obliterated any separation due to beam diameter effects.

The blackness of these spots is seen under the SEM to be due to a very rough surface. This roughness is expected from boundary layer theory as described on page 264 section 8.2.1.5. Although some black spots are wrinkled and suggest movement of the substrate due to thermal stress, others such as that shown in A2 (plates 6 fig 9 d have random rough surfaces. This result had a value of (P/D_b) of 9.0 W/cm just in the required zone but perhaps not quite hot enough

for thermal movements to occur. It should also be noted that the surface of a wrinkled sample, though patterned, also displayed a certain random roughness((e.g. F13, D9). plates 14,11).

A similar reasoning on crater formation shows the incidence of craters to be associated with a value of (P/D_b) in excess of 15 W/cm, a surface temperature of around 700°C for a 0.042 cm diameter beam as discussed on page 257 et seq. The variation of crater diameter with (P/D_b) follows the predicted trend of the 700°C isotherms (see graph 7.9).

8.2.3. Effect of radial location of deposit within the jet

8.2.3.1 Structure of an impinging jet

Figure 8.5 shows the three zones governed by different mass transfer conditions in an impinging jet flow system, the stagnation zone, transition zone and wall jet region.
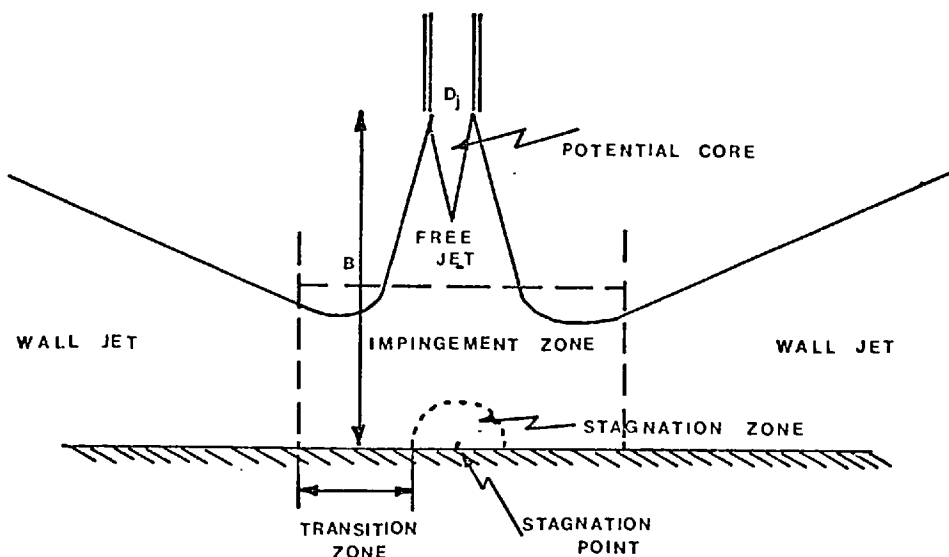
FIG 8.5   STRUCTURE OF AN IMPINGING JET

The mass transfer coefficient as described by the Sherwood No $(k_m D_j/D_{AB})$ is highest in the stagnation region due to the thin boundary layer formed under the rapidly decelerating, and therefore high turbulent energy, impinging gas. A fair correlation for the Sherwood number can be obtained from potential flow theory for this region, giving a Reynolds dependence to the power of $\frac{1}{2}$.

However Davies found from experiment a correlation to be:-

$$Sh_o \frac{B}{D_j} f = 0.625 \ Re^{0.80} \ Sc^{\frac{1}{3}} \qquad for \ 300 < Re < 5000$$

for the low Reynolds numbers used here.

The factor, f, allows for gas dilution due to entrainment in the free jet region. Very little additional entrainment occurs in the impingment zone $(R/D_j < 2.0)$ due to the small interface available for entrainment. Davies graph 8.6 shows a dip in Sh around $R/D_j = 2.5$ due to the build up of Naphthalene in the impingement zone of his napthalene erosion experiments.

In the jet system used here, no condensation or reaction occurred in the impingment zone, except the small amount due on the heated spot. Thus, all locations in the impingment zone would be expected to have the same vapour concentration. Graph 7.10 suggests a fairly uniform central Sherwood number up to $R/D_j = 2.0$.

In the wall jet entrainment occurs once more, and the boundary layer thickens. The Sherwood number depends on the Reynolds number as shown by a relationship such as that of Dawson and Trass (130)

$$Sh = 0.044 \ Re^{0.877} \ R*^{-1.0}$$

where the dimensionless radial position $R* = R/D_j$ illustrates mainly the effect of dilution, as well as boundary layer growth and reduction in turbulence. Now the variation in Sh with radial location noted by others is due partly to surface depletion, due to reaction at previous locations, partly due to surface reaction at the location considered, partly due to entrainment from above reducing the concentration gradient and partly due to the turbulence related diffusivities varying the boundary layer thickness. The present system will suffer all these except the historical depletion effects noted first. In the impingement region, where material is fed essentiallly from above, this should have little effect and so similar values of Sherwood No are expected. But in the wall jet region

SHERWOOD NUMBER AS A FUNCTION OF RADIAL POSITION[41]

fig(8.6)

Re = 7429
- ◐ B = 8 D$_j$
- ● B = 12D$_j$
- ○ B = 16D$_j$
- ⊗ B = 20D$_j$
- ◓ B = 24D$_j$

Sh

R / D$_j$
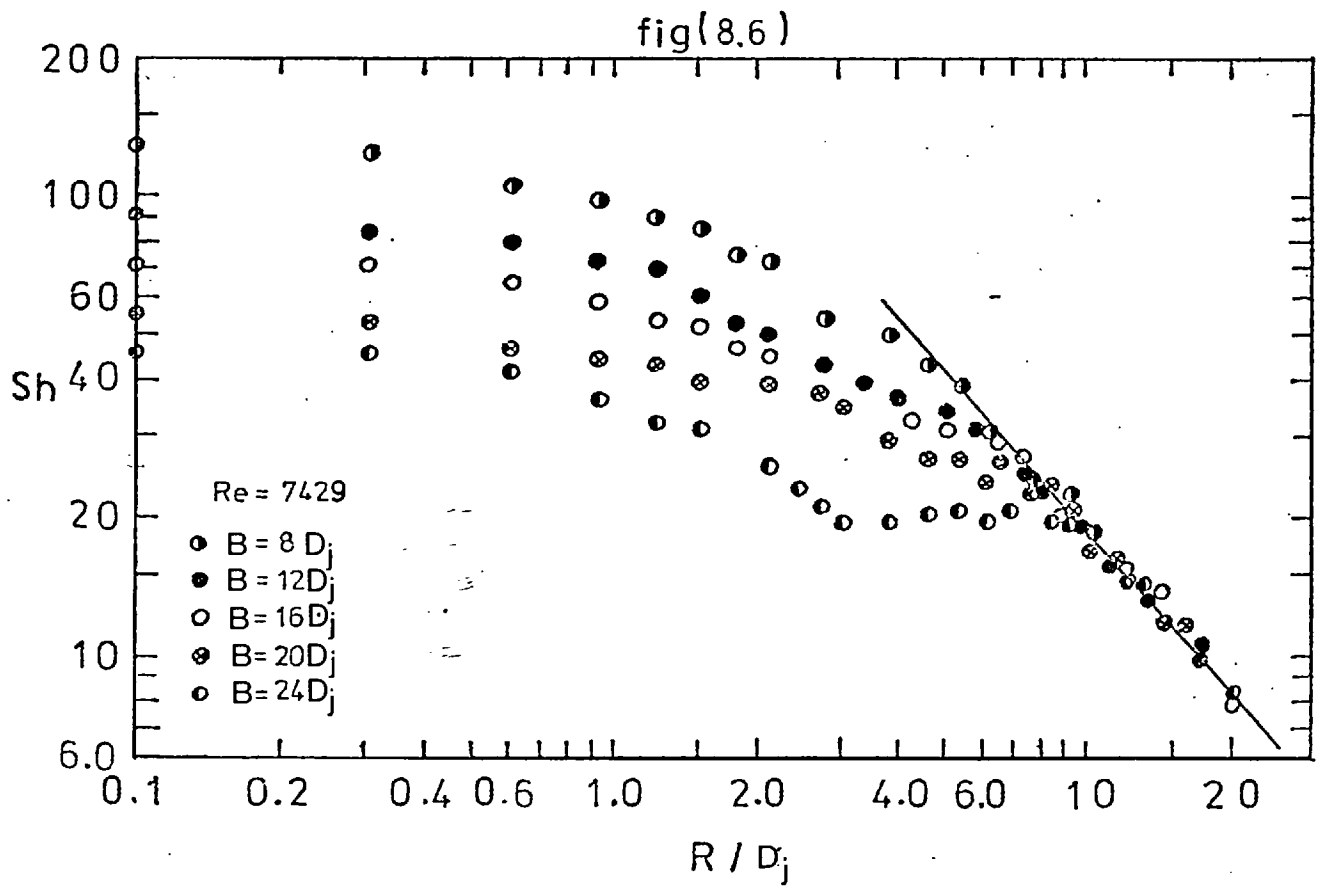
a significant boundary layer, apparently expanding from the stagnation point, occurs. This would not be similar to the present situation where a very much thinner boundary layer and therefore, faster deposition rates are expected, provided condensation does not occur. The 45° angle of impingment would quantitatively alter this analysis but not qualitatively.

8.2.3.2 Deposit thickness vs R*

Graph 7.10 shows the variation of deposit thickness with radial location; the lines join consecutive deposits. The expected faster growth at the jet centre is clearly seen. Unfortunately the scatter is too great and the distant deposits too thin to allow a quantitative comparison of the Sherwood number by this technique with the values for a uniformly heated plate found by Davies (41).

8.2.3.3 Outer spot diameter vs radial location

Graph 7.11 shows the outer diameter/beam diameter to be independent of the radial location except for two deposits which were so faint a reliable diameter could not be measured.

Previously (section 8.2.2.2) it was surmised that the outer diameter was described by the location of the 150-200°C isotherm. Thus, the outer diameter was not expected to vary with radial location. A trivial rise in diameter might be anticipated due to the slightly decreased convective heat loss. But this effect would be completely lost due to the cooler gas blowing over the substrate surface at remote locations.

8.2.3.4 Inner diameter vs radial location

Graph 7.12 shows the inner diameter becoming smaller with increasing radial distance from the jet centre. Now it might be expected that the inner diameter would behave as the outer diameter since it is associated with the 500°K film temperature isotherm. This is not so. The hypothesis regarding the inner diameter was that it was associated with the location of the rapidly changing rate of decomposition of chelate i.e. at a film

temperature of $500^{\circ}K$ for a vapour concentration of 0.306 ppm.

The concentration falls with increasing radial distance due to entrainment and so does the decomposition rate, being first order both for mass transfer control and chemical control. This gives rise to the curves of graph 8.7 in which the temperature of rapidly changing decomposition rate is seen to increase with dilution of the gas.

The extent of this movement and the resulting effect on the minimum value of (P/D_b) to cause an inner diameter for the E series, $D_b = 0.0128$ cm is shown in table :

Degree of Dilution of 0.306ppm vapour	Film temp. for rapid rate change $^{\circ}K$	Equivalent Surface Temperature ($T_a = 100^{\circ}C$) $^{\circ}C$	Approx. minimum value of (P/D_b) to produce an inner diameter W/cm
x1	500	354	6.00
$x\frac{1}{2}$	520	394	7.00
x1/4	540	434	7.5
x1/8	550	454	8.0
x1/16	NO	DISTINCT RATE CHANGE	

From this table it can be seen that the inner diameter is expected to fall with increasing dilution and is unlikely to occur, in the E series, at dilutions of more than 1/16th.
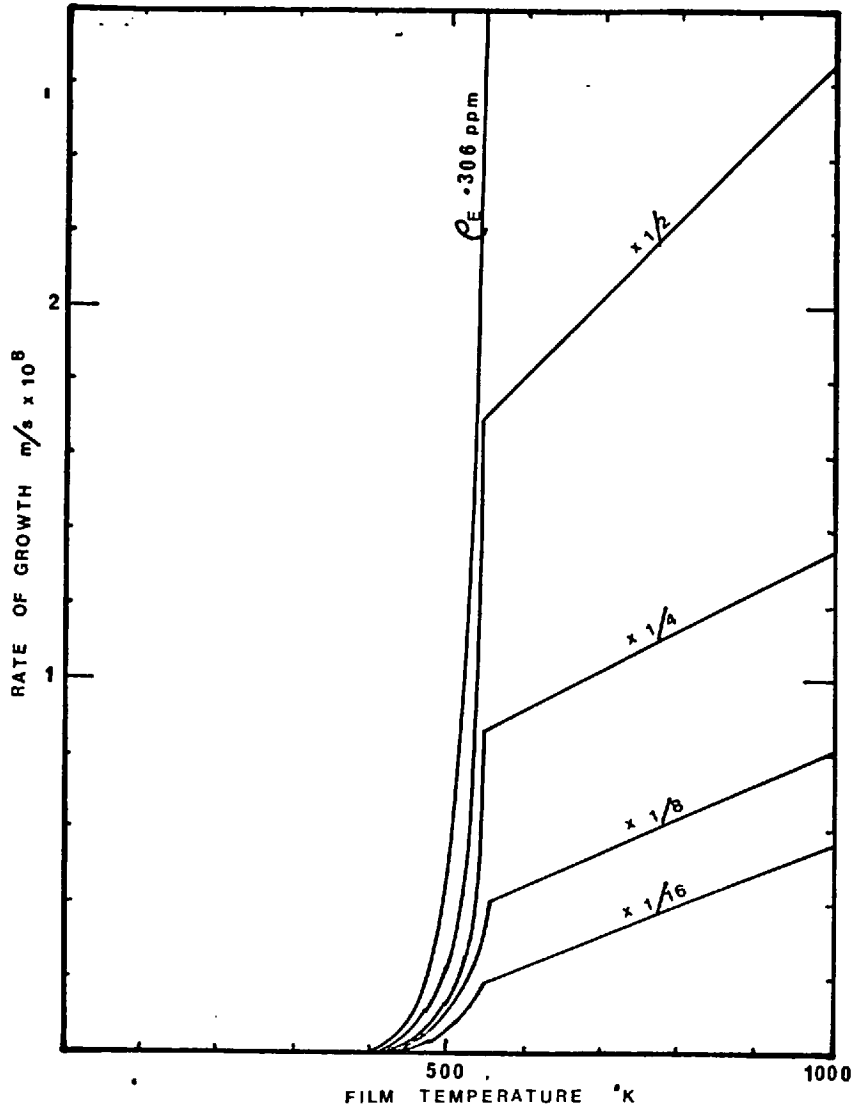
Figure 8.7 Graph showing the effect of varying
vapour concentration on the deposition
rate and in particular on the critical
temperature for forming an inner diameter
event.

8.2.4 <u>Variation of thickness and extent with time</u>

8.2.4.1 <u>Thickness</u>

A steady growth rate was observed with series I16–22, graph 7.13. This is in agreement with the theory which predicts thermal equilibrium after 4s (graph 8.8) for $D_b \simeq 0.00048m$ i.e. $\Theta^* = 100$.

The induction period observed, of between 10s and 20s, was far longer than predicted by the thermal conduction model ($\sim 0.4s$). No reasonable variation in(P/D_b) could explain such a difference.

The theoretical prediction is that a layer of CoO $0 [5°A]$ thick would be deposited in 5s which could be invisible being only a molecule or two thick and of a similar optical nature to glass. After 10s the thickness would be $0 [20°A]$ and hence still difficult to see. However, at 20s the thickness would be $0 [150°A]$, in agreement with the extremely hazy deposit seen. By this reasoning it is not necessary to assume a long induction period with related nucleation problems.

8.2.4.2 <u>Diameters</u>

Graph 7.14 shows the theoretical growth and the observed growth of the outer, inner and 'burnt' diameters. The trend of these results strongly suggests that an induction period does occur. However, if a 20°A layer of CoO on a glass surface is invisible then once more the results are compatible with the theory. For the measured diameter is then seen to relate to a certain thickness which is a time and temperature event.

The thermal history of a spot similar to the I series is shown in the theoretical curves of graph 8.8 in which the growth of the various isotherms can be seen. A near equilibrium value in the I series is obtained very quickly $\Theta^* = 25.5$ 1.3s. For most values of (P/D_b) a growth similar to graph (7.14) would be expected until the value of (P/D_b) pushes the 150°C isotherm into the tail region of the thermal history curves e.g. $T^*_{150} \simeq 0.3$. When this happens substantial late growth of the outer diameter would be expected.

Fig 8.8   Thermal history of a 0.48 mm diameter spot subject to $P/D_b = 10.4$ W/cm

Re 2079
B/D_j 3.38

500 °C 'burnt' for $P/D_b = 10.4$ W/cm

354 °C 'inner'

150 °C 'outer'

$\Theta^* = \infty$
$\Theta^* = 1000$
$\Theta^* = 100$
$\Theta^* = 25.5$

$\Theta^* = 0.94$

T^*

R^*

278
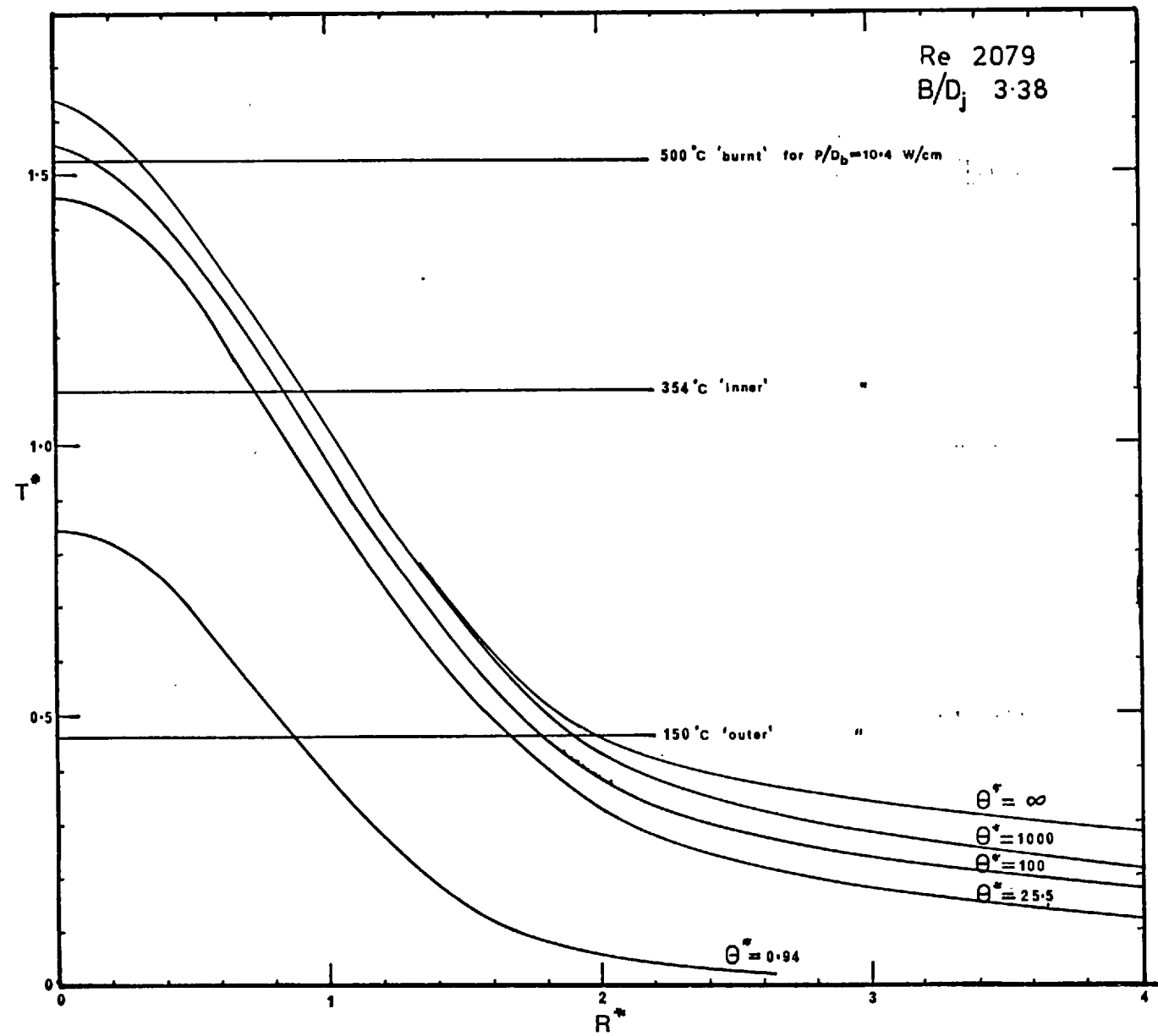
The rise in diameter with time shown on graph 7.14 indicates that very small deposits of O [1/10thbeam diameter] could be formed by carefully controlling the deposition time. This would mean that spots smaller than the minimum beam diameter should be possible, due to the temperature profile being approximately Gaussian and printing occurring at the point only. Such a "sharpened pencil" effect would not be very dramatic since very short pulses of controlled power would be required, the rise in size being fairly abrupt. Attempts to prove this possibility resulted in the rather feeble smudges of G19 and G20 which had visible outer diameters of only 70μ and 100μ respectively, using a 10.6μ beam and F5.0 optics (the diffraction limited spot would be around 130μ diameter =2.44λF). The estimated beam diameter allowing for truncation etc. was 270μ and 410μ). Further experiments on this line have been made by A. Young using a pulsed YAG laser, in which he was able to obtain a 1μ visible dot.

8.2.5 Effect of Jet exit Reynolds Number

8.2.5.1 Thickness

The reproducibility of deposit thickness, as opposed to spot diameters, was very poor, This is due principally to the integral nature of thickness previously referred to.

Thus graph 7.15 of thickness vs Re is an interesting display of theoretical curves with little experimental corroboration except on the general relationship. This general relationship is seen to be that the Re has little effect on the deposit thickness within the small range studied.

No further data would be gained by a statistical multiple regression analysis. If the results from the same Re v P/D_b are grouped together the standard deviation of the observed thickness about their mean is often greater than the mean (e.g. B7 $\longrightarrow$ 11, B13, 14, 16, 25, 27 have an average thickness of 0.47μ with a standard deviation of 0.87μ and a skew distribution).

From the theoretical curves it is interesting to note that at very high Re numbers a spot will not form due to excessive cooling e.g. for P/D_b = 10.4 W/cm D_b = 0.00192m and Re $>$ 10^5. On the other hand if the Re = 0.0 the lack of vapour would prevent deposition. Hence a maximum is seen on the theoretical curves at the extreme of the chemically controlled zone.

8.2.5.2 Diameter

Graphs 7.16 and 7.17 show the theoretical and experimental variation of outer and inner diameters with Reynolds numbers. The experimental fit is quite good. The general shrinkage of spot size with increased Reynolds number is due to the increased cooling effect. There are two observations which can be made:-

i)   The Re is not a very important parameter in the range of Re used here. Hence, results taken with Re numbers differing by less than a factor of 3.0 can be compared for their variation due to other causes.

ii) The 150°C isotherm can be arranged to lie on the region of steepest thermal gradient by suitably adjusting the Re, thus possibly improving the deposit clarity (see section 8.1.6). This is illustrated by graph 8.9.

8.2.6 Effect of Jet/Plate distance

8.2.6.1 Thickness

The jet/plate distance, expressed in dimensionless form as (B/D_j), affects not only the concentration of vapour impinging on the substrate surface but also the thickness of the thermal and concentration boundary layers.

Thus a close jet (low value of B/D_j) would decrease the rate of deposition by enhancing the cooling rate but increase the rate by increasing the vapour concentration at the surface both in the chemically controlled region (α D_j/B) (see page 64) and the
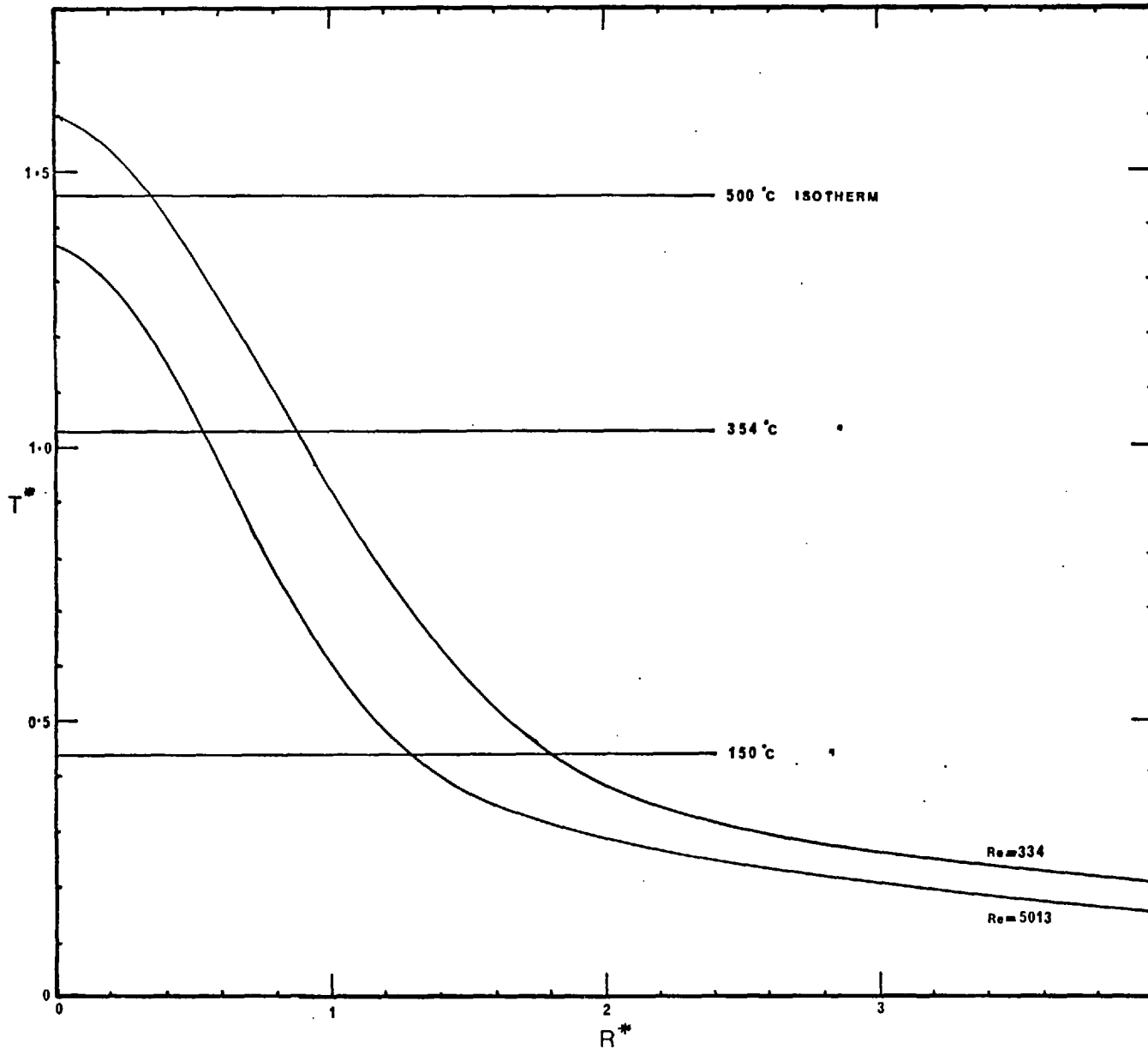
Fig 8.9

Theoretical curves illustrating
the effect of Reynolds number
on the temperature profile
calculated for:-

D_b = 0.0015 m

P/D_b = 11.0 W/cm

T_a = 100°C

B/D = 7.4

time = ∞

substrate = glass

281

transport controlled region ($\propto D_j/B^2$) (see page 57). These two effects would partly cancel.

The theoretical prediction of deposit thickness vs (B/D_j) for the F series is shown in graph 8.10. The growth results are too scattered to corroborate this graph.

8.2.6.2 Diameter

Graph 7.18 shows the theoretical and experimental variation of outer, inner and burnt diameters with (B/D_j). The general trend is that (B/D_j) is not strongly related to the spot outer diameters. The reason for this is seen in graph 8.11 which shows T^* vs R^* for B/D_j of 2.5 and 7.5.

The enhanced cooling for low values of (B/D_j) affects mainly the hottest areas resulting in only a small change in the outer diameter. The inner diameter would appear to be more seriously affected. However, due to the increased concentration of vapour for low values of (B/D_j) the isotherm appropriate to the "inner" event would be lowered - (see section 8.2.7.2). This would result in hardly any change of the "inner" diameter with B/D_j, as observed.

8.2.7 Effect of varying the vapour concentration

8.2.7.1 Thickness

Davies (41) has shown that the thermal decomposition of cobalt acetyl acetonate is a first order reaction both in the chemical and transport controlled regions - assuming no significant counter flow in the transport controlled region.

Based on this it is possible to plot graph 8.7 (page 276) showing the dependence of deposition rate upon both temperature and concentration. A decrease in growth with decrease in concentration should occur and is observed to do so (graph 7.10).
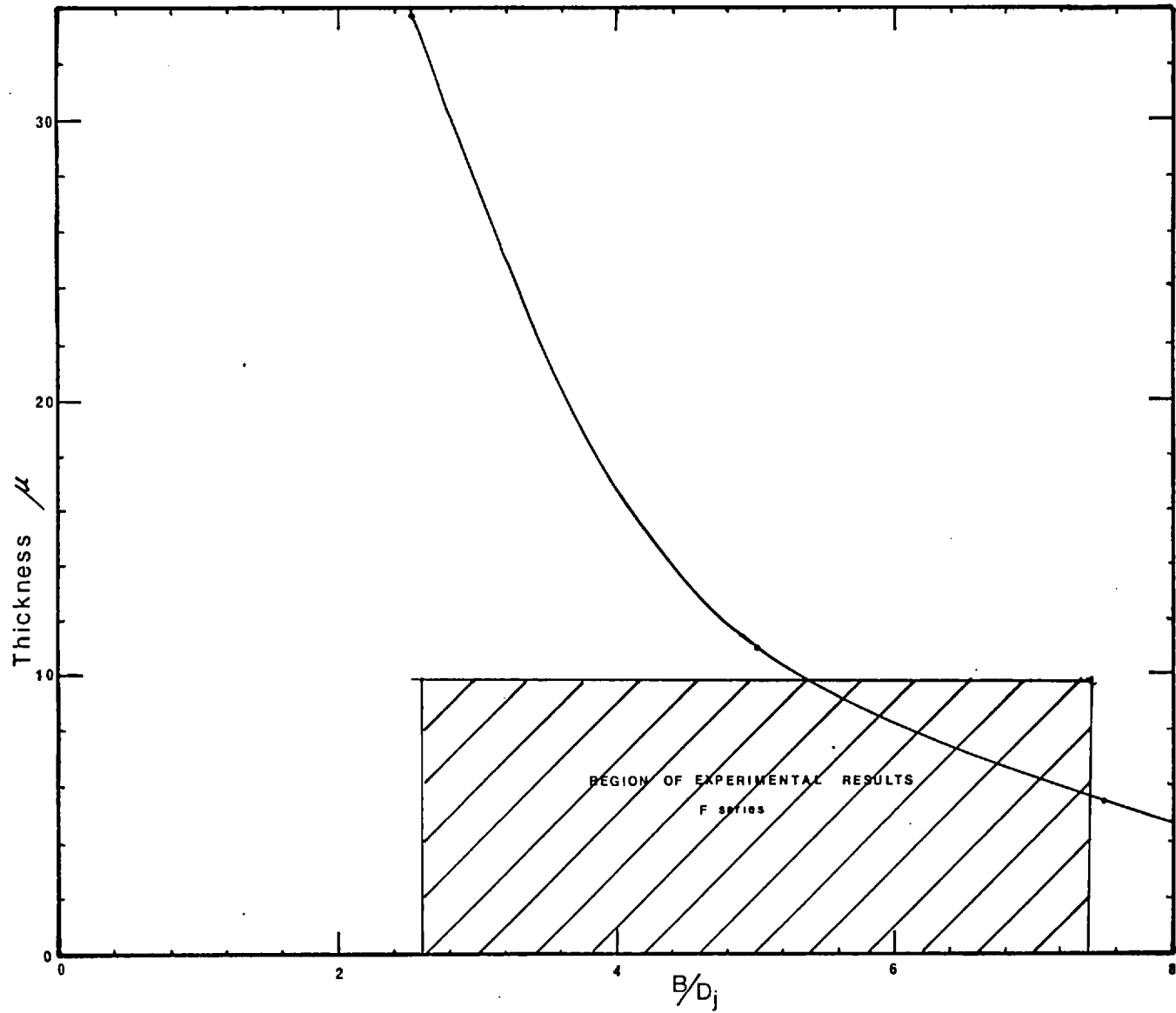
Fig 8.10

Theoretical curves
illustrating the effect
of jet/plate distance on
deposit thickness,
calculated for:-

D_b = 0.00128 m

P/D_b= 10.7 W/cm

E = .306 ppm

Re = 2018

Time = ∞
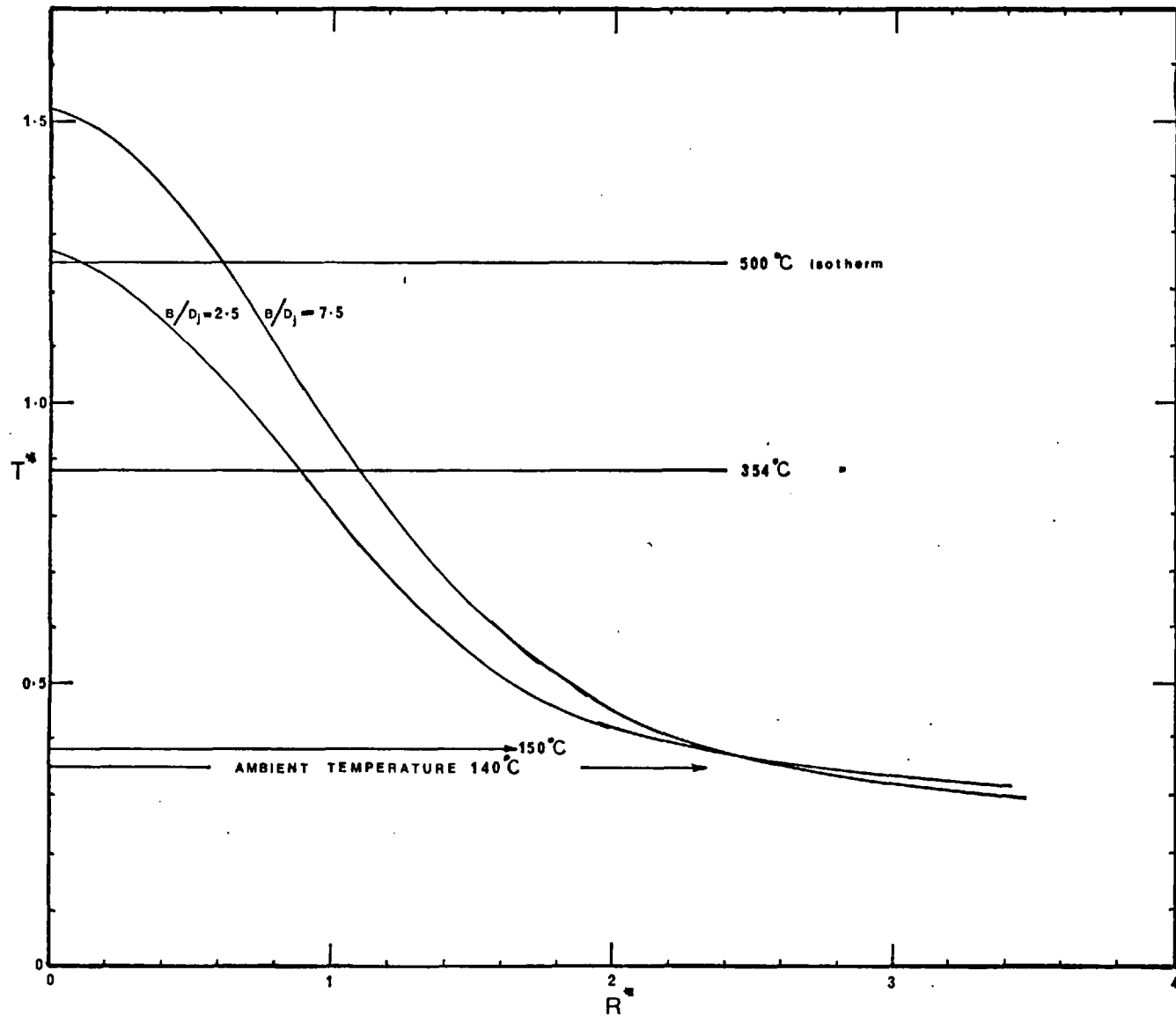
Fig 8.11

Theoretical curves
illustrating the effect
of jet plate distance on
the thermal profile
calculated for:-

D_b =   0.001 m

P/D_b =   12.8 W/cm

T_a =   140°C

Time =   ∞

8.2.7.2 Diameters

A change in the vapour concentration would not be expected to affect the heat transfer unless it is sufficiently large to introduce a significant chemical energy term into the heat balances of the system. With concentrations around 0.3ppm this is not the case and thus the position of the 150°C isotherm and therefore the outer diameter should remain unaltered by any variation of the vapour concentration. This is observed in graph (7.11 page 233).

However, the "inner" diameter, considered related to the steeply rising part of the rate curve, would be expected to alter as observed in graph 7.12(page 234) . This is an important aspect of the deposition process since it suggests a way of reducing the formation of a "skirt" (defined as (outer diameter - inner diameter)). Thus, if a concentration of   3ppm could be obtained an extremely steep rate curve 10 times steeper than that for 0.3ppm would be expected as shown in figure 8.12. It is seen that this would result in a marked reduction in the temperature variation between the inner and outer diameters. This promising line is at present being studied by A. Young under the author's supervision. He is working on the pyrolysis of silane using a YAG laser as the heat source.
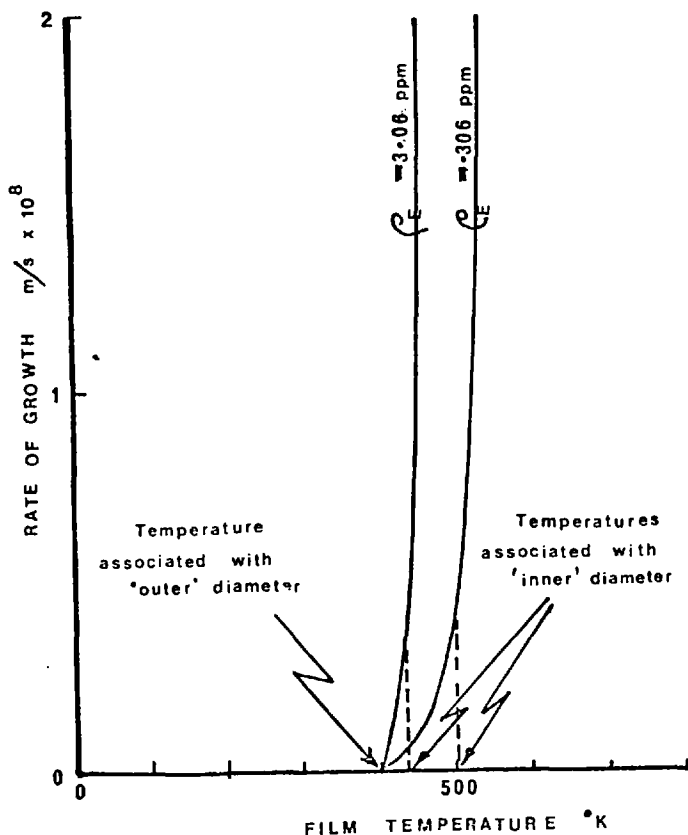
Figure 8.12

Effect of increase in concentration on temperature difference between "inner" and "outer" diameter events and on growth rate.

8.2.8 <u>Effect of varying the jet temperature (ambient temperature)</u>

The theoretical variation of deposit thickness with ambient temperature (assumed the same for both convection and radiation) is shown in graph 8.13. This could not be simulated by experiment due to the vapour concentration and jet temperature being related in the design of evaporator used.

This difficulty, however, does not affect the variation of the outer diameter with jet temperature. Since, as previously noted, page 241, the concentration would not be expected to affect the outer diameter. Thus, it is possible to use the small temperature difference of series A and B in this analysis. Graph 8.14 shows the expected diameter variations for specimen A14 and B13, these two having the same value of P/D_b (10.2 watts/ cm A14 and 10.6 watts/cm B13). They exhibit the expected slight trend. The slightly smaller diameter expected in the B series is not observed in graph 7.20, page 245. The expected difference is small and the uncertainty in (P/D_b) larger so no strong conclusions can be drawn.

The theoretical effect of a change in ambient temperature on the thermal profile of a spot is illustrated in graph 8.15. This graph was drawn on the assumption that (i) the ambient temperature was the same for convection and radiation and was equal to the gas temperature impinging on the surface. (ii) the substrate was semi-infinite and initially at $0^{\circ}C$.

The lower the ambient temperature the steeper the thermal profile. Also as the jet temperature approaches the vapour decomposition temperature so the thermal profile 'tail' rises above the outer diameter isotherm causing a large increase in the outer diameter of the spot.

8.2.9 <u>Effect of varying the substrate properties</u>

Graph 8.16 shows the thermal profiles expected on different substrates for the conditions indicated.
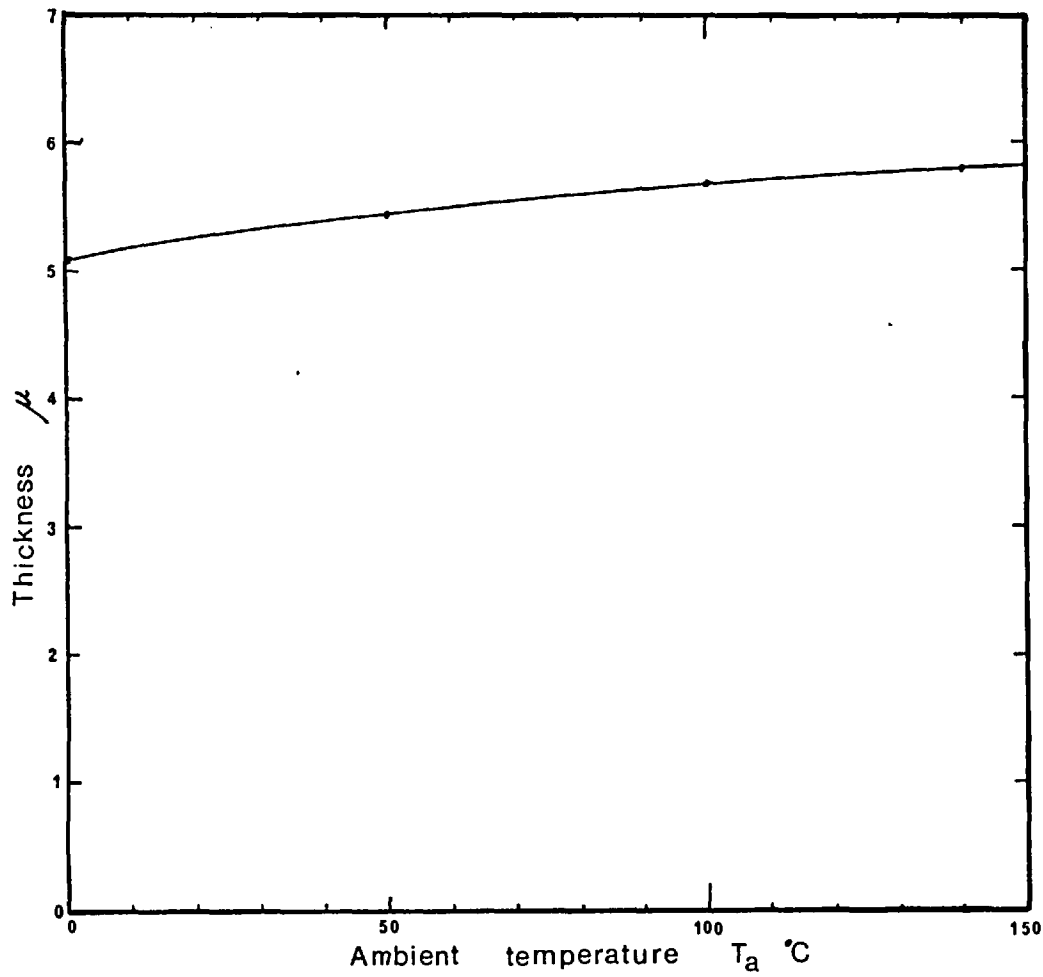
Fig 8.13

Theoretical curve showing the effect
of ambient temperature on deposit
thickness, calculated for:-

D_b = 0.0048

P/D_b = 20.8

E = 0.306 ppm

time = 120 s

substrate = glass

Re = 2078

B/D_b = 7.4

Fig 8.14 EFFECT OF AMBIENT TEMPERATURE ON DEPOSIT DIAMETER
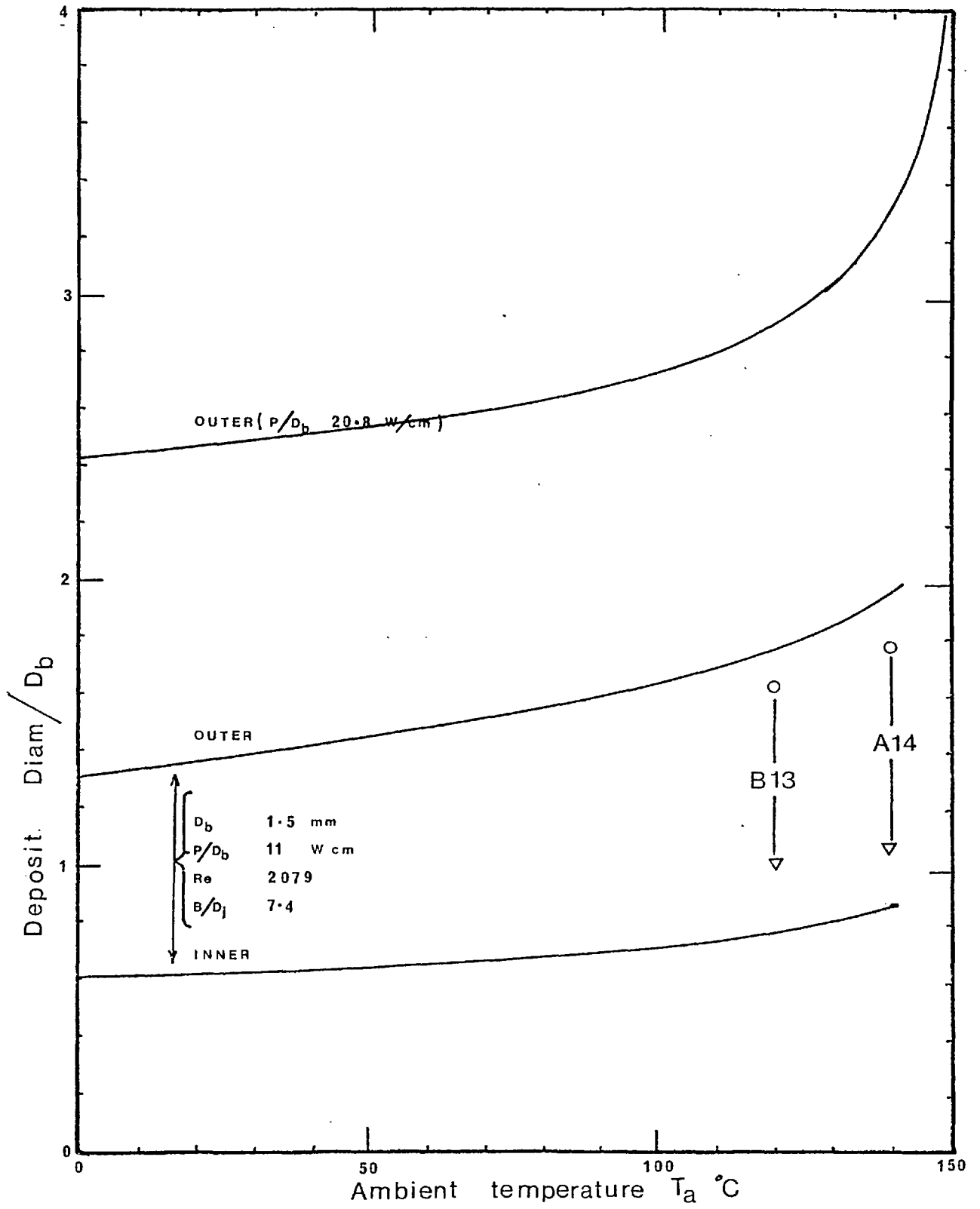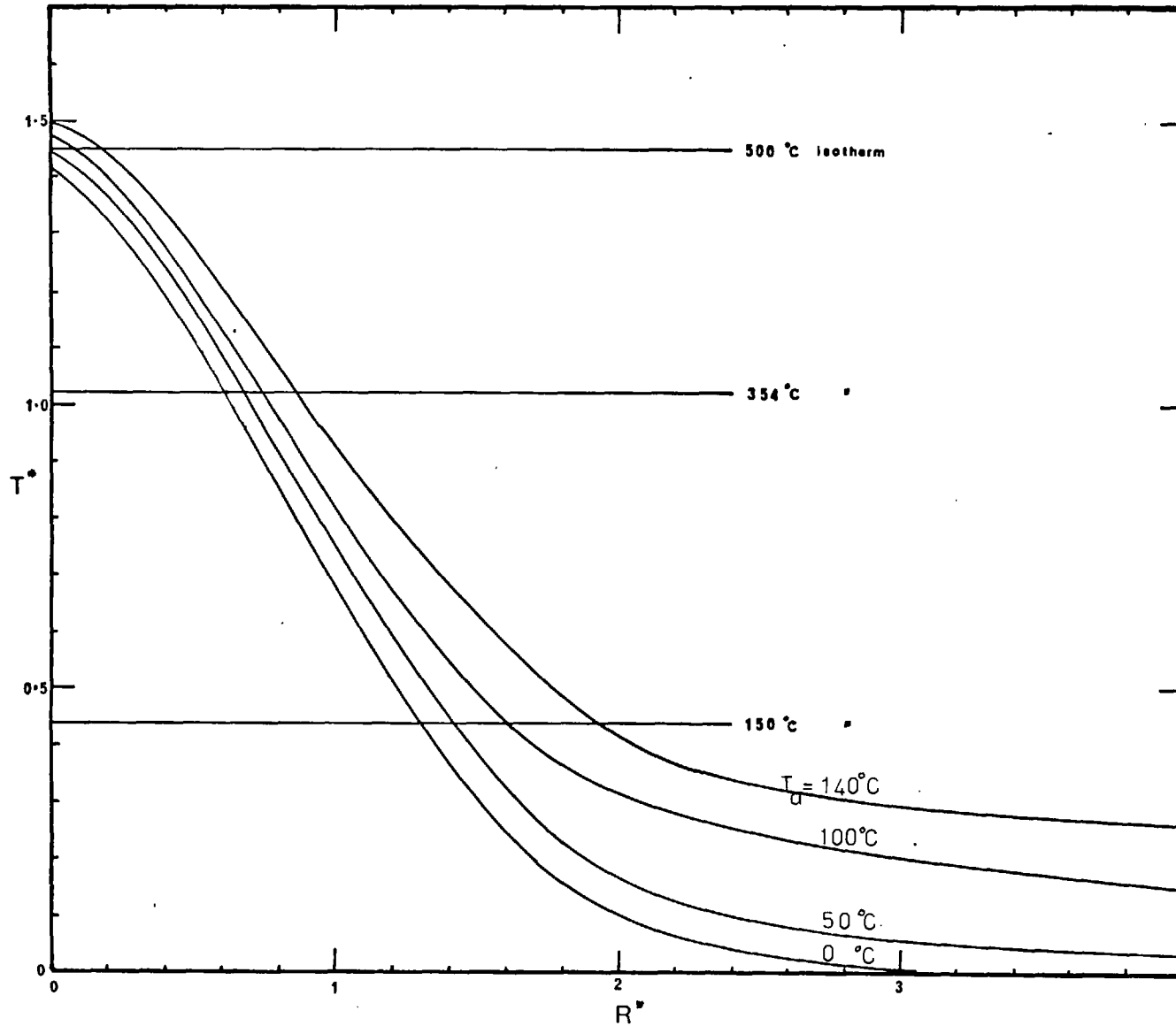
Fig 8.15

Effect of ambient temperature, T_a, on the thermal profile calculated for:-

D_b = 0.0015 m

P/D_b = 11.0 W/cm

R_a = 2079

B/D_j = 7.4

Substrate = glass

Time = 120 s
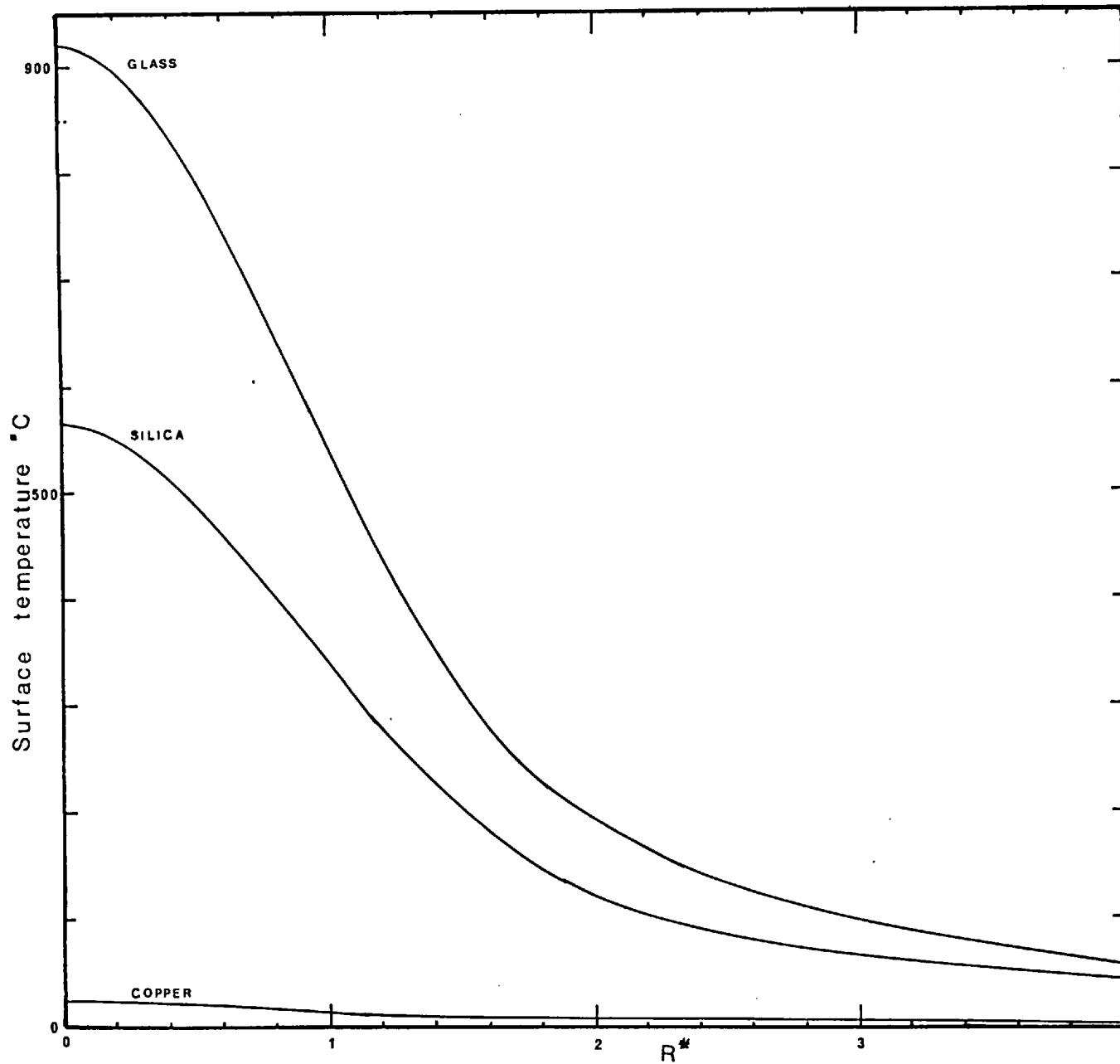
Fig 8.16

Theoretical temperature profiles at $\Theta^* = 25.5$ for various substrates, calculated for:-

$$D_b = 0.00048 \text{ m}$$

$$P/D_b = 20.8$$

$$\Theta^* = 25.5$$

	C_p J/Kg$^\circ$C	ρ Kg/m^3	k W/m$^\circ$K
Glass	668	2490	.84
Silica	838	2660	1.44
Copper	396	8930	38.5

$$Re = 2079$$

$$B/D_j = 7.4$$

$$T_a = 100^\circ C$$

It is immediately apparent why no deposit was formed on copper, particularly since the low reflectivity value of 0.18 has also been assumed, whereas a more appropriate value would have been 0.8 - 0.9.

Further it is apparent why more power is required on quartz than on glass for a given event.

It might be thought that the more highly conducting substrates would not support a large thermal gradient, as observed in graph 8.16 for a given power dissipation. However, if a calculation is made so that the centreline temperatures are the same on two different substrates (i.e. they would have the same values of $[\pi k/(P/D_b)]$) the temperature profiles would be identical. So, theoretically at least, what has been found for glass substrates regarding spread and growth (but not thermal damage) will apply for other substrates but at different powers.

What is being restated here is that the dimensionless plots of T^* vs R^* vs Θ^* vs η are unique relationships for all materials, powers etc. The case of $\eta = 0$ (the 'no loss' case) is well understood. For other values of η it is to be recalled that if a similar temperature profile is obtained the surface heat losses will be similar.

Thus, to achieve a given temperature, T, on two different substrate materials:

$$T^*_1 = \frac{T \pi k_1 D_{b_1}}{P_1(1 - r_{f_1})} \quad \text{and} \quad T^*_2 = \frac{T \pi k_2 D_{b_2}}{P_2(1 - r_{f_2})}$$

Calling $P_1(1 - r_{f_1}) = P_1$ etc.
we get

$$\frac{T^*_1}{T^*_2} = \frac{k_1 D_{b1}}{P_1} \times \frac{P_2}{D_{b2} k_2}$$

For a similar thermal profile and hence similar deposits on substrates 1 and 2

$$T^*_1 = T^*_2$$

assuming infinite or equivalent time.[N.B. since $\theta^* = (16\alpha t/D_b^2)$ events occur faster on high conductivity substrates.]

and hence $\quad \dfrac{k_2}{k_1} = (P_2/D_{2_b})/(P_1/D_{1_b})$

In the case of quartz and glass (series I):
   the thermal conductivity of quartz is 1.38 W/m $^\circ$K
   the thermal conductivity of glass is 0.84 W/m $^\circ$K

Thus if a deposit starts to form on glass at a value of (P/D_b) of 7 watts/cm then the same event should occur on quartz at 7 x 1.38 (0.82)/0.84 (0.89) = 11 watts/cm, where 0.82 and 0.89 allow for the different reflectivities observed in section 6.3.3.3. This is found to be so by comparing sample H1 on glass at (P/D_b) = 6.2 watts/cm with I26 on quartz at (P/D_b) = 11.5 watts/cm neither of which showed a deposit and comparing I21 on glass at 7.1 watts/cm with I24 on quartz at 14.4 watts/cm which did show a deposit.

The diameter of the deposits formed on quartz were smaller than expected for equivalent deposits on glass. This could be a refractive index problem making the 'skirt' less visible on quartz than glass. The refractive index of quartz is nearer to that of CoO than glass. (see section 8.2.4).
Support for this comes from sample I27, formed on quartz spectrosil over an extended time of 300s, which has an outer diameter of the expected size. The extra deposition time would allow additional growth so making the thin region visible.

8.2.10 Effect of surface reflectivity
   The surface reflectivity directly affects the power input and hence the important parameter (P/D_b). This was clearly demonstrated by attempting to form deposits on silvered glass slides.

No deposit was formed even with a value of (P/D_b) of 40 W/cm. the few thousand $^{\circ}A$ thickness of the silver film could not be expected to significantly alter the substrate thermal properties.

The appearance of the deposits on glass suggested that while deposition proceeded the surface reflectivity changed.

No experimental proof could be found for suggesting the reflectivity initially increases, causing an automatic cut off at certain thicknesses. No doubt this could be an effect in other deposition systems, especially those forming metal films.

However, for thicker deposits a fall in the reflectivity of the deposits showing colour fringes was found. Similarly a substantial fall in the reflectivity of rough black centres would be expected, though this could not be tested, the areas being too small.

The effect of this fall in reflectivity is shown in graph 8.17. This shows the theoretical thermal profiles at $\Theta^* = 25.5$ for the limiting case of the reflectivity falling to zero from 0.18 when the temperature exceeds $600^{\circ}C$. Under these conditions the effective power input is no longer Gaussian and hence a dissimilar thermal profile to those previously calculated would be expected. The curves show little movement in the location of the $400^{\circ}C$ or less isotherms during the calculation period. Some increase with further heating would be expected but it should not be very important.

The main effect would be on the location of the $500^{\circ}C$ isotherm previously associated with the 'burnt' diameter. The 'burnt' diameter was measured and compared to a constant reflectivity model from which the idea of $500^{\circ}C$ was derived. If this reflectivity change occurs then what alters is not the measured diameter but the temperature to be associated with the 'burnt' phenomenon. In the graph it is seen to be some $50^{\circ}C$ higher, in fact $550^{\circ}C$.

This size of change is not within the experimental accuracy to prove or disprove. Some increased deposition rate due to the increased temperature in the black zone would be expected, but being in the mass transfer controlled region this would not be big enough to account for the peaking phenomenon.
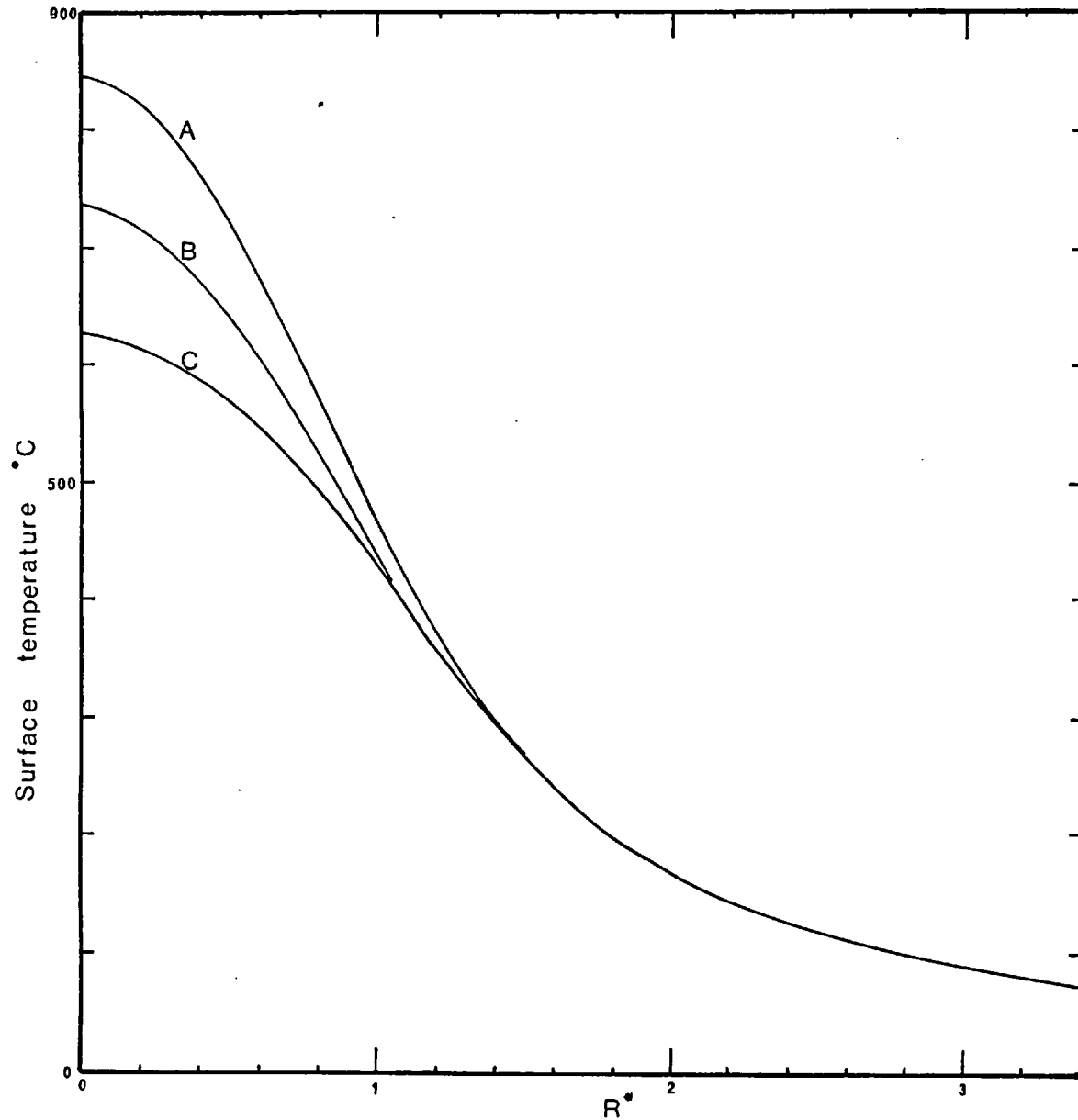
Fig 8.17

The effect of a variable reflectivity on the thermal profile calculated for:

$$\Theta^* = 25.5$$

for conditions see table 3.11.1 page 88

A — reflectivity = 0 if surface temp
$T_s > 600^{\circ}C$

B — reflectivity = 0.18 constant

C — reflectivity = 0.4 if $T_s > 600^{\circ}C$

294

CHAPTER 9

CONCLUSIONS

A system for printing complex shapes at atmospheric pressure using a noncontacting mask has been shown to be possible. The process is to blow thermally sensitive chemicals onto the heat image of a shaped aperture formed by passing a laser beam through the aperture and scaling the beam with a lens.

Prints have been obtained for the system Cobalt acetyl acetonate vapour in nitrogen blowing onto a spot heated by a 10.6μ radiant beam on glass and silica substrates.

The shapes of these prints were found to agree, within the range of the experimental accuracy, with a mathematical model of the process. The model was built on the assumption of thermal conduction within the substrate with surface heat loss by convection and radiation.

Thus, from experiment and theory the process parameters were established to be:

$$1) \quad T^* = \frac{\pi k D_b T}{P(1-r_f)}$$

$$2) \quad \Theta^* = \frac{16\alpha t}{D_b^2}$$

$$3) \quad \eta_{\underset{\Theta}{o}} = (h_c + h_r)(T^*_{\underset{\Theta}{o}} - T^*_{\underset{\Theta}{a}}) \frac{D_b}{4k}$$

$$4) \quad Sh = \frac{k_m D_j}{D_{AB}} = f(Re, \ Sc, \ B/D_j, \ R^*)$$

5) $\mathcal{C}_E$ - jet exit vapour concentration

6) Radial location of deposit relative to jet axis R^*.

The main structural features of the deposits were:-

(i)   The outer limit – associated with the isotherm at which decomposition starts.

(ii)   The limit of the bulk of the deposit – ("inner" diameter) associated with the steeply rising portion of the rate vs temperature relationship – a function of the vapour concentration.

(iii) A black region – associated with surface roughness thought to be due to the onset of boundary layer control of deposition and substrate thermal movement causing wrinkling, peaking and cratering.

(iv) A blue region – associated with dissolution of cobalt oxide in the substrate.

(v)   Thermal distortion and cracking at higher values of P/D_b due to thermally induced stresses.

The best quality of print was considered to be that with the minimum distance between inner and outer limits – a minimum 'skirt' region. The control of this region was considered possible by:

a)   high vapour concentration

b)   low ambient temperature

c)   careful control of the Reynolds number to locate the outer limit on the steepest part of the thermal profile.

d)   a particular value of (P/D_b) for a given system which can be calculated from a knowledge of the decomposition temperature, etc.

e.g. a value of $(P/D_b) \simeq 12 \times \left[\dfrac{k_{substrate}}{k_{glass}}\right] \times \left[\dfrac{1 - r_{f_{glass}}}{1 - r_{f_{substrate}}}\right]$ W/cm

$$\simeq 12.7 \frac{k_{substrate}}{(1 - r_f)_{substrate}} \quad \text{W/cm}$$

for the deposition of CoO from CoAcAt

e)   quality optics

f) Tem_{oo} beam mode structure, passing cleanly through the aperture.

Future Work

The present study aimed to build a foundation for this technique. From this foundation it is now possible to see various interesting areas for further study.

They are:-

(i)   The effect of pulsing the beam on spot diameters.

(ii) The possibility of drilling a hole with the laser and filling at reduced power.

(iii) The deposition of other materials, particularly a highly reflective metal, or hard alloy.

(iv) Deposition at high vapour concentrations and the effect this has on 'skirt' formation.

All these studies are, however, the background to actually making some electronic device, which works or surface alloying in precise patterns for wear or corrosion resistance, or simply making a patterned surface hardened region with no deposition.

APPENDIX 1

Manufacture of Microelectronic Circuits

Printed circuit manufacture

A printed circuit is an electrical circuit in which the wiring is replaced by patterns of conductive material applied on sheets of ceramic, glass, or laminated or solid plastic. The patterns are produced by photographic or mechanical procedures like those used in the graphic arts. There are numerous manufacturing processes currently employed. The most common are:

a) Etching
b) Plating
c) Metallising
d) Printing

a) Etching

A film of photo resist or similar photosensitive varnish (usually KMER or KTFR) is applied to the surface of a copper clad plastic board. A photographic negative of the circuit pattern is laid on the film. The film is exposed to u/v light. The exposed areas harden and the unexposed areas are readily soluble in an alcohol solution. The uncovered copper is dissolved in an acid, ferric chloride or ammonium persulphate etchant bath leaving the copper circuit pattern. The copper clad board is made by bonding copper foil to fibre glass cloth reinforced by laminating to an epoxy resin, or the later development of Dapon boards in place of the epoxy. Dapon boards are made of Diallyl isophthalate.

b) Plating

A plastic laminate is first coated with a conducting film such as silver by aldehyde reduction or evaporation processes as for the manufacture of mirrors. The circuit pattern is then marked out by silk screening or a stencilling process which covers all areas except the circuit pattern with a plating resist varnish. The circuit is electroplated with copper to a thickness

of 0.02-0.15mm. A solvent removes the plating resist. The exposed silver film is removed by etching which will leave the thicker copper pattern.

c) Metallising

For low current applications silver or other metal is evaporated directly onto an insulated plate through a stencil

d) Printing

This method is used mainly on ceramic or glass substrates. A silver paste is applied through a silk screeen to form the circuit pattern. After the silver paste has dried, the circuit is fired at about $300^{\circ}C$ which bonds the paste to the base. Resistance elements are also printed this way.

The scale of printed circuit conductor traces is 0.02 - 1.0 cm width and 1μ - 0.15mm thick.

Integrated circuit manufacture

There are two major classes of integrated circuit - semi-conductor I.C. and thin film I.C. - both are within the manufacturing capabilities of the spot imaging technique.

Semiconductor Integrated circuits

Semiconductor integrated circuits are manufactured on a pure silicon wafer~0.025 cm thick. They are of general size 2mm x 2mm with circuit interconnections > 10μ and approximately 1μ thick. To make them, a layer of the required material is deposited, coated with photoresist, contact printed by placing a glass photographic plate on the photoresist, and exposing to u/v radiation to harden the uncovered areas. Then the unexposed photoresist is washed away and the deposited layer etched to the required depth, producing the required pattern. A typical circuit may contain up to 10 such sequences. The glass photographic plate will only last around five prints, due to small spikes on the substrate damaging it. The precision required makes the capital investment for this process very large; for example, just a small spindle for spinning the wafer after coating in photoresist to ensure a uniform thickness of the varnish of 1μ, cost around £3000 in 1973.

The layers deposited are formed by the following processes:

a) <u>Si-N type</u> deposited by the pyrolytic decomposition of $SiCl_4$ or SiH_4 containing a trace of PCl_3 at around $1200^{\circ}C$.

b) <u>SiO$_2$</u> heat silicon to $1000^{\circ}C$ and oxidise with steam.

c) <u>Silicon -.P type</u> by diffusion of B at around $1200^{\circ}C$. The Boron is in the vapor as B_2O_3. Ion bombardment is a very promising new route.

d) <u>Contacts</u> contact holes through the SiO_2 insulating layers ($\sim$ 1μ thick) are required. Then aluminium is sputtered or evaporated over the wafer surface.

e) <u>Insulation</u> of one device from another can be achieved within a silicon chip by carefully arranged P-N junctions or by thin glass layers.

f) <u>Resistors</u> thin films of nickel-chromium, tantalum or tin oxide about 0.1μ thick.

g) <u>Capacitors</u> alternate layers of patterned metal; dielectric; metal laid down on SiO_2.

h) <u>Inductance</u> spiral film deposits allow small inductances to be built in. Large inductances cannot be built in.

A single circuit chip will be one of around 100 built at the same time on the same silicon wafer. It is separated from its neighbours by scribing, sometimes done with a YAG laser, and cracking along the scribed groove.

The separated chip is stuck to a package mount. Fine wires, usually gold ($\sim$ 0.0025 cm diam.), are connected by soldering between the package terminal leads and the integrated circuit. The package is then capped by welding, soldering, glassing or plastic moulding. The connection between I.C. and package terminals could be a patterned trace laid down by a laser imaging technique as discussed here.

Thin film integrated circuits   (ref. Motorola manual Ch. 13 1965).

The thin films are laid down on glass or ceramic bases and patterned as for semiconductor I.C. Their general size is 2cm x 2cm with conducting paths 3mm $\longrightarrow$ 0.03mm wide by 5°A $\longrightarrow$ 0.2mm thick. They usually have miniature components. attached. Apart from interconnections and isolation,the films are used for making resistors or capacitors or low valued inductances. Figure A.1 shows a cross section of a thin film circuit.

RESISTIVE FILM   DIELECTRIC FILM   METAL FILM

SUBSTRATE — GLASS / CERAMIC / GLAZED CERAMIC / OXIDISED SILICON
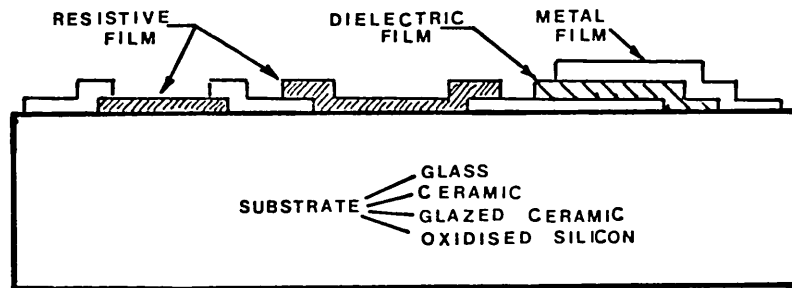
Figure A.1   Cross sectional representation of thin film resistors, and capacitors. (ref. Motorola manual Fig. 13.1)

The circuit may also be built on an active base such as a monolithic transistor. These are known as compatible thin film circuits. This system provides a greater degree of design freedom, better eletrical performance and other advantages. The laser deposition system discussed would offer the possibility of laying down directly active components on a passive base. The problem of epitaxy and single crystal growth of the silicon . may be soluble by suitable spot heat treatment, microzone refining etc. but needs a separate investigation.

In thin film circuits uniformity of film thickness and composition, good adhesion to the substrate and to other films with which the deposited film makes contact are necessary.

The present deposition techniques are listed in the table A1. It may be thought that the high temperature involved in laser deposition is its weakness. However, this contributes to deposit adhesion and a high temperature sequence is unavoidable by any manufacturing route. Since, apart from the elevated temperatures of most plating and diffusion processes (e.g. 1200°C for B diffusion) even in vacuum evaporation the substrate is deliberately heated for adhesion purposes. The finishing processes require the following approximate temperatures:-

Die bonding	∼ 400°C
Wire bonding	∼ 400°C
Packaging	∼ 400 - 500°C
High Stress Tests	∼ 500°C

As a consequence of this, the better circuits are made of metallurgically compatible material capable of being heated to high temperatures for extended periods of time. e.g. silicon bases, KOVAR leads, aluminium connectors, and SiO_2 dielectric.

Deposition Technique	Variations	Examples of Use in Present Thin Film Circuits	Advantages	Disadvantages
Vacuum Evaporation	Hot filament flash filament electron bombardment electron beam laser heating	Nichrome resistors SiO_2 dielectrics	1) High purity for elementary/ deposit especially with non contact heating methods. 2) Crystallite size is partially controllable by angle of incidence and rate of deposition.	1) Prone to fractionation of compound deposits such as NiCr, hence the need for flash heating methods 2) Not every element or compound required can be evaporated e.g. Al_2O_3. SiO_2, Ta, W etc.
Cathode Sputtering	High pressure reactive	Tantalum resistor Tantalum nitride resistor	1) Able to deposit thin films of refractory material	slower than vacuum evaporation
Vapour Deposition	Hydrogen reduction thermal decomposition	Al_2O_3 dielectric SiO_2 dielectric $Al_2O_3SiO_2$ dielectric SnO_2 semiconductor Si semiconductors	1) Better adhesion than lower temperature processes 2) Great flexibility, capable of depositing even semiconductor type films 3) Any film thickness may be built up.	1) Requires high temperatures (usually over 600°C)
Electroplating		Au plating on headers	1) Good adhesion, any thickness	1) Careful bath control required
Electroless plating		Ni metallisation of ceramics	1) Deposits on any reactive or activated surface	1) Careful bath control
Silk Screening		Mo/Mn – interconnectors cermet resistors and die bonders. (SiO + Cr;Ag + Pd + glass)	1) can cover any area 2) very quick	1) Not possible to have a fine pattern due to mesh size(320 mesh stainless steel screens).

TABLE A1 Deposition Processes

303

APPENDIX 2

Types of Lasers

Although it has been shown (A2.1) that many materials can exhibit the lasing action, few of these transitions are of commercial significance. These few lasers are listed in table A2.1. They fall into five classes as displayed in table A2.2.

The most notable lasers for use as heat sources at present are: the $CO_2/N_2/He$ laser with reported electrical to optical power efficiencies of up to 35%, the CO laser with efficiencies up to 5% and the YAG and YALO (yttrium ortho aluminate) with efficiencies of up to 1-3% (A2.4)).

References

A2.1 Handbook of Lasers, Ed. R.J. Pressley, Chemical Rubber Co., Ohio, 1971.

A2.2 Harry J.E.,"Industrial Lasers and their applications", Chapter 4, McGraw Hill (UK) Ltd., 1974.

A2.3 Hillier M., "Development and potentiality of gas lasers", Proc. I. Mech. E. vol 183, pt. 3D, 47-55, 1968-69.

A2.4 Russell J.D., Adams M.J., "Technical/Economic Appraisal of electron beam and laser welding", W.I. Report, 1973, 3378/1/73, June 1973.

Laser	Principal output wavelengths (μm)	CW output		Pulsed output*				Beam diameter between $1/e^2$ points (mm)	Beam divergence (half angle) millirad	Efficiency per cent	Comments
		TEM_{00}	Multimode	TEM_{00}	Multimode	Peak pulse power (W)	Pulse width (μs)				
Ruby	0.6943	0.025	---	1	4×10^2	10^8	$3 \times 10^{-3} - 10^3$	2-20	0.3-5	0.1	High power pulsed output in visible region. Applications in holography, ophthalmology, fabrication.
Nd^{3+}:YAG/glass	1.06	0.25-25	$1 - 10^3$	$2 \times 10^{-3} - 3$	$1 \times 10^{-3} - 6.5 \times 10^2$	10^9	$1 \times 10^{-2} - 7 \times 10^3$	1-25	0.15-7.5	1	High efficiency pulsed and CW outputs. Applications for range finding and fabrication processes
Helium-neon	0.6328	$6 \times 10^{-5} - 7.5 \times 10^4$	$1 \times 10^{-4} - 1.5 \times 10^{-1}$	---	---	—	---	0.73-10	0.125-3	0.1	Low cost, visible output. Used for surveying, metrology, holography.
	1.152	$0.3 \times 10^{-3} - 1 \times 10^{-3}$	—	—	—	—	—	0.8-1.5	0.5-0.75	0.1	
	3.391	1.5×10^{-3}	—	—	—	—	—	1.2-2	0.35-1.5	0.1	
Helium cadmium	0.325-0.4416	$2 \times 10^{-2} - 5 \times 10^{-2}$	5×10^{-2}	---	—	—	---	0.8-2.5	0.25-1	—	
Argon	0.3511-0.5145	$1 \times 10^{-3} - 10$	$1.5 \times 10^{-3} - 15$	$2.5 \times 10^{-6} - 2.6 \times 10^{-4}$	$1.5 \times 10^{-5} - 10$	—	$2 - 10^2$	0.65-4	0.25-1	0.1	High power CW output tunable over visible and near UV. Uses includes ophthalmology, holography.
Krypton	0.3507-0.7993	$2 \times 10^{-3} - 4$	---	2×10^{-5}	6×10^{-5}	---	40	1.4-4	0.25-0.5	0.1	High power CW output tunable over visible and near UV
Xenon	0.3645-0.5395	—	4×10^{-6}	—	$9 \times 10^{-5} - 2 \times 10^{-4}$	---	0.3-1	2.4-4	1-2.75	0.1	Pulsed output in visible region used for trimming thick and thin film circuits
Nitrogen	0.3371	—	---	—	$3 \times 10^{-6} - 6 \times 30^{-2}$	—	$3 \times 10^{-3} - 1 \times 10^{-2}$	2.5	0.38-1.5	—	High power pulsed output in near UV. Used for pumping some dye lasers
Carbonmonoxide	5.2-5.7	—	—	---	$10^{-3} - 10^{-2}$	—	0.1-0.25	5	1	—	
Carbon dioxide	9.2-10.8	$3 - 10^3$	$3 - 10^4$	$4 \times 10^{-3} - 10^2$	$1 - 2 \times 10^2$	—	$0.1 - 10^7$	0.8-25	0.25-4	10	High power output at high efficiency. Used for cutting and welding
Organic dyes	0.2650-0.9600	2×10^{-2}	—	---	2×10^3	2×12^8	—	2-5	0.2-3	0.1	Output tunable over broad range. Applications in spectroscopy, pollution detection etc.
Gallium arsenide	0.85-0.905	—	1	---	5×10^{-6}	24*	0.1-1	$0.2 \times 10^{-2} \times 40 \times 10^{-2}$ ‡	200	1-40	Small size but high divergence. Uses include range-finding and pollution detection.

*Normal operating mode
*At room temperature
‡Dimensions of emission region

Table A2.1 Principal characteristics of commercially available lasers (A.2.2)

Table A2.2 Common laser types and methods of excitation (ref A2.2)

Laser Type	Normal Operating Range (μm)	Normal Method of Excitation
Solid State	0.6–3	Optical
Gas (a) monatomic	0.2–3	Glow and arc discharge
(b) molecular	2–100	Glow discharge
(c) metal vapour	0.2–0.6	Glow discharge
Liquid organic dye	0.3–1.2	Flash tube and laser
Semiconductor	0.3–31	Electric field
Chemical	2–100	Chemical reaction

APPENDIX 3

Lasing Action of a CO_2-N_2 Laser

The lasing action of CO_2 was first reported by C.K.N. Patel et al (A3.1) in 1964. Since then considerable work has been done on this system so that powers have been raised from a few mW to several MW (A3.2) and the mechanism has become elucidated in fair detail.

The CO_2-N_2 laser is known as a "molecular laser" because the stimulated emission occurs between two molecular vibration states.

The CO_2 molecule is linear and symmetric, that is in the zero energy state the two oxygen atoms are equally displaced on either side of the carbon atom. The possible vibrational modes are shown in the diagram below:—

In plane of page

normal to page

Symmetric Stretching   2 Bending Modes   Assymmetric Stretching
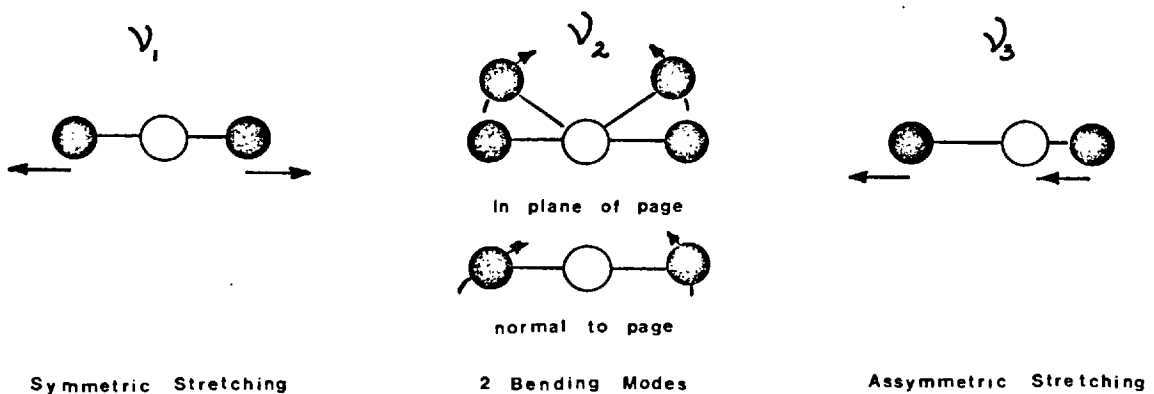
Figure A3.1   Oscillation modes of the CO_2 molecule

The number of quanta of energy in state ν_1, ν_2, ν_3 is p, q, r respectively and l is the number of quanta of angular momentum associated with the two bending modes. So that the vibrational energy of the molecule is denoted by $(pq^l r)$ i.e. If the molecule has one quantum of energy in state ν_3 it would be expressed as (00^o1).

The lower vibrational energy levels of the CO_2 molecule and N_2 molecule are shown in the diagram which is taken from (C.K.N. Patel (A3.3)).

The lasing action in a C.W. laser is from the $CO_2(00^o1) \longrightarrow CO_2(10^o0)$ radiating at 10.6μ wavelength. Though an alternative is possible from $CO_2(00^o1) \longrightarrow CO_2(02^o0)$ at 9.4μ wavelength and overlaid on these fundamental oscillations are an almost unlimited number of rotational levels, which also compete for the available (00^o1) molecules and are capable of lasing at wavelengths around 10μ. The $(00^o1) \longrightarrow (10^o0)$ route has a higher optical gain than the $(00^o1) \longrightarrow (02^o0)$ route and so is the exclusive output
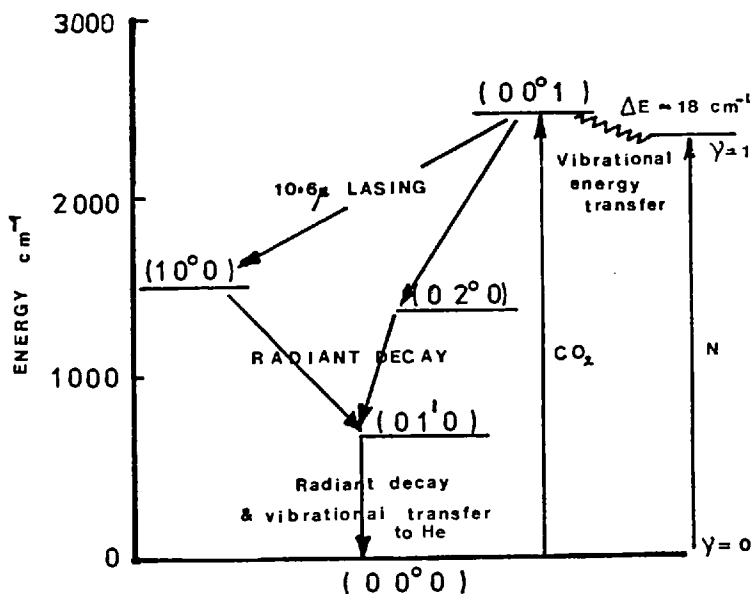
Figure A3.2   The lower vibrational energy levels of CO_2 and N_2 molecules

from a system with no wavelength selection. However, there is competition between the different rotational levels in the (00^o1) mode. The energy difference between these levels is small compared to the thermal energy of the system at 400^oK and so the time for thermal equilibrium to be satisfied is small. This time is called the rotational thermalisation time and is approximately 1μ sec for the low pressure system considered here (it is inversely proportional to the pressure). The distribution of energy between the levels would be expected to be given by a Boltzmann distribution for a given temperature. On the other hand the vibrational level lifetime is much longer, in the range 1-10 msec. Thus, if lasing starts on one of the more densely populated rotational levels, thermalisation will rapidly occur and reduce the energy in other

levels, eventually reducing those levels so that their populations are no longer sufficient to sustain the lasing action from them (i.e. the population is no longer inverted for those rotational levels).

To sustain the lasing action some form of pumping must be applied which produces CO_2 (00^O1). This can be done inefficiently by direct electron collisions and were this the only available route the CO_2 laser would not have been very remarkable. Fortunately it can also be done by collision with excited N_2 molecules whose energy level is within 18 cm^{-1} of the CO_2 (00^O1) state a difference which is easily accounted for by thermal energy, ($210 cm^{-1}$ at room temperature) to add to this fortune the N_2 molecule in its excited state can not decay through electric dipole radiation since it is a homonuclear diatomic molecule, and has no dipole moment. Thus, it can only decay by collision with other molecules or the walls. It thus has an effective lifetime of around 100msec. and populations of N_2^* ($\nu = 1$) of 10-30% have been reported (K. Dressler (A3.4)). It is due to this effective coupling between power input $\longrightarrow$ N_2 excitation $\longrightarrow$ CO_2 (00^O1) that efficiencies for a CO_2-N_2 laser (efficiency = laser power out/power in) are of the order of 10-20%, the theoretical quantum efficiency is 40-45%.

A classical and most elegant experiment of Patel's, demonstrated this action of N_2 beyond dispute. He arranged for a discharge to occur in a N_2 gas stream, passed the excited N_2 gas into another tube where it was mixed with CO_2 and noted that there was a laser emmission from the tube, even though there was no electric discharge in this second tube.

Another problem exists in maintaining the lasing action and that is to recycle the CO_2 molecules to the ground state. Decay from CO_2 (10^O0) and CO_2 (02^O0) is rapid but a bottleneck occurs at CO_2 (01^l0).

The process CO_2 (01^l0) $\longrightarrow$ CO_2 (00^O0) can be speeded by:-
a) a reduction in temperature of the system increasing the rate of radiant decay.
b) Collision with another molecule or the wall.

Some data on route (b) was complied·by V.N. Kondrat'ev (A3.5) for the reaction $CO_2(01'0) + M \rightarrow CO_2(00^{\circ}0) + M$ + Kinetic energy where M is another molecular species the results are:-

M	Rate sec^{-1} $torr^{-1}$
A	130
CO_2	130
N_2	180
He	4,000
H_2	13,000
CO	25,000
NO	25,000
HCl	50,000
H_2O	130,000

The laser efficiency is found to increase with the addition of He, H_2O, H_2 and O_2. He and H_2 also have high thermal conductivities and so help to remove heat from the system (route a). He has a further advantage in being inert and therefore will not attack mirrors, electrodes etc. (H_2 could form acids e.g. H_2CO_3 etc. in the plasma discharge). He is also considered to help create more excited N_2 molecules.

Thus, the gas mixture giving the best coupling between power in and lasing power out will consist of $CO_2/N_2/He$. The precise mixture is discussed under "Choice of lasing medium".

References

A3.1 Patel C.K.N., Faust N.L., McFarlane R.A., Bull A.M., Phys. Soc. (1964), 9.500.

A3.2 Foster H., "High Power CO_2 Lasers - a review", Optics and Laser Technology, June 1972, p121, (ref. 10).

A3.3 Patel C.K.N., Lasers Vol 2 ed. A.K. Levine, Edward Arnold, London 1968, p87, p102.

A3.4 Dressler K., J.Chem. Phys. 30, 1621, (1959).

A3.5 Kondrat'ev. V.N., "Chemical kinetics of gas reactions", Addison - Wesley, Reading, Mass 1964.

APPENDIX 4

EXPERIMENTAL RESULTS

Jet exit diameter = 0.508 cms
Aperture diameter = 0.500 cms

Materials A   'Axa'   Microslide   1.2 - 1.5mm

       B   annealed 'chance' glass 1.2 - 1.5mm

       C   unannealed 'chance' glass 1.5 - 1.8 mm

       D   unannealed 'chance' glass 1.2 - 1.5 mm

       E   unannealed 'chance' glass 1.2 - 1.4 mm

       F   unannealed 'chance' glass 0.8 - 1.0 mm

       G   silica, spectrosil   1.2 - 1.5 mm

       G'   ground silica, spectrosil

	SAMPLE	A1	A2	A3	A4	A5	A6	A7	A8	A9	A10	A11	A12	A13	A14	A15	A16	A17	A18	A19	A20
LASER	'P' TOTAL POWER – W	1.44 ±.1	1.35 ±.05	1.14 ±.1	1.31 ±.2	1.24 ±.15	1.5 ±.15	1.5 ±.1	1.37 ±.1	1.24 ±.1	1.07 ±.07	.87 ±.03	.64 ±.1	.4 ±.07	1.54 ±.08	1.34 ±.03	1.5 ±.14	1.34 ±.08	1.33 ±.1	1.43 ±.1	1.31 ±.1
	MAXIMUM POWER PEAK – W	1.54	1.40	1.54	1.51	1.39	1.65	1.6	1.47	1.34	1.14	0.9	0.74	0.47	1.62	1.37	1.64	1.42	1.43	1.53	1.41
	'P/D_b' POWER INTENSITY W/cm	9.6	9.0	7.6	8.7	8.3	10.0	10.0	9.1	8.3	7.1	5.8	4.2	2.7	10.2	8.9	10.0	8.9	8.8	9.5	8.7
OPTICS	FOCAL LENGTH OF LENS cms	29.5	←																		→
	LENS/OBJECT DIST:– cms	73.66	←																		→
	LENS/IMAGE DIST:– cms	33.00	←																		→
	'δ' – DIFFRACTION LIMIT SPOT – cms	0.068	←																		→
	'D_b' = δ+.08 SPOT DIAM. (ESTIMATED), cms	0.15	←																		→
	PLOTTING SYMBOL	+																			
GAS	FLOW RATE litres/min	8.4	←																		→
	JET REYNOLDS NO	1789	←																		→
	CHELATE CONC: AT JET gm/cc x 10^6						.35	.26			.44	.36	.26	.19			.25				.36
	TEMPERATURE °C	140	←																		→
	JET/PLATE DISTANCE cms	1.77	←																		→
	ANGLE TO SUBSTRATE °	45°	←																		→
	SUBSTRATE MATERIAL	A	←																		→
DEPOSIT	OUTER DIAM/BEAM	1.45	1.52	.88	.98	.88	1.57	1.40	1.23	1.25	1.23	.99	.62		1.77	1.49	1.25	1.34	1.52	1.51	1.29
	INNER DIAM/BEAM	.67					1.16	1.15	.70	.69	.71				1.07	.79	.94	.79	.88	1.05	.88
	BURNT DIAM/BEAM	.50															.64			.41	
	BLUE DIAM/BEAM																				
	TIME OF DEPOSITION s	180	120	60	180	180	120	←													→
	RADIAL POSITION IN JET cms	.648	.691	.341	.65	.22	.32	.90	.17	.17	.32	.27	.25	.25	.34	.29	.26	0.0	0.0	0.0	0.0
	DIAMETER SPOT OUTER cms	.220	.228	.132	.147	.132	.235	.210	.185	.187	.185	.149	.093	no	.265	.223	.188	.202	.228	.227	.193
	INNER cms	.147					.174	.172	.105	.104	.106			dep	.160	.119	.142	.119	.132	.157	.132
	BURNT cms	.109															.096			.061	
	BLUE cms																				
	DEPTH SPOT TALYSURF μ	.14	.22	<.1	.2	.1	.5	.12	–	.12	.12	<.1	<.1	–	.77	.2	2.0	.52	.65	.85	.52
	DOUBLE BEAM μ				.25	.1	.4	.1	.09	.1	.12	<.1			1.1	.14	1.7	.44	.7	.85	.35
	COLOUR FRINGES μ				.3		.4	.1		.16		.16					.9	.4	.68	.69	.3
	SHAPE OF DEPOSIT	–	⌢	–	⌢	–	⌢	–	–	⌢	–	–	–	/	⌒⌒	–	⌢	⌢	⌢	⌢⌢	⌢
	TYPE OF DEPOSIT	P	M	P	M	P	M	P	P	P	P	P	P		M +Ck	P	M	M	M	M	M
	MAIN VARIABLE	←——— TIME ———→						←——— POWER ———→							←——— REPRODUCIBILITY ———→						

	SAMPLE	B1	B2	B3	B4	B5	B6	B7	B8	B9	B10	B11	B12	B13	B14	B15	B16	B17	B18	B19	B20
LASER	'P' TOTAL POWER — W	1.15	1.27	1.60	1.62	1.8	2.04	1.03	1.34	2.0	2.4	1.54	1.70	1.60	1.24	1.08	1.25	1.46	1.48	1.57	1.68
		±.3	±.05	±.25	±.15	±.15	±.1	±.06	±.1	±.1	±.05	±.2	±.25	±.2	±.1	±.1	±.1	±.05	±.05	±.05	±.05
	MAXIMUM POWER PEAK —W	1.45	1.32	1.85	1.77	1.95	2.14	1.09	1.44	2.10	2.45	1.74	1.95	1.80	1.34	1.18	1.35	1.51	1.53	1.62	1.73
	'P/D_b' POWER INTENSITY W/cm	7.6	8.4	10.7	10.8	12.0	13.6	6.8	8.9	13.3	16.0	10.2	11.3	10.6	8.3	7.2	8.3	9.7	9.8	10.4	11.2
OPTICS	FOCAL LENGTH OF LENS cms	29.5	←————————————————————————————→																		
	LENS/OBJECT DIST: — cms	73.66	←————————————————————————————→																		
	LENS/IMAGE DIST: — cms	33.0	←————————————————————————————→																		
	'δ' — DIFFRACTION LIMIT SPOT cms	0.068	←————————————————————————————→																		
	'D'=δ+.08 SPOT DIAM CMS	0.15	←————————————————————————————→																		
	PLOTTING SYMBOL	+																			
GAS	FLOW RATE litres/min	5.6	9.8	←————————————————————→														5.6	2.57	←→	
	JET REYNOLDS NO	1238	2146	←————————————————————→														1238	562	←→	
	CHELATE CONC: AT JET gm/cc×10^6				.35	.32	.22						.31	.26	.23						
	TEMPERATURE °C	120	←————————————————————————————→																		
	JET/PLATE DISTANCE cms	1.77	←————————————————————————————→																		
	ANGLE TO SUBSTRATE °	45	←————————————————————————————→																		
	SUBSTRATE MATERIAL	A	←————————————————————————————→																		
DEPOSIT	OUTER DIAM/BEAM							.52	1.05	1.77	1.18	1.25	1.27	1.62	1.31	1.03	1.30	1.41	2.1	2.1	1.99
	INNER DIAM/BEAM							—	—	1.25	—	.81	.83	1.01	1.01	.17	1.10	—	1.43	1.60	1.43
	BURNT DIAM/BEAM							—	—	.94	.08	—	—	—	—	—	—	—	.64	.67	.67
	BLUE DIAM/BEAM							—	—	—	—	—	—	—	—	—	—	—	—	—	—
	TIME OF DEPOSITION s	120	←————————————————→							13.5	120	60	120	←————→			135	120	←————————→		
	RADIAL POSITION IN JET cms	0.0	0.0	.216	.21	.25	.25	.24	0.0	←————————————————→					.5	.6	.8	.8	.8	.7	.6
	DIAMETER SPOT OUTER cms							.078	.157	.265	.177	.187	.190	.243	.197	.154	.195	.22	.31	.32	.298
	INNER cms		Beam blocked by jet					—	—	.187	—	.122	.124	.152	.152	.025	.165		.215	.24	.215
	BURNT cms							—	—	.142	.012	—	—	—	—	—	—		.096	.101	.101
	BLUE cms							—	—	—	—	—	—	—	—	—	—		—	—	—
	DEPTH SPOT TALYSURF μ	no	no	.1	v.	no	no	.1	.25	2.6	Broke	.18	.1	.37	.1	.1	.1	Broke	6	5	5
	DOUBLE BEAM μ	dep	dep		faint	dep	dep	.06	.29			.14	.03	.29	.1	—	.05			4.4	
	COLOUR FRINGES μ								.23	.88		.16	—	—	—	—	—		—	—	—
	SHAPE OF DEPOSIT	/	/	—	—	/	/	—	⌒	⌒	⌒	—	⌒	—	—	—	⋀	⋀	⋀		
	TYPE OF DEPOSIT	—	—	P	P	—	—	P	M	Ck	Ck	M	P	Ck	P	P	P	Ck	Pk	Pk	Pk
	MAIN VARIABLE	INCORRECT ALIGNMENT						←——— POWER ———→					←——————— REYNOLDS NUMBER ———————→								

		B21	B22	B23	B24	B25	B26	B27	B28	B29	B30	B31	B32	BSI
LASER	'P' TOTAL POWER — W	1.70 ±.1	1.65 ±.05	1.65 ±.1	1.40 ±.1	0.83 ±.04	0.77 ±.06	1.06 ±.05	0.97 ±.07	1.03 ±.1	1.03 ±.1	1.06 ±.1	1.07 ±.1	1.22
	MAXIMUM POWER PEAK W	1.80	1.70	1.75	1.50	0.87	0.83	1.11	1.04	1.13	1.13	1.16	1.17	1.22
	'P/D_b' POWER INTENSITY W/cm	11.3	11.0	11.0	9.3	5.5	5.1	7.1	6.4	6.8	6.8	7.0	7.1	8.1
OPTICS	FOCAL LENGTH OF LENS	29.5	←										→	
	LENS/OBJECT DIST: cms	73.66	←										→	
	LENS/IMAGE DIST: cms	33.0	←										→	
	'δ' DIFFRACTION LIMIT SPOT cms	0.068	←										→	
	'D'=δ+.08 ESTIMATED SPOT DIAMETER: cms PLOTTING SYMBOL	0.15 +	←										→	
GAS	FLOW RATE litres/min	2.57	14.56	20.1	27.1	9.8	2.57	9.8	27.1	34.2	2.57	5.6	2.57	no jet
	JET REYNOLDS No	562	3188	4407	5948	2146	562	2146	5948	7502	562	1238	562	—
	CHELATE CONC: AT JET gm/ccx10^6	35	.17	.11	.08	.11			.32	.32		.34	.18	chelate on substrate
	TEMPERATURE °C	120	←										→	
	JET/PLATE DISTANCE cms	1.77	←										→	
	ANGLE TO SUBSTRATE °	45	←										→	
	SUBSTRATE MATERIAL	A	←										→	
DEPOSIT	OUTER DIAM/BEAM	2.04	1.83	1.76	1.76			.93	1.06	1.30	.88	1.28	.89	1.06
	INNER DIAM/BEAM	1.33	1.05	1.25	1.21			—	—	.88	—	.88	.51	—
	BURNT DIAM/BEAM	.33	—	—	—			—	—	—	—	—	.20	—
	BLUE DIAM/BEAM	—	—	—	—			—	—	—	—	—	—	—
	TIME OF DEPOSITION s	120	← →	130	120	←							→	10
	RADIAL POSITION IN JET cms	.57	.42	.34	.33	.33	.33	.32	.24	0.0	.23	.27	0.0	—
	DIAMETER SPOT OUTER cms	.306	.274	.264	.264			.139	.159	.195	.132	.192	.134	.159
	INNER "	.202	.158	.188	.182	—	—	—	—	.132	—	.132	.076	—
	BURNT "	.05	—	.127	—	—	—	—	—	—	—	—	.030	—
	BLUE "	—	—	—	—	—	—	—	—	—	—	—	—	—
	DEPTH SPOT TALYSURF μ	2.2	.37	.75	.1	no	no	.1		.25		.1	.25	
	DOUBLE BEAM μ	1.97	.36	.80	.1	dep	dep	.1		.20		.06	.3	
	COLOUR FRINGES μ	—	—	—	—			—		—	—		.4	.04
	SHAPE OF DEPOSIT	⋀	⌒	⌒	—	/	/	—		⌒		—	⌒	—
	TYPE OF DEPOSIT	Pk	M	M	P	—	—	P	M	M	M	P	M	—
	MAIN VARIABLE	← REYNOLDS NUMBER →												

	Sample	C1	C2	C3	C4	C5	C6	C7	C8	C9	C10	C11	C12	C13	C14	C15	C16	C17	C18	C19	C20
LASER	'P' TOTAL POWER — W	1.44 ±.06	1.41 ±.1	1.54 ±.2	0.97 ±.1	1.05 ±.1	1.05 ±.1	1.00 ±.05	1.07 ±.1	1.02 ±.1	1.07 ±.1	1.05 ±.05	0.93 ±.1	0.97 ±.1	1.15 ±.05	1.07 ±.05	0.95 ±.05	1.1 ±.1	1.0 ±.1	0.97 ±.1	1.0 ±.1
	MAXIMUM POWER PEAK W	1.50	1.51	1.74	1.07	1.15	1.15	1.05	1.17	1.12	1.17	1.1	1.03	1.07	1.20	1.12	1.0	1.2	1.1	1.07	1.1
	'P/D_b' POWER INTENSITY W/cm	7.9	7.8	8.5	5.4	5.9	5.9	5.5	5.9	5.9	5.9	5.9	5.1	5.4	6.3	5.9	5.2	6.1	5.5	5.4	5.5
OPTICS	FOCAL LENGTH OF LENS cms	29.5	←																		→
	LENS/OBJECT DIST: cms	74.3	←																		→
	LENS/IMAGE DIST: cms	35.2	←																		→
	'δ' DIFFRACTION LIMIT SPOT cms	0.10	←																		→
	'D_b'=δ+.08 ESTIMATED SPOT DIAM: cms	.18	←																		→
	PLOTTING SYMBOL	+																			
GAS	FLOW RATE litres/min	8.4	←																		→
	JET REYNOLDS NO	1789	←																		→
	CHELATE CONC: AT JET gm/ccx10^6	no jet		.50									.44		.44		.38		.38		.25	
	TEMPERATURE °C	140																			
	JET/PLATE DISTANCE cms	2.54	←																		→
	ANGLE TO SUBSTRATE °	45	←																		→
	OUTER DIAM/D_b	.66	1.05	1.03	.86	.56	.66	.63	.79	.79	.79	.71	.89	.84	.91	1.21	1.12	1.21	1.15	1.21	.49
	INNER DIAM/D_b		.71	.68	.56	.48	.42	.35	.47	.42				.49	.63	.62	.71	.71	.72	.70	.16
	'BURNT' DIAM/D_b		.21	.46																	
DEPOSIT	SUBSTRATE MATERIAL	A	←																		→
	TIME OF DEPOSITION s	on dep 15	120	←															140	120	←→
	RADIAL POSITION IN JET cms	.319	0.0	.275	0.345	1.114	0.98	0.82	0.65	0.36	0.347	.158	.282	.483	.309	.236	0.0	.23	.258	.459	0.0
	DIAMETER SPOT OUTER cms	.119	.190	.185	.154	.101	.119	.114	.142	.142	.142	.127	.16	.152	.164	.217	.202	.217	.207	.217	.088
	INNER cms	—	.127	.122	.101	.086	.076	.063	.084	.076	—	—	—	.088	.114	.112	.127	.127	.129	.126	.028
	BURNT cms	—	.038	.083	—	—	—	—	—	—	—	—	—	—	—	—	—	—	—	—	—
	DEPTH SPOT TALYSURF μ	rough	1.6	1.75	.1	.45	.07	.1	.2	.07	.1	—	—	—	.15	.14	.06	.1	.12	.21	.1
	DOUBLE BEAM μ	thin	1.2	.9	.1	?	.06	.05	.17	.1	.1	.1	.1	.09	.26	.26	.06	.6	.11	.16	.06
	COLOUR FRINGES μ	—	.28 edge	.57 edge	—	—	—	—	—	.08	.07	—	—	—	—	—	—	—	—	—	.05
	SHAPE OF DEPOSIT		Λ	Λ		⌐									⌃						
	TYPE OF DEPOSIT	—	M	M	P	?	P	P	P	P	P	P	P	P	M	M	P	M	P	P	P
	MAIN VARIABLE	←							RADIAL LOCATION IN JET												→

	Sample	C21	C22	C23	C24	C25	C26	C27	C28	C29	C30	C31	C32	C33	C34	C35	C36	C37	C38	C39
LASER	'P' TOTAL POWER W	1.27 ±.1	1.14 ±.1	1.04 ±.1	1.20 ±.05	1.17	1.27 ±.1	1.1 ±.05	1.27 ±.1	1.17 ±.1	1.10 ±.05	1.07 ±.1	1.00 ±.1	1.04 ±.1	0.89 ±.1	1.2 ±.1	0.98 ±.1	1.2 ±.1	1.14 ±.1	1.07 ±.05
	MAXIMUM POWER PEAK W	1.37	1.24	1.14	1.25	1.17	1.37	1.15	1.37	1.27	1.15	1.17	1.10	1.14	0.99	1.30	1.08	1.30	1.24	1.12
	'P/D_b' POWER INTENSITY W/cm	7.1	6.3	5.7	6.6	6.5	7.1	6.1	7.1	6.5	6.1	5.8	5.5	5.7	4.9	6.6	5.4	6.6	6.3	5.9
OPTICS	FOCAL LENGTH OF LENS cms	29.5	←──→																	
	LENS/OBJECT DIST:-cms	74.3	←──→																	
	LENS/IMAGE DIST: – cms	35.2	←──→																	
	'δ' DIFFRACTION LIMIT SPOT cms	0.10	←──→																	
	'D'=δ+.0S ESTIMATED SPOT DIAM: cms	.18	←──→																	
	PLOTTING SYMBOL	+																		
GAS	FLOW RATE litres/min	5.0	←───────────────────────→							13.2	←───────────────────→					17.8	←──────→		no jet
	JET REYNOLDS NO	1065	←───────────────────────→							2816	←───────────────────→					3791	←──────→		N/A
	CHELATE CONC: AT JET gm/ccx10⁶									.45		.31				.30				
	TEMPERATURE °C	140																		
	JET/PLATE DISTANCE cms	2.54	←──→																	
	ANGLE TO SUBSTRATE °	45	←──→																	
	OUTER DIAM/BEAM DIAM	.80	1.01	.91	.89	.90	1.01	1.15	1.12	.90	1.07	1.17	1.28	1.25	1.31	1.26	.76	.64	.41	
	INNER DIAM/BEAM DIAM	.49	.68	.59	.59	.48	.91	.71	.72	.63	.59	.89	1.03	1.00	1.06	.98	.86	.49	.39	
	BURNT DIAM/BEAM DIAM												.16	.11						
DEPOSIT	SUBSTRATE MATERIAL	A	←──→																	
	TIME OF DEPOSITION s	120	←──→																	5
	RADIAL POSITION IN JET cms	.491	.377	.411	.367	.372	0.0	.310	.325	.968	.872	.586	.543	.479	.357	.226	.309	0.0	.395	—
	DIAMETER SPOT OUTER cms	.144	.182	.164	.160	.162	.182	.207	.202	.162	.192	.210	.230	.225	.235	.227	.225	.137	.116	.073
	INNER cms	.088	.122	.106	.106	.087	.109	.127	.129	.114	.106	.160	.185	.180	.190	.177	.154	.088	.071	—
	BURNT cms	—	—	—	—	—	—	—	—	—	—	—	.028	.020	—	—	—	—	—	—
	BLUE cms	—	—	—	—	—	—	—	—	—	—	—	—	—	—	—	—	—	—	—
	DEPTH SPOT TALYSURF µ	.25	?	.12	.3	.25	.25	.25	.25	.12	.15	1.1	1.75	.43 missed	1.25	.25	.25	.35	.14	—
	DOUBLE BEAM µ	.09	.6	.15	.3	.17	.15	.18	.23	.09	.18	.8	2.2	1.6	1.8	.29	.09	.40	.18	—
	COLOUR FRINGES µ	—	—	—	—	.23	—	—	—	—	—	—	—	—	.7 edge	—	—	—	.28	—
	SHAPE OF DEPOSIT				⌢		⌢	⌢					∧	⋀	⌢					
	TYPE OF DEPOSIT	P	M	P	M	M	M	M	Ck	P	P	Ck	Pk	Pk	Pk	M	P	M	M	—
	MAIN VARIABLE	←──────────────────── RADIAL LOCATION IN JET AT VARIOUS Re ────────────────────→																		

-317-

Category	Sample	D1	D2	D3	D4	D5	D6	D7	D8	D9	D10	D11	D12	D13	D14	D15	D16	D17	D18	D19	D20
LASER	'P' TOTAL POWER W	2.43 ±.2	2.40 ±.2	2.30 ±.2	2.60 ±.2	2.43 ±.05	2.32 ±.05	2.18 ±.1	2.1 ±.3	1.78 ±.05	1.35 ±.1	1.34 ±.1	1.34 ±.1	1.55 ±.15	2.06 ±.1	2.08 ±.1	2.00 ±.05	2.00 ±.4	1.37 ±.3	1.98 ±.2	1.81 ±.2
	MAXIMUM POWER PEAK W	2.63	2.6	2.7	2.8	2.48	2.37	2.28	2.4	1.83	1.45	1.44	1.44	1.70	2.16	2.18	2.05	2.40	1.67	2.18	2.01
	'P/D_b' POWER INTENSITY W/cm	6.1	6.76	7.9	9.6	10.5	12.9	15.6	17.3	14.7	9.3	9.2	7.3	8.4	9.8	9.3	8.9	7.2	11.3	12.3	8.8
OPTICS	FOCAL LENGTH OF LENS cms	29.5 ←————————————————→																			
	LENS/OBJECT DIST: cms	104.1	106.7	109.2	111.7	114.3	116.8	119.4	121.9	121.9	124.5	124.5	127.0	127.0	128.3	129.5	129.5	132.0	120.6	118.1	115.6
	LENS/IMAGE DIST: cms	48.3	45.7	43.2	40.6	38.1	35.5	33.0	30.5	30.5	27.9	27.9	25.4	25.4	24.1	22.8	22.8	20.3	31.75	34.29	36.8
	'δ' DIFFRACTION LIMIT SPOT cms	.32	.275	.235	.19	.15	.10	.06	.041	.041	.065	.065	.104	.104	.13	.154	.154	.196	.041	.08	.125
	'D_b=δ+0.08 ESTIMATED SPOT DIAM: cms	.400	.355	.315	.270	.230	.180	.140	.121	.121	.145	.145	.184	.184	.210	.224	.224	.276	.121	.160	.205
	PLOTTING SYMBOL	x	x	x	+	+	+	+	+	+	+	+	+	+	+	+	+	+	+	+	+
GAS	FLOW RATE litres/min	9.8 ←————————————————→																			
	JET REYNOLDS NO	2086 ←———————————————→																			
	CHELATE CONC: AT JET gm/cc×10⁶		.47	.49			.22	.34	.34	.31	.21	.28	.18	.24	.15	.31	.14	.38	.32	.32	.18
	TEMPERATURE °C	140 ←————————————————→																			
	JET/PLATE DISTANCE cms	3.8 ←————————————————→																			
	ANGLE TO SUBSTRATE °	45 ←————————————————→																			
	OUTER DIAM/BEAM DIAM	.61	.68	.56	.88	1.03	1.18	1.35	1.67	1.20	.75	.75	.52	.83	.84	.45	1.07	.50	1.11	1.20	1.07
	INNER DIAM/BEAM DIAM			.32	.66	.66	.82	1.09	1.25	.89	.50	.42		.69	.28	.28	.62		.56	.87	.74
	BURNT DIAM/BEAM DIAM							.25	.83	.36											
DEPOSIT	SUBSTRATE MATERIAL	A ←————————————————→																			
	TIME OF DEPOSITION s	120	360	←——→	←——→	180	←——→	←——→	90	150	120	←——→	←——→	180	120	←→	300	240	120	120	300
	RADIAL POSITION IN JET cms	0.0	.688	.53	.51	.79	0.0	.27	.39	.39	.32	.34	—	.30	.30	.34	.53	.59	.54	.48	.37
	DIAMETER SPOT OUTER cms	.243	.240	.177	.238	.238	.212	.190	.202	.145	.109	.109	.096	.152	.177	.101	.239	.139	.134	.192	.220
	INNER cms	cryst only	—	.101	.177	.152	.147	.152	.152	.108	.072	.061	—	.127	.058	.063	.139	—	.104	.139	.152
	BURNT cms	—	—	—	—	—	—	.035	.101	.043	—	—	—	—	—	—	—	—	—	—	—
	BLUE cms	—	—	—	—	—	—	—	—	—	—	—	—	—	—	—	—	—	—	—	—
	DEPTH SPOT TALYSURF μ	.02	.12	.01	.04	.07	.1	9.13	20	6.0	.25	.6	no	.12	.1	.12	.04	spoilt excl. crack	2.6	.44	.37
	DOUBLE BEAM μ	v faint	.11	.01	.04	.06	.01	4.1	?	?	.26	.6	deposit	.11	.09	.17	.03		2.9	.62	.24
	COLOUR FRINGES μ	—	.07	—	—	—	.1	edge .4	—		.23	edge .23	—					.08	edge .4		.4
	SHAPE OF DEPOSIT	—	—	⌒	⌒	⌒	⌒	⋀	⋀	⋀⋀	ᴖ	⌒	/	⌒	—	—	—	—	⌒	⌒	⌒
	TYPE OF DEPOSIT	P	P	P	P	P	P	Pk	Cr	Pk	M	Ck	—	P	P	P	P	?	Pk	M	M
	MAIN VARIABLE	←————————————————→ DIAM BEAM and P/D_b ←————————————————→																			
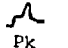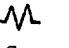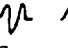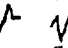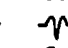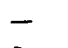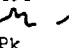
	Sample	D21	D22	D23	D24	D25
LASER	'P' TOTAL POWER W	1.50 ±.2	1.50 ±.2	1.70 ±.2	1.54 ±.2	1.27 ±.2
	MAXIMUM POWER PEAK W	1.7	1.7	1.8	1.74	1.47
	'P/D_b' POWER INTENSITY W/cm	11.5	10.0	13.7	12.0	9.9
OPTICS	FOCAL LENGTH OF LENS cms	29.5	$\longleftrightarrow$			
	LENS/OBJECT DIST cms	120.0	118.7	121.3	120.9	120.9
	LENS/IMAGE DIST cms	32.4	22.6	31.1	31.4	31.4
	'6' DIFFRACTION LIMIT SPOT cms	.050	.070	.044	.048	.048
	D_b=6+0.08 ESTIMATED SPOT DIAMETER cms	.13	.15	.124	.128	.128
	PLOTTING SYMBOL	+				
GAS	FLOW RATE litres/min	9.8	$\longleftrightarrow$			
	JET REYNOLDS NO	2086	$\longleftrightarrow$			
	CHELATE CONC: AT JET gm/cc x 10^6	.32	.18	.55	.59	
	TEMPERATURE °C	140	$\longleftrightarrow$			
	JET/PLATE DISTANCE cms	3.8	$\longleftrightarrow$			
	ANGLE TO SUBSTRATE °	45	$\longleftrightarrow$			
	OUTER DIAM/BEAM DIAM	1.55	1.21	1.37	1.48	1.33
	INNER DIAM/BEAM DIAM	1.17	1.03	1.12	1.14	.96
	BURNT DIAM/BEAM DIAM	.77		.84	.89	.69
DEPOSIT	SUBSTRATE MATERIAL	A	$\longleftrightarrow$			
	TIME OF DEPOSITION s	120	$\longleftrightarrow$			
	RADIAL POSITION IN JET cms	.308	.53	.50	.49	.38
	DIAMETER SPOT OUTER cms	.202	.182	.170	.190	.171
	INNER cms	.152	1.54	.139	1.46	.123
	BURNT cms	.101	—	.104	.114	.088
	BLUE cms	—	—	---	—	---
	DEPTH SPOT TALYSURF μ	7.5	2.0	5.6	7.7	.88
	DOUBLE BEAM μ	—	1.	—	—	.93
	COLOUR FRINGES μ	—	—	edge .9	edge .7	.9
	SHAPE OF DEPOSIT					
	TYPE OF DEPOSIT	Pk	M	Ck	Ck	M SEM
	MAIN VARIABLE	$\longleftarrow$ P/D_b and D_b $\longrightarrow$				

Sample		E1	E2	E3	E4	E5	E6	E7	E8	E9	E10	E11	E12	E13	E14	E15	E16	E17	E18	E19	E20
LASER	'P' TOTAL POWER W	1.58 ±.1	1.54 ±.14	1.60 ±.1	1.58 ±.2	1.50 ±.1	1.45 ±.15	1.35 ±.05	1.29 ±.25	1.58 ±.05	1.65 ±.1	1.41 ±.7	1.45 ±.1	1.38 ±.02	1.38 ±.15	1.38 ±.15	1.35 ±.1	1.35 ±.1	1.55 ±.1	1.50 ±.15	1.38 ±.1
	MAXIMUM POWER PEAK W	1.68	1.68	1.70	1.78	1.60	1.60	1.40	1.54	1.63	1.75	2.11	1.55	1.40	1.53	1.53	1.45	1.45	1.65	1.65	1.48
	'P/D_b' POWER INTENSITY W/cm	12.3	12.0	12.5	12.3	11.7	11.3	10.5	10.0	12.3	12.9	11.0	11.3	10.8	10.8	10.8	10.5	10.5	12.1	11.7	10.8
OPTICS	FOCAL LENGTH OF LENS cms	29.5	←																		→
	LENS/OBJECT DIST cms	121	←																		→
	LENS/IMAGE DIST cms	31.42	←																		→
	'δ' DIFFRACTION LIMIT SPOT cms	.048	←																		→
	'D'=δ+0.08 ESTIMATED SPOT DIAM cms	.128	←																		→
	PLOTTING SYMBOL	+																			
GAS	FLOW RATE litres/min	8.4	←								→	5.0	←								→
	JET REYNOLDS NO	1842	←								→	1092	←								→
	CHELATE CONC: AT JET gm/cc×10^6																				
	TEMPERATURE °C	120	←																		→
	JET/PLATE DISTANCE cms	38.1	←																		→
	ANGLE TO SUBSTRATE °	45	←																		→
	OUTER DIAM/BEAM DIAM	1.23	1.23	1.23	1.38	.59	.99	.99	1.14	1.28	1.19	.97	.99	.83	.63	.22	.99	1.05	.95	.93	1.05
	INNER DIAM/BEAM DIAM	.99	.79	.40	.99	.19	.99	.83	.85	.89	.77	.73	.99	.45			.69	.72		.79	
	'BURNT' DIAM/BEAM DIAM												.52								
DEPOSIT	SUBSTRATE MATERIAL	A																			
	TIME OF DEPOSITION s	90	←		→	120	←		→	90	←		→	120	←						→ 300
	RADIAL POSITION IN JET cms	.268	.266	.499	.717	1.20	0.0	.467	.572	1.02	1.4	0.0	0.0	.20	.58	1.0	0.0	.38	.84	1.1	1.5
	DIAMETER SPOT OUTER cms	.157	.157	1.57	.177 / .127	.076 / .025	1.27	.127	.146	.164	.152 / .101	.124	.127	.106	.081	.028	.127	.134	.122	.119	.134
	INNER cms	.127	.101	.0505	--	--	.127	.106	.109	.114	.098	.094	.127	.058	--	—	.088	.092	--	.101	--
	BURNT cms	--	--.	--	--	--	--	--	--	--	--	--	.066	--	--	--	--	--	--	--	--
	BLUE cms	--	--	--	--	--	--	--	--	--	--	--	--	--	--	--	--	--	--	--	--
	DEPTH SPOT TALYSURF μ	2.7	.25 missed	.1	.1	v faint	1.18	.3	.27	--	.06	--	4	.25	.1	v faint	--	.16	.1	--	--
	DOUBLE BEAM μ	1.8	1.2	.06	.1	--	crack	.35	.21	.1	.05	.17	crack	.18	.1		.15	.1	.1	.1	.12
	COLOUR FRINGES μ	.28	--	.06	--	--	.3	--	--	--	--	.23	.3	.2	--	--	--	—			
	SHAPE OF DEPOSIT	(symbol)	(symbol)	(symbol)	(symbol)	(symbol)	(symbol)	(symbol)	(symbol)	(symbol)	(symbol)	(symbol)	(symbol)	(symbol)	(symbol)	(symbol)	(symbol)	(symbol)	(symbol)	(symbol)	(symbol)
	TYPE OF DEPOSIT	Ck'	M	P	P	--	Ck	M	M	P	P	P	Ck	M	P	P	P	P	P	P	P
	MAIN VARIABLE	← various Re and Radial location →																			

	Sample	E21	E22	E23	E24	E25	E26	E27	E28	E29	E30	E31
LASER	'P' TOTAL POWER W	1.44 ±.05	1.49 ±.1	1.44 ±.05	1.44 ±.1	1.50 ±.08	1.45 ±.05	1.25 ±.1	1.30 ±.08	1.30 ±.02	1.35 ±.1	1.40 ±.2
	MAXIMUM POWER PEAK W	1.49	1.59	1.49	1.54	1.58	1.50	1.35	1.38	1.32	1.45	1.60
	'P/D_b' POWER INTENSITY W/cm	11.2	11.6	11.2	11.2	11.6	11.3	9.7	10.1	10.1	10.5	10.9
OPTICS	FOCAL LENGTH OF LENS cm	29.5	←									→
	LENS/OBJECT DIST: cms	121.0	←									→
	LENS/IMAGE DIST: cms	31.42	←									→
	'6' DIFFRACTION LIMIT SPOT cms	.048	←									→
	'D'=6+0.08 ESTIMATED SPOT DIAM cms	.128	←									→
	PLOTTING SYMBOL	+										
GAS	FLOW RATE litres/min	3.84	←								→	17.8
	JET REYNOLDS No	840	←								→	3892
	CHELATE CONC: AT JET gm/ccx10^6	.39			.20			.20			.39		.12
	TEMPERATURE °C	120	←									→
	JET/PLATE DISTANCE cms	3.81	←									→
	ANGLE TO SUBSTRATE °	45	←									→
	OUTER DIAM/BEAM DIAM	1.14	1.11	1.20	1.14 / .89	.35	.93	1.05	.91	.55		1.03
	INNER DIAM/BEAM DIAM	.97	.87	.83			.69	.49	.48			.76
DEPOSIT	SUBSTRATE MATERIAL	A										
	TIME OF DEPOSITION s	150	120	←								→
	RADIAL POSITION IN JET cms	0.0	.38	.59	.31	1.2	0.0	0.0	.21	.25	.74	.41
	DIAMETER SPOT OUTER cms	.146	.142	.154	.146 / .114	.045	.119	.134	.116	.071	—	.132
	INNER cms	.124	.112	.106	—	—	.088	.063	.061	—	—	.098
	BURNT cms	—	—	—	—	—	—	—	—	—	—	—
	BLUE cms	—	—	—	—	—	—	—	—	—	—	—
	DEPTH SPOT TALYSURF μ	.75	.1	.09	—	—	—	—	—	—	no deposit	.04
	DOUBLE BEAM μ	.9	.1	.09	.1	.1	.08	.1	.1	.1		—
	COLOUR FRINGES μ	—	.06	.06	—	v faint	—	.05	—	—	—	—
	SHAPE OF DEPOSIT	⌢	—	—	◡	—	—	—	—	—	/	—
	TYPE OF DEPOSIT	M	P	P	P	P	P	P	P	P	—	P
	MAIN VARIABLE	←				RADIAL LOCATION and Re						→

	Sample	F1	F2	F3	F4	F5	F6	F7	F8	F9	F10	F11	F12	F13	F14
LASER	'P' TOTAL POWER W	1.1 ±.1	1.3 ±.1	1.4 ±.1	1.5 ±1.0	2.08 ±.1	1.85 ±.1	1.6 ±.1	1.68 ±.1	1.54 ±.2	1.63 ±.1	1.35 ±.1	1.45 ±.1	1.67 ±.1	1.5 ±.3
	MAXIMUM POWER PEAK W	1.2	1.4	1.5	2.5	2.18	1.95	1.7	1.78	1.74	1.73	1.45	1.55	1.77	1.8
	'P/D_b' POWER INTENSITY W/cm	8.5	10.1	10.9	11.7	16.2	14.4	12.5	13.1	12.0	12.7	10.5	11.3	13.0	11.7
OPTICS	FOCAL LENGTH OF LENS cm	29.5	←												→
	LENS/OBJECT DIST: cms	121.0	←												→
	LENS/IMAGE DIST: cms	31.4	←												→
	'6' DIFFRACTION LIMIT SPOT cms	.048	←												→
	'D_b'=6+0.08 ESTIMATED SPOT DIAM cms	.128	←												→
	PLOTTING SYMBOL	+													
GAS	FLOW RATE litres/min	9.8	←												→
	JET REYNOLDS NO	2086	←												→
	CHELATE CONC: AT JET gm/ccx10⁶	.36	.44		.18	.24	.29		.33	.20		.47	.36		
	TEMPERATURE °C	140	←												→
	JET/PLATE DISTANCE cms	1.27	←					→	2.54	←		→	3.81	←	→
	ANGLE TO SUBSTRATE °	25	←												→
	B/D_j	2.5	←					→	5.0	←		→	7.5	←	→
DEPOSIT	OUTER DIAM/D_b	.83	.93	.79	1.33	.99	.79	.81	.89	1.10	.79	.98	.94	1.29	1.03
	INNER DIAM/D_b				.94					.69				1.15	.63
	BURNT DIAM/D_b	.54			.54	.58								1.06	
	SUBSTRATE MATERIAL	A													
	TIME OF DEPOSITION s	120	←										→	132.5	120
	RADIAL POSITION IN JET cms	0.0	←						→	.51	.54	←			→
	DIAMETER SPOT OUTER cms	.106	.119	.101	.17	.127	.101	.104	.114	.141	.101	.126	.121	.166	.132
	INNER cms	––	––	––	.12	––	––	––	––	.088	––	––	––	.148	.081
	BURNT cms	.07	––	––	.07	.075	––	––	––	––	––	––	––	.136	––
	BLUE cms	––	––	––	––	––	––	––	––	––	––	––	––	––	––
	DEPTH SPOT TALYSURF µ	.24	––	––	9.3	9.3	.27	––	––	2	.74	––	1.4	10	––
	DOUBLE BEAM µ	.23	.1	––	?	?	.26	.07	.1	?	.9	.15	.8	?	.11
	COLOUR FRINGES µ	––	––	––	––	––	––	––	––	.06	––	.4	––	––	––
	SHAPE OF DEPOSIT	⌐	—	/	ᴧᴧ	ᴧᴧ	⌐	—	—	⌐	⌐	—	⌐	ᴧᴧ	–
	TYPE OF DEPOSIT	P	P	––	Cr	Cr	M	P	P	Ck	M	P	Ck	Pk	P
			v faint	v faint											
	MAIN VARIABLE	←					JET PLATE DISTANCE								→

-322-

	Sample	G1	G2	G3	G4	G5	G6	G7	G8	G9	G10	G11	G12	G13	G14	G15	G16	G17	G18	G19	G20
LASER	'P' TOTAL POWER W	1.18 ±.2	1.42 ±.2	0.80 ±.2	0.5 ±.1	1.13 ±.1	0.75 ±.05	0.72 ±.05	0.70 ±.05	0.60 ±.1	0.36 ±.1	.15 ±.1	.60 ±.1	.70 ±.3	.41 ±.1	.41 ±.1	.47 ±.05	.44 ±.05	.35 ±.1	.33 ±.05	.32 ±.1
	MAXIMUM POWER PEAK W	1.38	1.62	1.00	0.6	1.23	0.80	.79	.75	.70	.46	.25	.90	.80	.51	.46	.52	.54	.40	.38	.42
	'P/D_b' POWER INTENSITY W/cm	6.4	44.3	14.8	22.7	26.9	17.8	10.9	31.8	27.2	16.3	6.8	18.7	21.8	12.8	9.3	14.7	20.0	14.6	10.3	6.9
OPTICS	FOCAL LENGTH OF LENS cm	5.3	←																		→
	LENS/OBJECT DIST: cms	144.8	147.3	147.6	147.0	146.7	146.7	146.4	147.0	147.0	147.0	147.0	147.3	147.3	147.3	146.7	146.8	147.0	147.2	147.3	147.5
	LENS/IMAGE DIST: cms	7.6	5.1	4.8	5.4	5.7	5.7	6.0	5.4	5.4	5.4	5.4	5.1	5.1	5.1	5.7	5.55	5.4	5.2	5.1	4.9
	'δ' DIFFRACTION LIMIT SPOT CMS	.17	.018	.040	.008	.028	.028	.052	.008	.008	.008	.008	.018	.018	.018	.030	.018	.008	.010	.018	.032
	'D'=δ+0.014 ESTIMATED DIAM: cms	.184	.032	.054	.022	.042	.042	.066	.022	.022	.022	.022	.032	.032	.032	.044	.032	.022	.024	.032	.046
	PLOTTING SYMBOL	+	▲	■	▲	■	■	■	▲	▲	▲	▲	▲	▲	▲	■	▲	▲	▲	▲	■
GAS	FLOW RATE litres/min	8.4	←																		→
	JET REYNOLDS NO	1842	←																		→
	CHELATE CONC: AT JET gm/cc×10^6															.41	.35				.19
	TEMPERATURE °C	120	←																		→
	JET/PLATE DISTANCE cms	3.81	←												→		1.59	←				→
	ANGLE TO SUBSTRATE °	45	←												→		25	←				→
	OUTER DIAM/D_b		4.8	1.81	2.14	1.62	.71	.061	1.72	1.50	1.04	1.00	.34	1.34	.91	.63	1.03	1.8	1.67	1.56	1.09
	INNER DIAM/D_b		3.0	1.17	1.55	1.21	.47		1.13	1.13						.47			.91	.83	.22	.22
	BURNT DIAM/D_b		1.34		1.00	.643	.35		.68	.68	.68				.56	.28		.72				
	BLUE DIAM/D_b															.41						
	TIME OF DEPOSITION s	120	←				→ 30	120	120	←			→ 30	120	←		→ 132.3	120	←			→
	RADIAL POSITION IN JET cms		.444	.45	.35	.15	.23	.11	.36	.35	.08	.32	.67	.30	.25	0.0	←				→
	DIAMETER SPOT OUTER cms		.154	.098	.047	.068	.030	.004	.038	.033	.023	.022	.011	.043	.029	.028	.033	.04	.04	.05	.05
	INNER cms		.096	.063	.034	.051	.020	—	.025	.025	—	—	—	—	.015	—	—	.020	.020	.007	.01
	BURNT cms		.043	—	.022	.027	.015	—	.015	.015	.015	—	—	.018	.009	—	.023	—	—	—	—
	BLUE cms		—	—	—	—	—	—	—	—	—	—	—	—	—	—	.013	—	—	—	—
	DEPTH SPOT TALYSURF μ	no	27.5	11	15	15	—	—	15	—	—	—	—	9.3	—	—	—	—	—	—	—
	DOUBLE BEAM μ	deposit?	?	?	?	.82	'	?		2	...	—	!	2.25	—	—	—	.3	.3	.12	
	COLOUR FRINGES μ	—	—	.2	—	.06?	—	—	—	.7+	—	—	—	.5	—	—	—				
	SHAPE OF DEPOSIT	/	⋏L	⋏L	⋏L	⋏	⌒	•	⋏	•	⋏	⋏	-	⋀	⌒			⌒	⌒	⌒	
	TYPE OF DEPOSIT	—	Cr	Pk	Cr SEM	Cr	Cr	?	Cr	Cr	Cr	Cr SEM	?	Pk	M	crusty ?	Cr?	?	M	M	M
	MAIN VARIABLE	←				→ P/D_b and D_b using 5.3cm FOCAL LENGTH LENS	←														→

	Sample	G21	G22	G23	G24	G25	G26	G27	G28	G29	G30	G31
LASER	'P'TOTAL POWER W	.4 ±.04	.5 ±.1	.4 ±.1	.07 ±.02	.03 ±.005	.03 ±.005	.12 ±.002	.31 ±.1	.20 ±.05	.09 ±.01	.25 ±.005
	MAXIMUM POWER PEAK W	.44	.60	.50	.09	.035	.035	.122	.41	.25	.10	.255
	'P/D_b' POWER INTENSITY W/cm	18.2	22.7	18.2	3.2	1.4	1.4	5.4	14.1	9.1	4.1	11.4
OPTICS	FOCAL LENGTH OF LENS cms	5.3	←————————————————————————————→									
	LENS/OBJECT DIST: cms	147.0	←————————————————————————————→									
	LENS/IMAGE DIST: cms	5.4	←————————————————————————————→									
	'δ' DIFFRACTION LIMIT SPOT cms	.008	←————————————————————————————→									
	'D'=δ+0.014 ESTIMATED SPOT DIAM: cms	.022	←————————————————————————————→									
	PLOTTING SYMBOL	▲										
GAS	FLOW RATE litres/min	8.4	←————→		5.6	←——→	8.4	←————————————————→				
	JET REYNOLDS NO	1842	←————————→		1238	←——→	1842	←————————————————→				
	CHELATE CONC: AT JET gm/ccx10^6	.23	.16	.16	.15	.19	.19	—	—	—	—	.09
	TEMPERATURE °C	120	←————————————————————————————→									
	JET/PLATE DISTANCE cms	1.59	←————————————————————————————→									
	ANGLE TO SUBSTRATE °	25	←————————————————————————————→									
	OUTER DIAM/D_b	1.61	1.41	1.04	—	—	—	—	2.2	1.04	—	.59
	INNER DIAM/D_b	—	—	—	—	—	—	—	—	—	—	—
	BURNT DIAM/D_b	.68	.23	.60	—	—	—	—	.91	.45	—	—
DEPOSIT	SUBSTRATE MATERIAL	A										
	TIME OF DEPOSITION s	72.5	60	30	120	120	120	126	90	90	90	60
	RADIAL POSITION IN JET cms	0.0	←————————————————————→						1.0	1.0	0.0	1.1
	DIAMETER SPOT OUTER cms	.0355	.031	.023	—	—	—	—	.048	.023	—	.013
	INNER cms	—	—	—	—	—	—	—	—	—	—	—
	BURNT cms	.015	.005	.013	—	—	—	—	crater .020	.010	—	—
	BLUE cms	—	—	—	—	—	—	—	—	—	—	—
	DEPTH SPOT TALYSURF μ	—	—	—	no dep	no dep.	no dep	no dep	10	—	no dep	—
	DOUBLE BEAM μ	?	.3	.5						1.2		.2
	COLOUR FRINGES μ	—	—	—	—	—	—	—	—	—	—	—
	SHAPE OF DEPOSIT	-√\-	-√\-	-√\-	/	/	/	/	√L	√\-	/	⌒
	TYPE OF DEPOSIT	Cr	Cr	Cr	—	—	—	—	Cr	Cr	—	M
	MAIN VARIABLE	←————————————————————→ P/D_b and D_b							←————————————→			

	Sample	H1	H2	H3	H4	H5	H6	H7	H8	H9	H10	H11	H12	H13	H14	H15	H16
LASER	'P' TOTAL POWER W	.5 ±.05	1.34 ±.2	1.53 ±.2	1.45 ±.1	1.24 ±.2	1.39 ±.3	1.48 ±.05	1.62 ±.05	1.73 ±.1	1.73 ±.1	1.73 ±.1	1.38 ±.1	1.94 ±.1	1.50 ±.2	1.66 ±.3	1.85 ±.3
	MAXIMUM POWER PEAK W	.55	1.95	2.00	1.55	1.44	1.69	1.53	1.67	1.83	1.83	1.83	1.48	2.14	1.60	1.96	2.15
	'P/D_b' POWER INTENSITY W/cm	5.3	14.2	19.3	22.6	22.9	27.2	29.0	28.9	26.2	21.1	18.4	12.7	17.8	16.0	17.6	17.4
OPTICS	FOCAL LENGTH OF LENS cms	13.7 ←——————————————————————————→															
	LENS/OBJECT DIST cms	139.7	139.7	139.4	139.1	138.8	138.4	138.4	138.1	137.8	137.5	137.2	136.9	136.9	139.7	139.7	140.0
	LENS/IMAGE DIST cms	12.7	12.7	13.0	13.3	13.6	13.97	13.97	14.3	14.6	14.9	15.2	15.5	15.5	12.7	12.7	12.4
	'δ' DIFFRACTION LIMIT SPOT cms	.060	.060	.045	.030	.020	.017	.017	.022	.032	.048	.060	.075	.075	.060	.060	.072
	'D'=δ+.034 ESTIMATED SPOT DIAM cms	.094	.094	.079	.064	.054	.051	.051	.056	.066	.082	.094	.109	.109	.090	.094	.106
	PLOTTING SYMBOL	●	●	■	■	■	■	■	■	■	●	●	+	+	●	●	+
GAS	FLOW RATE litres/min	8.4 ←——————————————————————————→															
	JET REYNOLDS NO	1842 ←—————————————————————————→															
	CHELATE CONC: AT JET gm/ccx10^6	--	.26	.26	.24	.14	.12	.24	.26	.21	.23	.24	.28	.36	.23	.46	
	TEMPERATURE °C	120 ←——————————————————————————→															
	JET/PLATE DISTANCE cms	3.81 ←—————————————————————————→															
	ANGLE TO SUBSTRATE °	45 ←———————————————————————————→															
	OUTER DIAM/D_b		1.02	1.21	1.58	1.92	1.88	1.33	1.30	1.15	1.07	.67		.79		1.21	1.05
	INNER DIAM/D_b		.67	.96	1.19	1.41	1.39	.98	1.09	.83	.46					.97	.78
	BURNT DIAM/D_b		.32	.52	.78	.92	.98	.71	.77	.56						.38	.30
DEPOSIT	SUBSTRATE MATERIAL	A															
	TIME OF DEPOSITION s	120 ←—————————————→						60 ←→ 120 ←—————————————————————→									
	RADIAL POSITION IN JET cms	0.0 ←——————————————————————————————→														.58	.42
	DIAMETER SPOT OUTER cms	--	.096	.096	.101	.104	.096	.068	.073	.076	.088	.063	--	.086	--	.114	.111
	INNER cms	--	.063	.076	.076	.076	.071	.050	.061	.055	.038	--	--	--	--	.091	.083
	BURNT cms	--	.030	.025	.050	.050	.050	.036	.043	.037	--	--	--	--	--	.036	.032
	BLUE cms	--	--	--	--	--	--	--	--	--	--	--	beam blocked?		--	--	--	--
	DEPTH SPOT TALYSURF μ	no	3.1	5.6	12.5	27.5	30	13.7	25	16.2	5	--	no	faint	no	5.0	2.3
	DOUBLE BEAM μ	dep	4.1	5.0	?	?	?	?	?	?	1.7?	.1	dep	--	dep	5.3	1.4?
	COLOUR FRINGES μ	--	--	--	--	--	--	.3	.7	.3	--	--	--	--	--	1.0	--
	SHAPE OF DEPOSIT	/	∧	∧	∧∧	∧	∧	∧	∧	∧	∧	—	/	—	/	∧	∧
	TYPE OF DEPOSIT	--	M	Pk Ck	Cr	Cr	Cr	Cr	Cr	Cr			--	P	--	Pk Ck	M Ck
	MAIN VARIABLE	←——————————————— POWER and D_b FOR 13.7 cm FOCAL LENGTH LENS ———————————————→															

Category	Sample	I1	I2	I3	I4	I5	I6	I7	I8	I9	I10	I11	I12	I13	I14	I15	I16	I17	I18	I19	I20
LASER	'P' TOTAL POWER W	1.08 ±.15	1.32 ±.15	1.20 ±.05	1.40 ±.10	1.47 ±.20	1.23 ±.5	1.27 ±.1	1.17 ±.1	1.12 ±.05	1.25 ±.05	0.45 ±.1	.4 ±.02	.50 ±.02	.43 ±.02	.43 ±.02	.43 ±.02	.43 ±.02	.43 ±.02	.43 ±.02	.43 ±.02
	MAXIMUM POWER PEAK W	1.23	1.47	1.25	1.50	1.67	1.73	1.37	1.27	1.17	1.30	.50	.42	.39	.27	.39	.34	.34	.34	.34	.34
	'P/D' POWER INTENSITY W/cm	19.3	23.5	21.4	25.0	26.2	21.9	22.6	20.9	20.0	22.4	8.0	7.1	8.9	7.6	7.6	7.6	7.6	7.6	7.6	7.6
OPTICS	FOCAL LENGTH OF LENS cm	13.7	←——————————————————————————————————→																		
	LENS/OBJECT DIST cms	138.1	←——————————————————————————————————→																		
	LENS/IMAGE DIST cms	14.3	←——————————————————————————————————→																		
	'δ' DIFFRACTION LIMIT SPOT cms	0.022	←——————————————————————————————————→																		
	'D'=δ+0.034 ESTIMATED SPOT DIAM cms	.056	←——————————————————————————————————→																		
	PLOTTING SYMBOL	●																			
GAS	FLOW RATE litres/min	8.4	←——————————————————————————————————→																		
	JET REYNOLDS No	1842	←——————————————————————————————————→																		
	CHELATE CONC AT JET gm/ccx10^6	.47	.41	.24	.22	.21	.17	.24	.23	.23	.25	.26	.21	.15	.14						.14
	TEMPERATURE °C	120	←——————————————————————————————————→																		
	JET/PLATE DISTANCE cms	3.81	←——————————————————————————————————→																		
	ANGLE TO SUBSTRATE °	45	←——————————————————————————————————→																		
	SUBSTRATE MATERIAL	B	C	D	E	F	B	C	D	E	F	B	C	D	E	F	C	C	C	C	C
DEPOSIT	OUTER DIAM/BEAM	1.44	1.44	1.39	1.66	2.18	1.57	1.48	1.48	1.62	1.71	.89	.77	.86	.68	.89	---	---	.44	.59	.77
	INNER DIAM/BEAM	1.21	1.21	1.27	1.30	1.71	1.21	1.08	1.12	1.12	1.27	.64	.41	.50	.59	.56					.35
	BURNT DIAM/BEAM	.82	.82	.86	.89	1.00	.77	.68	.71	.68	.68	.32	---	.32	.41	---					
	CRATER/BLUE DIAM/BEAM	.64	.71	.71	.68	.68	.64	.54	.59	.54	.59	---	---	---	---	---					
	TIME OF DEPOSITION s	120	←————————————————————————————→														5	10	20	45	80
	RADIAL POSITION IN JET cms	0.0	←—————————————→			.48	.57	.62	.60	.53	.72	.32	.33	.37	.62	0.0	←——————————→			
	DIAMETER SPOT OUTER cms	.081	.081	.078	.093	.122	.088	.083	.083	.091	.096	.050	.043	.048	.038	.050	---	---	.025	.033	.043
	INNER cms	.068	.068	.071	.073	.096	.068	.061	.063	.063	.071	.036	.023	.028	.033	.028	---	---	--	--	.020
	BURNT cms	.046	.046	.048	.050	.056	.043	.038	.040	.038	.038	.018	---	.018	.023	---	---	---	--	--	---
	CRATER BLUE CENTRE cms	.036	.040	.040	.038	.038	.036	.03D	.033	.030	.033	---	---	---	---	---	---	---	---	---	---
	DEPTH SPOT TALYSURF μ	22.5	27.5	25	25	18.7	21.5	20	24.2	17.5	22.5	.5	---	---	.5	2.4	no dep	no dep	.1	.1	.3
	DOUBLE BEAM μ											.5	.2	.4	.5	2.1	"	"	---	---	.1
	COLOUR FRINGES μ	skirt 2.5	0.8	1.0	1.0	←——————————————————————→					.8			.4	.6	.2	---	---	---	—	.1
	SHAPE OF DEPOSIT	ᴧᴧ	ᴧᴧ	←————————————————————→							ᴧ	ᴧ	ᴧ	ᴧ	ᴧ	/	/	—	—	ᴧ	
	TYPE OF DEPOSIT	Cr	Cr	Cr	Cr	←————————————→					Cr	M	M	M	M	M	---	—	P	P	M
	MAIN VARIABLE	←————————→ SUBSTRATE AND POWER ←————————→																			

	Sample	I21	I22	I23	I24	I25	I26	I27
LASER	'P' TOTAL POWER W	.43 ±.02	.43 ±.02	.43 ±.02	.60 ±.1	1.72 ±.2	.48 ±.05	.93 ±.2
	MAXIMUM POWER PEAK W	.34	.34	.34	.70	1.92	.53	.95
	'P/D' POWER INTENSITY W/cm	7.6	7.6	7.6	10.7	30.7	8.5	16.6
OPTICS	FOCAL LENGTH OF LENS cms	13.7	←———————————————→					
	LENS/OBJECT DIST cms	138.1	←———————————————→					
	LENS/IMAGE DIST cms	14.3	←———————————————→					
	'δ' DIFFRACTION LIMIT SPOT cms	0.022	←———————————————→					
	'D'=δ+0.034 ESTIMATED SPOT DIAM cms	.056	←———————————————→					
	PLOTTING SYMBOL	■						
GAS	FLOW RATE litres/min	8.4	←———————————————→					
	JET REYNOLDS NO	1842	←———————————————→					
	CHELATE CONC: AT JET gm/ccx10^6	30	.23	.24	.25	.24	.23	
	TEMPERATURE °C	120	←———————————————→					
	JET/PLATE DISTANCE cms	3.81	←———————————————→					
	ANGLE TO SUBSTRATE °	45	←———————————————→					
	SUBSTRATE MATERIAL	C	C	G	G	G	G	G'
	OUTER DIAM/BEAM	1.12	1.36	--	.09	.68	--	1.04
DEPOSIT	INNER DIAM/BEAM	.54	.64	--	--	.29	--	
	BURNT DIAM/BEAM	--	.50	--	--	--	--	
	BLUE DIAM/BEAM	--	--	--	--	--	--	
	TIME OF DEPOSITION s	160	320	120	←————————→			300
	RADIAL POSITION IN JET cm	0.0	.43	0.0	0.0	0.58	←———→	
	DIAMETER SPOT OUTER cms	.063	.067	--	.005	.038	--	.058
	INNER cms	.030	.036	--		.016	--	
	BURNT cms		.028	--	--	--	--	--
	BLUE cms	--	--	--	--	--	--	--
	DEPTH SPOT TALYSURF μ	0.7	1.2	no dep	--	0.6	no dep	too rough
	DOUBLE BEAM μ	0.8		--	.12	.4	--	
	COLOUR FRINGES μ	0.7	.9	--	.1	.6	--	
	SHAPE OF DEPOSIT	⌒	⌒⌒	/	⌒	⌃	/	—
	TYPE OF DEPOSIT	M	M	--	M	M	--	--
	MAIN VARIABLE	←————→		SUBSTRATE	←————→			

-327-

APPENDIX 5

COMPUTER PROGRAMME FLOW CHART

THE COMPUTER PROGRAMME

```
IC***********************************************************************     -0006
.C*      THERMAL CONDUCTION MODEL OF AN AXIALLY SYMMETRIC SPOT       *        -0007
!C*      HEATED BY A LASER.   THE MODEL INCLUDES SURFACE HEAT        *        -0008
;C*      LOSS AND SURFACE DEPOSITION.                                *        -0009
·C***********************************************************************     -0010
IC                                                                           -0011
.C                                                                           -0012
'C***********************************************************************     -0013
IC*      METHOU OF SOLUTION:   A FINITE DIFFERENCE SOLUTION         *        -0014
IC*      OF THE ELLIPTIC EQUATIONS FROM FOURIERAS SECOND LAW        *        -0015
C*       BY A CRANK  NICHOLSON METHOD.                              *        -0016
C*          THE MATRIX EXPANDS EXPONENTIALLY AND ERROR FUNCTION     *        -0017
'C*      THERMAL GRADIENTS ARE USED AT THE SOUTHERN AND EASTERN      *        -0018
.C*      BOUNDARIES.                                                 *        -0019
C*                                                                  *        -0020
.C*      THE PROGRAMME WAS WRITTEN BY W.M.STEEN                     *        -0021
C*       LAST MODIFIED   MARCH 1975                                 *        -0022
C***********************************************************************      -0023
C                                                                            -0024
C                                                                            -0025
C                        LIST OF VARIABLE NAMES                              -0026
C                                                                            -0027
C                                                                            -0028
C       ALPHA    =  THERMAL DIFFUSIVITY  -  M**2/S                           -0029
C       B        =  JET/SUBSTRATE DISTANCE  -  M                             -0030
C       BIG      =  LARGEST DIFFERENCE BETWEEN ESTIMATED AND CALCULATED      -0031
C                   TEMPERATURES  -  K                                       -0032
C       COND     =  THERMAL CONDUCTIVITY OF SUBSTRATE  -  W/M K              -0033
C       COUNT    =  NUMBER OF ITERATIONS / STEP                             -0034
C       D        =  JET DIAMETER  -  M                                       -0035
C       DENS     =  DENSITY OF SUBSTRATE  -  KG/M**3                         -0036
C       DR       =  RADIAL INCREMENT  -  M                                   -0037
C       DT       =  TIME INTERVAL/STEP  -  S                                 -0038
C       GCOND    =  THERMAL CONDUCTIVITY OF THE GAS  -  W/M K                -0039
C       GCP      =  HEAT CAPACITY OF THE GAS  -  J/KG K                      -0040
C       GDENS    =  DENSITY OF THE GAS AT NTP  -  KG/M**3                    -0041
C       GDIFF    =  DIFFUSIVITY OF CHELATE THROUGH NITROGEN  -  M**2/S       -0042
C       GRSURF() =  SURFACE TEMPERATURE GRADIENT WHOSE TIME AVERAGE          -0043
C                   IS GRMURF()                                              -0044
C       GVEL     =  VELOCITY OF GAS AT JET EXIT  -  M/S                      -0045
C       GVISC    =  VISCOSITY OF GAS AT NTP  -  N S/M**2                     -0046
C       HCONV    =  CONVECTIVE HEAT TRANSFER COEFICIENT  -  W/M**2 K         -0047
C       HRAD     =  RADIANT HEAT TRANSFER COEFICIENT  -  W/M**2 K            -0048
C       IBEAM    =  NUMBER OF RADIAL MATRIX POINTS OVER WHICH POWER IS       -0049
C                   INCIDENT                                                 -0050
C       IOUT     =  PRINT ESCAPE                                             -0051
C       IPRINT   =  NUMBER OF STEPS BETWEEN ANSWER PRINT OUTS                -0052
C       IR+1     =  NUMBER OF RADIAL MATRIX POINTS                           -0053
C       IY+1     =  NUMBER OF DEPTH MATRIX POINTS                            -0054
C       LIM      =  NUMBER OF PROGRAMME STEPS TO BE TAKEN                    -0055
C       PTOTAL   =  TOTAL INCIDENT POWER  -  W                               -0056
C       RBEAM    =  RADIUS  OF LASER BEAM  -  M                              -0057
C       REFLEC   =  SURFACE REFLECTIVITY                                     -0058
C       RHOE     =  CONCENTRATION OF VAPOUR AT JET EXIT  -  KG/M**3          -0059
C       RSTAR()  =  DIMENSIONLESS RADIUS                                     -0060
C       SCHEM()  =  CHEMICALLY CONTROLLED DEPOSITION THICKNESS IN TIME DT    -0061
C       SMASS()  =  MASS TRANSFER CONTROLLED DEPOSITION THICKNESS IN TIME DT -0062
C       SPHT     =  HEAT CAPACITY OF SUBSTRATE  -  J/KG K                    -0063
C       SURFT()  =  SURFACE TEMPERATURE  -  K                                -0064
C       TEMP(K,I,J)  =  TEMPERATURE AT LOCATION : K  RADIAL. I  DEPTH.J TIME -0065
C       TEMPA    =  AMBIENT TEMPERATURE  -  K                                -0066
C       TEST     =  CONVERGENCY CRITERION                                    -0067
C       THETA    =  DIMENSIONLESS TIME                                       -0068
C       THICK()  =  DEPOSIT THICKNESS  -  M                                  -0069
C       TSTAR()  =  DIMENSIONLESS TEMPERATURE        ·                       -0070
C       W        =  WEIGHTING FACTOR                                         -0071
C       YSTAR()  =  DIMENSIONLESS DEPTH                                      -0072
C
```

```
                                                                              _0073
      PROGRAM ISOTE1(INPUT,OUTPUT,TAPE7,TAPE5=INPUT,TAPE6=OUTPUT)            _0074
      COMMON/CWIDTH/IR,IY,IT                                                 _0075
      COMMON/CGEN/SIGMA,PTOTAL,RBEAM,RE                                      _0076
      COMMON/CPROP/ALPHA,COND,DENS,SPHT,GVISC,GDENS,GVEL,O,B                 _0077
      COMMON/CSURF/POWER(40),REFLEC,HCONV,TEMPA,HRAD(40,3),SURFT(40,3)       _0078
      COMMON/COIM/TSTAR(40,40,3),THETA(40),RSTAR(40)                         _0079
      COMMON/CTIME/TIME                                                      _0080
      COMMON/CTYPE/TYPE(40)                                                  _0081
      COMMON/CGRID/R(40),Y(40),T(40)                                         _0082
      COMMON/CTEMP/TEMP(40,40,3),GRSURF(40,3)                                _0083
      COMMON/CPRINT/OT,OISTR(40)                                             _0084
      COMMON/CTRAN/CONV(40)                                                  _0085
      COMMON/COEP/THICK(40),RHOE,SC,GOIFF                                    _0086
      COMMON/COUT/IOUT                                                       _0087
      COMMON/CREF/REFL(40)                                                   _0088
      DIMENSION HEAO(12)                                                     _0089
      WRITE(6,110)                                                           _0090
  110 FORMAT(* VARIABLE MATRIX*)                                            _0091
C    ****************************************************************        _0092
C    *    SET INITIAL OATA ON :    LASER BEAM PROPERTIES          *        _0093
C    *                             SUBSTRATE PROPERTIES           *        _0094
C    *                             GAS JET PROPERTIES             *        _0095
C    ****************************************************************        _0096
      IOUT=0                                                                 _0097
      IT=3                                                                   _0098
      IY=10                                                                  _0099
      IR=24                                                                  _0100
      SIGMA=0.0000000567                                                     _0101
      PTOTAL=2.0                                                             _0102
      REFLEC=.18                                                            _0103
      RHOE=.000306                                                          _0104
      RBEAM=0.00055                                                          _0105
      GVEL=6.2204                                                           _0106
      GCONO=0.024                                                           _0107
      GCP=1000.                                                            _0108
      TEMPA=100.                                                           _0109
      B=.038                                                              _0110
      GDIFF=0.000032                                                        _0111
      D=.00508                                                             _0112
      SPHT=1176.                                                          _0113
      OENS=2490.                                                          _0114
      CONO=0.84                                                           _0115
      GOENS=1.25                                                          _0116
      GVISC=0.000017                                                        _0117
      IIY=IY+1                                                             _0118
      IIR=IR+1                                                             _0119
      DO 100 K=1,IIR                                                       _0120
      DO 100 I=1,IIY                                                       _0121
      DO 100 J=1,IT                                                        _0122
      TEMP(K,I,J)=0.                                                      _0123
      SURFT(K,J)=0.                                                       _0124
      GRSURF(K,J)=0.                                                      _0125
      THICK(K)=0.                                                         _0126
      R(K)=0.                                                             _0127
      Y(I)=0.                                                             _0128
      T(J)=0.                                                             _0129
      POWER(K)=0.                                                         _0130
      HRAO(K,J)=0.                                                        _0131
      REFL(K)=REFLEC                                                      _0132
  100 CONTINUE                                                             _0133
C    ****************************************************************        _0134
C    CALCULATION OF PROPERTIES                                             _0135
C    ****************************************************************        _0136
      IBEAM=19                                                             _0137
      ALPHA=CONO/(OENS*SPHT)                                               _0138
      WRITE(6,102)GDENS,GVISC,GVEL,O,GCP,GCONO,B                           _0139
  102 FORMAT(10H JET DATA ,/20H        GAS OENSITY =,F10.5,20H       GAS VISCOS_0140
     +ITY =,F10.8,20H       GAS VELOCITY =,F10.5,20H       JET OIAMETER =,F10.5/20_0141
     +H GAS SPECIFIC HEAT =,F10.6,20H  GAS CONOUCTIVITY =,F10.6,20H JET/PLATE OI_0142
     +STANCE=,F10.4)                                                       _0143
      WRITE(6,107) RHOE                                                    _0144
  107 FORMAT(23H JET EXIT CONCENTRATION,F10.8)                             _0145
      WRITE(6,104) REFLEC,SPHT,OENS,CONO,TEMPA,ALPHA                       _0146
  104 FORMAT(16H SUBSTRATE OATA ,/20H        REFLECTIVITY =,F10.4,20H       SUBST_0147
     +RATE SPHT =,F10.4,20H SUBSTRATE OENSITY =,F10.5,20H  SUBSTRATE CONOTY =,F1_0148
     +0.4/20H        AMBIENT TEMP =,F10.5,20H THERM OIFFUSIVITY =,14E9.2)  _0149
      WRITE(6,105) PTOTAL,RBEAM                                            _0150
  105 FORMAT(11H LASER OATA,/20H         TOTAL POWER =,F10.4,20H        BEAM RA_0151
     +DIUS =,F10.4)                                                        _0152
      RE=(GOENS*GVEL*O)/GVISC                                              _0153
      PR=GCP*GVISC/GCONO                                                   _0154
      SC=(GVISC)/(GDENS*GDIFF)                                             _0155
      WRITE(6,103) RE,PR,RBEAM                                             _0156
  103 FORMAT(8H  RE NO ,F10.2,8H   PR NO ,F10.4,10H BEAM RAO ,F10.6)       _0157
      HCONV=13.*(RE**0.5)*(PR**0.33)*GCONO/B                               _0158
C    ****************************************************************        _0159
C    *    SET UP MATRIX POINTS ANO TIME STEPS                    *        _0160
C    ****************************************************************        _0161
      CALL INIT                                                            _0162
C                                                                         _0163
```

```
C     *******************************************************************        -0164
C     *    SET UP GAUSSIAN POWER DISTRIBUTION                       *           -0165
C     *******************************************************************        -0166
C                                                                               -0167
      DO 101 K=1,IBEAM                                                          -0168
      GAUSK=1./(EXP((R(K)**2)/(RBEAM**2)))                                      -0169
      POWER(K)=(PTOTAL*GAUSK)/(3.142*(RBEAM**2))                                -0170
 101  CONTINUE                                                                  -0171
      IRRR=IR-1                                                                 -0172
      WRITE(6,106)(POWER(K),K=1,IRRR,2)                                         -0173
      WRITE(6,106)(POWER(K),K=2,IR,2)                                           -0174
 106  FORMAT(* POWER DISTRIBUTION WATTS/METER 2 =*,9G10.3)                      -0175
C                                                                               -0176
C     *******************************************************************        -0177
C         MAIN CALCULATION CYCLE                                               -0178
C     *******************************************************************        -0179
C                                                                               -0180
      CALL CALC                                                                 -0181
      STOP                                                                      -0182
      END                                                                       -0183
C                                                                               -0184
C     *******************************************************************        -0185
C     *                                                            *           -0186
C     *    SUBROUTINE INIT   -   TO FORM MATRIX AND DT             *           -0187
C     *                                                            *           -0188
C     *******************************************************************        -0189
      SUBROUTINE INIT                                                           -0190
      COMMON/CWIDTH/IR,IY,IT                                                    -0191
      COMMON/CGEN/SIGMA,PTOTAL,RBEAM,RE                                         -0192
      COMMON/CPROP/ALPHA,COND,DENS,SPHT,GVISC,GDENS,GVEL,D,B                    -0193
      COMMON/CSURF/POWER(40),REFLEC,HCONV,TEMPA,HRAD(40,3),SURFT(40,3)          -0194
      COMMON/CDIM/TSTAR(40,40,3),THETA(40),RSTAR(40)                            -0195
      COMMON/CTIME/TIME                                                         -0196
      COMMON/CTYPE/TYPE(40)                                                     -0197
      COMMON/CGRID/R(40),Y(40),T(40)                                           -0198
      COMMON/CTEMP/TEMP(40,40,3),GRSURF(40,3)                                   -0199
      COMMON/CPRINT/DT,DISTR(40)                                                -0200
      COMMON/CTRAN/CONV(40)                                                     -0201
      COMMON/CDEP/THICK(40),RHOE,SC,GDIFF                                       -0202
C                                                                               -0203
C     CALCULATION OF EXPONENTIAL R-Y MATRIX                                    -0204
C                                                                               -0205
      IIR=IR+1                                                                  -0206
      IIY=IY+1                                                                  -0207
      TIME=0.                                                                   -0208
      DR=RBEAM/10.                                                              -0209
      R(1)=0.                                                                   -0210
      DO 300 I=2,IIR                                                            -0211
      IL=I-1                                                                    -0212
      AI=I                                                                      -0213
      R(I)=R(IL)+DR*EXP(AI/5)                                                   -0214
 300  CONTINUE                                                                  -0215
      DO 301 J=1,IIY                                                            -0216
      Y(J)=R(J)                                                                 -0217
 301  CONTINUE                                                                  -0218
C                                                                               -0219
C     CALCULATION OF TIME INTERVAL AT START                                    -0220
C                                                                               -0221
      DT=(R(2)-R(1))**2/(16.*(2.*ALPHA))                                        -0222
      DT=DT*4.                                                                  -0223
      WRITE(6,304)(Y(I),I=1,IY)                                                 -0224
 304  FORMAT(8H DEPTH =,10F10.5)                                                -0225
      WRITE(6,303)(R(I),I=1,IR),DT                                              -0226
 303  FORMAT(9H RADIUS =,10F10.5/16H TIME INTERVAL =,F10.8,8H SECONDS.)         -0227
      RETURN                                                                    -0228
      END                                                                       -0229
```

```
·L                                                                              -0230
C    *************************************************************              -0231
·C   *                                                            *              -0232
·C   *    SUBROUTINE CALC  -  MAIN CALCULATION                    *              -0233
·C   *                                                            *              -0234
C    *************************************************************              -0235
C                                                                              -0236
     SUBROUTINE CALC                                                           -0237
     COMMON/CWIDTH/IR,IY,IT                                                    -0238
     COMMON/CGEN/SIGMA,PTOTAL,RBEAM,RE                                         -0239
     COMMON/CPROP/ALPHA,COND,DENS,SPHT,GVISC,GDENS,GVEL,D,B                    -0240
     COMMON/CLIM/AJ,LIM                                                        -0241
     COMMON/CSURF/POWER(40),REFLEC,HCONV,TEMPA,HRAD(40,3),SURFT(40,3)          -0242
     COMMON/CDIM/TSTAR(40,40,3),THETA(40),RSTAR(40)                           -0243
     COMMON/CTIME/TIME                                                         -0244
     COMMON/CTYPE/TYPE(40)                                                     -0245
     COMMON/CGRID/R(40),Y(40),T(40)                                           -0246
     COMMON/CTEMP/TEMP(40,40,3),GRSURF(40,3)                                  -0247
     COMMON/CPRINT/DT,DISTR(40)                                                -0248
     COMMON/CTRAN/CONV(40)                                                     -0249
     COMMON/CDEP/THICK(40),RHOE,SC,GDIFF                                      -0250
     COMMON/CREF/REFL(40)                                                      -0251
     DIMENSION GRMURF(40)                                                      -0252
     DIMENSION SCHEM(40),SMASS(40)                                            -0253
     DATA C,BOU/1HC,1HM/                                                       -0254
     IPRINT=5                                                                  -0255
C    *************************************************************              -0256
C    *    SET LIMIT ON NUMBER OF CALCULATION STEPS AND ALLOW DT  *              -0257
C    *    TO GROW AS THERMAL GRADIENTS SUBSIDE.                  *              -0258
C    *                                                            *              -0259
C    *    STATEMENT NUMBER 203 IS STEP LOOP                      *              -0260
C    *    STATEMENT NUMBER 206 IS ITERATION LOOP                 *              -0261
C    *                                                            *              -0262
C    *************************************************************              -0263
     DO 203 LIM=1,1000                                                         -0264
     IF(LIM.EQ.6) DT=DT*8                                                      -0265
     IF(LIM.EQ.200) DT=DT*2.                                                   -0266
     IF(LIM.EQ.250) GO TO 251                                                  -0267
     COUNT=0.                                                                  -0268
     TIME=TIME+DT                                                              -0269
 206 CONTINUE                                                                  -0270
     COUNT=COUNT+1.                                                            -0271
     TOT=0.                                                                    -0272
     J=1                                                                       -0273
     M=2                                                                       -0274
     IJ=3                                                                      -0275
C                                                                              -0276
C    CALCULATION OF SURFACE GRADIENTS                                          -0277
C                                                                              -0278
     DO 201 K=1,IR                                                            -0279
     IF(SURFT(K,J).GT.600.) REFL(K)=0.0                                       -0280
     HRAD(K,J)=SIGMA*(1.-REFL(K))*((SURFT(K,J)+273.)**2+(TEMPA+273.)**2)       -0281
    +*((SURFT(K,J)+273.)+(TEMPA+273.))                                         -0282
     HRAD(K,M)=SIGMA*(1.-REFL(K))*((SURFT(K,M)+273.)**2+(TEMPA+273.)**2        -0283
    +)*((SURFT(K,M)+273.)+(TEMPA+273.))                                        -0284
     GRSURF(K,J)=-((POWER(K)*(1.-REFL(K)))-(HCONV+HRAD(K,J))*(SURFT(K,J)       -0285
    +-TEMPA))/(COND)                                                           -0286
     GRSURF(K,M)=-((POWER(K)*(1.-REFL(K)))-(HCONV+HRAD(K,M))*(SURFT(K,M)       -0287
    +-TEMPA))/(COND)                                                           -0288
     GRMURF(K)=-GRAD(GRSURF(K,J),GRSURF(K,M))                                  -0289
 201 CONTINUE                                                                  -0290
C                                                                              -0291
C    CALCULATION OF FINITE DIFFERENCE TERMS                                    -0292
     DO 202 I=2,IY                                                            -0293
     DO 202 K=2,IR                                                            -0294
     IK=K+1                                                                    -0295
     IKM=K-1                                                                   -0296
     II=I+1                                                                    -0297
     IIM=I-1                                                                   -0298
     DFY1R1=((TEMP(1,I,J)-TEMP(1,IIM,J))/(Y(I)-Y(IIM)))                       -0299
     DSY1R1=((TEMP(1,I,M)-TEMP(1,IIM,M))/(Y(I)-Y(IIM)))                       -0300
     DFY2R1=((TEMP(1,II,J)-TEMP(1,I,J))/(Y(II)-Y(I)))                          -0301
     DSY2R1=((TEMP(1,II,M)-TEMP(1,I,M))/(Y(II)-Y(I)))                          -0302
     DFY2Y1=((TEMP(K,2,J)-TEMP(K,1,J))/(Y(2)-Y(1)))                           -0303
     DSY2Y1=((TEMP(K,2,M)-TEMP(K,1,M))/(Y(2)-Y(1)))                           -0304
     DFR2R1=((TEMP(2,I,J)-TEMP(1,I,J))/(R(2)-R(1)))                            -0305
     DSR2R1=((TEMP(2,I,M)-TEMP(1,I,M))/(R(2)-R(1)))                            -0306
     DFR2Y1=((TEMP(IK,1,J)-TEMP(K,1,J))/(R(IK)-R(K)))                         -0307
     DSR2Y1=((TEMP(IK,1,M)-TEMP(K,1,M))/(R(IK)-R(K)))                         -0308
     DFR1Y1=((TEMP(K,1,J)-TEMP(IKM,1,J))/(R(K)-R(IKM)))                       -0309
     DSR1Y1=((TEMP(K,1,M)-TEMP(IKM,1,M))/(R(K)-R(IKM)))                       -0310
     DFR12=(TEMP(2,1,J)-TEMP(1,1,J))/(R(2)-R(1))                               -0311
     DSR12=(TEMP(2,1,M)-TEMP(1,1,M))/(R(2)-R(1))                               -0312
     DFY12=(TEMP(1,2,J)-TEMP(1,1,J))/(Y(2)-Y(1))                               -0313
     DSY12=(TEMP(1,2,M)-TEMP(1,1,M))/(Y(2)-Y(1))                               -0314
     DFY2=((TEMP(K,II,J)-TEMP(K,I,J))/(Y(II)-Y(I)))                            -0315
     DSY2=((TEMP(K,II,M)-TEMP(K,I,M))/(Y(II)-Y(I)))                            -0316
     DFY1=((TEMP(K,I,J)-TEMP(K,IIM,J))/(Y(I)-Y(IIM)))                          -0317
     DSY1=((TEMP(K,I,M)-TEMP(K,IIM,M))/(Y(I)-Y(IIM)))                          -0318
     DFR2=((TEMP(IK,I,J)-TEMP(K,I,J))/(R(IK)-R(K)))                            -0319
     DSR2=((TEMP(IK,I,M)-TEMP(K,I,M))/(R(IK)-R(K)))                            -0320
     DFR1=((TEMP(K,I,J)-TEMP(IKM,I,J))/(R(K)-R(IKM)))                          -0321
     DSR1=((TEMP(K,I,M)-TEMP(IKM,I,M))/(R(K)-R(IKM)))                          -0322
```

```
      RM=(R(IK)+R(IKM))/2.
      REA=R(IK)-R(K)                                                    _0323
      RW=R(K)-R(IKM)                                                    _0324
      RO=R(IK)-R(IKM)                                                   _0325
      DFR1M=(DFR1*REA+DFR2*RW)/RO                                       _0326
      DSR1M=(DSR1*REA+DSR2*RW)/RO                                       _0327
      DSR1M1=(DSR1Y1*REA+DSR2Y1*RW)/RO                                  _0328
      DFR1M1=(DFR1Y1*REA+DFR1Y1*RW)/RO                                  _0329
      DTR1M1=GRAD(DFR1M1,DSR1M1)                                        _0330
      DTR1M=GRAD(DFR1M,DSR1M)                                           _0331
      DTR1=GRAD(DFR1,DSR1)                                              _0332
      DTY1=GRAD(DFY1,DSY1)                                              _0333
      DTR2=GRAD(DFR2,DSR2)                                              _0334
      DTY2=GRAD(DFY2,DSY2)                                              _0335
      DTR12=GRAD(UFR12,DSR12)                                           _0336
      DTY12=GRAD(DFY12,DSY12)                                           _0337
      DTR1Y1=GRAD(DFR1Y1,DSR1Y1)                                        _0338
      DTR2Y1=GRAD(DFR2Y1,DSR2Y1)                                        _0339
      DTY2Y1=GRAD(DFY2Y1,DSY2Y1)                                        _0340
      DTY2R1=GRAD(DFY2R1,DSY2R1)                                        _0341
      DTY1R1=GRAD(DFY1R1,DSY1R1)                                        _0342
      DTR2R1=GRAD(UFR2R1,DSR2R1)                                        _0343
      D2TY11=((2.*GRMURF(1))/(Y(2)-Y(1)))+(2.*DTY12/(Y(2)-Y(1)))        _0344
      D2TYY1=((2.*GRMURF(K))/(Y(2)-Y(1)))+(2.*DTY2Y1/(Y(2)-Y(1)))       _0345
      D2TR11=2.*(DTR12/(R(2)-R(1)))                                     _0346
      D2TY=(DTY2-DTY1)/((Y(II)-Y(IIM))/2.)                              _0347
      D2TR=(DTR2-DTR1)/((R(IK)-R(IKM))/2.)                              _0348
      D2TYR1=(DTY2R1-DTY1R1)/((Y(II)-Y(IIM))/2.)                        _0349
      D2TRY1=(DTR2Y1-DTR1Y1)/((R(IK)-R(IKM))/2.)                        _0350
      IMR=IR-1                                                          _0351
      IMY=IY-1                                                          _0352
      IM=IY+1                                                           _0353
      IL=IR+1                                                           _0354
C     ***********************************************************************  _0355
C        CENTRAL REGION  - REGION 1                                     _0356
C     ***********************************************************************  _0357
      TEMP(K,I,IJ)=TEMP(K,I,J)+ALPHA*DT*(D2TR+(DTR1M/RM  )+D2TY)        _0358
C     ***********************************************************************  _0359
C        SURFACE BOUNDARY  - REGION 2                                   _0360
C     ***********************************************************************  _0361
      TEMP(K,1,IJ)=TEMP(K,1,J)+ALPHA*DT*(D2TRY1+(DTR1M1/RM  )+D2TYY1)   _0362
C                                                                       _0363
C     ***********************************************************************  _0364
C        AXIAL BOUNDARY  - REGION 3                                     _0365
C     ***********************************************************************  _0366
      TEMP(1,I,IJ)=TEMP(1,I,J)+ALPHA*DT*(D2TYR1+(4.*(DTR2R1)/(R(2)   )))  _0367
·C                                                                       _0368
C     ***********************************************************************  _0369
C        EASTERN BOUNDARY SEMI INFINITE - REGION 4                      _0370
C     ***********************************************************************  _0371
      AJ=LIM                                                            _0372
      PHI2=400.                                                        _0373
      PHI=400.                                                          _0374
      IF((R(IL)-R(IR)).GT.0.0001) GO TO 230                            _0375
      IF((Y(IM)-Y(IY)).GT.0.0001) GO TO 230                            _0376
      IF(TIME.LT.1.2) GO TO 230                                        _0377
      PHI2=EXP(12.*((Y(IM)-Y(IY))**2)/(4.*ALPHA*TIME))                 _0378
      PHI=EXP(39.*((R(IL)-R(IR))**2)/(4.*ALPHA*TIME))                  _0379
  230 CONTINUE                                                         _0380
      TEMP(IL,I,IJ)=TEMP(IR,I,M)/PHI                                   _0381
                                                                        _0382
      ***********************************************************************  _0383
C        SOUTHERN BOUNDARY - SEMI INFINITE - REGION 5                   _0384
C     ***********************************************************************  _0385
      TEMP(K,IM,IJ)=TEMP(K,IY,M)/PHI2                                  _0386
C                                                                       _0387
C     ***********************************************************************  _0388
C        AXIAL SURFACE POINT - REGION 6                                 _0389
C     ***********************************************************************  _0390
      TEMP(1,1,IJ)=TEMP(1,1,J)+ALPHA*DT*((4.*(DTR12)/(R(2)   ))+D2TY11)  _0391
C                                                                       _0392
C     ***********************************************************************  _0393
C        AXIAL SOUTHERN BOUNDARY POINT - REGION 7                       _0394
C     ***********************************************************************  _0395
      TEMP(1,IM,IJ)=TEMP(1,IY,M)/PHI2                                  _0396
C                                                                       _0397
C     ***********************************************************************  _0398
C        EASTERN BOUNDARY SURFACE POINT - REGION 8                      _0399
C     ***********************************************************************  _0400
      TEMP(IL,1,IJ)=TEMP(IR,1,M)/PHI                                   _0401
C                                                                       _0402
  202 CONTINUE                                                         _0403
      BIG=0.                                                            _0404
      TEST=0.5+(TEMP(1,1,1)/1000.)                                     _0405
                                                                        _0406
```

```
C                                                                   _0407
C  TEST CONVERGENCY                                                 _0408
C                                                                   _0409
   DO 221 K=1,IR                                                    _0410
   DO 221 I=1,IY                                                    _0411
   RES=ABS(TEMP(K,I,IJ))-ABS(TEMP(K,I,M))                           _0412
   IF(ABS(RES).GE.BIG) BIG=ABS(RES)                                 _0413
   IF(BIG.GE.TEST) GO TO 223                                        _0414
   TOT=TOT+ABS(RES)                                                 _0415
   221 CONTINUE                                                     _0416
   223 CONTINUE                                                     _0417
   W=1.                                                             _0418
   IF(COUNT.GT.6) W=4.                                              _0419
   IF(COUNT.GT.10) W=8.                                             _0420
   IF(COUNT.GT.25) W=16.                                            _0421
C                                                                   _0422
C    RESET TEMPERATURES BY VARIABLE DAMPING                         _0423
C                                                                   _0424
   DO 204 K=1,IL                                                    _0425
   DO 204 I=1,IM                                                    _0426
   TEMP(K,I,M)=(TEMP(K,I,M)*W+TEMP(K,I,IJ))/(W+1)                   _0427
   SURFT(K,M)=(EMP(K,1,M)                                           _0428
   SURFT(K,IJ)=TEMP(K,1,IJ)                                         _0429
   204 CONTINUE                                                     _0430
   IF(BIG.GE.TEST) GO TO 206                                        _0431
   WRITE(6,222) COUNT                                               _0432
   222 FORMAT(F10.2)                                                _0433
   DO 207 K=1,IL                                                    _0434
   DD 207 I=1,IM                                                    _0435
C                                                                   _0436
C     CALCULATION OF THE FILM TEMPERATURE                          _0437
C                                                                   _0438
   TEMP(K,1,M)=((GRAD(TEMP(K,1,J),TEMP(K,1,IJ))+TEMPA+546.)/2.)     _0439
   TEMP(K,I,J)=TEMP(K,I,IJ)                                         _0440
   SURFT(K,J)=IEMP(K,1,J)                                           _0441
C                                                                   _0442
C    ******************************************************************   _0443
C    *   CALCULATION OF DEPOSIT THICKNESS                          *   _0444
C    ******************************************************************   _0445
C                                                                   _0446
   IF(TEMP(K,1,M)-423.) 214,214,213                                 _0447
   214 SCHEM(K)=0.                                                  _0448
   60 TO 215                                                        _0449
   213 CONTINUE                                                     _0450
   SCHEM(K)=0.233E+06*DT*RHOE*D/(B*EXP(0.12008E+05/TEMP(K,1,M)))    _0451
   215 CONTINUE                                                     _0452
   DIFF=71.247*((TEMPA+273.)**1.5)/(10.**10)                       _0453
   STMASS=(0.0U0123*(RE**0.8)*(SC**0.333)*D*RHOE*DIFF*DT)/(B**2)   _0454
   SMASS(K)=STMASS*(TEMP(K,1,M)/273.)**0.90                        _0455
   IF(SCHEM(K)-SMASS(K))210,210,211                                _0456
   210 THICK(K)=THICK(K)+SCHEM(K)                                  _0457
   TYPE(K)=C                                                        _0458
   60 TO 212                                                        _0459
   211 THICK(K)=THICK(K)+SMASS(K)                                  _0460
   TYPE(K)=BOU                                                      _0461
   212 CONTINUE                                                     _0462
   207 CONTINUE                                                     _0463
C                                                                   _0464
C    WRITE OUT ANSWER IF REQUIRED AT THIS STEP                      _0465
C                                                                   _0466
   IF(LIM-IPRINT)208,209,208                                       _0467
   209 CALL ANSWER                                                  _0468
   IPRINT=IPRINT+10                                                 _0469
   208 CONTINUE                                                     _0470
C                                                                   _0471
C    RESET FILM TEMPERATURES READY FOR NEXT CALCULATION STEP        _0472
C                                                                   _0473
   DO 220 K=1,IL                                                    _0474
   DO 220 I=1,IM                                                    _0475
   TEMP(K,I,M)=TEMP(K,I,IJ)                                         _0476
   220 CONTINUE                                                     _0477
   203 CONTINUE                                                     _0478
   60 TO 252                                                        _0479
C                                                                   _0480
C    STORE FINAL ARRAY FOR FURTHER RUNS                             _0481
C                                                                   _0482
   251 CONTINUE                                                     _0483
   WRITE(7)(((IEMP(K,I,M),K=1,IL),I=1,IM),M=1,3),TIME              _0484
   252 CONTINUE                                                     _0485
   RETURN                                                           _0486
   END                                                              _0487
```

```
C                                                                        _0488
C      ********************************************************************  _0489
C      *                                                                *   _0490
C      *       SUBROUTINE ANSWER - PRINT OUT                            *   _0491
C      *                                                                *   _0492
C      ********************************************************************  _0493
C                                                                        _0494
      SUBROUTINE ANSWER                                                  _0495
      COMMON/CLIM/AJ,LIM                                                 _0496
      COMMON/CWIDIH/IR,IY,IT                                            _0497
      COMMON/CGEN/SIGMA,PTOTAL,RBEAM,RE                                  _0498
      COMMON/CPROP/ALPHA,COND,DENS,SPHT,GVISC,GDENS,GVEL,D,B             _0499
      COMMON/CSURF/POWER(40),REFLEC,HCONV,TEMPA,HRAD(40,3),SURFT(40,3)   _0500
      COMMON/CDIM/TSTAR(40,40,3),THETA(40),RSTAR(40)                     _0501
      COMMON/CTIME/TIME                                                  _0502
      COMMON/CTYPE/TYPE(40)                                              _0503
      COMMON/CGRID/R(40),Y(40),T(40)                                     _0504
      COMMON/CTEMP/TEMP(40,40,3),GRSURF(40,3)                            _0505
      COMMON/CPRINT/DT,DISTR(40)                                         _0506
      COMMON/CTRAN/CONV(40)                                              _0507
      COMMON/CDEP/THICK(40),RHOE,SC,GDIFF                                _0508
      COMMON/COUT/IOUT                                                   _0509
      COMMON/CREF/REFL(40)                                               _0510
      DIMENSION YSTAR(40)                                                _0511
      DIMENSION RR(40)                                                   _0512
      DIMENSION YY(40)                                                   _0513
C                                                                        _0514
C     CALCULATION OF DIMENSIONLESS GROUPS, DISTANCES IN METERS AND HEAT LOSS _0515
C                                                                        _0516
      J=1                                                                _0517
      M=2                                                                _0518
      AJ=LIM                                                             _0519
      IL=IR+1                                                            _0520
      IM=IY+1                                                            _0521
      THETA(J)=(4.*ALPHA*TIME)/(RBEAM**2)                                _0522
      DO 404 I=1,IL                                                      _0523
 404  RR(I)=R(I)*1000.                                                   _0524
      DO 422 I=1,IM                                                      _0525
      YY(I)=Y(I)*1000.                                                   _0526
 422  CONTINUE                                                           _0527
      DO 413 K=1,IR                                                      _0528
      DO 413 I=1,IY                                                      _0529
C     DIMENSIONLESS PLOT FOR CHECK ON DEMING ET AL                       _0530
      TSTAR(K,I,J)=(TEMP(K,I,J)*RBEAM*3.142*4.*COND)/(2.*PTOTAL*(1.-REFLEC)) _0531
      RSTAR(K)=(R(K)/RBEAM)                                              _0532
      YSTAR(I)=Y(I)/RBEAM                                                _0533
      HRAD(K,3)=HRAD(K,J)*(SURFT(K,J)-TEMPA)                             _0534
      CONV(K)=HCONV*(SURFT(K,J)-TEMPA)                                   _0535
 413  CONTINUE                                                           _0536
C                                                                        _0537
C      ********************************************************************  _0538
C      *   PRINT OUT                                                    *   _0539
C      ********************************************************************  _0540
C                                                                        _0541
      WRITE(6,400) LIM,TIME                                              _0542
 400  FORMAT(23H1TIME INTERVAL NUMBER =,I4,18H TIME FROM START =,F10.4)  _0543
      WRITE(6,403)(RR(I),I=1,IR)                                         _0544
 403  FORMAT(26H RADIAL POSITION IN MMS   ,/10X,10F10.4/)                _0545
      IF(IOUT) 418,419,418                                               _0546
 419  CONTINUE                                                           _0547
      WRITE(6,423)(REFL(K),K=1,IR)                                       _0548
 423  FORMAT(* REFLECTIVITY *,10G10.3)                                   _0549
      WRITE(6,412)(CONV(K),K=1,IR)                                       _0550
 412  FORMAT(* CONV WATT *,10G10.3)                                      _0551
      WRITE(6,415)(HRAD(K,3),K=1,IR)                                     _0552
 415  FORMAT(* RAD WATTS *,10G10.3)                                      _0553
      WRITE(6,414)(THICK(K),K=1,IR)                                      _0554
 414  FORMAT(* THICKNESS*,10E10.4)                                       _0555
      WRITE(6,417)(TYPE(K),K=1,IR)                                       _0556
 417  FORMAT(* CHEM/MASS*,10A10)                                         _0557
      WRITE(6,416)(TEMP(K,1,M),K=1,IR)                                   _0558
 416  FORMAT(* FILM TEMP *,10F10.4)                                      _0559
 418  CONTINUE                                                           _0560
      WRITE(6,407)(TEMP(K,1,J),K=1,IL)                                   _0561
 407  FORMAT(* SURFACE*,10F10.5)                                         _0562
      IF (IOUT) 420,421,420                                              _0563
 421  CONTINUE                                                           _0564
      DO 406 I=2,IM                                                      _0565
      WRITE(6,405) YY(I),(TEMP(K,I,J),K=1,IL)                            _0566
 405  FORMAT(12F10.5)                                                    _0567
 406  CONTINUE                                                           _0568
      WRITE(6,408) THETA(J)                                              _0569
 408  FORMAT(* DIMENSIONLESS TIME=*,F10.5/)                              _0570
      WRITE(6,409)(RSTAR(K),K=1,IR)                                      _0571
 409  FORMAT(10H  RSTAR    ,10F10.2)                                     _0572
      DO 411 I=1,IY                                                      _0573
      WRITE(6,410) YSTAR(I),(TSTAR(K,I,J),K=1,IR)                        _0574
 410  FORMAT(11F10.5)                                                    _0575
 411  CONTINUE                                                           _0576
 420  CONTINUE                                                           _0577
      RETURN                                                             _0578
      END                                                                _0579
C                                                                        _0580
C      ********************************************************************  _0581
C      *     ARITHMETIC MEAN PACKAGE                                    *   _0582
C      ********************************************************************  _0583
C                                                                        _0584
C                                                                        _0585
      FUNCTION GRAD(A,B)                                                 _0586
      GRAD=(A+B)/2.                                                      _0587
      RETURN                                                             _0588
      END                                                                _0589
                                                                         _0590
                                                                         _0591
```

TIME INTERVAL NUMBER = 35 TIME FROM START =   .7187
RADIAL POSITION IN MMS

```
           0      .0821     .1823     .3047     .4542     .6368     .8578    1.1322    1.4630    1.8714
```

RADIAL POSITION IN MMS

```
        2.3677    2.9740    3.7145    4.6190    5.7237    7.0730    8.7210   10.7339   13.1925   16.1954
```

RADIAL POSITION IN MMS

```
       19.8631   24.3429   29.8145   36.4976
```

REFLECTIVITY | .180 | .180 | .180 | .180 | .180 | .180 | .180 | .180 | .180 | .180
REFLECTIVITY | .180 | .180 | .180 | .180 | .180 | .180 | .180 | .180 | .180 | .180
REFLECTIVITY | .180 | .180 | .180 | .180
CONV WATT | .170E+06 | .167E+06 | .155E+06 | .131E+06 | .936E+05 | .492E+05 | .967E+04 | -.147E+05 | -.247E+05 | -.276E+05
CONV WATT | -.282E+05 | -.283E+05 | -.283E+05 | -.283E+05 | -.283E+05 | -.283E+05 | -.283E+05 | -.283E+05 | -.283E+05 | -.283E+05
CONV WATT | -.283E+05 | -.283E+05 | -.283E+05 | -.283E+05
RAD WATTS | .247E+05 | .238E+05 | .199E+05 | .137E+05 | .698E+04 | .234E+04 | 299. | -342. | -514. | -555.
RAD WATTS | -564. | -565. | -565. | -565. | -565. | -565. | -565. | -565. | -565. | -565.
RAD WATTS | -565. | -565. | -565. | -565.
THICKNESS | .2026E-07 | .1982E-07 | .1775E-07 | .1137E-07 | .1273E-08 | .3459E-10 | 0 | 0 | 0 | 0
THICKNESS | 0 | 0 | 0 | 0 | 0 | 0 | 0 | 0 | 0 | 0
THICKNESS | 0 | 0 | 0 | 0
CHEM/MASSM | M | M | M | C | C | C | C | C | C |
CHEM/MASSC | C | C | C | C | C | C | C | C | C |
CHEM/MASSC | C | C | C
FILM TEMP | 617.4321 | 614.2443 | 596.6159 | 561.5904 | 508.0021 | 443.9325 | 386.9553 | 351.8268 | 337.3194 | 333.1195
FILM TEMP | 332.2571 | 332.1421 | 332.1328 | 332.1323 | 332.1323 | 332.1323 | 332.1323 | 332.1323 | 332.1323 | 332.1323
FILM TEMP | 332.1323 | 332.1323 | 332.1323 | 332.1219
SURFACE | 589.66422 | 582.48865 | 547.23173 | 477.18675 | 370.00427 | 241.86501 | 127.91059 | 57.65351 | 28.63872 | 20.23890
SURFACE | 18.51415 | 18.28418 | 18.26551 | 18.26461 | 18.26458 | 18.26458 | 18.26458 | 18.26458 | 18.26458 | 18.26458
SURFACE | 18.26458 | 18.26458 | 18.26455 | 18.24382 | .04560
```
 .08205 461.07784 453.61324 429.16065 379.20079 301.09581 204.38731 113.57221  53.14870  25.94979  17.57987  15.82509
15.58998  15.57085  15.56993  15.56990  15.56990  15.56990  15.56990  15.56990  15.56990  15.56990  15.56990  15.56986
15.54901  .03986
 .18227 338.91810 335.34397 319.04472 285.58241 232.09439 163.47735  95.39072  46.48542  22.48551  14.59248  12.88463
12.65294  12.63398  12.63306  12.63303  12.63303  12.63303  12.63303  12.63303  12.63303  12.63303  12.63303  12.63300
12.61324  .03153
 .30467 234.09098 231.26328 221.31858 200.50180 166.55110 121.47432  74.27913  37.75488  18.24331  11.35979   9.80806
 9.59315   9.57536   9.57449   9.57447   9.57447   9.57447   9.57447   9.57447   9.57447   9.57447   9.57447   9.57444
 9.55716  .02389
 .45418 146.85511 145.45407 139.85595 128.07374 108.49710  81.66903  52.14291  27.63906  13.44407   8.06494   6.79249
 6.61114   6.59687   6.59512   6.59509   6.59509   6.59509   6.59509   6.59509   6.59509   6.59509   6.59509   6.59507
 6.58151  .01645
 .63678  81.15179  80.42720  77.65415  71.76379  61.82273  47.81901  31.71504  17.49186   8.61646   5.01051   4.11177
 3.97914   3.96772   3.96714   3.96713   3.96713   3.96713   3.96713   3.96713   3.96713   3.96713   3.96713   3.96711
 3.95797  .00989
 .85982  37.36979  37.07050  35.90991  33.43028  29.19222  23.08668  15.80692   9.03104   4.52091   2.56722   2.05419
 1.97553   1.96857   1.96821   1.96820   1.96820   1.96820   1.96820   1.96820   1.96820   1.96820   1.96820   1.96819
 1.96319  .00490
1.13224  13.33450  13.23591  12.85346  12.03252  10.61600   8.54015   5.99519   3.52691   1.79533   1.00287    .78457
  .74981    .74665    .74648    .74647    .74647    .74647    .74647    .74647    .74647    .74647    .74647    .74647
  .74442  .00186
1.46497   3.38598   3.36244   3.27109   3.07438   2.73265   2.22574   1.59165    .95777    .49493    .27361    .21013
  .19968    .19870    .19865    .19865    .19865    .19865    .19865    .19865    .19865    .19865    .19865    .19865
  .19807  .00049
1.87137    .55127    .55754    .54306    .51180    .45724    .37564    .27210    .16650    .08709    .04785    .03624
  .03427    .03408    .03407    .03407    .03407    .03407    .03407    .03407    .03407    .03407    .03407    .03407
  .03397  .00008
2.36774    .00140    .00139    .00136    .00128    .00114    .00094    .00069    .00042    .00022    .00012    .00009
  .00009    .00009    .00008    .00008    .00008    .00008    .00008    .00005    .00008    .00008    .00008    .00008
  .00008      0
```

DIMENSIONLESS TIME= 2.72629

RSTAR	0	.15	.33	.55	.83	1.16	1.56	2.06	2.66	3.40
RSTAR	4.30	5.41	6.75	8.40	10.41	12.88	15.86	19.52	23.99	29.45
RSTAR	36.11	44.26	54.21	66.36						
0	1.04385	1.03115	.96874	.84473	.65500	.42816	.22643	.10206	.05070	.03583
.03277	.03237	.03233	.03233	.03233	.03233	.03233	.03233	.03233	.03233	.03233
.03233	.03233	.03230								
.14918	.81622	.80301	.75972	.67128	.53301	.36182	.20105	.09409	.04594	.03112
.02801	.02760	.02756	.02756	.02756	.02756	.02756	.02756	.02756	.02756	.02756
.02756	.02756	.02753								
.33139	.59997	.59364	.56479	.50555	.41086	.28940	.16887	.08229	.03980	.02583
.02281	.02240	.02237	.02236	.02236	.02236	.02236	.02236	.02236	.02236	.02236
.02236	.02236	.02233								
.55395	.41440	.40939	.39179	.35494	.29484	.21504	.13149	.06684	.03230	.02011
.01736	.01698	.01695	.01695	.01695	.01695	.01695	.01695	.01695	.01695	.01695
.01695	.01695	.01692								
.82578	.25997	.25749	.24758	.22672	.19207	.14457	.09231	.04893	.02380	.01428
.01202	.01170	.01168	.01167	.01167	.01167	.01167	.01167	.01167	.01167	.01167
.01167	.01167	.01165								
1.15779	.14366	.14238	.13747	.12704	.10944	.08465	.05614	.03096	.01525	.00887
.00728	.00704	.00702	.00702	.00702	.00702	.00702	.00702	.00702	.00702	.00702
.00702	.00702	.00701								
1.56331	.06615	.06562	.06357	.05918	.05168	.04087	.02798	.01599	.00800	.00454
.00364	.00350	.00348	.00348	.00348	.00348	.00348	.00348	.00348	.00348	.00348
.00348	.00348	.00348								
2.05861	.02361	.02343	.02275	.02130	.01879	.01512	.01061	.00624	.00318	.00178
.00139	.00133	.00132	.00132	.00132	.00132	.00132	.00132	.00132	.00132	.00132
.00132	.00132	.00132								
2.66358	.00599	.00595	.00579	.00544	.00484	.00394	.00282	.00170	.00088	.00048
.00037	.00035	.00035	.00035	.00035	.00035	.00035	.00035	.00035	.00035	.00035
.00035	.00035	.00035								
3.40248	.00099	.00099	.00096	.00091	.00081	.00066	.00048	.00029	.00015	.00008
.00006	.00006	.00006	.00006	.00006	.00006	.00006	.00006	.00006	.00006	.00006
.00006	.00006	.00006								

9.00
8.00
9.00
8.00
9.00
8.00
9.00
8.00
9.00
8.00

APPENDIX 6

Measurement of Thermal Diffusivity by a laser flash

Parker et al (107) proposed this technique in 1961. It has the virtue over other techniques of eliminating the problem of thermal contact resistance and minimising heat losses due to the rapidity of the measurement. It has the further advantages of using straightforward apparatus, on small specimens, and data reduction is quite simple. However, as this work has indicated the flash source needs to be able to supply megawatt pulses of less than 1ms duration. Susumu Namba et al (106) report using a 2 MW ruby pulse. It may be that this is why the author has not read of any results from this method on ceramic materials, since pulses of this size would almost certainly break the microslide specimens used here.

The theory of the method is well described by both Parker et al and A.B. Donaldson (108). It is as follows:-

Given an initial temperature distribution T(x,o) in a thermally insulated solid of thickness (L) metres the temperature distribution at a later time (t)s can be calculated from Fourier's second law to be:-

$$T(x,t) = \frac{1}{L} \int_{o}^{L} T(x,o)dx + \frac{2}{L} \sum_{n=1}^{\infty} \exp\left(\frac{-n^2\pi^2\alpha t}{L^2}\right)$$

$$x \cos\frac{n\pi x}{L} \int_{o}^{L} T(x,o) \cos\left(\frac{n\pi x}{L}\right) dx \qquad (A6.1)$$

where α = thermal diffusivity.

If a pulse of radiant energy Q J is instantaneously absorbed into a surface layer of thickness (g) metres at the front surface then T(x,o) is known to be:-

$$T(x,o) = \frac{Q}{\mathcal{C}Cg} \quad \text{for} \quad 0 < x < g \quad \text{where} \quad \mathcal{C} = \text{density kg/m}^3$$

$$C = \text{specific heat J/kg}^o\text{C}$$

$$T(x,o) = 0 \quad \text{for } g < x < L$$

this theoretical step function can be integrated in equation (A6.1) to yield:-

$$T(x,t) = \frac{Q}{\rho CL}\left[1 + 2 \sum_{n=1}^{\infty} \cos\left(\frac{n\pi x}{L}\right) \frac{\sin\left(\frac{n\pi g}{L}\right)}{\left(\frac{n\pi g}{L}\right)} \exp\left(-\frac{n^2\pi^2\alpha t}{L^2}\right)\right] \quad (A6.2)$$

If it is assummed that g is very small - as it usually is for opaque materials - then $\sin\left(\frac{n\pi g}{L}\right) \simeq \left(\frac{n\pi g}{L}\right)$ and the temperature of the rear surface at any time can be found from:-

$$T(L,t) = \frac{Q}{\rho CL}\left[1 + 2 \sum_{n=1}^{\infty} (-1)^n \exp\left(-\frac{n^2\pi^2}{L^2}\alpha t\right)\right] \quad (A6.3)$$

For an insulated specimen the maximum temperature of the rear surface $= \frac{Q}{\rho CL} = T_{max}$

So define $V(L,t) = \frac{T(L,t)}{T_{max}}$

and $\quad w = \frac{\pi^2 \alpha t}{L^2}$

as two dimensionless groups from equation A6.3. Substituting in A6.3 gives:-

$$V = 1 + 2 \sum_{n=1}^{\infty} (-1)^n \exp(-n^2 w) \quad (A6.4)$$

if $V = \frac{1}{2}$ $\quad w = 1.38 = \frac{\pi^2 \alpha t_{\frac{1}{2}}}{L^2}$ and $\alpha = \left(\frac{1.38 L^2}{\pi^2 t_{\frac{1}{2}}}\right) \quad (A6.5)$
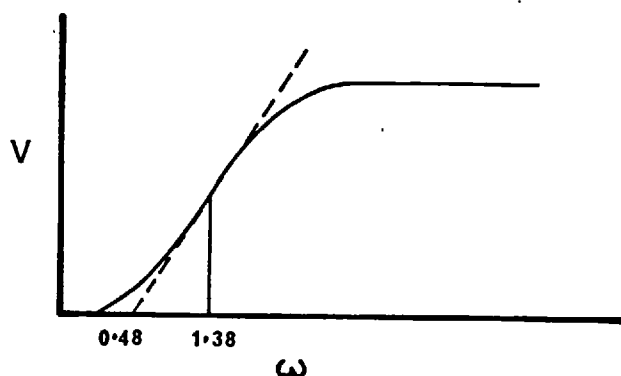
Figure A6.1 Typical back face thermocouple trace of dimensionless temperature V vs dimensionless time, w.

and the extrapolated straight line portion of the curve cuts the time axis at w = 0.48

$$\text{yielding} \quad \alpha = (\frac{0.48L^2}{\pi^2 t_x}) \qquad \text{(A6.5)}$$

Insufficient power was available in millisecond pulses and consequently these two equations (A6.5 and A6.6) do not work reliably - see results.

It was felt that the method could still be adapted if one took the relatively easy measurement of the time taken for a signal to pass from the front face to the back face (t_F) i.e. the "velocity of heat" in the material.

For this A6.4 becomes:-

$$0 \leq 1 + 2 \sum_{n=1}^{\infty} (-1)^n \exp(-n^2 w)$$

$$\text{i.e.} \quad \sum_{n=1}^{\infty} (-1)^n \exp(-n^2 w) \geq -\tfrac{1}{2}$$

solving this equation yields $w \leq 0.40$

$$\text{and therefore} \quad \alpha = \frac{0.40 \ L^2}{\pi^2 t_F}$$

t_F should not be affected by any thermal event subsequent
to the initiation of the pulse on the front face provided a
sharp start to the pulse was applied.

The results for t_F are shown in the section on thermal
diffusivity and are in reasonable agreement with the literature.

Experiments were made on brass sheet in which the pulse
overlapped with the back face signal as in figure A6.2.
This trace makes a nonsense of t_x and $t_{\frac{1}{2}}$ but still yields
a reasonable result for t_F, even though short.
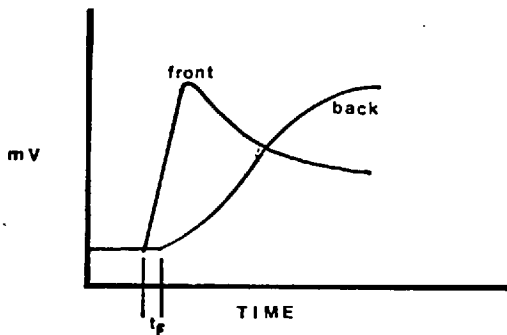
Figure A6.2   Diagram of thermo-
couple traces for
a thin brass sample

This amendment to the flash technique allows pulses of
varying length. However, it still requires pulses of sufficient
power to give a clear take off point for the back face temperature.

APPENDIX 7

Possible Routes for depositing

different metals by spot heating

The chart (A7.1) lists nine thermal decomposition routes
and notes which routes have been proved as experimentally
feasible for forming vapour deposits from different metals.
These routes should be adaptable to the spot heating process
with experimental reservations on possible thermal damage for
the higher temperature reactions. Thermal damage in these cases
would be reduced, however, if the whole substrate were heated to
a temperature just below the decomposition temperature.

Since the chart is limited to reporting experimentally
proven routes, many possible routes, which have not been
investigated, are not shown. In particular, the hydrogenolysis of
organometallic compounds is easier the more electropositive the
metal and the more ionic the C—metal bond. This would favour
the lefthand side of the chart and the Lanthanides, or rare
earths (A7.1).

The ninth route listed includes all transport reactions in
a temperature gradient of the type:-

$$A(s) + B(g) = R(g)$$
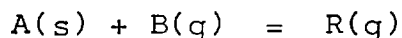
The Van Arkel—de Boer subhalide disproportionation process
and the indirect distillation as described by Gross and Levi
(A7.4) or practiced in the TORCO process form the main routes
in this group. The work of Nicoll[A.73] using photographers' lamps
suggests that such a route could be exploited by spot heating
with a laser. The experimental arrangement would be something
like that shown over the page.
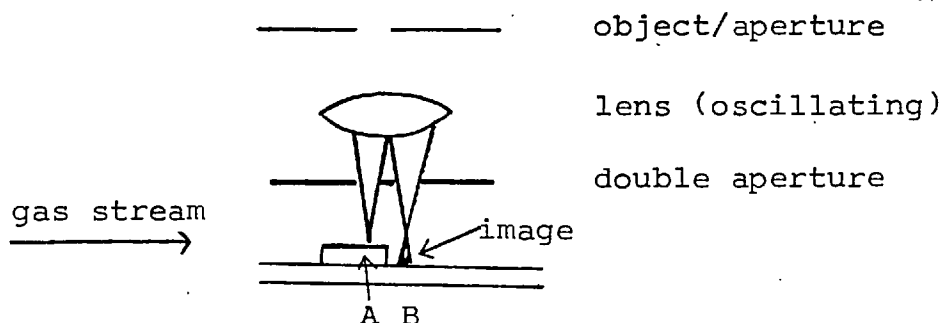
Figure A7.1 Possible method for performing a Van-Arkel de Boer type of disproportionation reaction.

The narrow beam at A would yield the required higher temperature, the broader beam at B the lower disproportionation temperature.

However, the feasibility of such a route would form the basis of a separate study.

In Nicoll's work he used two photographers' lamps. one aimed . at the source the other at the seed. The two areas being in very close proximity (less than 1/10 the diameter of source and seed).

References

A.7.1 C.F. Powell, J.H. Oxley, J.H. Blocher "Vapour deposition" Wiley 1966.

A.7.2 E.W. Berg and J.T. Truemper, Analytica Chemica Acta 32 (1965) 245-252, "Vapour pressure-temperature data for various metal and diketone chelates"

A.7.3. F.H. Nicoll, J. Electrochem Soc. 110, 1165, 1963, (& Powell et al p 634).

A.7.4 Gross P. and Levi D.L., Paper 19 "Symposium on the extraction metallurgy of some of the less common metals", I.M.M. March (1956)

1	2	3	4	5	6	7	8	9	10	11	12	13	14	15	16	17	18
H																	He
Li	Be 3+ 9											B 2 9	C 4	N	O	F	Ne
Na	Mg											Al 2 9 2a 3	Si 2 4 9	P (4)	S	Cl	A
K	Ca	Sc	Ti 2 3 9	V 1 3	Cr 2 9 1 3	Mn 2a	Fe 1 3	Co 2 2a 3	Ni 1 2a	Cu 2 2a 3	Zn 2	Ga 9	Ge 2 9 (3)	As 3 4	Se	Br	Kr
Rb	Sr	Y	Zr 3 9	Nb 3 9	Mo 1 2 3	Tc	Ru 1 7	Rh 7	Pd 2a‡	Ag	Cd	In 9	Sn 5 2 3	Sb 3 4	Te	I	Xe
Cs	Ba	La	Hf 2 9	Ta 2 3 9	W 1 2 3	Re 3 8 7	Os 7	Ir 1 7	Pt 7 2a‡	Au 6 9	Hg	Tl	Pb 2	Bi 3 4	Po	At	Rn
Fr	Ra	Ac															

Ce	Pr	Nd	Pm	Sm	Eu	Gd	Tb	Dy	Ho	Er	Tm	Yb	Lu

Th 9	Pa	U 3	Np	Pu	Am	Cm 2	Bk	Cf

+ only with Na, K, Zn or Al vapour reductants
‡ ref A7.1
1 = via carbonyl
2 = organometallic compounds
2a = Chelates   Berg and Truemper (A7.2)
3 = Halides   ref. Powell, Oxley, Blocher   (A7.1)
4 = Hydrides   "   "   "   "   "
5 = Monoxides   "   "   "   "   "
6 = Organophosphines halides "   "   "
7 = Carbonyl chlorides   "   "   "
8 = Oxychlorides   "   "   "   "
9 = Van Arkel type   "   "   "   "
   disporportionation
   de Boer

NOMENCLATURE

Symbol	Meaning
A	area - m^2
a	aperture radius - m
a(subscript)	ambient conditions
B	jet/plate distance - m
b(subscript)	beam condition
b	confocal radius - m
b'	beam parameter - m
C or C_p	specific heat - J/kg $^{\circ}$K
c(subscript)	continuous condition or correct value
D	substrate thickness - m
D_{AB}	diffusivity-m^2/s
D_b or d_b	beam diameter - m
D_{BR}	burnt diameter - m
D_i	inner diameter of deposit - m
D_j	jet diameter - m
D_o	outer diameter of deposit - m
d	distance between the cavity mirrors - m
d_p	depth of penetration - m
E	truncation error
E(r,θ)	amplitude of wavefront
E(subscript)	eastern location
e(subscript)	jet exit condition
f	focal length - m
g_1	cavity parameter - $(1-d/R_1)$
G	mass flow rate-kg/s
Gr	Grashof number $(D^3 g \beta \Delta T C^2/\mu^2)$

Symbol	Meaning
ΔG^O_T	Gibbs standard free energy at temperature T ^{O}K
h	heat transfer coefficient - W/ ^{2} ^{O}K
h_c	convective transfer coefficient - W/m^2 ^{O}K
h_r	radiative transfer coefficient - W/m^2 ^{O}K
h_{tot}	combined transfer coefficient - W/m^2 ^{O}K
I	intensity
i(subscript)	instantaneous condition
k	thermal conductivity-W/m^{O}K
k'	absorptivity-cm^{-1}
k_m	mass transfer coefficient
$L^{\prime}_p$ (x)	Laguerre polynomial
L	distance between the cavity mirrors - m
M	beam scale factor
M(subscript)	mean value
m or M	molecular weight
N	Fresnel number ($a^2/\lambda d$)
N(subscript)	northern location
Nu	Nusselt no (hD/k)
n	refractive index
o(subscript)	central value
P	incident power - W
p	pressure - N/m^2 or atmos.
P(r)	incident power density - W/m^2
P_o	central power density - W/m^2
P_{TOTAL}	total incident power - W
P_{net}	net absorbed power - W
Pr	Prandtl no ($C_p\mu/k$)
p(subscript)	location of point p

Symbol	Meaning
p	partial pressure - N/m^2 or atmos
Q	incident energy - J
Q	incident energy density - J/m^2
Q'	central power density - W/m^2
q_{loss}	heat loss - W
R	gas constant - 8.314 kJ/kmol $^{\circ}K$
R_1, R_2	curvature of lens or mirror surface - m
R*	dimensionless radius - (r/r_b)
Re	Reynolds number - $(\rho\, ud/\mu)$
r	radial distance - m
r(subscript)	radial location
r_b	beam radius - m
r_E	radius of eastern point - m
r_f	reflectivity
r_M	$(r_E + r_W)/2$ - m
r_W	radius of western point - m
$\bar{r}$	radial coordinate of point source - m
s	deposit thickness - m
s(subscript)	southern location
Sc	Schmidt number $(\mu/D_{AB}\rho)$
Sh	Sherwood number $(k_m D_j/D_{AS})$
surf(subscript)	surface condition
t	time - s
T	temperature - $^{\circ}K$ or $^{\circ}C$
t(subscript)	time location, or total
tot(subscript)	total value
T*	dimensionless temperature $\pi k D_b T/P_{tot}(1-r_f)$
u	gas jet velocity - m/s
w	beam radius = r_b - m

w(subscript)	western location
X_{IR}	radial distance to point IR from edge of disc source
y	. . depth - m
y(subscript)	depth location
z	compressibility factor
z	depth - m
z	distance along optic axis from intersection of lateral focal points and optic axis. - m
α	thermal diffusivity-m^2/s
λ	wavelength - m
μ	viscosity - kg/ms
η	dimensionless heat loss ($h(T^*_o - T^*_a)D_b)/4k$)
ψ	field amplitude
ϕ	gradient ratio or angular direction
ρ_{Ae}	density of A at jet exit - kg/m^3
ρ_{AS}	density of A in solid - kg/m^3
ρ	density - kg/m^3
Θ^*	dimensionless time - $16\alpha t/D_b^2$
Θ	time - s
σ_t	tangential stress-MN/m^2
σ_r	radial stress-MN/m^2
Ω	Leonard Jones parameter
'(subscript)	value at time (t+1)

REFERENCES

1) METALS AND MATERIALS, April 1973, p159.

2) R.J. VON GUTFIELD and P. CHAUDHARI, J. App. Phys. Vol43 No 11 1972.

3) P. CHAUDHARI, S.R. HERD, D. AST, M.N. BRODSKY and R.J. GUTFIELD, J. Noncryst. Solids 8-10 (1972) 900-908.

4) J. FEINLEIB, J. de NEUFVILLE, S.C. MOSS, S.R. OVSHINSKY App. Phys. Lett. 18, 254, (1971).

5) J.P. RILEY, "Seminar on Laser Welding, Drilling, Cutting" W.I. June 1975.

6) V.I. LITTLE, D.M. ROWLEY, R. WILTSHER, "Optical transmission and reflexion gratings by laser evaporation", Nature, vol 228, p49, 50, Oct. 1970.

7) B.F. SCOTT and D.L. HODGETT, "Pulsed solid state lasers for engineering fabrication processes", Proc. Inst. Mech. Eng., vol 183, pt 3D pp75-84, 1969.

8) V. CROFT, Ph.D. Thesis, Sheffield University, 1964.

9) P.E. GLASER and R.F. WALKER, "Thermal imaging techniques" Plenum Press, New York, 1964.

10) H. FOSTER, Optics and laser technology , June 1972, p121-128

11) C.F. POWELL, J.H. OXLEY, J.M. BLOTCHER, "Vapour Deposition", J. Wiley, New York, 1966.

12) H.A. TOULMIN Jr., U.S. Pat, 2,847,330, (Aug 12, 1958).

13) R. BAKISH "Introduction to electron beam technology", J. Wiley, New York, 1962.

14) J.F. READY "Effects of high power laser radiation", Academic Press, 1971.

15) M.I. COHEN and J.P. EPPERSON "Applications of lasers to microelectronic fabrication". Advances in Electronics and Electron Physics, Supplement, 4, p139-186, (New York Academic Press Inc. 1968).

16) J.F. READY Proc. New. Indust. Tech. Seminar. Penn State. Univ. June 27-30, 1965.

17) F. SEPOLE, Seminar on laser welding drill and cutting. W.I. June 1975.

18) J.N. GONSALVES and W.W. DULEY. Can. J. Phys. 49, 13, 1971, pp1708-1713.

/

19) J.N. GONSALVES and W.W. DULEY Can. J. Phys. 50, 3, 1972, pp216-221.

20) H.G. LANDAU Quart. appl. math. 8, 1, pp81-94, 1950.

21) J.F. READY J. App. Phys. 36, 462-468, 1965.

22) A.B.J. SULLIVAN, P.T. HOULDCROFT. Br. We.d J., 14, 443, 1967.

23) F.W. LUNAU, E.W. PAINE, Weld. Met. Fab. Jan. 9. 1969.

24) F.W. LUNAU, E.W. PAINE, M. RICHARDSON, M.D. WIJETUNGE, Opt. Tech. 1, 255, 1969.

25) M.J. ADAMS, Adv. in Weld. Proc. Harrogate, April, 1970 paper 14.

26) MEREK INDEX, 7th edition, Merch and Co Inc, New Jersey, USA 1960

27) Electronic Prod. April 1973, p15.

28) S.J. LINS and R.D. Morrison, Wescon 166 Tech. Paper, Western Elect. show. and convention pt 2, 1-9 (Aug. 23-26, 1966).

29) T.J. ROWE and D.J. MOULE, "Laser machining of photolithographic masks", Proc. Inst. Mech. Eng. vol 183, pt 3D, p13-18, 1969.

30) J.N. GONSALVES and W.W. DULEY, J. App. Phys. 43, 11, Nov. 1972 p4684-7.

31) B. COCKAYNE and D.B. GASSON, Mat. Sci., 6, 126, 1971.

32) E.V. LOCKE, E.D. HOAG, R.A. HELLA, I.E.E.E. Journ. Quant. Elect. vol QE8.2, Feb. 1972.

33) E.K. PFITZER and R. TURNER, J.Sci. INSTRUM (J.Phys.E) , 1, 360, 1968.

34) C.M. BANAS, "Laser welding developments", CEGB, Int. Conf. on Weld, Res., Sept. 1972, Marchwood.

35) E. ARCHIBALD, D.W. HARPER, and T.P. HUGHES, "Spectroscopy of laser generated microplasmas". Brit. J. Appl. Physics., Vol 15, pp1323, 1964.

36) J. CLARKE, 3rd year project report, Royal School Mines, 1975.

37) M.S. HESS and J.F. MILKOSKY "Vapour deposition of Platinium using CW laser energy", J. App. Phys. Vol 43, No 11, Nov 1972 p4680.

38) H.M. SMITH and A.F. TURNER, App. Opt. 4.147, 1965.

39) G. GROH, J. App. Phys. 39, 5804, 1968.

40) P.D. ZAVITSANOS, L.E. BREWER, W.E. SAUER, Proc. Nat. Electron Conf. 24, 864, 1968.

41) G.J. DAVIES, "Mass transfer from a turbulent impinging jet with and without chemical reaction", Ph.D. Thesis, London University, 1971.

42) T.M. JACKSON and P.G. ELDRIDGE, "Applications of thin films to electronic engineering. A micro engraving technique for thin films". Proc. J.I.E.R.E-I.E.E. conf. July 24, 1966.

43) E. RAUB, K. MÜLLER, "Fundamentals of metal deposition" Elsevier Amsterdam, 1967.

44) A.E. De BARR and D.A. OLIVER, "Electrochemical machining" MacDonald Tech. and Scientific 1968.

45) F.H. NICOLL, J. Electrochem. Soc. 110, 1165, (1963).

46) L.B. LESEM, P.M. HIRSCH, J.A. JORDAN "Digital holograms and kinoforms, phase shaping objects"., IBM pub. 320, 2348 Oct 1968.

47) G.J. PERT, Plasma Physics, Nov 1974, Vol16, p1019-1033 and 1035-1049 .

48) J.L. BOBIN Physics fluids, 14, 2341 (1971).

49) P. LAURES app. opt. 6 747 (1967).

50) H.S. CARSLAW, J.C. JAEGAR "Conduction of heat in solids", Oxford Press 1959.

51) J.L. DEMING, L.C. TAO, J.H. WEBER "Numerical solutions of disk source problems" AICh.E. Journ. vol 13, No6, p1214 (1967).

52) K. BRUGGER "Exact solutions for the temperature rise in a laser heated slab", J.Appl. Phys. Vol 43, No2 Feb 1972, pp577-583.

53) D.T. SWIFTHOOK and A.E.F. GICK, "Penetration welding with lasers", Weld. J. 52, (11), 4925-4995, Nov 1973.

54) GUENOT RACINET Brit. Weld. J. p427-435, Aug (1967).

55) J.N. GONSALVES, W.W. DULEY, "Cutting of thin metal sheets with the CW CO_2 laser". J. App. Phys. 43, 11 Nov (1972).

56) M.I. COHEN J. Franklin Inst. 283, 271, (1967).

57) B.F. SCOTT "Seminar on laser welding, drilling and cutting" W1. June 1975.

58) V.S. DORN and D.D. McCRACKEN "Numerical methods and Fortran programming", Wiley, (1964).

59) E. SCHMIDT Foppls. Festschrift, Springer, Berlin (1924), pp179-198.

60) G.M. DUSINBERRE "Numerical analysis of Heat Flow" McGraw Hill, New York (1949).

61) C. RUNGE Math. ann. vol 46, 167-178, 1895.

62) W. KUTTA   Z. Math. Phys. vol 46, 435-453, 1901.

63) A. RALSTON "Runge-Kutta methods with minimum error bounds",
Mathematics of computation, 16, 431-437 (1962).

64) G. LEIBMANN   Brit. J. App. Phys., $\underline{6}$, 129, (1955), 3.

65) J. CRANK and P. NICOLSON   "A practical method for
numerical evaluation of solutions for partial differential
equations of the heat conduction type". Proc. Cam. Phil.
Soc., $\underline{43}$, 50, (1947).

66) L.F. RICHARDSON   Math. Ganette, $\underline{12}$, 415, (1925).

67) D.L. HODGETT and B.F. SCOTT   "Pulsed laser machining",
Inst. E.E. conf. publ. 61, pp229-38, London 1970.

68) R. GARDON, J. COBONPUE,   Int. Heat Trans. Conf. ptII,
pp454-460, (1961).

69) E.Z. POLHAUSEN   Angew Math. U. Mech. I p115 (1921).

70) R.H. PERRY, C.H. CHILTON, S.D. KIRKPATRICK Chemical
Engineers Handbook 3-230, 4th Edition (1963).

71) S.G. STARLING and A.J. WOODALL, Physics 2nd ed. Longmans,
Green,London (1957).

72) R.B. BIRD, W.E. STEWART, E.N. LIGHTFOOT, "Transport
phenomena" (1961), John Wiley and Sons Inc.

73) Cobalt Monograph (1960) publ. centre d'information du Cobalt.

74)   DUTTA Ph.D. thesis, Birmingham University, October 1974.

75) A.E. SIGMUND "Unstable optical resonators" app. opt. vol 13
pp353-367, 1974

76) L. ALLEN "Optimum output coupling of gas laser light from
inhomogeneously broadened lines" J. Phys. (E) Series, 2,
$\underline{1}$, 794, (1968).

77) R.S. ANDERSON and M.S. WILLS SERL Tech. Report T11 Sept 1968.

78) M.J. WRIGHT   SERL Technical Report No M256 Nov 1967.

79) F. HORRIGEN, C. KLEIN, R. RUDKO, D. WILSON   "Windows for
high powered lasers" Laser Technology, Jan 1969, p68.

80) ROFIN   IR Laser Optics Information sheet 1975.

81) G.J. BULLEN (1959) Acta Cryst. 12, p703.

82) R.L. Van HEMERT, L.B. SPENDLOVE, R.E. SIEVERS, J. Electrochem.
Soc. 112, 1123, (1965).

83) E.W. BERG, J.T. TRUEMPER Anal Chim Acta 32, p245, 1965

84) J. Von HOENE, R.G. CHARLES, W.M. HICKAM, J. Phys. Chem. 62, p1098 (1958).

85) E.J. JABLONOWSKI Cobalt 14, 28 (1962).

86) R.G. CHARLES and P.G. HAVERLOCK J. Inorg. Nucl. Chem. 1969, vol 31, p995-1005.

87) M.J. WRIGHT SERL Technical Report M268.

88) L.G. DESHAZER and J.H. PARKS "Damage in laser materials" NBS Special publication 356.

89) L. ALLEN, D.G.C. JONES Principles of Gas Lasers", Butterworth, 1967.

90) H. KOGELNIK "Modes in optical resonators","Lasers" vol 1 edited by A.K. Levine, p295, Edward Arnold, London 1966.

91) H. KOGELNIK and T. LI "Laser beams and resonators", App. Opt. Vol 5 No10, p1550, Oct 1966.

92) A.G. FOX and T.LI Bell Syst. Tech. J. 40, 453 (1961).

93) O. KUBACHEWSKI, K. KELLY Bull. U.S. Bureau of Mines, 1949, No 476.

94) R.W. WAYNANT, J.H. CULLOM, J.T. BASIL and G.D. BALDWIN App. Opt. 4, 1648-1651, (1965).

95) L. MARSHALL Laser Focus April 1971, p26.

96) G.D. BOYD and J.P. GORDON Bell Syst. Tech. J. 40, 489, (1961).

97) G.A. DESCHAMPS and P.E. MAST Proceedings of the symp. on quasi optics", p379, Polytechnic Press, New York, 1964.

98) D.G. SINCLAIR and E.W. BELL "Gas Laser Technology", New York, Holt, Rinehart and Winston 1969.

99) A.L. BUCK Proc. I.E.E.E. 55, 450 (1967).

100) J.P. CAMPBELL and L.G. DESHAZER J. Opt. Soc. Am. 59, 1427, (1969).

101) L.D. DICKSON App. Opts. Vol 9, No 8 p1854, Aug (1970).

102) C. FISHER "The Microscope", vol 19, 1, pp1-20, 1971.

103) J.E. HARRY "Industrial Lasers and their Applications" McGraw Hill, 1974, p27.

104) W.L. WOLFE and S.S. BALLARD "Optical materials, films, and filters for infra-red instrumentation" Proc. I.R.E., 47, (9), 1590-1545 (1959).

105) G.W. MOREY "The properties of glass" 2nd Ed. Reinhold Pub. Corp., New York (1954).

106) S. NAMBA ; P. HYON KIM , N. KINOSHITA and T. Arai, Laser review, vol 1 No 1 p6, Jan (1968).

107) W.J. PARKER, R.J. JENKINS, C.P. BUTLER and G.L. ABBOTT, "Flash method of determining thermal diffusivity, heat capacity and thermal conductivity". J. App. Phys. 32 9, 1679 Sept (1961).

108) A.B. DONALDSON J. App. Phys. 43, 10, 4226, Oct (1972).

109) M.R. BRAMSON "Infra red radiation: handbook for applications" (1968), Plenum Press.

110) F. HERZOG Industrie - Anzeiger No 60 27 July, (1962).

111) J.S. HILL "Measurement of transparent thin films, Min. Tech. Report No 69025, July (1969).

112) B. ROSENTHAL Trans ASME 68, pp849-865, Nov 1946.

113) L.O. HELFINGER, R.F. WUERKER, R.E. BROOKS, "Holographic Interferometry" J. Appl. Phys. 1966, 37, 642.

114) W.M. STEEN "Holograph a new engineering tool?" University vision No 3, 1969.

115) C. BEADLE "The Quantimet 720 image analysing computer", Practical Metallograph, vol 7 5, pp249-56, 1967.

116) D. HACMAN Balzers Report - 4th July 1965.

117) K. MASUBUCHI "Calculation and measurement of residual stresses due to spot heating " Welding research abroad, vol 9 no9 Nov (1963) p 91-95.

118) M. WATANABE and K. SATO "Thermal stresses and residual stresses of a circular plate heated at its centre". J. Soc. Nav. Arch. of Japan No 86, (1954).

119) H. KIHARA, M. NISIDA, and Y. FUJITA "On residual stresses due to spot heating" Int. Inst. Welding Commission x document x 267-61 (1961).

120) K. MASUBUCHI "Control of distortion and shrinkage in welding" Weld. Res. Bulletin no 149, April 1970.

121) H. KIHARA "Researches on welding stress and shrinkage distortion in Japan". 60th Anniv. Series No 4 Soc. Naval Arch of Japan 13-21 (1959).

122) M. OTANI "Graphical solution of thermal stresses in welding". (1st report) Journ of Japan Welding Society, Vol 17 (1948).

123) S. TIMOSHENKO and J.N. GOODIER "Theory of elasticity" p416 et seq. McGraw Hill (1951).

124) H. MOORE "Selenium, telurium, cobalt and nickel in glass making", Mond Nickel Company Limited.

125) R. H. DOREMUS "Glass Science", Wiley, London 1973.

126) J.F. ASMUS and F.S. BAKER Record 10th Symp. on electron ion and laser beam tech: San Francisco Press, San Francisco p241, (1969).

127) J.M. MORAN "Laser machining with a holographic lens" Appl. Opt. 10 (2), 412-415, 1971.

128) New Scientist 41 (637), 402, 1969, "Printing a book at a time by laser holograph".

130) D.A. DAWSON, O. TRASS (1966) Can J. Chem. Eng. June p121 and D.A. Dawson (1965) M.A.Sc. Thesis, Department of Chemical Engineering, University of Toronto.

131) F.D. SEAMAN and D.S. GNANAMUTHU "Using the industrial laser to surface harden and alloy" Metal Progress. Aug. 1975, p67-74.

132) J.D. RUSSELL "Development of the laser as a welding and cutting tool", Welding Inst. Res. Bulletin, Dec. 1975, p345-350.

133) E.L. BAARDSEN, D.J. SCHMATRY and R.E. BISARO "High speed weldingof sheet steel with a CO_2 laser" Welding Journ. April 1973, 227-229.

134) R.C. CRAFER "A 2kW CO_2 system for welding sheet material" Third International Conf. on advances in welding processes 1974, paper 26, p178-184.

135) M.J. ADAMS "Gas jet laser cutting" Proceedings of the conference on advances in welding processes 1970, paper 14, p140-146.

136) C.M. ADAMS, R.H. FAIRBANKS Welding J., 43, 97S-102S, (1964).

LIST OF FIGURES

ACKNOWLEDGMENTS

In 1967 Dr. A.W.D. Hills kindly introduced the author to the idea of forming shaped deposits directly from the vapour phase by means of suitably structured jets of thermally sensitive chemical blowing onto a heated surface. This led to the Ph.D. thesis of Dr. G.J. Davies on "Mass Transfer from a Turbulent Impinging Jet with and without Chemical Reaction" – London University, 1971, supervised by the author. However, it became progressively clearer to the author as the work proceeded that really clean shaped, small deposits could not be produced this way. Shaping the heat, as opposed to the jets, might be a possible solution. With the help and encouragement of Dr. A.W.D. Hills this present work was then started.

The author would like to acknowledge the help and support of his two supervisors, Dr. A.W.D. Hills (1968–1971) and Professor A.V. Bradshaw (1971–1975) both of whom gave encouragement when this complex set of equipment was behaving in Maverick style.

Sincere thanks are extended to A. Young for his help in operating the equipment, particularly the evaporator system, and for his faith and enthusiasm in laser deposition processes, to Dr. G.J. Davies for his excellent background work and to Professor W. Welford of Applied Optics, who helped in confirming some of the optics work.

The author is grateful to the Science Research Council for their financial support of this project. To the Metallurgy Department of Imperial College for allowing it space, and to his fellow members of staff and workshop technicians whose proficiency and co-operation helped solve many difficult problems.

Finally thanks are due to Miss G. Page for typing this thesis, and to Dr. J.H.E. Jeffes for filling the breach after Professor A.V. Bradshaw left and when it appeared that for bureaucratic reasons a supervisor was essential.